Uwe Kätzel

Dynamic Light Scattering for the Characterization of Polydisperse Fractal Systems by the Example of Pyrogenic Silica

Dresden 2007

2007

Bünaustr. 54, D-01159 Dresden

Satz und Redaktion: Uwe Kätzel

Printed in Germany 2007

Dynamic Light Scattering for the Characterization of Polydisperse Fractal Systems by the Example of Pyrogenic Silica

von der Fakultät Maschinenwesen
der Technischen Universität Dresden
zur Erlangung des akademischen Grades

Doktoringenieur (Dr.-Ing.)

genehmigte Dissertation

von

Dipl.-Ing. Uwe Kätzel
aus Dresden

Dresden 2007

Tag der Einreichung: 21.03.2007
Tag der Verteidigung: 12.11.2007

Gutachter: Prof. Dr.-Ing. habil. W. Klöden
Prof. Dr.-Ing. habil. H. Nirschl
Dr. rer. nat. H. Barthel

Vorsitzender der Promotionskommission: Prof. Dr.-Ing. B. Kieback

Abstract

Dynamic light scattering (DLS) is a method to size submicron particles by measuring their thermal motion (diffusion) in suspensions and emulsions. However, the validity of the Stokes-Einstein equation that relates the diffusion coefficient and the particle size is limited to spherical particles and very low concentrations. Within this thesis, DLS is used for the characterization of diluted and concentrated suspensions of pyrogenic silica which consists of fractal-like aggregates composed of sintered spherical primary particles. Additionally, both the primary particle sizes and the aggregate sizes show polydispersity. These structural features clearly complicate the understanding of DLS experiments and have been a severe obstacle to employing DLS as routine standard tool for the characterization of pyrogenic silica. Nevertheless, the method is fast, robust, easy-to-use and in principal sensitive to the structural properties of pyrogenic silica. The main objective of this thesis has therefore been to evaluate the application of DLS in product development and quality assurance of pyrogenic silica industry, what essentially means to identify those structural properties of fractal aggregates which are measurable with DLS and to quantify the method's sensitivity to changes in these properties. The investigations presented here are split up into four parts.

Firstly, simulations are employed to establish a relation between structural (i.e. fractal) properties of the aggregates and their hydrodynamic behavior. Therefore, an algorithm is developed that enables the generation of aggregates with a tunable fractal dimension while the number of primary particles per aggregate remains arbitrary. The calculated hydrodynamic diameters of translation are then compared to the structural radii of gyration for pyrogenic silica. The concept of hydrodynamic dimensions is introduced to account for a different scaling of the hydrodynamic radii. Furthermore, the effect of rotational aggregate diffusion is shown to be important for the interpretation of DLS data.

The theoretical results are then verified in experiments. The structure of different pyrogenic silica grades is, therefore, characterized by static light and X-ray scattering. The hydrodynamic radii are obtained from multi-angle DLS measurements where the effect of rotation is reflected in the scattering-angle dependence of the effective diffusion coefficient. It is evinced that the generation of pyrogenic silica aggregates can be described as a diffusion-limited cluster aggregation but that a complete description should include the change of sintering during aggregation. Finally, the influence of rotational diffusion is characterized in terms of a master-curve. The existence of such a curve has already been predicted by simulations in the literature.

The third part of this thesis deals with the characterization of concentrated suspensions. As theoretical models only exist for spherical particles, the results of pyrogenic silica are analyzed in comparison to spherical silica sols. It is shown, that the diffusion coefficient spectra obtained by an inversion of the DLS data represent different concentration effects such as collective diffusion and suspension structuring. The influence of interparticle interactions is obtained by a screening of the counterionic repulsion forces in the suspensions.

Eventually two specific measurement tasks are addressed, which are highly relevant for pyrogenic silica suspensions: the observation of fluid-solid phase transitions and the detection of smallest fractions of unwanted coarse particles in the suspension. For the gelation of pyrogenic silica a literature approach is adapted to neglect non-ergodic contributions in the measured signals. The use of a combined exponential/stretched-exponential fit of consecutive DLS runs then enables the determination of the phase transition time and the transition kinetics. The detection of coarse particles is of great relevance, e.g. for the process of Chemical-Mechanical Planarization in the microelectronics industry. It is experimentally shown that the state-of-the-art analysis techniques of DLS do not provide sufficient sensitivity. By the use of a principal components analysis the sensitivity is enhanced by two orders of magnitude.

Zusammenfassung

Die Dynamische Lichtstreuung (DLS) ist eine Messmethode zur Größenbestimmung submikroner Partikel. Dabei wird primär die stochastische Bewegung der Teilchen (Diffusion) in Suspensionen und Emulsionen bewertet. Die Stokes-Einstein Gleichung, die das Verhältnis zwischen gemessenem Diffusionskoeffizienten und Partikelgröße wiedergibt, ist jedoch nur für kugelförmige Teilchen, die in sehr niedriger Konzentration vorliegen, gültig. In der vorliegenden Arbeit wird die dynamische Lichtstreuung zur Charakterisierung von verdünnten und konzentrierten Suspensionen pyrogener Kieselsäure eingesetzt. Diese besteht aus fraktalen Aggregaten, die wiederum aus versinterten aber meist kugelförmigen Primärpartikeln zusammengesetzt sind. Zusätzlich liegen sowohl die Primärpartikelgrößen als auch die Aggregatgrößen verteilt vor. Diese strukturellen Eigenschaften erschweren die Anwendbarkeit der DLS bzw. die Interpretation der Messergebnisse und verhinderten bisher den Einsatz der DLS als Routinemethode zur Charakterisierung pyrogener Kieselsäuren. Gleichwohl ist das Messverfahren prinzipiell sensitiv für die strukturellen Eigenschaften und aufgrund der einfachen, schnellen und robusten Funktionsweise prädestiniert für den industriellen Einsatz. Das Hauptziel dieser Arbeit ist daher eine Bewertung der Möglichkeiten der DLS für die Produktentwicklung und Qualitätssicherung in der Herstellung pyrogener Kieselsäuren. Das bedeutet im Besonderen, dass sowohl die messbaren granulometrischen Eigenschaften als auch die Sensitivität der Methode bei Eigenschaftsänderungen ermittelt werden müssen. Die hier durchgeführten Arbeiten können in vier Teile gegliedert werden.

Zuerst werden Simulationen beschrieben, die eine Beziehung zwischen strukurellen (d.h. fraktalen) Eigenschaften der Aggregate und ihrem hydrodynamischen Verhalten herstellen. Dazu wird ein Algorithmus entwickelt, der die Erstellung von Aggregaten mit frei wählbarer fraktaler Dimension ermöglicht, wobei auch die Anzahl der Primärpartikel im Aggregat nicht eingeschränkt wird. Die berechneten hydrodynamischen Translationsradien für pyrogene Kieselsäuren werden dann mit den jeweiligen Gyrationsradien verglichen. Um eine unterschiedliche

Skalierung der hydrodynamischen Radien zu berücksichtigen, wird das Konzept der hydrodynamischen Dimensionen eingeführt. Des Weiteren wird gezeigt, dass die Rotationsdiffusion der Aggregate einen starken Einfluss auf die DLS-Daten hat.

Die erhaltenen Resultate werden im nächsten Teil mit experimentellen Befunden verifiziert. Dazu wird die Struktur verschiedener pyrogener Kieselsäuren mittels statischer Licht- und Röntgenstreuung charakterisiert. Die hydrodynamischen Radien werden durch Mehrwinkel-DLS bestimmt, wobei der Einfluss der Rotationsdiffusion aus der Abhängigkeit der Ergebnisse vom Streuwinkel erhalten wird. Es wird aufgezeigt, dass die Erzeugung von Aggregaten pyrogener Kieselsäure am Besten durch eine diffusionslimitierte Clusteraggregation beschrieben werden kann, wobei eine vollständige Beschreibung die Veränderung des Versinterungsgrades während der Aggregation berücksichtigen muss. Schließlich wird der Einfluss der Rotationsdiffusion in Form einer Masterkurve charakterisiert. Die Existenz einer solchen Kurve wurde bereits in der Literatur vorhergesagt.

Der dritte Schwerpunkt dieser Arbeit ist die Charakterisierung konzentrierter Suspensionen. Da theoretische Modelle nur für kugelförmige Partikel existieren, werden die Ergebnisse für pyrogene Kieselsäuren im Vergleich zu Daten sphärischer Kieselsole betrachtet. Es wird gezeigt, dass in den durch Inversion der primären Messdaten erhaltenen Diffusionskoeffizientenverteilungen verschiedene Konzentrationseffekte wie Kollektivdiffusion und eine Strukturierung der Suspensionen beobachtet werden können. Der Einfluss von Zwischenpartikelwechselwirkungen wird durch eine Abschirmung der abstoßenden Doppelschichtkräfte näher betrachtet.

Der letzte Teil berichtet über die problembezogene Analyse von DLS-Daten am Beispiel der Charakterisierung von Fest-Flüssig Phasenübergängen sowie zur Detektion kleinster Fraktionen unerwünschter Grobpartikel in den Suspensionen. Zur Beobachtung der Gelierung von pyrogenen Kieselsäuren wird ein Literaturansatz adaptiert, um nichtergodische Signalanteile vernachlässigen zu können. Der Einsatz eines kombinierten Exponential-/Potenzansatzes ermöglicht dann die Bestimmung des Phasenübergangszeitpunktes und der Übergangskinetik. Die Detektion von Grobpartikeln ist von hoher technischer Bedeutung, z.B. beim Prozess des Chemisch-Mechanischen Planarisierens in der Mikroelektronikindustrie. Es wird experimentell gezeigt, dass die Standardanalysealgorithmen der DLS keine genügende Sensitivität für diese spezielle Fragestellung aufweisen, während diese durch den Einsatz einer Hauptkomponentenanalyse um zwei Größenordnungen verbessert werden kann.

Preface

This thesis originates from my work at the Research Group Mechanical Process Engineering of the Institute of Process Engineering and Environmental Technology, Faculty Mechanical Engineering, TU Dresden. During this time I had the opportunity to work on different research projects and to supervise a couple of student projects and diploma theses. Pyrogenic material systems and dynamic light scattering techniques, respectively, always remained an affiliating point in these multifaceted tasks.

A thesis is not something you just write in an unimpeded moment. During the last three and a half years many people have supported me, sometimes in experiments, often with advice or simply mental. Therefore, I would like to take the opportunity to thank all those who had a contribution to this final result.

In particular I have to make a serious acknowledgment to Professor Klöden for the supervision of this thesis and for giving me inspiring advice.

I would like to thank Professor Nirschl from the University of Karlsruhe and Dr. Barthel from Wacker-Chemie AG, Burghausen for the attendance to write an expertise for this thesis.

For their conceptual contributions to my thesis, I have to thank Dr. Stintz (TU Dresden), Dr. Barthel and Dr. Gottschalk-Gaudig (Wacker-Chemie AG). Our half-yearly R&D meetings have laid the basis for the conducted experiments and simulations. Of course, I am very grateful for the financial support I received from Wacker-Chemie AG during the last years.

I will not forget all the colleagues and students that supported me. Especially, I want to thank Dr. Babick for the intensive technical discussions and for multiple proofreadings of the manuscript of this thesis, Dipl.-Ing. Richter and Dipl.-Phys. Bedrich for their contributions during their diploma theses and Dipl.-Ing. (BA) Vorbau and André Kupka for their help in the experiments.

Last but not least, I would like to gratefully acknowledge the support I received from my family and especially from my wife Lydia. She has always shown appreciation for the problems arising in this work and during the set up of the manuscript.

Uwe Kätzel Dresden, March 2007

Contents

Nomenclature

Latin Variables

a	Scattering amplitude	[-]
A_{131}	Hamaker constant between particles (1) through medium (3)	[J]
B	Intensity level constant	[a.u.]
b	Coherence factor	[-]
C	Constant	[-]
c	Molar concentration	$[\mathrm{mol\,l^{-1}}]$
C_v	Coefficient of variation	[-]
D	Dimension	[-]
E	Electric field	$[\mathrm{V\,m^{-1}}]$
erf	Gauss error function	[-]
F	F-test variable	[-]
f	Heywood factor	[-]
F_s	Self-intermediate scattering function	[-]
G'	Storage modulus	[Pa]
G''	Loss modulus	[Pa]
G^*	Complex shear modulus	[Pa]
G_1	First-order electric field correlation function	$[\mathrm{V^2 m^{-2}}]$
g_1	Normalized field-correlation function	[-]
G_2	Second-order intensity correlation function	[a.u.]
g_2	Normalized intensity autocorrelation function	[-]
h	Height	[m]

I	Intensity	[a.u.[1]]
I_m	Moment of inertia	$[\mathrm{kg\,m^2}]$
I_s	Ionic strength	$[\mathrm{mol\,l^{-1}}]$
K	Cumulant of a distribution	[a.u.]
k	Wave number	$[\mathrm{m^{-1}}]$
k_f	Fractal prefactor	[-]
k_h	Hydrodynamic prefactor	[-]
k_p	Permeability	$[\mathrm{m^2}]$
l	Length scale	[m]
M	Moment of a distribution	[a.u.]
m	Mass	[kg]
N	Number	[-]
n	Medium refractive index	[-]
P	Particle form factor in Rayleigh-Debye-Gans scattering	[-]
p	Pressure	[Pa]
p_r	Probability of rejection	[-]
PDI	Polydispersity index	[-]
q	Probability density	[a.u.]
R	Radius	[m]
r	Distance or position	[m]
Re	Reynolds number	[-]
S	Spectral density	[-]
s	Magnitude of the scattering vector	$[\mathrm{m^{-1}}]$
S_m	Mass-specific surface area	$[\mathrm{m^2\,kg^{-1}}]$
T	Temperature	[K]
t	Time	[s]
u	Complex scattering amplitude	$[\mathrm{V\,m^{-1}}]$

[1] The SI-Unit of Intensity is $[\mathrm{W/m^2}]$ but in the scattering experiments treated in this thesis an equivalent to intensity is measured either as a total photon count which is dimensionless or as a photon count rate [Hz]. The conversion to the SI-unit is not helpful and is therefore neglected in the relevant literature.

V	Potential of interaction	[J]
v	Velocity	[ms^{-1}]
Var	Variance	[-]
x	Particle size	[m]
x_{ST}	Sauter diameter	[m]
z	Valency of ions	[-]

Greek Variables

α	Regularization parameter	[-]
β	Stretch parameter	[-]
γ	Strain	[-]
δ	Sliplength	[m]
ε	Porosity	[-]
ε_r	Relative permittivity	[-]
ζ	Zeta potential	[V]
η	Dynamic viscosity	[Pa s]
θ	Observation (scattering) angle	[-]
Θ_{rot}	Rotational diffusion coefficient	[s^{-1}]
κ	Debye-Hückel parameter	[m^{-1}]
λ	Wavelength	[m]
λ_i	Eigenvalue	[-]
μ	Fit parameter	[-]
ν	Interaction parameter	[-]
$\Xi_{1,2,3}$	Eigenvalues of the rotation matrix $\mathbf{\Xi}$	[-]
ρ	Density	[$kg\,m^{-3}$]
σ	Stress	[Pa]
τ	Lag time	[s]
$\tau_{1,2}$	Decay times	[s]
φ	Volume fraction	[-]
Ψ	Sphericity of Wadell	[-]

$\Psi_{1,2,3}$	Eigenvalues of the translation matrix $\mathbf{\Psi}$	[-]
ω	Circular frequency	$[\mathrm{s}^{-1}]$

Vectors and Matrices

$\mathbf{D}$	Data matrix for principal components analysis	[-]
$\mathbf{E}$	Electric field vector	$[\mathrm{V\,m}^{-1}]$
$\mathbf{e}$	Unit vector	[-]
$\mathbf{F}$	Force vector	[N]
$\mathbf{K}$	Kernel matrix	[-]
$\mathbf{k}$	Wave vector	$[\mathrm{m}^{-1}]$
$\mathbf{M}$	Covariance matrix	[-]
$\mathbf{R}$	Displacement vector	[m]
$\mathbf{r}$	Position vector	[m]
$\mathbf{R}_{eg}$	Regularizor	[-]
$\mathbf{s}$	Scattering vector	$[\mathrm{m}^{-1}]$
$\mathbf{T}$	Torque vector	[N m]
$\mathbf{v}$	Velocity vector	$[\mathrm{m\,s}^{-1}]$
$\mathbf{\Gamma}$	Transformation matrix	[-]
γ	Eigenvector to eigenvalue λ_i	[-]
$\boldsymbol{\epsilon}$	Error vector	[-]
$\mathbf{\Theta}$	Inertia tensor	[N m]
$\mathbf{\Xi}$	Rotation matrix	[-]
$\mathbf{\Pi}$	Pressure tensor	[Pa]
$\boldsymbol{\phi}$	Rotation angle	[-]
$\mathbf{\Psi}$	Translation matrix	[-]

Constants

e	Euler's number	$[\approx 2.71828]$
$\mathrm{k_B}$	Boltzmann's constant	$[1.380658 \cdot 10^{-23}\ \mathrm{J\,K}^{-1}]$
$\mathrm{N_A}$	Avogadro constant	$[6.0221367 \cdot 10^{23}\ \mathrm{mol}^{-1}]$
$\mathrm{e_0}$	Elementary charge	$[1.60219 \cdot 10^{-19}\ \mathrm{C}]$

g	Acceleration due to gravity	$[9.81\,\mathrm{ms}^{-2}]$
i	Imaginary unit	$[\sqrt{-1}]$
ϵ_0	Vacuum permittivity	$[8.854 \cdot 10^{-12}\,\mathrm{C}^2\,\mathrm{N}^{-1}\,\mathrm{m}^{-2}]$
π	Ratio of a circle's circumference to its diameter	$[\approx 3.14159]$

Common Indices

agg	Aggregate
c	Static
f	Fractal
fl	Fluctuating
g	Gyration
h	Hydrodynamic
i	Counting index
inc	Incident
j	Counting index
l	Liquid
m	Mass-related
prim	Primary particle
pt	Phase transition
S	Surface-related
s	Solid
sca	Scattered

Abbreviations

a.u.	Arbitrary units
ACF	Auto-Correlation Function
APD	Avalanche Photodiode
BET	Brunauer-Emmett-Teller model for gas adsorption
CFF	Correlation Function of the Fluctuating field
CMP	Chemical-Mechanical Planarization
CONTIN	Constrained Regularization Method for Inverting Data

DLCA	Diffusion-Limited Cluster Aggregation
DLS	Dynamic Light Scattering
FCF	Field Correlation Function
FOQELS	Fiber-Optic Quasi-Elastic Light Scattering
HPPS	High Performance Particle Sizer
HS	Hard-Sphere
NNLS	Non-Negative Least Squares
PCA	Principal Components Analysis
PCS	Photon Correlation Spectroscopy
PMT	Photomultiplier Tube
QELS	Quasi-Elastic Light Scattering
RLCA	Reaction-Limited Cluster Aggregation
ROI	Region of Interest
rpm	Revolutions per Minute
SANS	Small-Angle Neutron Scattering
SAXS	Small-Angle X-ray Scattering
SLS	Static Light Scattering
TEM	Transmission electron microscope / microscopy

Vectors and Matrices are printed in **bold** throughout the thesis.

1 Introduction

1.1 Dynamic Light Scattering

This thesis addresses the application of Dynamic Light Scattering (DLS) in industrially relevant systems and processes. In particle size analysis DLS has been established over several years for the characterization of sub-micron particles and macromolecules [1–3]. The names Quasi-Elastic Light Scattering (QELS) and Photon Correlation Spectroscopy (PCS) are treated as synonyms for DLS in publications, though this is not fully correct for PCS. The measurement principle is based on a time-resolved measurement of the scattered light intensity from a sample cell that contains the particle system in a solvent. Due to the erratic motion of the particles caused by non-compensated impacts of the solvent molecules (so-called Brownian motion or diffusion [4]) the intensity oscillates round an average value. The frequency of these fluctuations contains information about the diffusion coefficient of the particles, which in turn is size-dependent.

The measurement principle requires that diffusion is the only cause of motion in the sample, i.e. that effects of sedimentation, thermal convection and fluid flow have to be avoided. This usually limits the upper particle size that can be measured with DLS to some micrometers. The lower size limit is determined by the time resolution of the specific measurement device and lies typically in the range of a few nanometers. Therefore, DLS is an addendum to the laser diffraction technique (which is the workhorse for particle scientists in the micrometer range) for particle sizing in the sub-micrometer scale.

The interpretation of DLS data has to be carried out with care, since an unambiguous relationship between the measured diffusion coefficient and the particle size can only be found for dilute dispersions of spherical particles [1, 5, 6]. Hence, there are limitations regarding sample concentration and particle shape.

In conventional DLS high sample concentration is a big problem. If the scattered light from one particle encounters other particles before it is registered at the detector (so-called multiple scattering) the size information of the signal is lost. In the last years commercially available instruments that suppress multiple scattering effects have been developed. Thus, the measurable concentration range is now remarkably extended.

1.2 Pyrogenic Silica

Pyrogenic is a composition of the two Greek words *pyro*, which means fire or heat, and *genes*, which means to generate or to produce. In the sense of a material description it means that the material is produced by burning or high temperature processes. The term *fumed* is also widely used as a synonym to *pyrogenic*.

There are many materials in industry today, whose production may be called pyrogenic. Probably the one with the highest annual production is carbon black ($\sim$ 7.000.000 tons in 1997 [7]) followed by pyrogenic silica with an annual production of roughly 180.000 tons and pyrogenic alumina (no more than 20.000 tons/year). Production rates of pyrogenic titania, ceria or zirconia are much lower. In the last years many high temperature processes for the production of other materials have been developed but these have not yet reached a remarkable market volume [8].

Pyrogenic silica has many applications in suspensions as thixotropic or thickening agent and as anti-settling agent, e.g. in paints, resins or inks [9]. Additionally, pyrogenic silica suspensions are used in the microelectronics industry in the process of Chemical-Mechanical Planarization (CMP). Thus, there is a need for the characterization of pyrogenic silica suspensions for the purpose of quality assurance as well as in product development. As shown later in this work, dynamic light scattering techniques provide a multitude of possibilities in the accomplishment of these targets.

The production process of pyrogenic silica is a high temperature hydrolysis. Gaseous silicon tetrachloride reacts in a hydrogen/oxygen flame to produce pyrogenic silica and hydrogen chloride.

$$\mathrm{SiCl_4\,(g) + 2\,H_2 + O_2 \Rightarrow SiO_2\,(s) + 4\,HCl\,(g)}$$

First, very small protoparticles containing only few SiO_2 molecules are formed, which sinter completely in the hot zone of the flame to give primary particles with sizes of $5-100$ nm. These primary particles sinter further in flame zones with lower temperature. Here, the sintering is not complete, i.e. colloidal aggregates with a size of $\sim 100-500$ nm are formed instead of larger primary particles.[1] By the virtue of van-der-Waals forces these aggregates form micron-sized agglomerates.[2] Figure 1.1 shows the production process schematically.

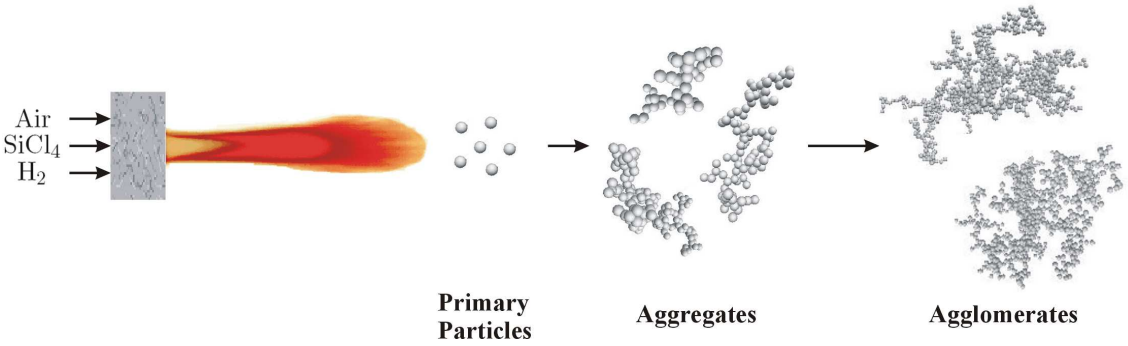

Figure 1.1: Scheme of the production of pyrogenic silica by high temperature hydrolysis

The hydrogen chloride remains partly adsorbed onto the silica surface after the generation process. It has to be removed by flushing air in a fluidized bed. The final product then contains only minor portions of hydrogen chloride (~ 50 ppm). Other contaminations lie in the lower ppm or even in the ppb-region [12], so pyrogenic silica can be considered a chemically very pure product.

Changing the feed composition of the burner results in different flame temperatures as well as different residence times of the primary particles in the flame. This finally leads to different silica grades that are most often distinguished by their different specific surface area S_m and the corresponding Sauter diameter x_{ST},[3]

$$x_{ST} = \frac{6}{S_m \rho_s} \tag{1.1}$$

[1] Colloids have at least one dimension in space whose extension is lower than 1 µm and larger than 1 nm. Thus, thin films, low diameter fibres and of course small particles such as pyrogenic silica aggregates are called *colloidal*.

[2] The terms aggregate and agglomerate are used in this work in compliance with [10, 11], i.e. an aggregate and an agglomerate are both composed of smaller primary particles but while an agglomerate can be decomposed under the expense of (mostly) mechanical energy such as shear stress or ultrasound, an aggregate cannot be further disintegrated.

[3] The formal definition of the Sauter diameter [13, 14] includes a shape factor, either the Heywood-factor f [15] or the sphericity of Wadell Ψ [16], which are inverse pairs. However, these shape factors are not used to describe fractal aggregates, so they are avoided here.

where ρ_s is the solid density. The Sauter diameter can be understood as a mean diameter of the primary particle size distribution. However, one has to keep in mind that the primary particles are sintered in an aggregate and therefore do not possess their whole surface area, so the use of the Sauter diameter is slightly questionable.

Powders with specific surface areas ranging from $50\,\mathrm{m}^2/\mathrm{g}$ to $400\,\mathrm{m}^2/\mathrm{g}$ are commercially available. Analysis of the different grades with transmission electron microscopy (TEM) reveals that samples with low specific surface area have a broad distribution of primary particle sizes (typically from $5-100\,\mathrm{nm}$) while this distribution becomes narrower for the samples with higher specific surface area. Figure 1.2 illustrates the difference for two silica grades. Interestingly, it seems that the size of the primary particles in a single aggregate does not vary much.

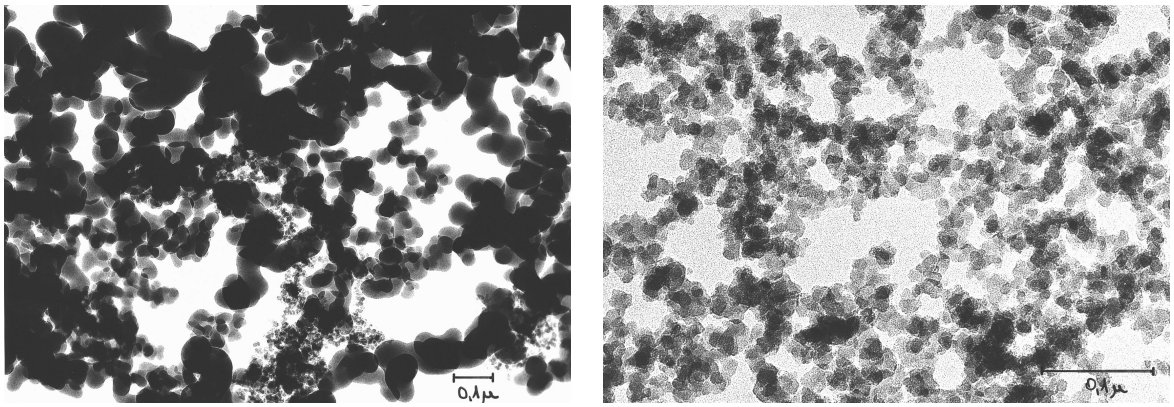

(a) (b)

Figure 1.2: Transmission electron micrograph of pyrogenic silica with (a) $S_\mathrm{m} = 50\,\mathrm{m}^2/\mathrm{g}$ and (b) $S_\mathrm{m} = 300\,\mathrm{m}^2/\mathrm{g}$, please note the different scales of the images.

It is this intrinsic polydispersity of the primary particle sizes as well as the occurrence of the particle aggregates which hampers the analysis and definition of equivalent particle sizes. On the other hand a characterization of the state of dispersion is greatly demanded by today's requirements in product quality assurance as well as in the development of new products.

1.3 Aim of the Work and Outline

The primary goal of this work is to highlight and extend the potential of applications of dynamic light scattering techniques for the characterization of polydisperse fractal systems. Attention will be paid to industrially relevant, i.e. mainly concentrated systems. Therefore, it is necessary

to deal with the specifics and details of the measurement principle in concentrated suspensions on the one hand and with the particular diffusive behavior of polydisperse fractal aggregates on the other hand.

The following tasks will have to be addressed:

- Which (geometrical) property of a fractal aggregate of pyrogenic silica determines the diffusional behavior?
- How is the diffusional behavior of pyrogenic silica aggregates reflected in DLS measurement results?
- Which effects are to be ascribed to the solids concentration and how are these related to the properties of the suspensions?
- How can DLS be used to investigate fluid-solid phase transitions that often occur in concentrated dispersions?
- What analysis technique is feasible to provide information on contaminations of pyrogenic silica suspensions with particles in the micrometer range which is an important issue in quality assurance?

In order to define the subjects of this work more precisely first a review on the state-of-the-art in DLS techniques and their application to interacting and fractal suspensions will be given. The results of the experimental and theoretical work will be presented in parts that handle a specific characterization task. This enables the reader to identify the relevant issues with more ease.

It is not the intention of this work to develop a new DLS instrument. A commercially available instrument is used for the majority of the conducted measurements since it is established in industry though it is restricted to a single scattering angle. This is a slight disadvantage compared to DLS goniometers which are often used in academic research. However, this is outweighed by a compact and easy-to-use set-up that additionally enables a suppression of multiple scattering effects.

Pyrogenic silica will be treated as the most relevant example for polydisperse fractal systems but the results can also be extended to other systems. The industrial manufacturers, the developers of suspensions containing pyrogenic materials and also the end-users of these suspensions will gain more insight into the underlying mechanisms that affect the measurement results and the

possible data analysis techniques for specific applications. This can extend the usage of dynamic light scattering in the laboratory and on-site[4] or even open up new ranges of applications.

[4] On-site is meant as a permanent process quality control during the manufacture of suspensions. As DLS instruments are not able to be mounted in the process line, the characterization has to take place in the vicinity.

2 State of the Art

2.1 Structure Description of Pyrogenic Silica

2.1.1 The Principle of Fractality

The word *fractal* stems from the Latin word *fractus* which means *broken* and was firstly introduced by B.B. Mandelbrot [17]. A fractal object is meant to be self-similar or scale-invariant, i.e. under magnification always the same basic elements of the structure are found. Perfect fractals are found in mathematics (Koch's snowflake, Cantor set). In nature many objects can be approximately described as fractals (clouds, trees, leaves, coastlines). The scale of a self-similar object obeys a power law between the number of basic elements N and their length scale l.

$$N \sim l^{D_f} \tag{2.1}$$

D_f is called the Hausdorff-Besicovitch-dimension or more frequently the fractal dimension [17]. Many regular objects such as a line, a disc or a sphere have integer fractal dimensions that are identical to their dimension of the Euclidean space, i.e. 1, 2 and 3, respectively. Fractals mostly have non-integer Hausdorff dimensions. The power-law behavior was firstly found by Richardson [18] when he investigated the length of different borders between countries but he did not recognize them as fractals. In memorial of this fundamental finding the log-log plots to determine D_f are also called Richardson-plots [19].

2.1.2 Relevance of Fractal Description for Pyrogenic Silica

The shape description of pyrogenic silica aggregates is clearly dependent on the magnification one looks at it [20]. On a molecular length scale the chemical structure of a primary particle is observed. If the scale is reduced the shape of the primary particles is firstly discovered. Though

it is considered that the primary particles are spheres, under this magnification the surface structure can be modelled as a fractal. Thus, the surface area shows a power law dependence with the radius of the primary particle with an exponent called D_f^S, the surface fractal dimension with values between 2 (perfect sphere) and 3 (very rough surface). Indeed, it could be shown that different grades of pyrogenic silica show varying surface fractality [21].

Further reducing the magnification reveals the structure of a single aggregate of sintered primary particles. On a certain length scale, the structure is self-similar and can be described as a fractal [20]. Now the power-law exists between the volume or mass of the aggregate and the length scale R_g, the radius of gyration.

$$m \sim {R_g}^{D_f^m} \tag{2.2}$$

R_g is defined as the square root of the moment of inertia divided by the total mass of a particle aggregate.

$$R_g = \sqrt{\frac{I_m}{m}} \tag{2.3}$$

If the primary particles of the aggregate are considered as point masses, the following general formula is derived:

$$R_g = \sqrt{\frac{\sum_{i=1}^{N_{prim}} m_i \left|\vec{r_i} - \vec{r_{cg}}\right|^2}{\sum_{i=1}^{N_{prim}} m_i}} \quad \xrightarrow{\text{for } m_i = \text{const.}} \quad R_g = \sqrt{\frac{1}{N_{prim}} \sum_{i=1}^{N_{prim}} \left|\vec{r_i} - \vec{r_{cg}}\right|^2} \tag{2.4}$$

where N is the total number of primary particles in the aggregate, $\vec{r_i}$ is the position vector of the i-th particle and $\vec{r_{cg}}$ is the position vector of the center of gravity of the aggregate.

The fractal dimension of single pyrogenic silica aggregates varies considerably due to the small number of primary units. However, if fractal analysis is performed at powders or suspensions the sample volume usually contains a huge number of different aggregates. Thus, averaging gives reproducible shape descriptions with only a few parameters. This also enables a comparison of differently produced powders.

An alternative way of describing a single aggregate employs its smallest circumsphere. The aggregate is then considered as a porous sphere with size x and porosity ε which also enables the comparison of different pyrogenic powders. However, it is inherent in the assumption that two aggregates cannot interpenetrate and that the porosity will always be the same in the whole

sphere. This must lead to physically wrong conclusions as the porosity of an aggregate is smallest in the center while it enlarges to the outer regions [22]. Therefore, the concept of the porous sphere approximation is not adequate for the characterization of pyrogenic silica and will not be examined further.

In the succeeding chapter 2.1.3 it will be demonstrated that the fractal description is natural for pyrogenic silica due to the production process.

2.1.3 Theoretical Description of Fractal Formation

Generally, every aggregate starts with a single seed particle. Aggregate growth is now accomplished by adding other primary particles to the seed particle. This scheme can also be easily realized in a computer simulation. Mostly Monte-Carlo algorithms [23] are used.

There are four different parameters that can be varied to achieve different types of aggregates:

Aggregate formation Aggregation is allowed only from primary particles to an existing aggregate (particle-cluster aggregation) or different clusters may also collide and stick together (cluster-cluster aggregation). The first option is very easy to implement in a simulation as the growing aggregate can be kept fixed in the center of a simulated box, while only the primary particle moves in the box until it sticks to the aggregate. Afterwards, the next primary particle is introduced. The second option involves more computational effort, since all clusters in the simulated box have to move simultaneously in a time step of the simulation. Thus, each time step involves multiple operations. Furthermore, the check for an occurring sticking event is more extensive. However, it is immediately obvious that the second option is closer to reality than the first one.

Particle trajectories The trajectories of the moving particles in the box may be linear (ballistic aggregation) or random and erratic, respectively (diffusive aggregation). The second option is accomplished by randomly choosing the direction of the motion vector in every time-step. Both modes have their physical interpretation. As diffusion is induced by impacts of solvent molecules, ballistic aggregation will occur in the gas phase at low solvent densities (i.e. low pressure) while at higher densities or in the fluid phase diffusive aggregation takes place.

Simulation lattice Particles might move only on specified positions in the simulated box (on-lattice simulations) or they may take every position (off-lattice simulations). Surely, off-lattice aggregation is more realistic but also more time-consuming in simulations.

Sticking probability A particle (or cluster) may stick to another particle immediately when they come in contact (diffusion-limited aggregation) or a sticking probability might be introduced (reaction-limited aggregation). Again, both possibilities have physical reasons. When a strong attractive force acts between two particles, they will have a 100 % sticking probability. On the other hand, when there are also some repulsive forces, the sticking probability will be reduced.

Definitely, there are other influencing parameters such as a distribution in the sizes of the primary particles, non-spherical primary particles, breakage of weak agglomerates or sintering of primary particles. However, as it was shown in Chap. 1.2 the primary particles in a single aggregate of pyrogenic silica are mostly spherical and of uniform size.

Breakage often occurs in liquid agglomeration [24–26]. If the breaking agglomerate is a true fractal then breakage results in two smaller agglomerates of the same mass-fractal dimension. Thus, it is not necessary to incorporate breakage in an aggregate generation simulation but it must not be neglected in population balances for agglomerating systems. Sintering indeed leads to other types of aggregates and it is also relevant for pyrogenic silica (c.f. Chap. 1.2). However, when calculations are performed at the simulated aggregates, the definition of the boundaries and the application of boundary conditions is hampered. Thus, sintering is mostly not considered in aggregate formation algorithms.

The interest in structure formation by aggregation of small particles, either in a dry or in a wet process, has early motivated researchers to find suitable simulation algorithms that give comparable results to experimental observations. Schaefer [27] and Meakin [28] give an overview of the six mainly used concepts that combine the above named parameters.

The first model proposed for pyrogenic silica growth was diffusion-limited aggregation introduced by Witten and Sander [29–31]. It incorporates particle-cluster aggregation, diffusive motion of the particles, on-lattice simulation (in later versions also off-lattice aggregation was accomplished) and 100 % sticking probability.

Schaefer and Hurd [20] later tried to give a complete explanation of the generation of silica aggregates in the flame process by the use of fractal growth models. They describe the formation

of the primary particles by a ballistic polymerization of protoparticles. The linear trajectories result from a mean free path estimation in the flame of about 5000 Å which is much larger than the size of the protoparticles. The growth mechanism is explained as particle-cluster aggregation as the probability of cluster-cluster collisions is very low [20].

In flame zones of lower temperature, when all the reactants have been exhausted, the concentration of protoparticles has dropped. The evolving primary particles begin to solidify. Resulting collisions still lead to an immediate sticking while the sintered area is reduced. This mechanism describes the aggregate formation. The mean free path of the molecules in the background gas ($\sim 50\,$Å) is now smaller than the particle size of the primary particles, hence the particles motion becomes diffusive. This growth process (cluster-cluster aggregation, diffusive motion, 100 % sticking probability) is usually called Diffusion-Limited Cluster Aggregation (DLCA) simultaneously introduced by Meakin [32] and Kolb et al. [33]. DLCA and the reduced sticking probability algorithm of the same model (Reaction-Limited Cluster Aggregation, RLCA) [34–36] have become the most popular kinetic growth models for particle scientists not only in the gas phase but also in a vast number of agglomeration studies of liquid suspensions, see e.g. [24–26, 37–46].

Batz-Sohn [11] describes another algorithm for the generation of fractal aggregates to be used for pyrogenic oxide materials. Here, a particle-cluster aggregation is performed in a way, that the next primary particle always occurs randomly at the envelope of the existing aggregate and then linearly adds to the nearest primary particle in the aggregate. Batz-Sohn also was the first to add a sintering factor in the generation algorithm.

If DLCA and RLCA are processed with a huge number of primary particles ($N_{prim} \rightarrow \infty$) or an averaging of many different aggregates is conducted, fractal analysis yields values for the mass-fractal dimension D_f^m of 1.86 and 2.05, respectively [24, 39, 40, 42, 46, 47]. As in RLCA a primary particle needs many collision events to stick to the aggregate nearly all positions in the aggregate are probed while in DLCA the outer regions are preferred. Thus, RLCA leads to denser clusters than DLCA which is reflected in the fractal dimensions. The fractal dimension of the Batz-Sohn aggregates is not unique but seems to depend on the number of primary particles in an aggregate. Thus, the algorithm does not show scale-invariant behavior.

Summarizing, it could be shown that the fractal structure of pyrogenic silica aggregates is inherent in its production process. Models that are able to reproduce the structure formation have

been developed and widely used in the past years. DLCA is suggested to be the most probable mechanism for pyrogenic silica though also a reduced sticking probability is conceivable.

2.1.4 Determination of Fractal Properties

2.1.4.1 Scattering Techniques

The most frequently used methods to examine the structure of fractal materials are based on static light scattering (SLS) and small-angle X-ray (SAXS) or neutron scattering (SANS) because they are quite fast, reproducible and non-intrusive. A prerequisite for the application of these techniques is a difference in refractive index between medium and particles in SLS while for SAXS a difference in the electron density and for SANS a difference in the mass of the atomic nuclei is required. With SLS only low-concentrated solutions can be examined[1], while SAXS and SANS provide the opportunity to measure dry powders, concentrated suspensions or even dispersed particles in cured epoxy-resins [21]. As the suspension medium contributes to the scattering signal background corrections with the pure medium are necessary.

For the structural investigation of matter a collimated beam is incident on the sample. It is scattered by interactions with the particles in the sample, the dispersed particles as well as the solvent molecules. The mean scattered intensity $\bar{I}_{sca}$ is recorded in dependence of the observation angle θ. The momentum transfer between the incident field and the scattered field is characterized by the vectorial difference of the respective wave vectors, $\mathbf{k}_{inc}$ and $\mathbf{k}_{sca}$. The resulting vector is called the scattering vector $\mathbf{s}$ (see Fig. 2.1). Its magnitude can be computed from triangular relations under the assumption of elastic scattering (i.e. no frequency change of the scattered wave compared to the incident wave). Then the magnitudes of the two wave vectors are the same and equal:

$$|\mathbf{k}_{inc}| = |\mathbf{k}_{sca}| = \frac{2\pi}{\lambda} = \frac{2\pi n}{\lambda_0} \tag{2.5}$$

where n is the refractive index of the medium and λ_0 is the wavelength of the incident beam in vacuum. The magnitude of the scattering vector $\mathbf{s}$ can then be computed to give:

$$|\mathbf{s}| = s = \frac{4\pi n}{\lambda_0} \sin\left(\frac{\theta}{2}\right) \tag{2.6}$$

[1] This is due to multiple scattering effects at higher concentrations.

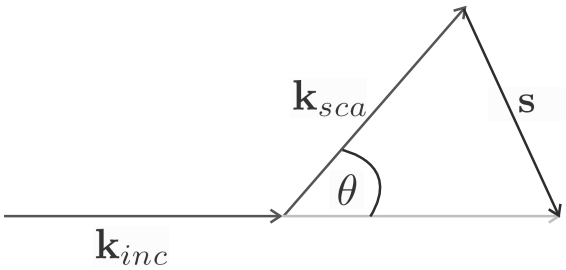

Figure 2.1: The geometrical definition of the scattering vector with respect to the wave vectors of the incident and the scattered field.

It is obvious from eq. 2.6 that s is changed when either the wavelength of the radiation or the scattering angle is altered. The inverse of the magnitude of the scattering vector has a unit of length and can be understood as the structure size of matter under investigation. By using SAXS or SANS (s-range: $0.01-1\ \mathrm{nm}^{-1}$) and SLS (s-range: $0.002-0.03\ \mathrm{nm}^{-1}$) several orders of magnitude can be spanned.

To get an impression of the scattering behavior of fractal aggregates in suspension Fig. 2.2 shows a model scattering pattern. If this pattern is investigated from low to high s-values the same happens as when the magnification of a microscope is increased. At high s the material is probed at atomic levels. Structural investigations reveal crystallinity and crystal structures. These features are not of interest here and are thus not shown in Fig. 2.2. If s is lowered the atomic structure of the materials is no longer resolved, rather the surface of the primary particles. According to Porod [48, 49] the surface of a particle (i.e. a sphere in Porod's investigations) can be decomposed into small spherical scattering elements bisecting the particle/matrix interface. From the proportionalities of the number of such spheres to the surface area and the number of electrons per particle (for X-ray scattering) Porod yielded:

$$I(s) \sim s^{-4} \tag{2.7}$$

In memorial this relation is called Porod's law. If now fractal instead of smooth surfaces are considered eq. 2.7 can be generalized to give:

$$I(s) \sim s^{-(6-D_f^S)} \tag{2.8}$$

This power-law decay can be linearized by a log-log plot of the measured intensity versus the scattering vector. It is marked in Fig. 2.2.

If s is further reduced the scattering vector may fall into one primary particle. Thus, scattering arises from interference in one solid particle. Guinier [52] was the first to investigate the scat-

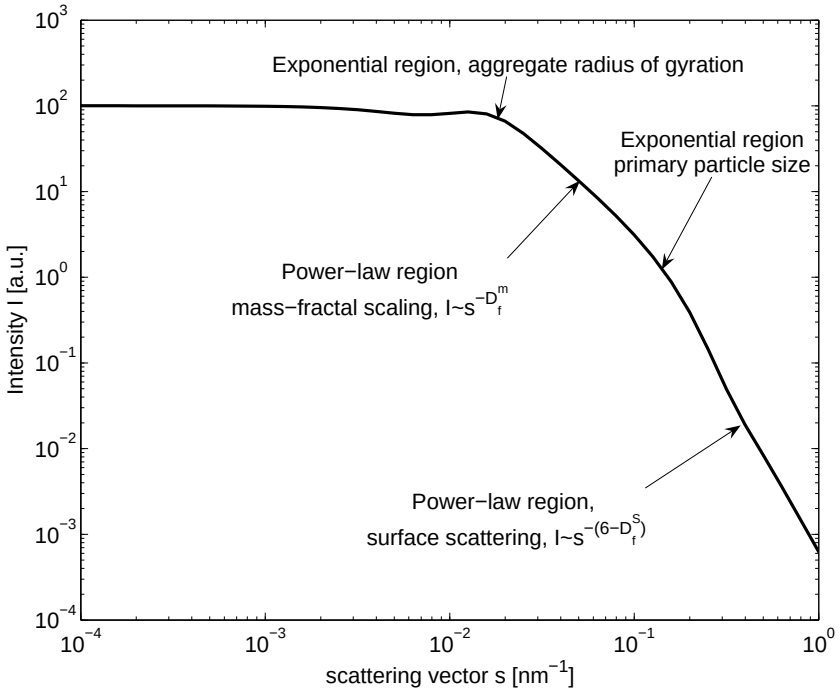

Figure 2.2: A model scattering pattern of fractal aggregates with primary particle size of 31.6 nm, aggregate radius of gyration 200 nm, mass and surface fractal dimensions 1.8 and 2.2, respectively. Calculated using the unified equation (c.f. eq. 2.11) of Beaucage [50, 51].

tering behavior. He obtained an exponential decay of the scattered intensity with increasing s depending on the radius of gyration R_g of the solid particle:

$$I(s) \sim \exp\left(-s^2 \frac{R_g^2}{3}\right) \tag{2.9}$$

There are two exponential regions in the scattering pattern (Fig. 2.2). The first one arises from the primary particles while the second one is a measure of the radius of gyration of an aggregate. In between these two regions one can again observe a power-law decay. This is due to dimensional scaling. For a disk it can be shown that the scattering is proportional to s^{-2}, for a rod there is a proportionality to s^{-1} or in general:

$$I(s) \sim s^{-D_f^m} \tag{2.10}$$

For s-values below the exponential decay of the aggregate radius of gyration the scattered intensity remains unchanged because here it is proportional to the aggregate volume which does not change.

It was shown that the fractal properties of an aggregate as well as two size parameters can be obtained from scattering data of SLS, SAXS or SANS if the s-range is sufficiently large.

In practice, the different exponential and power-law regions cannot be easily distinguished. Therefore, Beaucage [50, 51] developed a unified equation that is able to fit a whole measured scattering pattern to give the fractal dimensions and the size parameters:

$$I(s) \simeq B_1 \exp\left(-s^2 \frac{R_{g,agg}^2}{3}\right) + B_2 \exp\left(-s^2 \frac{R_{g,prim}^2}{3}\right) \left[\frac{\left(\operatorname{erf}\left(C s \frac{R_{g,agg}}{\sqrt{6}}\right)\right)^3}{s}\right]^{D_f^m} + \\ + B_{1,S} \exp\left(-s^2 \frac{R_{g,prim}^2}{3}\right) + B_{2,S} \left[\frac{\left(\operatorname{erf}\left(C_S s \frac{R_{g,prim}}{\sqrt{6}}\right)\right)^3}{s}\right]^{6-D_f^S} \tag{2.11}$$

Here, the B's are constants of the intensity level, where the respective scattering region starts. The function erf is the Gauss error function. The constants C and C_S account for an approximation in the power-law limit and are usually close to 1 (1.06 is used in [50, 51]). Eq. 2.11 is now mostly used to determine fractal properties of aggregates from scattering experiments.

2.1.4.2 Dynamic Rheological Measurements

Dynamic rheological measurements mean the application of oscillatory shear or strain $\gamma(t)$ on a sample [53]:

$$\gamma(t) = \gamma_0 \exp(\mathrm{i}\omega t) \tag{2.12}$$

where γ_0 is the strain amplitude, ω is the circular frequency and t is the time. The response to the strain is a time-dependent stress $\sigma(t)$ that is measured by the rheometer. A complex shear modulus can then be obtained by the following relation:

$$\sigma(t) = G^*(\omega)\,\gamma(t) \tag{2.13}$$

The real part of this modulus is termed G', the storage modulus and the imaginary part is referred to as G'', the loss modulus. The storage modulus characterizes the elastic portions of a sample while the loss modulus stands for the viscous portions.

From a frequency sweep the microstructure of a suspensions can be obtained. At low frequencies the energy of the deformation is dissipated by Brownian motion and thus the loss modulus is higher than the storage modulus. At high frequencies the energy is elastically stored in the suspension and the storage modulus increases.

In a dynamic strain sweep the amplitude of the oscillation instead of the frequency is varied. At low amplitudes the storage modulus is independent of strain. This is called the linear viscoelastic region. At a certain critical strain γ_c the independency is lost. Systems of pyrogenic silica then often show strain softening [54], i.e. the storage modulus decreases with increasing strain. This is also referred to as the Payne effect.

From the dependency of G' and γ_c on the solids volume fraction φ in a suspension also fractal properties can be determined. A scaling relationship $G' \sim \varphi^C$ predicted from the calculation of the elasticity of a fractal cluster is often found [55] with C varying from 3.5 for DLCA aggregates ($D_f^m = 1.75 - 1.85$) to 4.5 for RLCA aggregates ($D_f^m = 2 - 2.1$).

Wu et al. [56] developed a model that directly determines the mass-fractal dimension of aggregates from the scaling exponents of $G' \sim \varphi^{C_1}$ and $\gamma_c \sim \varphi^{C_2}$. This is based on the earlier work of Shih et al. [57]. The following relations for the exponents C_1 and C_2 apply:

$$C_1 = \frac{\mu}{3 - D_f^m} \tag{2.14}$$

$$C_2 = \frac{3 - \mu - 1}{3 - D_f^m} \tag{2.15}$$

The parameter μ is determined by the arrangement of the fractal aggregates, e.g. in a colloidal gel and by the relative contributions of interfloc and intrafloc linkage to the elastic properties of the examined sample.

Using the above equations Gottschalk-Gaudig [54] determined fractal dimensions of 2.01 and 2.03, respectively, for two samples of hydrophobic pyrogenic silica in a UP-resin, which is larger than the values returned from scattering techniques ($D_f^m \approx 1.8$) [58, 59] but is in good agreement with other rheological investigations on pyrogenic silica gels [60–63]. Gottschalk-Gaudig explains the difference by different aggregation mechanisms during the gel formation when different aggregates of pyrogenic silica are grouped together.

Compared to scattering techniques, the determination of fractal properties using dynamic rheological measurements is rather elaborate. Additionally, only the mass-fractal dimension can be determined and no conclusion can be drawn concerning surface fractality and the size of the aggregates and primary particles.

2.1.4.3 Sedimentation

The sedimentation of solid colloidal particles can be described by Stokes' law which predicts a proportionality of the square of the diameter of a spherical particle to its creeping flow (i.e. no recirculation or turbulence). Limitations are, that the flow field has to be undisturbed, i.e. solid concentration must be low and that Brownian motion can be neglected compared to the sedimentation velocity. In the case of fractal aggregates there is still a power-law dependence of some characteristic size to the sedimentation velocity, though it need not to be an integer power [64].

In a concentrated suspension sedimentation is hindered due to particle interactions. At a high enough concentration all particles in a suspension sink with the same speed. This is called the zone sedimentation regime. Still the reduced sedimentation velocity seems to obey a power-law dependence on the size of the fractal aggregates in the system. Gmachowski [64–68] therefore supposes that the two sedimentation velocities are interrelated by the fractal structure.

To derive a relationship for the settling velocity of a single aggregate, Gmachowski equates the force balance of buoyancy and gravitation to derive:

$$v_{s,agg} = \frac{2}{9}\frac{(\rho_s - \rho_l)\mathrm{g}}{\eta}\frac{N_{prim}R_{prim}^3}{R_h} \tag{2.16}$$

where ρ_s and ρ_f are the respective densities of the solid and the fluid, η is the fluid dynamic viscosity, g is the acceleration due to gravity and R_h is the radius of a sphere with the same mass and the same hydrodynamic properties as the aggregate. Using a mass-radius relation of fractal aggregates:

$$N_{prim} = \left(\frac{R_h}{R_{prim}}\right)^{D_f^m} \tag{2.17}$$

Gmachowski arrives at:

$$\frac{v_{s,agg}}{v_{s,prim}} = \left(\frac{R_h}{R_{prim}}\right)^{D_f^m - 1} \tag{2.18}$$

In the zone sedimentation regime the concentration of the aggregates is supposed to be high such that the fluid flow can be approximately described by a flow through a porous network. Then the Brinkman equation [69] applies, which gives the following dependence of the permeability k_p to the solid volume fraction φ_s:

$$k_p = C_1 \cdot \varphi_s^{\frac{2}{D_f^m - 3}} \tag{2.19}$$

Gmachowski [68] determined the constant C_1 to be:

$$\frac{R_{prim}}{\sqrt{C_1}} = \frac{11.6}{\left(3 - D_f^m\right)^{1.82}} \tag{2.20}$$

The relation between k_p and the cluster sedimentation velocity $v_{s,C}$ is given by:

$$k_p = \frac{\eta}{(\rho_s - \rho_l)\,\mathrm{g}} \frac{v_{s,C}}{\varphi_s} \tag{2.21}$$

Using eqns. 2.18-2.21 and a fractal scaling law for φ_s Gmachowski yields [64]:

$$\frac{v_{s,agg}}{v_{s,C}} = \frac{2}{9} \left[\frac{2\left(4 - D_f^m\right)}{D_f^m - 1} \right]^{\frac{D_f^m - 1}{D_f^m - 3}} \frac{135}{\left(3 - D_f^m\right)^{3.64}} \tag{2.22}$$

Eq. 2.22 is the basis for the determination of fractal properties using sedimentation experiments. Measurements have to be conducted in a very dilute suspension to obtain the single aggregate sedimentation velocity and in a concentrated suspension in the zone sedimentation regime. From the relation of the two velocities, the mass-fractal dimension can be determined. If additionally the size of the primary particles is known, eq. 2.16 can be used to compute a hydrodynamic diameter of the aggregate.

Thus, with medium effort compared to dynamic rheology experiments and scattering techniques, two parameters of fractal aggregates are accessible via sedimentation techniques. On the other hand, it is not an easy task to accomplish the condition of measuring the sedimentation velocity of aggregates in a very dilute suspension, since the measurable quantities (e.g. light extinction or X-ray absorption) also vanish. Gmachowski overcomes this limitation by the observation of single aggregates with a video camera [64] but this technique is only suitable for comparably large aggregates or agglomerates.

2.2 Interactions in Suspensions

In a suspension of micron-sized particles the behavior is mostly controlled by volume forces such as gravity. If the size of the particles is lowered, their surface is reduced with x^2 while their mass shrinks with x^3. Thus, the portion of surface atoms that are in contact with the suspension medium compared to the bulk atoms that are only neighbored with their own kind, rises. As a consequence, the influence of surface-mediated forces between the particles and with the

suspension medium on the suspensions behavior becomes larger. As an example, a colloidal suspension with properly controlled surface interactions may remain macroscopically stable for months or years, i.e. no phase separation will occur as sedimentation and diffusion are in equilibrium. If the surface properties are changed instead, fast agglomeration and sedimentation will occur in the time of seconds to minutes.

For pyrogenic silica, most industrial applications rely on specific interactions that lead to the use e.g. as a thickening agent. Additionally, these interactions have a significant impact on measurement results in particle sizing with DLS especially at high solids concentrations. Hence, a brief introduction into the relevant interaction energies for colloidal systems in general (Chap. 2.2.1 and 2.2.2) and specifically for pyrogenic silica (Chap. 2.2.3) is necessary.

2.2.1 Interparticle Interactions

Most particles in aqueous solution carry an electric charge. This is due to the dissociation of surface groups, to imperfect crystal lattices with ending ions or the specific adsorption of ions from the solution medium. As equal particles are supposed to be equally charged, they should repel each other. In practice, the surface charge is compensated by an excess of counterions in an adjacent liquid layer surrounding the particles. This layer may be structured in a fixed part where ions are directly attached to the surface of the particle (Stern layer) and a diffusive layer where the ions remain mobile and are subject to Coulomb and osmotic forces. Both layers together are often referred to as the dielectric double layer [70]. The extent of the diffusive layer may be as small as several layers of solvent molecules but may also be enlarged up to several hundreds of nanometer. The potential decreases in general from the particles surface to the bulk (differences may appear for specific adsorptions e.g. of multivalent ions that may even lead to a charge inversion). Elimelech et al. [71] give the following exponential for the energetic interaction potential between two spheres of equal size x at surface-to-surface distance r:

$$V_{el} = 16\pi\varepsilon_r\epsilon_0 x \left(\frac{\mathrm{k_B}T}{z\mathrm{e}_0}\right)^2 \left[\tanh\left(\frac{z\mathrm{e}_0\zeta}{4\mathrm{k_B}T}\right)\right]^2 \exp\left(-\kappa r\right) \tag{2.23}$$

Here, ϵ_0 is the permittivity of free space, ε_r is the relative permittivity, $\mathrm{k_B}$ is the Boltzmann constant, T is the temperature, e_0 is the elementary charge and z is the valency of the dissolved ions in the bulk solution. The zeta potential ζ is a potential induced from a charge separation in the dielectric double layer by external forces (e.g. an electric or acoustic field) [72, 73]. It is measured at the shear plane between surface and liquid. The inverse of the exponent κ, which is

usually referred to as the Debye-Hückel parameter, gives the distance from the particles surface, where the potential has decreased to $1/\mathrm{e}$ of the surface value. It is defined as:

$$\kappa = \sqrt{\frac{2\mathrm{e}_0^2 \mathrm{N_A}}{\varepsilon_r \epsilon_0 \mathrm{k_B} T} I_s} \tag{2.24}$$

where $\mathrm{N_A}$ is the Avogadro constant and I_s is the ionic strength that is computed from the molar concentration c_i and the respective valency z_i of each ionic species in the bulk solution:

$$I_s = \frac{1}{2} \sum_i c_i z_i^2 \tag{2.25}$$

It is readily available from eq. 2.24 and eq. 2.23 that an increase of the salinity leads to screening of the electrostatic potential, i.e. the thickness of the double layer decreases (see Fig. 2.3). The temperature has a reversed effect. An increase in T leads to an extension of the double layer due to an increased mobility of the dissolved ions. Strictly speaking, eq. 2.23 is only valid for distances r large compared to κ^{-1} ($\kappa r > 5$) and for $r \ll x$ but it is often applied in more general cases.

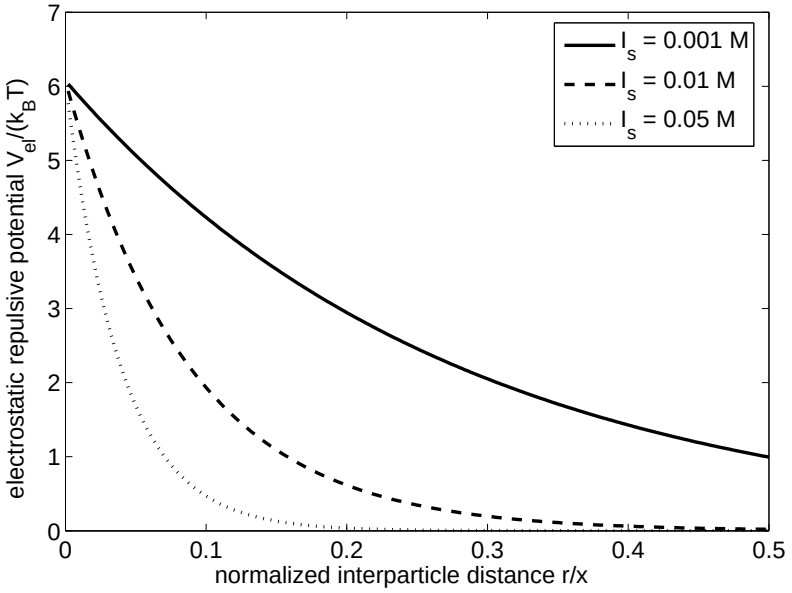

Figure 2.3: Characteristics of the electrostatic repulsion potential for different values of the ionic strength I_s, computed from eq. 2.23 with $x = 50$ nm, $\zeta = -15$ mV, $\varepsilon_r = 80$ (water), $T = 298$ K and monovalent ions with marked ionic strength.

If the double layers of two approaching particles begin to overlap the increase of ion concentration in the overlap zone leads to an osmotic pressure that drives the particles apart. Moreover, local repulsion of the equally-charged counterions may occur. This is the main reason why colloidal suspensions may remain microscopically stable.

To this point, it has not been discussed why a stabilization of colloidal particles is needed to prevent aggregation. The attractive potential is due to van-der Waals forces. These forces are always present between molecules and atoms. They result from the fluctuations in the electron orbitals that may be described as a dipole. A fluctuating dipole emits an electromagnetic wave that induces other fluctuating dipoles if it encounters other molecules or atoms. The computation of the resulting potential leads to a proportionality in distance to $\sim r^{-6}$ [70]. The interaction potential in colloids can be obtained by summing over all possible atom or molecule pairs in two particles (Hamaker theory) [70, 74]. This leads to the following relation for the attractive potential between two spheres of size x at distance r:

$$V_{vdW} = -\frac{A_{131}}{12}\left\{\frac{x^2}{r^2+2rx}+\frac{x^2}{(r+x)^2}+2\ln\left[1-\left(\frac{x}{r+x}\right)^2\right]\right\} \tag{2.26}$$

In this equation A_{131} is the Hamaker constant, which is dependent on the material of the particles and the medium between them. For amorphous silica in water very different values can be found (e.g. $0.849\cdot10^{-20}$ J [70], $0.46\cdot10^{-20}$ J [75]). These are due to the variety of methods to determine the Hamaker constant and the assumptions and measurement errors therein [76].

Additionally, at large interparticle distances a correction factor to eq. 2.26 has to be introduced [70]. This is due to a retardation effect, as the electromagnetic wave and thus the induction of the dipoles travels just with the speed of light.

The DLVO-theory (named after Derjaguin, Landau, Verwey and Overbeek [77, 78]) was the first attempt to describe the stability behavior of colloids in aqueous dispersions. It is assumed that the interaction potential of the counterionic stabilization and the van-der-Waals attraction can be superimposed:

$$V_{DLVO} = V_{vdW} + V_{el} \tag{2.27}$$

Fig. 2.4 shows the progression of the superposed interaction potential calculated with the same values as in Fig. 2.3 and a Hamaker constant of $0.8\cdot10^{-20}$ J for silica. The characteristics of the van-der-Waals attraction and the electrostatic potential have been highlighted additionally. At short distances, the attractive potential dominates, i.e. particles at these distances aggregate irreversibly. At intermediate distances, V_{el} causes a potential barrier that stabilizes the suspension. Usually, if the barrier is about 15 $k_B T$ in height, the suspension will not aggregate. At large distances and with a large attractive potential a secondary minimum may occur that leads to a very weak agglomeration. However, this is not observed for suspensions of amorphous silica.

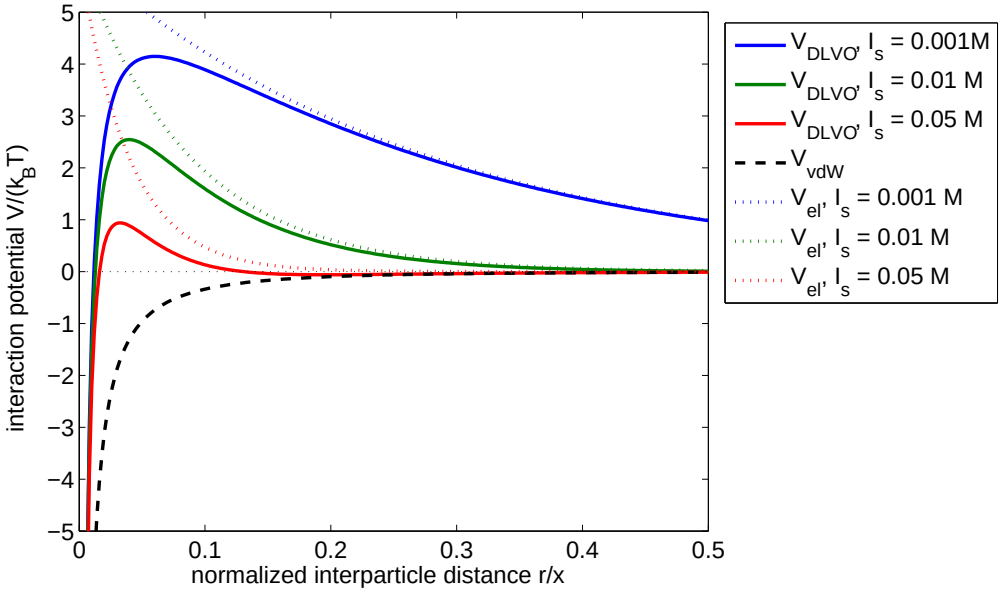

Figure 2.4: Computed interaction potentials (same values as in Fig. 2.3 and $A_{131} = 0.8 \cdot 10^{-20}$ J) for different values of the ionic strength I_s; V_{DLVO}: solid lines; V_{el}: dotted lines; V_{vdW}: dashed line.

The effect of the salinity can be clearly observed in Fig. 2.4. As the thickness of the double layer is reduced, also the potential barrier is lowered so that other particles may overcome the barrier by diffusion and thus aggregate. As a rule of thumb, the higher the ionic strength of a suspension the more likely are the particles to aggregate. In this consideration it is assumed that the van-der-Waals attraction does not change with I_s. In general, this is not exactly the case but the changes can be neglected in comparison to V_{el}.

Nowadays, still the DLVO-theory is the basis to describe the stability behavior of colloids in aqueous solutions. Additional influencing effects are incorporated in terms of additional potentials. One self-evident extension shall be shortly described here since it is relevant in the further progression. When two approaching particles are in very close contact the electron orbitals of the respective surface atoms begin to overlap. This leads to a strong repulsive potential known as Born repulsion. The exact potential can only be obtained from elaborate calculations of the molecular or atomic structure [79]. In many cases a general treatment with a proportionality to $\sim r^{-C}$ where C is in the range of $7-16$ is used [80–82]. Another possibility is the application of the Hard-Sphere model (HS). The potential is then described as:

$$V_{HS} = \begin{cases} \infty & \text{for} \quad r = 0 \\ 0 & \text{for} \quad r > 0 \end{cases} \tag{2.28}$$

i.e. the potential is in fact a delta function at zero distance. This model has its origin in the treatment of ideal gases and molecules. The advantage that it can be most easily applied in simulations (Molecular Dynamics, Brownian Dynamics) as a non-overlap condition of the simulated atoms or colloidal particles has made it very familiar. Some colloidal model systems such as spherical latices and silica have been tuned to possess the behavior of a HS-suspension to prove simulation results. Therefore, many theoretical models rely on the HS-model rather than on a DLVO-potential as will be seen in later chapters. Their transferability to the more realistic DLVO-type interaction has always to be scrutinized.

In suspensions of pyrogenic silica also non-DLVO effects are present. They will be further reviewed in Chap. 2.2.3.

2.2.2 Hydrodynamic Interactions

Hydrodynamic interactions are forces between particles that are mediated via the suspension medium and that do not have their origin in the molecular properties of the particles itself. Herein, mainly forces that arise from a relative movement between particles and medium are to be considered. This movement generates disturbances in the flow field around the particle that extend into the bulk phase by multiples of the particle size. Fig. 2.5 shows the flow fields of two moving particles. Though the particles are far from contact, their respective flow fields interact with each other.

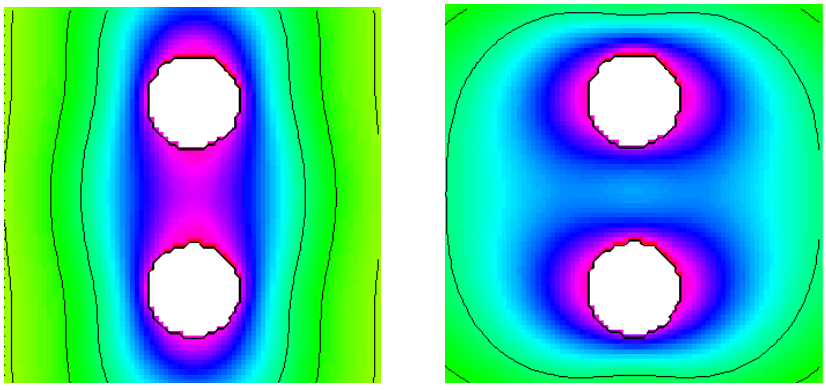

(a) (b)

Figure 2.5: Interacting flow fields of two spheres moving in a quiescent solution, a) top-down movement b) left-right movement; fluid velocity increases from yellow to violet.

Since colloidal particles are in a permanent movement due to Brownian motion, hydrodynamic

effects are always present. Additionally, these effects have to be accounted for in methods that require a relative movement such as sedimentation or centrifugation.

As long as a particle can be considered to be alone in the fluid, the regard to hydrodynamics is expressed in the solvent friction characterized by the viscosity. This regime is called the dilute limit. Hence, hydrodynamic interactions have to be considered in suspensions at higher concentrations of the disperse phase. In a theoretical treatment of the problem there is another transition in the modelling approach. While at low concentration ($\varphi < 0.1$ for HS systems) only pairwise interactions are important (see e.g. [83]), multi-body interactions have to be taken into account at higher concentrations [84–87].

2.2.3 The Stability Behavior of Aqueous Pyrogenic Silica Suspensions

The stability of aqueous suspensions of pyrogenic silica depends on specific properties of the suspension medium, namely the pH value, the salinity and the type of dissolved ions [88]. The chemical structure of pyrogenic silica consists of $SiO_{4/2}$ tetrahedrons that are interconnected by siloxane bridges ($Si-O-Si$). Surface atoms must show a discontinuity in this structure. Thus, nearly every second surface atom carries a hydroxyl group ($Si-O-H$) which is also called a silanol group. These silanol groups are able to establish hydrogen bonds with the surrounding water molecules. Hence, they make pyrogenic silica hydrophilic. Depending on the suspension properties the silanol groups can be deprotonated. The remaining SiO^- groups cause a negative surface charge. This dissociation reaction is mainly favored under alkaline conditions ($pH \geq 9$). Thus, silica suspensions in this regime are stabilized by counterionic stabilization that can only be screened at very high ionic strengths.

If the pH is lowered, the surface charge is reduced. Thus, the effect of counterionic stabilization diminishes and is completely absent at the isoelectric point which lies around pH 2 for amorphous silica. Here, the so-called hydration forces which are a non-DLVO interaction prevent the silica particles from agglomeration. The formation of hydrogen bonds between the silanol groups lead to ordered layers of water molecules at the particles surface which in turn give rise to a hydration pressure driving approaching particles apart [89, 90]. As the attractive van-der-Waals forces are of low strength due to the low Hamaker constant for silica in water, this hydration force is sufficient to keep a suspension stable.

In the light acidic to light basic range, the hydration layer is disturbed by the beginning deprotonation of the silanol groups and the surface charge has not yet gained a high enough value, i.e. here, silica suspensions can be most easily destabilized e.g. by increasing the ionic strength of the suspension. At specific solid concentrations this might even lead to a liquid / solid phase transition, most favorably at pH 6 [91].

2.3 The Principle of Dynamic Light Scattering

2.3.1 Measurement Principle

2.3.1.1 Brownian Motion

Colloidal particles in suspension are in permanent motion due to non-compensated impacts of the solvent molecules. The kind of motion is erratic as the motion of dissolved species such as ions or the solvent molecules itself. This fundamental finding of Albert Einstein [92, 93] led to a first description of the previously only experimentally asserted phenomenon of Brownian motion. When a particle is moving in space, Einstein showed that its mean square displacement in time t is equal to:

$$\langle \Delta r^2 \rangle = 6 D_t t \tag{2.29}$$

although eq. 2.29 is the general three-dimensional result while Einstein considered only the one-dimensional case [93]. A relation between the translational diffusion coefficient and the particle size can be obtained from a force balance between the thermodynamic osmotic force and the fluid friction. This gives the famous Stokes-Einstein equation:

$$D_t = \frac{\mathrm{k_B} T}{3\pi\eta x} \tag{2.30}$$

which is the fundamental equation for particle sizing using DLS techniques.

2.3.1.2 The Dynamic Light Scattering Effect

If a light beam impinges on particles they interact with the electromagnetic radiation, the light is scattered. A basic assumption in the theory of DLS is that the scattered light has the same frequency as the incident light beam (cf. Chap. 2.1.4). However, due to the motion of the

particles an optical Doppler effect occurs for the resting observer. The frequency of the scattered light is shifted by a small portion that is proportional to the velocity of the particle [94]:

$$\Delta\omega = \mathbf{s} \cdot \mathbf{v} \tag{2.31}$$

Thus, the scattered light intensity is not constant but fluctuates about a mean value $\langle I \rangle$ (see Fig. 2.6). The brackets $\langle \ldots \rangle$ denote a time average.

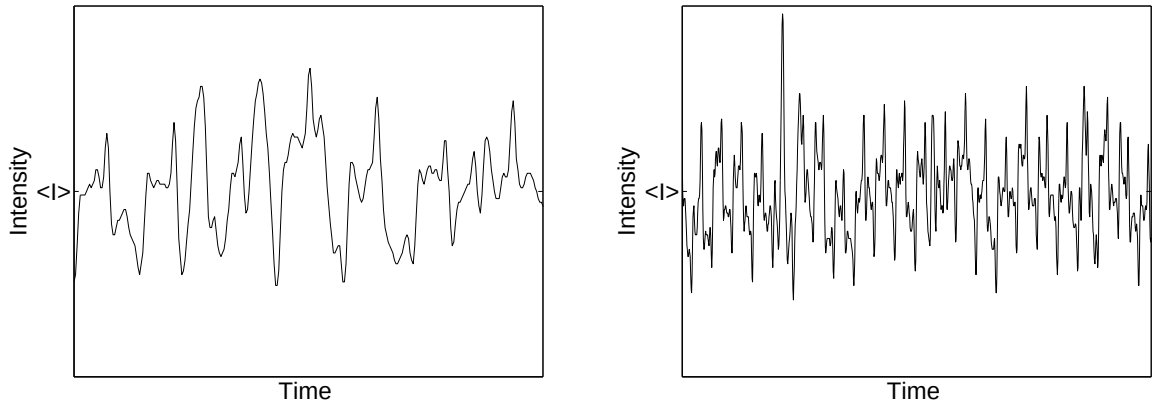

(a) Large particles = slow fluctuations (b) Small particles = fast fluctuations

Figure 2.6: Fluctuations in intensity of scattered light due to thermal motion of dispersed particles.

The incident beam encloses a huge number of particles[2] all moving in different directions with different velocities. Thus, a continuous spectrum of frequency shifts $S(\omega)$ which is centered above the frequency of the impinging beam ω_0 is obtained. Fig. 2.7 shows an example of such a power spectrum. This is the basic principle of a dynamic light scattering experiment.

2.3.1.3 Assembly of a DLS Measurement

In a typical set-up of a DLS experiment the sample is contained in a fixed holder. It is illuminated from a coherent monochromatic light source. Typically, lasers (often He-Ne with 632.8 nm or Ar-ion with 592 nm wavelength) with vertical polarization are used. The scattered light from the particles is collected by a detector under the scattering angle θ. In industrially relevant commercial instruments usually one or a set of fixed scattering angles is used while in academic applications goniometers that allow for measurements at different scattering angles

[2] Focused beams that are most often used in DLS devices have a waist diameter of about 100 µm.

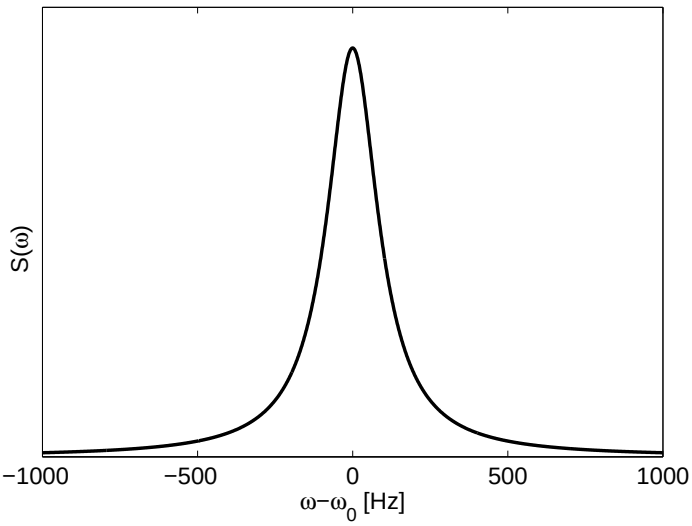

Figure 2.7: Spectral density of frequency shifts in scattered light due to Brownian motion of the particles in suspension.

can be found. In recent developments also fiber optics are used that act simultaneously as illuminating and detection optics ($\theta = 180°$) [94, 95].[3] The scattered light is then coupled out in a Y-coupler and led to the detector.

Photomultiplier tubes (PMT) or Avalanche Photodiodes (APD) are used as detectors in DLS set-ups. A photomultiplier has a photocathode at the entry window. When a photon of the scattered light hits the photocathode, an electron is produced by the photoelectric effect. This electron is then multiplied at the following dynodes by secondary emission which finally leads to a measurable current at the anode. Avalanche photodiodes can be regarded as the semiconductor analogue to photomultipliers. A high barrier voltage leads to an enormous internal gain of an incoming photon by ionization in the barrier layer.

From the functional principle of a PMT and an APD it is clear that the measurement of the scattered intensities means counting the impinging photons. The photon count rate (Number of photons per unit time in kHz) is taken as an equivalent to the intensity.

The detected scattering signal is processed to obtain information on the diffusional properties of the sample. The underlying theory and data treatment will be reviewed in the next chapter 2.3.1.4. Finally, a computer is used for data output and handling. A principal scheme of a DLS set-up is given in Fig. 2.8.

[3] This technique is usually denoted as Fiber-Optic Quasi-Elastic Light Scattering (FOQELS)

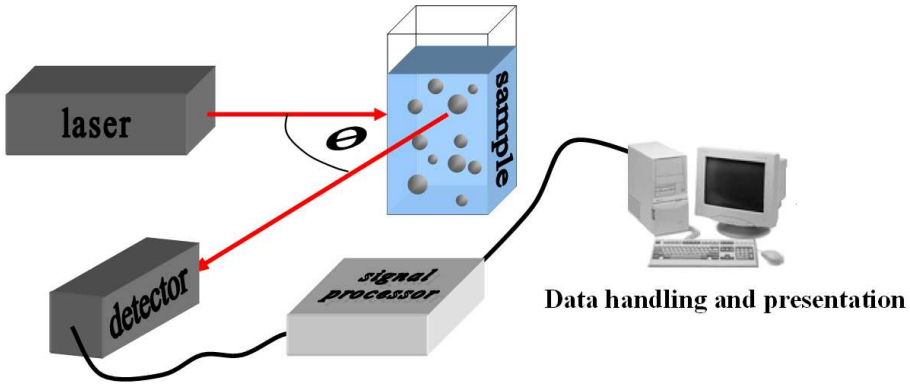

Figure 2.8: Scheme of a typical DLS set-up.

2.3.1.4 From Scattered Light to the Diffusion Coefficient

The incident light that illuminates the particles can approximately be described as a plane wave in a cartesian coordinate system (X, Y, Z) where the beam propagates in Z-direction [96]:

$$\mathbf{E}(\mathbf{r},t) = \mathbf{e}_Y E_{inc}(X,Y)\exp(\mathrm{i}kZ - \mathrm{i}\omega t) \tag{2.32}$$

Here, $\mathbf{E}$ is the electric field vector, E_{inc} is the magnitude of the incident electric field, $\mathbf{r}$ is a position vector and $\mathbf{e}_Y$ is the unit vector in Y-direction. The scattered light wave of particle i can then be described by a scattering amplitude a_i and an optical phase $\sim \mathbf{r}_i \cdot \mathbf{s}$:

$$\mathbf{E}_{sca,i}(\mathbf{s},t) = \mathbf{e}_Y E_{inc}(X_i,Y_i)a_i \exp(\mathrm{i}\mathbf{s}\mathbf{r}_i - \mathrm{i}\omega t) \tag{2.33}$$

Next, the scattered light contributions are summed over all particles in the scattering volume. If the explicit time dependence is suppressed a complex scattering amplitude is obtained [96]:

$$u(\mathbf{s},t) = \sum_{i=1}^{N} E_{inc}(X_i,Y_i)a_i(\mathbf{r}_i)\exp(\mathrm{i}\mathbf{s}\mathbf{r}_i) \tag{2.34}$$

Modern DLS instruments use one of two different strategies to get information about the diffusion coefficient and thus the size of particles out of the frequency shift spectra.

Most systems compute the intensity auto-correlation function $G_2(\tau)$ from the measured photon counts:

$$\begin{aligned} G_2(\tau) &= \langle I(t)I(t+\tau)\rangle \\ &= \lim_{t_{meas}\to\infty} \frac{1}{t_{meas}} \int_0^{t_{meas}} I(t)I(t+\tau)\, dt \end{aligned} \tag{2.35}$$

where the angle brackets $\langle \ldots \rangle$ denote a time average, τ is the lag time between the two points in time where the correlation is performed and t_{meas} is the duration of a DLS measurement.

The calculation of this function requires extremely fast operating devices since the region of interest in lag times τ starts at 10^{-9} s. In the 1970's and 80's only hardware correlators were used. Simply speaking, these are simple computers that are only able to perform additions and multiplications. Their output is directly the correlation function. A review on the development und functional principal of hardware correlators is given by Schätzel [96]. Today, the power of modern computers is sufficient to obtain the correlation function from software correlators.

It is easy to show that $G_2(\tau)$ decays from $\langle I(t)^2 \rangle$ to $\langle I(t) \rangle^2$ [97]. Assuming photon counting as a Gaussian process, Schätzel [96] showed that the intensity autocorrelation function can be expressed in terms of the scattered field amplitudes:

$$G_2(\tau) = \left\langle |u(t)|^2 \right\rangle \left\langle |u(t+\tau)|^2 \right\rangle + \langle u(t)u(t+\tau)^* \rangle \langle u(t)^* u(t+\tau) \rangle \tag{2.36}$$

The expression in the second term on the right hand side is just the square of the autocorrelation function of the electric field amplitudes, the so-called field correlation function (FCF) $G_1(\tau)$. Eq. 2.36 was firstly derived by Siegert [98] and is therefore called the Siegert-relation. Today, usually the form:

$$g_2(\tau) = 1 + b\, g_1(\tau)^2 \tag{2.37}$$

is used. Here, g_2 and g_1 are auto- and field-correlation functions normalized by $G_2(\infty)$ and $G_1(0)$, respectively. The parameter b is referred to as the coherence factor and is dependent on the detector area, the optical alignment and the scattering properties of the system. Typically, values of $0.9 - 1$ can be achieved.

For monodisperse particles of size x and translational diffusion coefficient D_t the field correlation function is a simple exponential:

$$g_1(\tau) = \exp\left(-D_t s^2 \tau\right) \tag{2.38}$$

The derivation of eq. 2.38 requires some elaborate mathematics and has therefore been forwarded to Annex A. This equation is the basis to obtain diffusional properties of the system under consideration using the correlator method.

Early in the development of PCS, spectrum analyzers where used to determine the spectrum of the frequency shifts $S(\omega)$ directly. The relation of $S(\omega)$ and the diffusion coefficient can be obtained from eq. A.3 making use of the Wiener-Khinchine theorem [96]:

$$S(\mathrm{i}\omega) = \int_0^\infty G_1(\tau) \exp(-\mathrm{i}\omega\tau)\, d\tau \tag{2.39}$$

that states that the power spectrum and the first-order amplitude correlation function are Fourier transform pairs. After some manipulation this yields [94]:

$$|S(\mathrm{i}\omega)| = S(\omega) = \frac{\langle I_{sca} \rangle}{\pi} \left[\frac{D_t s^2}{(D_t s^2)^2 + (\omega_0 - \omega)^2} \right] \tag{2.40}$$

This equation describes the shape of the curve in Fig. 2.7 which is a Lorentzian or Cauchy distribution centered at the frequency of the incident beam ω_0 and with half-width at half-height $D_t s^2$. However, spectrum analyzers were not able to accurately determine both the spectral density and the frequency [1].

Today, the direct determination of the frequency spectrum has again come into focus by the use of light emitting fibres in the devices that act simultaneously as incident and detecting fibre. The signal is then coupled out in a Y-connector and led to the detector. Since the coupling is not ideal the detected scattered light is mixed with a portion of the incident beam.[4] The signal then shows a light beating effect, i.e. a variation of the signal with a frequency that equals the shift frequency $\omega - \omega_0$. Thus, the determination of $S(\omega)$ can be carried out with more ease.

2.3.2 Data Analysis

The data analysis techniques are different in some aspects for devices operating with the correlation method and those working with the frequency spectrum. As the devices used in this work operate with a correlator, data analysis will be described specifically for this purpose.

The primary measurement result is the unnormalized autocorrelation function (ACF) $G_2(\tau)$. The first step in data analysis is the normalization with the baseline-term $G_2(\infty)$ [6]. This can either be done experimentally with long-time correlator-channels that measure the value $\lim_{\tau\to\infty} G_2(\tau)$ or with monitor channels that determine the total photon count and average by the measurement run-time (computed baseline) [96]. Xu [5] proposes to use the difference of both values as an estimate of the accuracy of a DLS experiment since they should be identical under ideal conditions.

Secondly, most analysis algorithms require $g_2(\tau)$ to be converted to $g_1(\tau)$. This introduces some difficulties for the handling of negative values that may arise due to noise in the measured

[4] This detection mode is called heterodyne mode while the detection of only scattered light is called homodyne mode.

signal [99]. The most appropriate way of conversion is:

$$g_1(\tau_i) = \begin{cases} \sqrt{\frac{g_2(\tau_i)-1}{b}} & \text{for} \quad g_2(\tau_i)-1 \geq 0 \\ -\sqrt{\frac{|g_2(\tau_i)-1|}{b}} & \text{for} \quad g_2(\tau_i)-1 < 0 \end{cases} \tag{2.41}$$

Now, if the particles are monodisperse eq. 2.38 can be used to determine the diffusion coefficient. If on the other hand, as is mostly the case, the system is polydisperse the exponential decay of each particle's diffusion coefficient contributes and the normalized FCF reads (for spherical particles):

$$g_1(\tau) = \int_0^\infty q(D_t) \exp\left(-D_t s^2 \tau\right) dD_t \tag{2.42}$$

Here, $q(D_t)$ is a density distribution of translational diffusion coefficients. The question arises with which weight a particle contributes to the measured distribution. As DLS measures the stray light of the particle ensemble this results to be the scattering efficiency. Thus, primarily distributions obtained by DLS are weighted by scattered light intensity.

The determination of $q(D_t)$ from eq. 2.42 poses some mathematical difficulties. This type of equation is known as a Fredholm integral equation of the first kind. In principal, the solution is possible if the equation is discretized by an appropriate quadrature such as the trapezoidal rule. Eq. 2.42 then reads:

$$g_1(\tau_i) = \sum_{j=1}^{N_{cl}} \Delta Q(D_{t,j}) \exp\left(-D_{t,j} s^2 \tau_i\right) \tag{2.43}$$

$$\mathbf{g_1} = \mathbf{K} \cdot \mathbf{\Delta Q} \tag{2.44}$$

where N_{cl} is the number of discrete diffusion coefficient classes. The matrix $\mathbf{K}$ contains the relation between the diffusion coefficients and the lag times and is usually designated as the kernel of the matrix equation. A discrete distribution $\mathbf{\Delta Q}$ can now be obtained from an inversion of the kernel. For an experimentally obtained FCF an additional term to eq. 2.44 has to be taken into account:

$$\mathbf{g_1} = \mathbf{K} \cdot \mathbf{\Delta Q} + \boldsymbol{\epsilon} \tag{2.45}$$

where $\boldsymbol{\epsilon}$ stands for the a priori unknown measurement error contribution to the measured signal. This term makes the inversion of measurement data to a distribution of diffusion coefficients an ill-posed problem [1, 5, 6, 94, 100], i.e. that in the range of the measurement error usually an infinite number of equally probable solutions to $q(D_t)$ may be found. Even very small variations in $g_1(\tau)$ may result in a completely different distribution [101], it is said that the inversion errors

are unbounded. Thus, data analysis algorithms have to cope with the mathematical nature of the inversion problem. There are, in general, three different approaches to deal with DLS data:

Algorithms requiring no a priori information Here, mostly no distribution of diffusion coefficients is determined but only some mean values and moments of it. The one best known in DLS data analysis is the method of cumulants originally developed by Koppel [102]. This method is fast and easy-to-use and is therefore even incorporated in the International standard ISO 13321 [3]. The processing, the advantages and disadvantages of the cumulants method will be treated in the next chapter 2.3.2.1. Finsy et al. [103, 104] developed the singular value and reconstruction method (SVR) that also requires no additional information but has not gained significant value in DLS data analysis.

Functional fitting A known distribution type with only a few adjustable parameters is assumed. The parameters are then estimated by a nonlinear optimization procedure such as a Levenberg-Marquardt method. The goodness of the optimization relies on the initial guesses of the variables. Commonly used functionals are single and double exponentials, normal and log-normal distributions (mono- and bimodal) or Schulz-Zimm distributions [5].

Laplace inversion schemes Algorithms of this kind do not assume a certain type of the distribution of diffusion coefficients so they are the most general. Several assumptions are made to deal with the mathematical problem. Since these algorithms are of great value for the purpose of this thesis, they will be discussed in more detail in Chap. 2.3.2.2.

2.3.2.1 Method of Cumulants

In statistics, the cumulant generating function $\mathscr{K}(t)$ is defined as the natural logarithm of the characteristic function $\Phi(t)$ of a probability distribution $q(X)$ [105]:

$$\mathscr{K}(t) = \ln(\Phi(t)) = \ln\left[\int_{-\infty}^{\infty} \exp(\mathrm{i}tX) q(X)\, dX\right] \tag{2.46}$$

For the purpose of DLS data analysis Koppel [102] used:

$$q(X) = q(D) \tag{2.47}$$

$$\Phi(-\tau, s) = \int_{-\infty}^{\infty} \exp(-Ds^2\tau) q(D)\, dD = g_1(\tau, s) \tag{2.48}$$

$$\mathscr{K}(-\tau, s) = \ln|g_1(\tau, s)| \tag{2.49}$$

The cumulants $K_i(s)$ are defined as the coefficients of a series expansion of $\mathscr{K}(-\tau,s)$ in a MacLaurin series [105]:

$$\mathscr{K}(-\tau,s) = \sum_{i=1}^{\infty} K_i(s) \frac{(-\tau)^i}{i!} \tag{2.50}$$

Hence, the cumulants can be related to the moments M_i of $q(D)$ where M_1 is the mean and $M_{i,i>1}$ are central moments about the mean:

$$\begin{aligned} K_1 &= M_1 = \bar{D} = \int_0^{\infty} D\, q(D)\, dD \\ K_2 &= M_2 = \int_0^{\infty} (D-\bar{D})^2\, q(D)\, dD \\ K_3 &= M_3 \\ K_4 &= M_4 - 3(M_2)^2 \end{aligned} \tag{2.51}$$

i.e. the first cumulant describes a mean diffusion coefficient, while the second describes the relative width of the distribution $q(D)$ if normalized by $(K_1)^2$. The normalized variable is usually referred to as the polydispersity index *PDI*:

$$PDI = \frac{K_2}{(K_1)^2} \tag{2.52}$$

Similarly, K_3 and K_4 contain information about the skewness and the curtosis, respectively, of the measured distributions.

The procedure of performing a cumulants analysis on measured DLS data should now be clear. From the ACF perform a conversion to $g_1(\tau)$ (c.f. eq. 2.41), then take the natural logarithm (eq. 2.49). Afterwards $\ln|g_1(\tau)|$ is fitted by a polynomial (eq. 2.50) to obtain the cumulants.

However, some help warnings have to be given in using this simple procedure. Firstly, the correlation function has to be cut at a certain data point (i.e. lag time), otherwise the results are distorted by the fit algorithm itself and measurement errors. Usually the cut is done when the autocorrelation has decayed to 10 % of the maximum value. This is obviously a rather simplistic approach as it may ignore important contributions to the distribution of diffusion coefficients or introduce measurement errors if the maximum value of the correlation function is already low. On the other hand, a manual cut-off can only be done by experienced users so this compromise is still used in commercially available instruments.

Secondly, even with a very accurate measurement device, random errors induce variations in the fitted cumulants. Thus, while K_1 can usually be determined within 1 % uncertainty, already K_2 induces errors up to 20 % so that the determination of K_3 and K_4 is not recommended in most cases [102].

Thirdly, in taking the logarithm of the FCF the weights of the data points are altered. Thus, either a proper weighting function has to be introduced or the field correlation function has to be fitted directly without taking the logarithm [5, 106]. Here, the opportunity of using a linear least squares algorithm is lost. A nonlinear method such as Gauss-Newton or Levenberg-Marquardt has to be applied instead. Fortunately, the results of the non-weighted linear fit may serve as good initial guesses for the nonlinear fit.

2.3.2.2 Inversion of the Measured Spectra

As already noted, constraints or *a priori information* have to be introduced to obtain a solution to the mathematical ill-posed problem of a general inverse Laplace transformation of $g_1(\tau)$. In general, after discretization of eq. 2.42 one is left with a vector of the FCF measured at i data points in τ and a vector of j classes of the distribution of diffusion coefficients where $i \lessgtr j$. This shows that already the step of discretization involves a constraint on the algorithm, i.e. the range of diffusion coefficients to be expected and the spacing of the classes. Often, geometrical spacing is preferred over linear spacing based on a eigenvalue analysis of the Laplace transform [107].

The first and most evident constraint introduced by nearly all inversion algorithms is the demand of all values $\Delta Q(D_j) \geq 0$. This nonnegativity constraint greatly confines the set of possible solutions and is physically true for all imaginable types of distributions. Grabowski and Morrison [108, 109] developed an algorithm that uses just this constraint and the geometrical spacing of the distribution. It is usually referred to as *NNLS*, Non-Negative Least Squares.

However, it turned out that this algorithm is very sensitive to small variations in the measured data and the measurement errors. Thus, additional constraints were looked for. Two approaches have gained significant value in DLS data analysis. The first one is the Maximum-Entropy method originally developed by Livesey, Licinio and Delaye [110] and modified for geometrical spacing by Nyeo and Chu [111]. It makes use of the Shannon-Jaynes entropy formulation invented in statistical mechanics. The solution adopted for DLS data analysis is the one maximizing the entropy. As this algorithm is not used throughout this thesis, it will not be explored in detail.

Another algorithm which is widely used to reveal distributions of diffusion coefficients from DLS data is CONTIN (Constrained Regularization Method for Inverting Data) developed by

Provencher [112–115]. In NNLS the term which is minimized with respect to the non-negativity constraint is:

$$\chi^2 = \left\| \mathbf{M}^{-0.5} \cdot (\mathbf{g_1} - \mathbf{K} \cdot \mathbf{\Delta Q}) \right\|^2 \tag{2.53}$$

where $\mathbf{M}$ is the positive-definite covariance matrix of the measured data.[5] To further constrain the solution Provencher uses Tikhonov regularization [116] which introduces an additional term to be minimized:

$$\chi^2(\alpha) = \left\| \mathbf{M}^{-0.5} \cdot (\mathbf{g_1} - \mathbf{K} \cdot \mathbf{\Delta Q}) \right\|^2 + \alpha^2 \left\| \mathbf{R}_{eg} \cdot \mathbf{\Delta Q} \right\|^2 \tag{2.54}$$

Here, $\mathbf{R}_{eg}$ is the regularizor which introduces an additional constraint on the solution. Provencher [113] devised the role of the regularizor to introduce parsimony in the solution. Effectively, this means that the most probable solution is the one which *"reveals the least amount of detail or information that was not already known or expected"* [113]. Thus, CONTIN looks for a smooth distribution rather than for multimodal solutions. In consequence the second derivative of the distribution $q(D)$ is mostly chosen as regularizor to penalize changes of the gradient of the distribution. CONTIN also incorporates the choice of other derivatives but these have not gained significant value in DLS data analysis.

The regularization parameter α controls the strength of the constraint. If α is set zero, CONTIN behaves as a NNLS algorithm. If on the other hand α is chosen to be very high, the data are underestimated in the solution, so that not all extractable information is achieved. From this point of view it is clear that the selection of an optimum regularization parameter is the main problem in regularization methods. Different attempts to deal with the problem have been developed. Provencher [113, 114] used a Fisher F-test between a reference solution where $\alpha_0 \approx 0$ and a penalized solution with $\alpha > 0$. The test calculates a probability of rejection if the standard deviation of the smoothed solution differs too much from the reference standard deviation. The formulation is:

$$p_r(\alpha) = Q_F\left(F(\alpha), N_{DF}(\alpha_0), N_{\mathbf{g_1}} - N_{DF}(\alpha_0)\right) \tag{2.55}$$

$$F(\alpha) = \frac{\chi^2(\alpha) - \chi^2(\alpha_0)}{\chi^2(\alpha_0)} \cdot \frac{N_{\mathbf{g_1}} - N_{DF}(\alpha_0)}{N_{DF}(\alpha_0)} \tag{2.56}$$

where $p_r(\alpha)$ is the probability of rejection, $F(\alpha)$ is the F-test variable, N_{DF} is the number of degrees of freedom which is effectively the number of significant singular values of the kernel in

[5] In CONTIN it is assumed that $\mathbf{M}$ is diagonal so that each row of $\mathbf{g_1} - \mathbf{K} \cdot \mathbf{\Delta Q}$ is only multiplied with a constant factor.

the NNLS solution and $N_{\mathbf{g_1}}$ is the number of data points in the FCF. It is obvious that for small α p_r will have a number close to zero (corresponding to a NNLS solution), while for large values p_r approaches 1 and the solution is oversmoothed. Thus, Provencher [113, 114] recommends to use a probability of rejection of 0.5, though reasonable results may also be obtained with slightly smaller and larger values depending on the amount of other a priori information on the distribution [6].

Another commonly applied procedure to find an optimum α is the $\mathscr{L}$-curve criterion [117]. Here, different solutions with varying α are computed. Afterwards, the logarithmic norms $\log \|\mathbf{g_1} - \mathbf{K} \cdot \mathbf{q}\|^2$ and $\log \left\|\mathbf{R}_{eg} \cdot \mathbf{q}\right\|^2$ are plotted against each other. Fig. 2.9 shows an example.

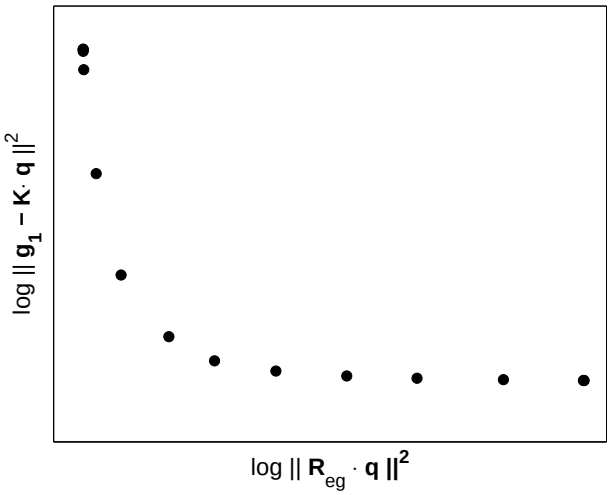

Figure 2.9: $\mathscr{L}$-curve of the regularized solution for the distribution of diffusion coefficients for a bimodal suspension of 15 nm and 100 nm spheres.

When increasing α the norm of the regularizer term is reduced accounting for the penalization of the solution. The norm of the kernel is kept nearly constant. At a certain point, the regularization begins to affect the norm of the kernel (left side of the diagram), hence, the solution begins to get oversmoothed by the regularization. An optimum α is obtained at the inflexion of the two *legs* of the $\mathscr{L}$-curve.

As shown above, the regularization of the inverse problem greatly enhances its solvability and the stability of the solution. CONTIN was the first set of algorithms that used this concept for DLS data analysis. Due to its modular concept the user was able to completely specify the parameters for the regularized fit and to incorporate all the a priori information that was available.

However, CONTIN still operated with the FCF which had to be derived from the ACF using eq. 2.41. This procedure deteriorates the inversion problem due to the earlier discussed problem with negative values. Therefore, Honerkamp et al. [118–121] and Weese [122] developed the NLREG program that is able to directly process the autocorrelation function. The inversion problem is now reformulated as:

$$g_2(\tau) - 1 = b \cdot \left[\int \exp\left(-Ds^2\tau\right) q(D)\, dD \right]^2 \tag{2.57}$$

This makes the integral equation nonlinear and thus Tikhonov regularization may not be used. The implemented method in NLREG, however, uses an equivalent (NLREG = Nonlinear Regularization) [122]. Additionally, a complicated error model developed by Schätzel [123] is implemented to compute the covariance matrix $\mathbf{M}$. The results are shown to fit simulated data better than linear regularization methods such as CONTIN [118]. Thus, nonlinear regularization offers to be the best choice to extract distributions of diffusion coefficients from DLS data.

2.3.3 Concentration Effects

Most industrially relevant suspensions are concentrated (i.e. solid content > 1 v.-%). When DLS experiments are conducted at such systems without previous dilution, data interpretation has to account for several limitations. Firstly, with an increasing number of particles in the scattering volume, the probability, that a photon scattered at a certain particle encounters another particle before it is registered at the detector, rises. This so-called multiple scattering effect will be shortly reviewed in the following chapter 2.3.3.1. Other effects stem from the particles itself. The theory of Brownian motion as outlined in Chap. 2.3.1.1 assumes the motion of one particle in a quiescent fluid with no contact to neighboring particles. This holds only for very dilute systems. In concentrated systems the particles interact via interparticle and hydrodynamic interactions and thus their motion, i.e. their respective diffusion coefficient, changes. These effects will be explained in Chap. 2.3.3.2.

2.3.3.1 Multiple Scattering

Multiple scattering leads to complications in DLS data analysis due to averaging effects that cannot be easily retrieved [124]. The net effect of multiple scattering contributions on measured autocorrelation functions is shown in Fig. 2.10. Firstly, the coherence factor b of the ACF

drops due to a destructive interference of the multiply scattered light [1] and secondly, the significant decay of the ACF is shifted towards smaller lag times. Additionally, the spectrum is broadened [125]. If such measurements are analyzed, broad distributions with a larger mean diffusion coefficient are obtained. Therefore, ISO 13321 [3] suggests a minimum value of b to be 0.8 in a measurement, so that multiple scattering contributions may be neglected in data analysis. In the past, when multiple scattering occured during a DLS experiment, the only way to overcome the problem was to dilute the sample and repeat the measurement.

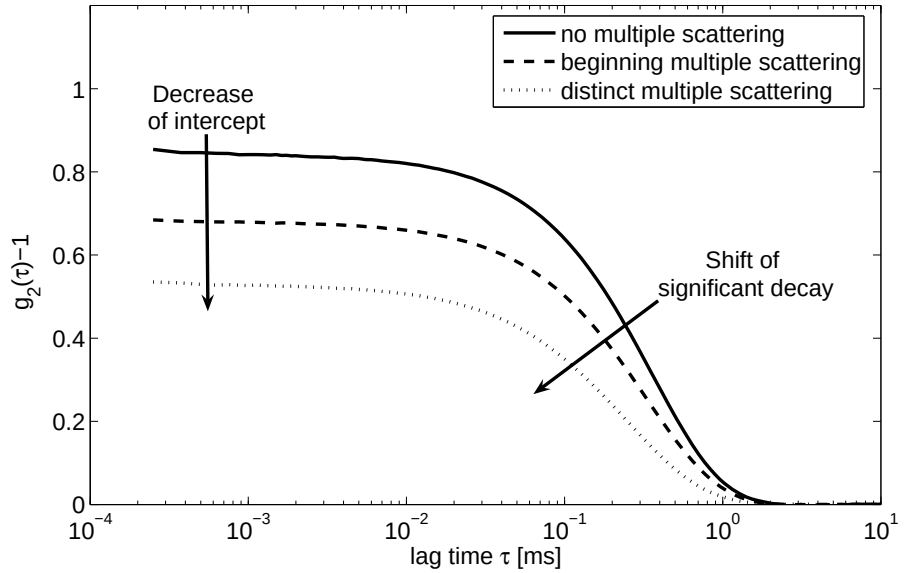

Figure 2.10: Net effect of the contribution of multiple scattering to the measured autocorrelation functions at different solid concentrations from an aqueous suspension of silica spheres with a size of 220 nm.

Today, there are three modifications to a classical DLS experiment dealing with the problem. The first uses a diffusion model to describe the way of a photon in the sample. Therefore, very strong multiple scattering is required. The so-called *Diffusing-Wave Spectroscopy* is then able to determine a mean particle diffusion coefficient in the sample while the information about the distribution is lost [5, 126, 127].

In the second case X-rays instead of visible light are used as impinging beam [128]. Most of the particles to be examined show a very low scattering cross section for X-rays. Thus, the contribution of multiple scattering to the measured signal drops significantly and reliable measurements can be attained in suspensions of up to 30 v.-% [129]. However, the costs for such a dynamic X-ray scattering set-up and the effort of conducting the experiments is not acceptable for standard analyses.

A third way to deal with multiple scattering of light is to suppress its contribution in the measured signal as much as possible. In general three approaches are pursued to achieve this:

Photon Cross-Correlation Techniques These are based on the basic idea of Phillies [130] to conduct two distinct scattering experiments at the same time and to compute the second-order intensity cross-correlation function as:

$$G_2^{cc}(\tau) = \langle I_1(t) I_2(t+\tau) \rangle \tag{2.58}$$

It can be proven that G_2^{cc} involves the same function for single scattering events while multiple scattering does not contribute in a perfect geometry of the set-up [124]. *Perfect* in this regard means an alignment of the two scattering vectors $\mathbf{s_1}$ and $\mathbf{s_2}$ so that either $\mathbf{s_1} = \mathbf{s_2}$ or $\mathbf{s_1} = -\mathbf{s_2}$. In practice this is not achieved but still the suppression ratio of multiple scattering is at least [124]:

$$\frac{\sqrt{\frac{\pi}{2}}}{R_b \delta s} \approx \frac{1.25}{R_b \delta s} \tag{2.59}$$

where R_b is the beam radius of the impinging laser and δs is the misalignment of the scattering vectors. In principle there are three different set-ups that can be thought of [124] but only two of them have been incorporated in commercially available instruments [131–133].

However, due to practical requirements in the alignment procedures the suppression ratio of multiple scattering is finite. Additionally, the decorrelation leads to a decrease of the coherence factor. For samples with strong multiple scattering the coherence factor can take values in the range of the electrical noise of the device. Then, no cross-correlation function can be found and the measurable concentration range is limited.

Non-Invasive Back-Scattering This technique uses a laser-detector installation with a fixed scattering angle of 173° [134]. In the backscattering regime multiple scattering is much less pronounced due to the shorter paths that a photon travels through the suspension and because the decay rates of doubly and singly scattered light are equal [135] i.e. that the first occurring multiple scattering mode does not influence the DLS result. Additionally, this technique uses a movable sample-holder that enables the user to change the position of the scattering volume in the sample and thus the optical path lengths (see Fig. 2.11).

Hence, it is possible to observe the reduction of multiple scattering contributions by the value of the coherence factor in a measurement without diluting the sample [136]. Of

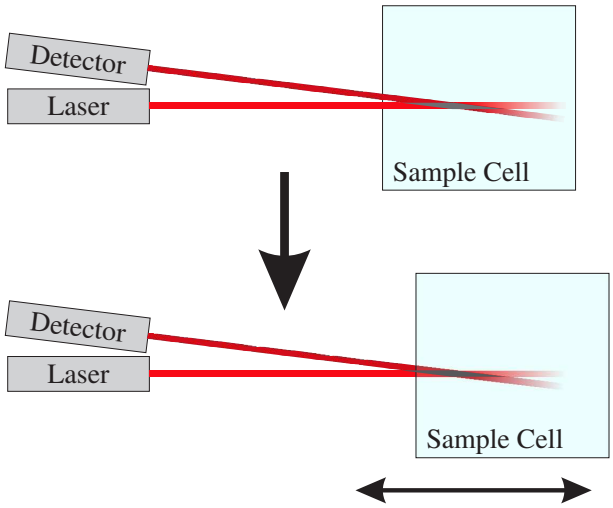

Figure 2.11: Scheme of the movable sample holder used in the non-invasive backscattering technique. The measurement volume is displayed in gray as the overlap of the incident beam and the aperture of the detection optics.

course, the suppression factor is also limited. In suspensions with a high optical contrast, the coherence factor drops below 0.8 and the sample has to be diluted. However, the measurable concentration range is comparable to cross-correlation techniques.[6]

Fiber-Optic Quasi-Elastic Light Scattering The idea of using fiber optics in Dynamic Light Scattering is not new [137]. However, substantial contributions from multiple scattering were reported in the first experiments by Auweter and Horn. Wiese and Horn used Single-Mode fibers that overcame the problem [135]. The basic idea is quite simple. The set-up uses a 3-port fiber optical coupler. The illuminating light beam passes the coupler and enters the suspension through an optode. The backscattered light enters the optode and is led to the photomultiplier tube by the optical coupler. Therefore, the scattering angle of such an experiment is $\approx 180°$. To reduce the reentrance of reflections of the impinging beam and thus circumvent a heterodyne measurement, the optode may be slanted.

This set-up guarantees very short path lengths of the photons in the sample and consequently a very good suppression of multiple scattering is achieved. On the other hand the path length varies with concentration and so does the measurement volume which implies some complications. A second disadvantage is that the scattering vector $\mathbf{s}$ is not well de-

[6] This result has been obtained by the author and his colleagues of the Research Group Mechanical Process Engineering of TU Dresden, who had the opportunity to directly compare non-invasive backscattering and 3D-cross-correlation instruments. As these devices are not yet widespread such parallel experiments could not be found in literature.

fined since the immersed fiber does not constitute a far-field measurement but averages over some scattering angles.

Due to the relatively cheap and easy assembly the FOQELS technique has been used in several scientific self-constructions, see e.g. [94, 138]. Today, there are two commercial instruments that use this technique as well.

2.3.3.2 Effects of Interactions

The effect of interactions (interparticle and hydrodynamic) on the measured diffusion coefficient is not easily accessible. At first the probing scale of the actual experiment needs to be known. The inverse of the scattering vector gives the length scale of observation just as in static scattering experiments. This is compared to the mean interparticle spacing r_m which is concentration dependent. If $s^{-1} \gg r_m$ a large number of individual particle motions is measured simultaneously. Thus, a mutual or collective diffusion coefficient is determined by DLS. If on the other hand $s^{-1} \leq r_m$ the individual motion of one particle in a suspension of others is measured. Hence, the obtained diffusion coefficient is the self-diffusion coefficient. For monodisperse particles the interparticle spacing can be readily computed from the number concentration. Fig. 2.12 shows the regimes of self and collective diffusion in dependence of the particle size and the particle volume fraction for monodisperse particles at a scattering angle of 173° and 632.8 nm wavelength (NIBS technique). It is readily identifiable that for particles larger than about 100 nm self-diffusion is measured over the whole concentration range. Collective diffusion is measured for particles smaller than 10 nm. In between these size ranges crossovers from self to collective motion occur.

Self and collective diffusion show different dependencies on hydrodynamic interactions. These can be calculated for hard sphere systems where interparticle interactions are absent. Batchelor [83] probably was the first to arrive at an analytical solution for the concentration dependence of the collective diffusion coefficient D_t^c that accounted for the pairwise hydrodynamic interactions of hard spheres:

$$\frac{D_t^c}{D_t^0} = 1 + 1.45\,\varphi + O(\varphi^2) \tag{2.60}$$

For simplicity he used a virial expansion that was cut after the linear term. This restricts the validity of eq. 2.60 to volume fractions smaller than 0.05. Later on, Felderhof [139] and Ohtsuki

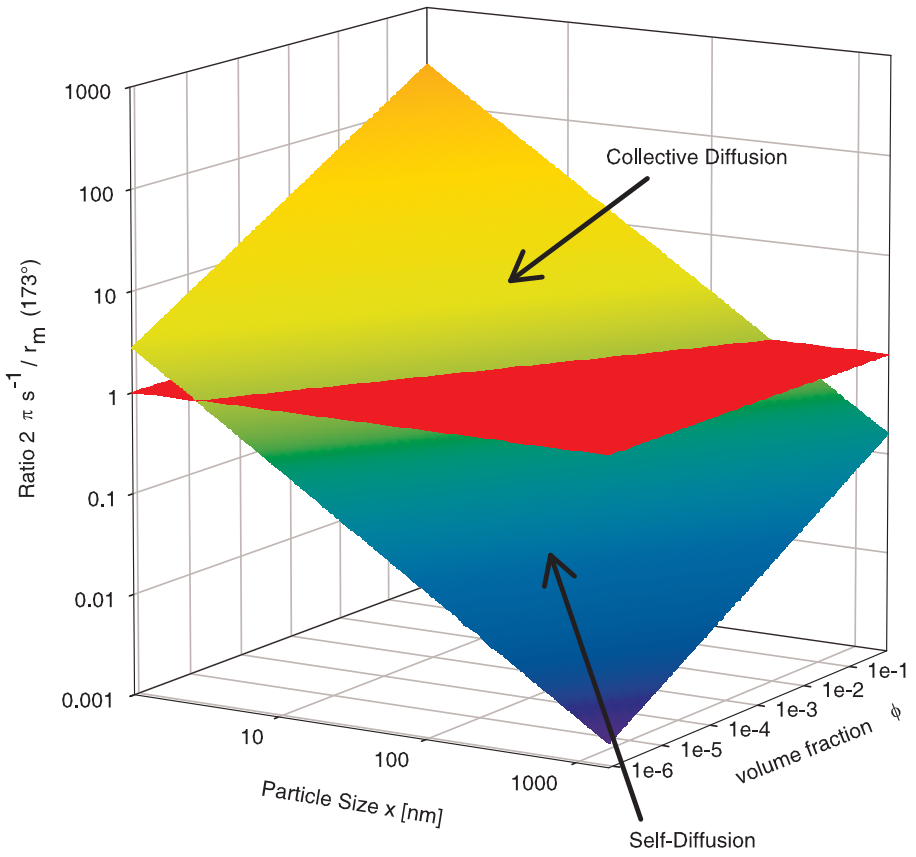

Figure 2.12: Measurement regimes of self and collective diffusion for suspensions of monodisperse particles of different sizes and concentrations. The scattering vector has been calculated for a scattering angle of 173°, 632.8 nm wavelength and water refractive index 1.332 (25 °C).

and Okano [140] slightly corrected the result of Batchelor to a value of 1.56 for the virial coefficient. For the self-diffusion coefficient D_t^s Ohtsuki and Okano obtained a similar expression:

$$\frac{D_t^s}{D_t^0} = 1 - 1.73\,\varphi + O(\varphi^2) \tag{2.61}$$

It is remarkable that self-diffusion slows down with concentration while collective diffusion is enhanced.

As already mentioned at higher concentrations many-body hydrodynamic interactions have to be considered to correctly describe the diffusion behavior. In a pioneering work Beenakker and Mazur [84–87] incorporated these for hard sphere suspensions. In the case of three-body interactions another virial expansion was given [84]:

$$\frac{D_t^c}{D_t^0} = 1 + 1.56\,\varphi + 0.91\,\varphi^2 + O(\varphi^3) \tag{2.62}$$

$$\frac{D_t^s}{D_t^0} = 1 - 1.73\,\varphi + 0.88\,\varphi^2 + O(\varphi^3) \tag{2.63}$$

Later, Mazur and Geigenmüller [141] revised the equation for the self-diffusion coefficient using an effective viscosity approach of Saitô [142]:

$$\frac{D_t^s}{D_t^0} = \frac{1-\varphi}{1+1.5\,\varphi} \tag{2.64}$$

Eq. 2.64 can be brought in the same form like eq. 2.63 by expanding in a Taylor series:

$$\frac{D_t^s}{D_t^0} = 1 - 2.5\,\varphi + 3.75\,\varphi^2 + O(\varphi^3) \tag{2.65}$$

which gives good approximations for $\varphi < 0.1$. The original equations 2.63 and 2.64 differ slightly for $\varphi > 0.15$ but are both supported by experimental results of different authors (see [141] for details). The validity range was given to $\varphi \approx 0.3$ but still no polydispersity and no direct interactions between the particles were considered. Pusey [74] was the first to give a correlation for polydisperse HS systems with a small polydispersity:

$$\frac{D_t^c}{D_t^0} = 1 + \varphi\left(1.56 - 9.80\,C_v^2\right) \tag{2.66}$$

$$\frac{D_t^s}{D_t^0} = 1 - \varphi\left(1.73 + 0.21\,C_v^2\right) \tag{2.67}$$

where C_v is the coefficient of variation of the size distribution. It is remarkable that polydispersity nearly has no effect on self-diffusion but makes a remarkable contribution to collective diffusion. Unfortunately, research has not gone any further in this.

Batchelor [143] expanded his model in 1983 to incorporate direct interactions in the virial expansion of the collective diffusion coefficient:

$$\frac{D_t^c}{D_t^0} = 1 + (1.45 - 0.56\nu)\,\varphi + O(\varphi^2) \tag{2.68}$$

Here, ν is a dimensionless interaction parameter which is positive for dominant repellent forces and negative for dominant attractive forces. This concept has later been used by Finsy [144] to generally describe interaction effects in DLS measurements.

Nägele [145] reviewed the existing theories for HS systems for their use in counterionic stabilized suspensions of monodisperse spheres. He finds that for small repulsive forces and moderate concentrations ($\varphi \leq 0.1$), the behavior can be predicted equally well with the hard sphere results. For larger concentrations deviations are found that are due to excluded volumes of the

suspension medium by a strong double layer repulsion. Nägele introduces the concept of an *enhanced hard sphere* diameter x_{EHS} and gives the following expression:

$$\frac{D_t^s}{D_t^0} = 1 + \varphi \cdot \left[-\frac{15x}{8x_{EHS}} + \frac{9x^3}{64x_{EHS}^3} + O\left(\left(\frac{x_{EHS}}{x} \right)^{-5} \right) \right] \tag{2.69}$$

Four possibilities to determine x_{EHS} are given, the simplest is obtained in dependence of the DLVO repulsive potential V_{el}:

$$\left(\frac{x_{EHS}}{x} \right)^3 = 1 + 3 \int_1^\infty r^2 \left(1 - \exp\left(-\frac{V_{el}(r)}{\mathrm{k_B} T} \right) \right) dr \tag{2.70}$$

These results are confirmed by experiments of Nägele [145]. Experimental results for bidisperse systems are also given. They can be modeled if the number of effective charges on the particles surface is left as an optimization parameter. However, simplistic conclusions for true polydispersity cannot be drawn.

To shortly summarize this chapter the following general guidelines, how diffusion is influenced by interaction effects, can be given:

1. One should at least have a crude idea what the size of the particles in a concentrated suspension is. Then it can be concluded from the measurement conditions whether the self or collective diffusion coefficient is measured.

2. Self-diffusion is generally hindered in concentrated suspensions with little effect of polydispersity. Collective diffusion is enhanced. This is counteracted by the polydispersity of the particles.

3. The effect of direct interactions can be simplified as follows:

    a) Attractive forces act as an additional drag force on the particles, therefore diffusion is hindered and slows down with decreasing interparticle distance, i.e. concentration.

    b) Repulsive forces act as a diffusion enhancement in moderate concentrations when only two-particle interactions are significant [146]. This is due to the repellent effect of the double layers. In high concentrations, where many-particle effects have to be accounted for, diffusion is again hindered by an increasing *caging* of particles. A pseudo-lattice is formed.

2.3.4 Dynamic Light Scattering for Fractal Aggregates

2.3.4.1 Relevance of the Hydrodynamic Particle Size

The analysis of dynamic light scattering data from fractal aggregates bears some complications. First of all it is necessary to scrutinize how the hydrodynamic particle size determined from eq. 2.30 can be related to structural properties of the aggregates. It is a difficult task to access this feature experimentally. A monodisperse distribution of clusters all having the same number and size of primary particles is required. Thus, theoretical models and simulations have been used as a tool for clarification.

One approach is based on the porous sphere model, where the Stokes equation outside the cluster is coupled with the Brinkman equation inside the cluster to model the hydrodynamic behavior [147–149]. As already pointed out in Chap. 2.1.2 this model leads to unphysical predictions. Therefore, Veerapaneni and Wiesner [22] introduced an onion model where a spherical aggregate is composed of shells with a varying permeability.

Another approach to model the hydrodynamic behavior is the Kirkwood-Riseman theory [150]. It has been used by many researchers to predict the hydrodynamic particle size of computer-generated aggregates in dependence of their radius of gyration and their fractal dimension [151–155]. It was found that the hydrodynamic radius is proportional to the radius of gyration for a fractal aggregate but the proportionality constant R_h/R_g differs between 0.765 for $D_f = 1.85$ and 0.831 for $D_f = 2.05$ [153]. This is consistent with the upper limit of $R_h/R_g = \sqrt{5/3}$ for a sphere with $D_f = 3$. However, the exact values of the proportionality constant are still under debate since the Kirkwood-Riseman theory is also just an approximation.

Based on the proportionality relation Griffin and Griffin [156] and Ju et al. [157] have developed analysis schemes for DLS measurements that allow for the monitoring of aggregation processes in terms of aggregate size and fractal dimension either via the second cumulants analysis or the CONTIN inversion.

Filippov [158] used a direct method to integrate the Stokes equation and to derive the complete friction and torque tensors of an aggregate. This approach is the most accurate and has become quite popular but involves the solution of a large system of equations and is, therefore, computationally expensive.

Simulations based on finite volumes [159], Lattice-Boltzmann or Stokesian Dynamics [160] may also be used to obtain the hydrodynamic properties. Especially, Lattice-Boltzmann methods have the charm that also sintered structures may be examined but to the expense of an enormous computational effort.

2.3.4.2 Influence of Rotational Diffusion

As fractal aggregates do not show a homogeneous structure the impacts of the solvent molecules induce stochastic torques. This so-called rotational diffusion also leads to fluctuations of the scattered light intensity and thus influences the decay of the auto- or cross-correlation function. Xu [5] gives a relation for this contribution for regular particles where the particle form factor $P(s,x) = \sum_i P_i(s,x)$ may be defined using the Rayleigh-Debye-Gans approximation to describe the scattering behavior:

$$g_1(\tau,s) = \sum_{i=0,\text{even}} P_i(s,x) \exp\left[\left(-D_t s^2 - i(i+1)\Theta_{rot}\right)\tau\right] \tag{2.71}$$

where Θ_{rot} is the rotational diffusion coefficient. In the small s-limit ($s \to 0$) all $P_i(s,x) = 0$, except for $i = 0$. Therefore, rotational diffusion does not contribute in this region. Xu [5] recommends to conduct multi-angle measurements and to extrapolate the results to $s = 0$ to overcome the effect.

For fractal aggregates there have been very limited investigations concerning rotational diffusion. The first consideration was by Lindsay et al. [47, 161]. Through a multipole expansion they were able to calculate the rotational contribution of computer-generated clusters. By averaging over several aggregates they obtained master-curves that are shown in Fig. 2.13.

It can be obtained that independent of aggregate size, the effect of rotational diffusion leads to an overestimate of their diffusion coefficient by about 70 % and thus to an underestimate of their hydrodynamic particle size. The condition of measuring at least 50 pairs of aggregates simultaneously to obtain a good averaging is easily fulfilled in DLS experiments. It can additionally be concluded that if the master-curve is known for a certain sample, measurements at a single scattering angle might be corrected for the effect of rotational diffusion. Lindsay et al. [161] proved this with experiments on agglomerating gold particles.

Recently, Lattuada et al. [155] revised the results of Lindsay et al. using an extension of the Kirkwood-Riseman theory [162] to compute the rotational diffusion coefficient Θ_{rot} of sim-

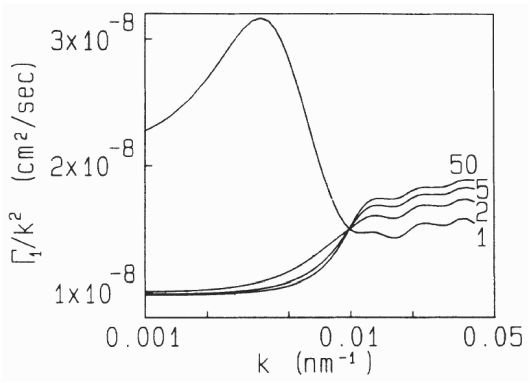

(a) Evolution of the decay rate $\Gamma_1 = Ds^2$ for 1, 2, 5 and 50 pairs of DLCA aggregates consisting of 100 and 1000 primary particles.

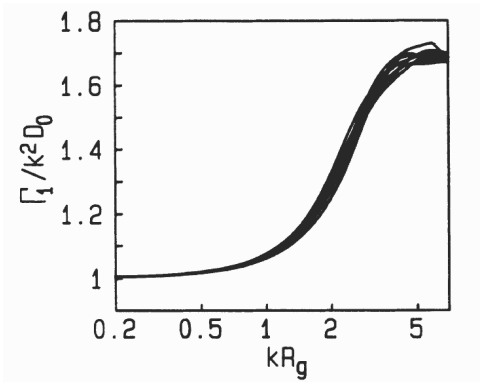

(b) Master-curve of the first cumulant for DLCA aggregates of 100, 200, ..., 1000 primary particles. Proportionality constant $R_h/R_g = 0.87$.

Figure 2.13: Effect of rotational diffusion of DLCA aggregates on DLS data obtained by a second cumulants analysis. The wave vector s is designated as k and D_0 is the Stokes-Einstein diffusion coefficient measured at $s = 0$. Reprinted with permission from [161]. Copyright (**2007**) by the American Physical Society.[7]

ulated aggregates. The rotational hydrodynamic radius $R_{h,rot}$ can also be obtained from this diffusion coefficient using an equivalent to the Stokes-Einstein equation:

$$\Theta_{rot} = \frac{k_B T}{8\pi\eta R_{h,rot}^3} \tag{2.72}$$

Typically, to compute the effect of rotational diffusion on DLS results $R_{h,rot} = R_h$ is assumed. Lattuada et al. [155] showed that this underestimates the rotational hydrodynamic radius and thus the overestimate of the diffusion coefficient in the large s-range of the master-curve (Fig. 2.13) is not 70 % as obtained by Lindsay et al. [155] but only about $40 - 42$ %. The principal shape of the master-curve is not influenced by these results so that corrections of DLS data can be altered accordingly.

[7] Readers may view, browse, and/or download material for temporary copying purposes only, provided these uses are for noncommercial personal purposes. Except as provided by law, this material may not be further reproduced, distributed, transmitted, modified, adapted, performed, displayed, published, or sold in whole or part, without prior written permission from the American Physical Society.

Abstract available online at: `http://prola.aps.org/abstract/PRA/v38/i5/p2614_1`

3 Motivation

Hitherto, investigations on the explanatory power of DLS measurements for the characterization of polydisperse fractal aggregates are insufficient. At first sight, it is an important prerequisite to obtain an understanding of the granulometric properties that are measurable with DLS for e.g. pyrogenic silica. Additionally, the available sensitivity is of great relevance.

As can be deduced from the state of the art, experimental studies will not provide enough insight into the relevant mechanisms. Therefore, simulations are used. These have to make several assumptions about the particle system such as a known and monodisperse size of the primary particles, the generation mechanism of the aggregates and the number of primary particles per aggregate. Averaged values are obtained from different aggregates but with the same size and number of primary particles. Mostly, approximate methods such as Kirkwood-Riseman theory are afterwards used to evaluate the hydrodynamic properties.

However, there are two aspects that have not been considered in the past. First, all the generation mechanisms mentioned produce aggregates whose fractal dimension scatters round a mean value for finite numbers of primary particles. Thus, the *true* effect of the structural parameters on the hydrodynamic properties could never be investigated. Then, a second restraint is that the alterations introduced by the approximations cannot be separately observed.

Therefore, in this thesis another approach will be pursued. The hydrodynamic behavior will be computed using the direct method of Filippov [158] to avoid any unnecessary assumptions (c.f. Chap. 5). The generation mechanism that is most probable for pyrogenic silica (DLCA [20]) will be compared to model aggregates with fixed structural properties.

The results obtained in the simulations will be verified with experiments since not all practically relevant aspects (sintering, aggregate polydispersity) can be taken into account due to the computational effort (Chap. 6). Structural properties will be determined from SAXS and SLS

measurements while the diffusional properties will be obtained from multi-angle DLS to determine the influence of rotational diffusion. Simulations and experiments together will firstly give an insight into the relation between structure and diffusion for polydisperse fractal systems.

The third large concern of this work is the characterization of industrially-relevant systems, i.e. concentrated suspensions. Here, effects of interparticle and hydrodynamic interactions have to be taken into account. These have attracted much attention in the past for hard-sphere systems and counterionic-stabilized spherical suspensions. However, the theoretical treatment is limited to monodisperse or at maximum bidisperse spherical particles.

It is at least questionable whether the models developed for such systems are applicable for polydisperse fractal aggregates. As a theoretical treatment of this problem is not feasible, an experimental approach will be pursued in Chap. 7. A detailed comparison between mono- and polydisperse silica sols and pyrogenic silica suspensions will reveal the origin and extent of interaction effects that have to be considered in DLS data analysis.

The solution of these principal characterization tasks of suspensions of fractal aggregates is essential for the understanding of DLS. However, the analysis of well dispersed and stabilized suspensions covers only a small part of the relevant technical applications. Often problems concerning e.g. the dispersibility of a powder, the detection of smallest off-specification shifts of a product or the observation and quantification of a gelation process e.g. in product design have to be solved since these bother the application process of a suspension at the end-user. On the other hand, these tasks can hardly be handled using standard analysis techniques. Two examples will be investigated in Chap. 8. It will be shown how a sophisticated treatment of the measured DLS data can be used to explore new fields of application for DLS techniques. DLS might afterwards be used to predict gelation times and kinetics or to detect coarse grained contaminants that evolve e.g. from product handling and storage.

4 Materials and Methods

4.1 Pyrogenic Silica

The investigations in this thesis were conducted in cooperation with Wacker-Chemie AG, Burghausen, Germany. Therefore, the used pyrogenic silica samples (Wacker HDK®) were produced in Burghausen, Germany and afterwards sent to TU Dresden for analysis as powder material in containers of 200 g each. Table 4.1 gives an overview of the samples that were employed for DLS characterization and their properties:[1]

Table 4.1: Employed pyrogenic silica samples and their relevant physical properties.

HDK® Grade	Spec. Surface Area S_m (BET) $\left[\mathrm{m}^2/\mathrm{g}\right]$ (Mean of Specification)	Mean Sauter Diameter x_{ST} [nm] (eq. 1.1)	Bulk Density ρ_B $\left[\mathrm{kg}/\mathrm{m}^3\right]$	Refractive Index n_p
D05	50	54.5	≈ 50	1.46
C10P	100	27.3	≈ 100	1.46
S13	125	21.8	≈ 50	1.46
V15	150	18.2	≈ 50	1.46
N20	200	13.6	≈ 40	1.46
T30	300	9.1	≈ 40	1.46
T40	400	6.8	≈ 40	1.46

[1] Excerpt from the product descriptions of Wacker HDK® that are available online at http://www.wacker-hdk.com (Reprinted with permission). Only the mean of the specific surface area specification is given since all employed samples were selected at mid values by Wacker-Chemie AG. The BET method is used to determine the specific surface area by gas adsorption (mostly nitrogen). The adsorption isotherm is exploited using the model of **B**runauer, **E**mmett and **T**eller.

The solids density is not explicitly given in the table, since there is still debate about the exact value (between $2150 - 2250\ \mathrm{kg/m^3}$) for each grade. Wherever necessary in this work a value of $2200\ \mathrm{kg/m^3}$ has been used.

The most important property for the DLS investigations is the specific surface area. As already mentioned in Chap. 1.2 grades with a high specific surface area (i.e. HDK® N20 or T30) possess a very small distribution width of primary particle sizes while those with a small specific surface area (i.e. HDK® D05 or C10P) generally have a broad distribution. Thus, the effect of polydispersity may be studied using different silica grades. HDK® T40 is an exception. Here, the very high specific surface area is not only obtained by very small primary particles but also by an intrinsic porosity of these primary particles. Therefore, differences in the analysis results might be due to this structural difference.

All the grades used in this thesis were hydrophilic and could, therefore, be well dispersed in aqueous solutions. Though, there were some differences in required dispersion energy that will be addressed in Chap. 4.3. Attention has to be paid to HDK® C10P since this grade has been compacted in the dry phase to gain a higher bulk density.

4.2 Colloidal Silica Sols

To get an impression of the influence of the fractality of pyrogenic silica aggregates in DLS experiments, complementary investigations have been concucted with four different samples of colloidal silica sols (Table 4.2). These samples were delivered in stabilized aqueous solutions from the manufacturers. Thus, they contained unknown dispersing agents that influence the interactions between the particles. Therefore, the sample Fuso PL-3 has been purified for a clarification of these influences (for details see Chap. 4.3).

Size and polydispersity information have been obtained from a second cumulants analysis of DLS measurements in highly diluted samples. To keep the suspensions stabilized the pH and the conductivity of the original was kept constant during dilution with KOH and KNO_3, respectively. The results are listed in Table 4.2.

It can be deduced from these results that the Levasil samples are nearly monodisperse while the Köstrosol and Fuso samples show a broad distribution of particle size. Thus, the effect of polydispersity can again be separately observed in the DLS experiments.

Table 4.2: Employed colloidal silica sols, size information has been obtained by DLS experiments in highly diluted suspensions by keeping the pH and the conductivity constant.

Sample	Harmonic mean size x_{DLS} [nm]	Polydispersity Index *PDI*	Original concentration [wt.%]	Manufacturer
Levasil 02T063	42.5	0.074	31.2	H.C. Starck GmbH & Co. KG, Goslar, Germany
Levasil 02T144	91.8	0.071	30.7	H.C. Starck GmbH & Co. KG, Goslar, Germany
Köstrosol AD	28.4	0.286	31.1	CWK Chemiewerk Bad Köstritz, Bad Köstritz, Germany
Fuso PL-3	73.6	0.127	10.0	Fuso Chemical Co., Ltd., Osaka, Japan

4.3 Sample Preparation Procedures

The exact and reproducible dispersion of the pyrogenic silica powders in an aqueous solution is an important prerequisite for the DLS experiments and data analysis. Effects of imperfect dispersion such as smaller diffusion coefficients due to agglomerates have to be avoided.

Based on earlier dispersion experiments with agglomerated colloidal spherical silica powders at the TU Dresden [163, 164] a sample preparation procedure for pyrogenic silica has been developed together with Vorbau [165] that contains the following general steps:

1. Depending on the desired solids concentration the appropriate amount of pyrogenic silica was suspended in the electrolyte solution using a magnetic stirrer.[2] This solution was produced from deionized water and a mother solution of high electrolyte concentration. In this thesis, only KNO_3 was used as electrolyte since the dissolved ions do not react specifically (e.g. adsorption to the surface) with the silica surface at low salt concentrations. The employed salt concentrations ranged from 10^{-3} M to 10^{-1} M.

[2] It has to be noted, however, that magnetic stirrers are not appropriate for a long-term homogenization of pyrogenic silica suspensions. At higher pH, PTFE from the stirring bars is released which attaches to the silica surface and leads to hydrophobic behavior. Thus, flocs of silica are generated that float to the surface of the suspension.

2. Subsequently, a first dispersion was carried out using a rotor-stator disperser (UltraTurrax T50, IKA Werke GmbH & Co. KG, Germany with dispersion tool S50N-G40F). Here, agglomerates are destroyed in the shear slit between rotor and stator (slit width 0.5 mm, Ø 32 mm). Dispersion lasted for 10 min at 7000 rpm.

3. The pH of the solution was adjusted to the desired value. The pH of a freshly dispersed pyrogenic silica suspension is approximately 4.5, a counterionic stabilized suspension is obtained at pH $\geq$ 9. KOH was used for the alkalification. Since at a too high pH the ionic strength of the total suspension changes strongly due to dissociation of the base a maximum of pH 9 was used in the experiments.

4. State of dispersion was controlled (baseline) via laser diffraction (measurement instrument HELOS 12 KA/LA, Sympatec GmbH, Clausthal-Zellerfeld, Germany). The dispersed sample was diluted for the measurement with distilled water and a focal length of 20 mm was used. Although laser diffraction techniques are not able to measure the size distribution of pyrogenic silica aggregates the progress of dispersion may well be followed by observing the diminishment of particles larger than 1 micron (agglomerates). Fraunhofer diffraction model was used for data analysis. Though this is not fully correct for smallest particles, it offers the charm of a continuous change of particle size while the often applied Mie model cannot follow small deviations in the particle size distributions due to numeric problems.

5. Afterwards, further dispersion was carried out using an ultrasonic disintegrator (VibraCell VCX 600, 600 W, Sonics & Materials Inc., Newtown, USA). Here, the dispersion effect is mainly due to highly turbulent flow fields induced by cavitation. Sonification lasted 2 min with full power of 600 W. To avoid a too strong heating, the probe was used in pulse mode, i.e. after 2 s of sonification the sonifier was stopped for 2 s.

6. After sonification, the suspension was cooled to room temperature in a water bath and the state of dispersion was again controlled with laser diffraction.

7. Steps 5 and 6 were repeated until no alteration of the measured size distributions was recognized between two consecutive measurements.

8. The pH was again controlled and corrected if necessary.

9. The sample was finally homogenized for at least 12 hours using an overhead stirrer (EUROSTAR Digital, IKA Werke GmbH & Co. KG, Germany). Directly before the measurement, pH and conductivity were checked again.

At high solids concentration ($\approx$ 15 wt.%) a good suspension of the powder is not achievable using a magnetic stirrer in step 1 because a gel is formed that cannot be broken by the power of these instruments. Thus, the powder was directly fed into the rotor-stator disperser.

Fig. 4.1 exemplarily shows two dispersion processes of HDK® D05 and S13, respectively. Plotted are the size distributions as obtained from laser diffraction. The shift towards smaller particle sizes with increasing dispersion energy can very well be observed. Additionally, it can be seen that different silica grades may require a varying number of sonification steps to get a good dispersion. Thus, the permanent control of the state of dispersion is a duty for correct analysis results. Laser diffraction techniques are preferred for their quick and easy implementation.

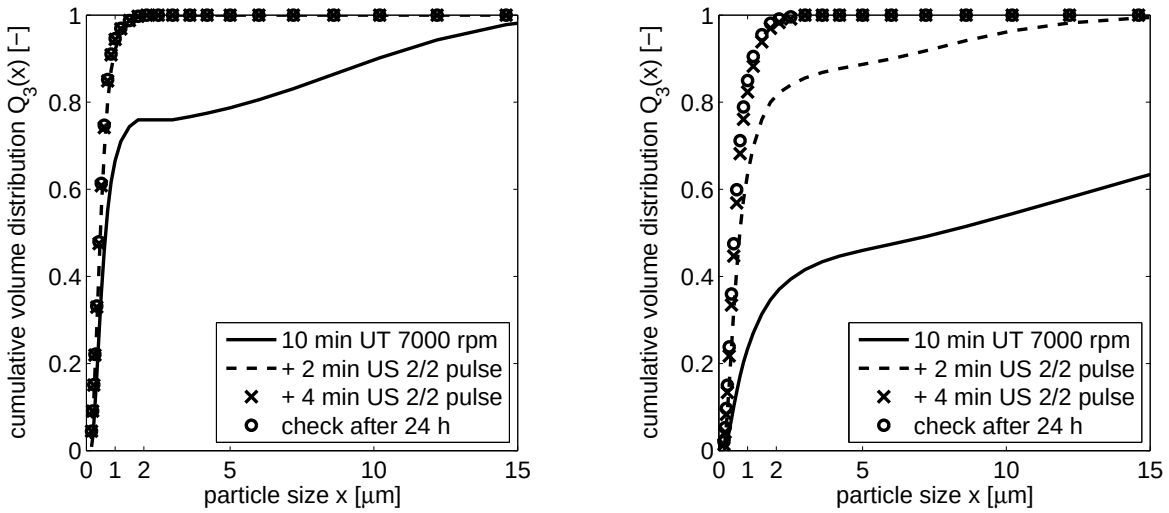

(a) HDK® S13, easily dispersable

(b) HDK® D05, difficult to disperse

Figure 4.1: Observation of the dispersion process of pyrogenic silica samples via laser diffraction. Particle size distributions obtained after subsequent dispersion steps that are marked in the diagrams. (Abbr.: UT = UltraTurrax, US= Ultrasonic Disintegrator).

As already mentioned in Chap. 4.2 the silica sols did not need to be dispersed because they were already in the liquid phase. However, since the original concentration of Fuso PL-3 was too low to obtain a good concentration series in DLS it was concentrated and thereby purified by centrifugation. Centrifugation was carried out with a Labofuge I (Heraeus Christ GmbH, Hanau, Germany) at 4500 rpm for 10 h. Subsequently, the supernatant was removed and the beakers filled up with an electrolyte solution (10^{-3} M KNO_3 at pH 9). Suspension was homogenized and dispersed using sonification. The state of dispersion was controlled via DLS measurement (second cumulants analysis). This procedure was carried out 3 times. Finally, the total solids

concentration of the purified sample was 35.24 wt.%.

If dilution was necessary during the experiments it was carried out using a dilution medium of exactly the same composition (electrolyte, pH) as the original suspension. However, this was not possible for the silica sols where unknown dispersing agents existed. Here, dilution was accomplished by keeping the pH and the conductivity constant with KOH and KNO_3, respectively. Before measurements that required a high purity of the suspension, the dilution medium was filtered through a 0.2 micron membrane. The suspension itself had to pass a 20 micron paper filter to remove unwanted coarse particles that may originate from drying agglomerates, dispersion tool abrasion or dust contamination.

4.4 Dynamic Light Scattering - HPPS

Within this thesis a Malvern HPPS DLS instrument (Malvern Instruments Ltd., Worcestershire, UK) was used as a commercially available device. In the meantime, the name HPPS, which means High Performance Particle Sizer, has been replaced by the name Zetasizer Nano. Despite several changes in the mechanical set-up, the measurement procedure remains the same.

The system uses a vertically polarized He-Ne gas laser (632.8 nm wavelength in vacuum). The power of the laser can be attenuated by neutral gray filters to 22 different intensity levels so that strongly and weakly scattering samples can both be measured. For laser power stabilization, the instrument had to run at least 1 h before the first measurement.

To suppress multiple scattering contributions in concentrated systems the instrument is equipped with NIBS (Non-Invasive Backscattering) technology. The scattered light is registered at a scattering angle of 173°. A movable sample holder set-up additionally enables the change of the measurement volume for further reduction of multiple scattering (c.f. Chap. 2.3.3.1).

The detector is an avalanche photodiode that works in homodyne mode. The registered photon counts are processed by a hardware correlator (ALV 5000E, ALV Laservertriebsgesellschaft mbH, Langen, Germany). The smallest sampling time of the instrument, i.e. the first data point of the autocorrelation function, is only 125 ns. The patented multiple-tau technology allows for a nearly perfect logarithmic spacing of lag times so that fast and slow fluctuations can be acquired in a single experiment. Further on, this spacing stabilizes the solution of the inversion problem in data analysis.

The sample holder includes a Peltier element that can be used to keep the sample temperature at a fixed value in the range of 8 °C to 55 °C. Polystyrene cuvettes of 10 x 10 x 48 mm size (Sarstedt AG & Co., Nümbrecht, Germany) were applied in the investigations. Sample volume per measurement was about 2 ml. Temperature equilibration typically lasted for 15 min in these cells.

Control of the instrument parameters such as cuvette position, temperature, measurement time and repetitions as well as data acquisition and analysis was attained via the ALV Correlator Software V.3.0. The software includes cumulants analysis (linear, second and third cumulants), inversion via CONTIN, a nonlinear regularization method and a nonlinear fit tool with a model data base. Within this thesis, only second cumulants and the nonlinear regularization method were used.

Each measurement is separately written to an ASCII-file that can also be used for further analysis with external programs.

4.5 Multi-Angle DLS

To reveal the *s*-dependence of the measured diffusion coefficients in pyrogenic silica, angle-dependent DLS measurements were conducted at the Faculty of Science, Department of Chemistry and Food Chemistry, Professorship Physical Chemistry of Polymers of the TU Dresden.

The employed instrument was an ALV/DLS/SLS-5000 laser light scattering spectrometer (ALV Laservertriebsgesellschaft mbH, Langen, Germany) with a ALV-5000/EPP multiple tau correlator and a ALV/CGS-8F S/N 025 goniometer system. The goniometer provides an angular range of 10°-150° with a resolution of 0.003°. A He-Ne gas laser (Uniphase 1145P, output power 22 mW, JDS Uniphase Corp., Milpitas, USA) at 632.8 nm wavelength in vacuum, that could be mitigated by a compensated optical attenuator, was used as light source. Laser power stabilization lasted for at least 1 h before a measurement.

The sample was contained in a cylindrical glass cell (Ø 10 mm), sample size was about 5 ml. The cell was placed in an index-matching vat (toluene) with an accuracy of centricity of $\pm$ 5 µm to avoid light scattering effects at the sample/cell interface. The vat is also used to keep the temperature of the sample. Before, a measurement run was started, temperature of vat and

sample were equilibrated for 15 min. For each measured scattering angle the data aquisition time was changed according to eqns. 2.38 and 2.6:

$$\frac{t^1_{meas}}{t^2_{meas}} = \frac{\sin\left(\frac{\theta_2}{2}\right)}{\sin\left(\frac{\theta_1}{2}\right)} \tag{4.1}$$

to probe the same dynamic range and yield the same statistics for each data point of the measured ACF. As a starting time 90 s duration for $\theta = 173°$ was chosen.

Data acquisition and analysis was again carried out with the ALV Correlator Software V.3.0.

4.6 Static Light Scattering

Static light scattering was employed to examine structural properties of diluted aqueous pyrogenic silica suspensions. Measurements were also conducted at the polymer characterization lab of the Professorship Physical Chemistry of Polymers at TU Dresden.

A modified FICA 50 (Applied Research Laboratories GmbH, Neu-Isenburg, Germany, modified by SLS Systemtechnik G. Baur, Denzlingen, Germany) equipped with a He-Ne gas laser was used. The angular range of the instrument is 15°-145°.

The samples ($\approx$ 10 ml) were again contained in a temperature-controlled index-matching vat. No background signal and no refractive index increment was measured since this is not necessary for the determination of the radius of gyration.

4.7 Small Angle X-ray Scattering

In addition to SLS, SAXS measurements of pyrogenic silica suspensions were conducted at the Institute of Mechanical Process Engineering and Mechanics, Faculty of Chemical Engineering and Process Engineering of the University of Karlsruhe.

The experimental set-up is a modified Kratky camera with a block collimation system as described by Dingenouts [166]. The measurable s-range is 0.04 $nm^{-1} - 1$ nm^{-1}. A disadvantage to synchrotron SAXS measurements is the finite width of the primary beam which leads to a smearing of the intensity. Thus, desmearing is a very important step in data analysis.

Samples are measured in a glass capillary in the beam. As the capillary itself and the suspension medium contribute to the scattering signal, background measurements are necessary.

Data acquisition and analysis have been carried out in the following way:

1. Background measurement and measurement of sample, duration $\approx$ 8 h per sample
2. Correction of the measured scattering intensity for background scattering and desmearing
3. Structural analysis using the Irena 2 package (Argonne National Laboratory, Argonne, USA) for Igor Pro (WaveMetrics Inc., Lake Oswego, USA).

5 Simulation of Single Aggregate Diffusion Behavior

5.1 Objectives

The simulations conducted in this work shall reveal the connection between structural properties of pyrogenic silica aggregates and their respective hydrodynamic properties, i.e. the translational and rotational diffusion coefficient. Therefore, it is a prerequisite to virtually generate aggregates. With respect to Chap. 2.1.3, relevant mechanisms will be chosen. Afterwards, the structure of the simulated aggregates must be characterized in terms of size and fractal dimension. There are different methods to obtain these parameters. It will be shown that for simulated aggregates resembling pyrogenic silica only one approach gives reliable results (Chap. 5.2.2).

To reveal a basic understanding of the relations between the fractal parameters (esp. the fractal dimension) and the diffusional behavior another algorithm has been developed together with Bedrich [167] (Chap. 5.2.3). Here, aggregates with predefined structural properties may be generated without large variations in fractal dimension that are inherent in the previously described algorithms (c.f. Chap. 2.1.3).

The determination of hydrodynamic properties of fractal aggregates has also been pursued by different approaches in the literature (c.f. Chap. 2.3.4). Here, the direct computation using a multipole expansion of the flow field around an aggregate originally developed by Filippov [158] will be used to obtain an as exact as possible solution. For large aggregates ($N_{prim} > 1000$ at the moment) this method is not recommended since the computational effort rises significantly with the number of primary units per aggregate [167]. However, transmission electron micrographs of single pyrogenic silica aggregates obtained by Wacker-Chemie AG, Burghausen, Germany, have shown that the number of primary particles per aggregate is

typically in the range of $20-1000$. Thus, the restriction of the multipole method is not obstructive. The implementation of the algorithm has been conducted by Bedrich [167] and will therefore only be described in excerpts in Chap. 5.3. To describe the structural dependence of the hydrodynamic behavior a power law comparable to eq. 2.2 will be chosen.

A comparison of the results obtained with the used algorithm with former results will be given in Chap. 5.4. The consequences that arise in the analysis of DLS measurements will be described.

5.2 Aggregate Formation

5.2.1 Algorithms

As described by Schaefer and Hurd [20], the most relevant algorithm for pyrogenic aggregates is the Diffusion-Limited Cluster Aggregation (DLCA). The implemented Monte-Carlo simulation works as follows:

1. The number of primary particles the generated cluster shall consist of must be chosen.
2. All the particles are placed randomly in a virtual cubic box so that no overlap occurs. Particles are equally sized with a normalized size of 1. The size of the box is essential for the computation speed of the algorithm. If the box is too small the particles cannot perform a random-walk, the discrete equivalent to Brownian motion. If it is too large, too many steps of the algorithm must be run through until a collision occurs. Here, the length of one side of the cube is determined by:

$$l = 12.6 \sqrt[3]{N_{prim}} \tag{5.1}$$

   to guarantee a constant particle density independent of the number of primary particles.
3. A uniformly distributed direction vector is assigned to each particle.
4. All the particles move along their respective direction vector with a step width of 0.5.
5. The distance matrix of all particles is computed. This matrix is of size $N_{prim} \times N_{prim}$ so that $N_{prim}^2 - N_{prim}$ distances have to be checked for an occurring collision. This makes the algorithm slow for large aggregates.

6. If a collision happened, the particles stick together, a small aggregate occurs. If no sintering is included, the particles touch each other in a single point. Additionally, a sintering factor C_{sint} can be predefined which is:

$$C_{sint} = 1 - \frac{l_{cc}}{x_{prim}} \tag{5.2}$$

where l_{cc} is the center-to-center distance of the two colliding particles and x_{prim} is the size of these particles.

7. Aggregates are treated like primary particles in the subsequent steps of the algorithm. They are assigned a unique direction vector and move with the same step width.

8. Aggregation continues until only one large aggregate remains. Fig. 5.1 shows an example of this generation process. The coordinates of the primary particles with respect to the center of gravity of the aggregate are finally computed and saved to a file.

It might happen that particles hit the wall of the box during the aggregation process. Then, periodic boundary conditions are applied, i.e. the particle leaves the box and enters it again at the opposite side.

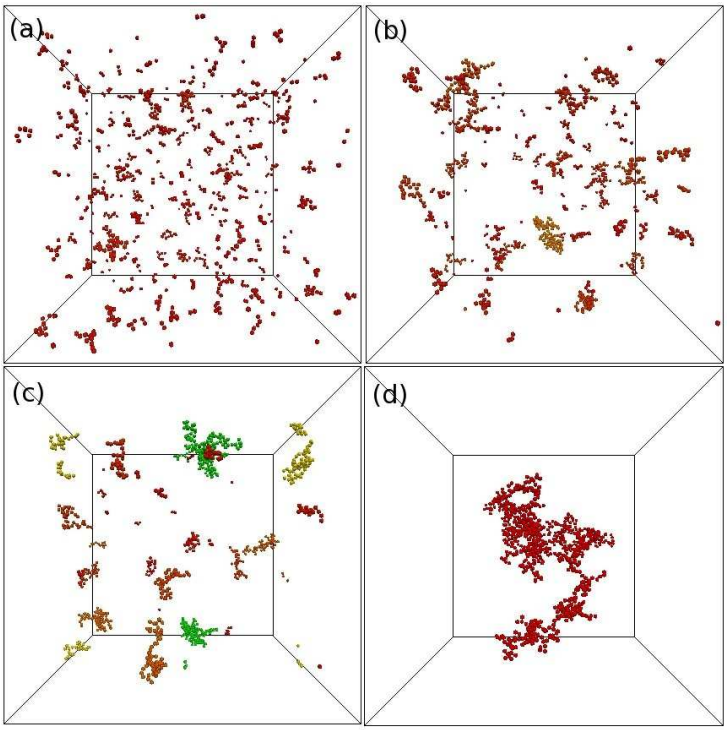

Figure 5.1: Representation of the DLCA generation process with $N_{prim} = 1000$ [167]. In (a) 300, (b) 100, (c) 30 and (d) 1 cluster is formed.

As already noted, the DLCA algorithm becomes very slow for large aggregates. With 1000 primary units a state-of-the-art computer needs about 2 days for the generation process. This is

unsatisfactory if relations have to be checked with large aggregates. Therefore, Bedrich [167] developed a new algorithm where the generated aggregates resemble DLCA formation but with an enormously increased generation speed. This cluster-cluster aggregation (CCA) process requires the aggregate to consist of $N_{prim} = 2^i$ primary particles where i is a natural number. Then, the first step includes the combination of every 2 particles under a random angle. Afterwards, the two-particle-aggregates are grouped together to form 4-particle-aggregates and so forth. As the random-walk is omitted in this procedure, this algorithm is faster by far than DLCA with the restriction that only specific numbers of primary particles are possible.

5.2.2 Determination of Fractal Properties of the Generated Aggregates

There are two structural properties of the simulated aggregates that are important for the further processing, the radius of gyration R_g and the mass-fractal dimension D_f^m. The surface fractal dimension D_f^S is set to 2 since the generation algorithm considers perfect spheres as primary particles.

The radius of gyration is readily accessible from the formation process. It can be computed from eq. 2.4. Therefore, only the coordinates of the primary particles have to be read from the file, since all primary particles possess the same size.

The fractal dimension can be determined in three different ways. First, as already shown by Witten and Sander [29], the particle-density correlation function shows a power-law behavior such as:

$$G_\rho = \frac{1}{N_{prim}} \sum_{r'} \rho(r')\rho(r'+r) \tag{5.3}$$

$$G_\rho \propto r^{D_f^m - D_{eu}} \tag{5.4}$$

Here, D_f^m is directly the fractal dimension and D_{eu} is the normal dimension of the Euclidian space under consideration.

A second method is the so-called Boxcounting. The aggregate is overlaid with small boxes of edge length l and the number of boxes N_B needed to completely cover it is determined. In the limit of infinitely small edge length, the fractal dimension is obtained:

$$D_f^m = -\lim_{l \to 0} \frac{\log N_B}{\log l} \tag{5.5}$$

These two methods are the standard procedures in physics but, unfortunately, only work for very large aggregates. As the number of primary particles in this concern is almost all times smaller than 1000 they cannot be applied here.

The radius of gyration also shows a power-law behavior with the mass of the aggregate already at small numbers of primary particles (see eq. 2.2). As all primary particles have the same size and density, this equation can be simplified to:

$$N_{prim} = k_f \left(\frac{R_g}{R_{prim}} \right)^{D_f^m} \tag{5.6}$$

where k_f is the fractal prefactor. For large N_{prim} the so-determined fractal dimension is equal to the other methods. However, in the region of interest considerable fluctuations between different aggregates are to be expected. To obtain an impression for DLCA 100 aggregates with $N_{prim} = 150$ and for CCA 100 aggregates with $N_{prim} = 128$ have been generated and the fractal dimensions calculated from eq. 5.6.[1] Fig. 5.2 displays the distribution function of the determined dimensions for the two algorithms.

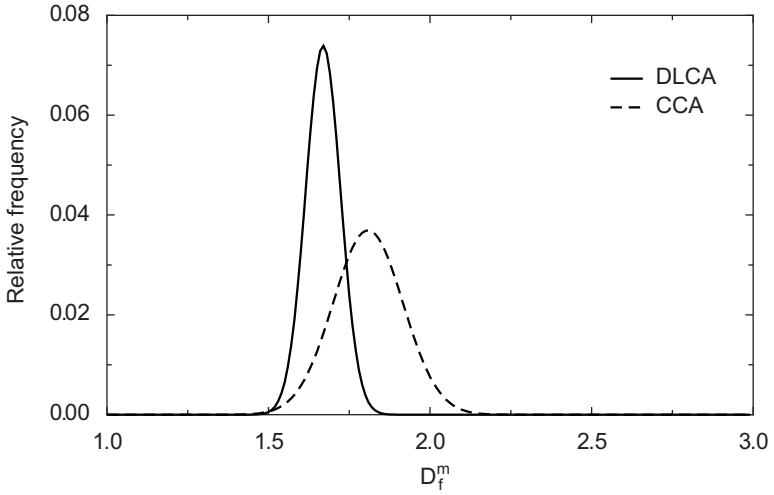

Figure 5.2: Frequency distributions of fractal dimension D_f^m for DLCA and CCA aggregates with 150 and 128 primary particles, respectively [167].

CCA shows slightly larger fractal dimensions than DLCA with a broader distribution width. The overlap between both algorithms is, however, better than with any other method tested by

[1] As this determination requires a linear fit in a double-logarithmic plot of N_{prim} vs. R_g pairs of N_{prim} and R_g need to be determined. For CCA this can be easily achieved since these aggregates grow from smaller sub-aggregates. For DLCA, one aggregate for each N_{prim} needs to be generated and the respective radius of gyration computed. The fractal dimension determined in this way is, therefore, an average over several aggregates and not a property of a single aggregate.

Bedrich [167] (Diffusion-limited aggregation, Ballistic aggregation) so CCA can be used as a complement to DLCA at primary particle numbers larger than 1000. Nevertheless, it has to be concluded that the fluctuations in D_f^m will cause problems when trying to find general relations between structural and hydrodynamic, i.e. diffusional, properties. Therefore, another algorithm has to be developed.

5.2.3 Generation of Aggregates with Fixed Structure

In fact, the concept of a generation procedure with predefined fractal dimension is straightforward. Contrary to DLCA the algorithm starts with one seed particle. Before the addition of the next primary particle, the fractal dimension of the emerging aggregate has to be calculated. Therefore, a lattice of points is placed around the existing cluster with equal distance of the lattice points and a distance of one primary particle radius from the aggregate. Now, the fractal dimension of each lattice point can be computed and the next primary particle is added at the point that accords closest with the predefined value. If multiple attachment points are possible one is chosen randomly. Fig. 5.3 shows four generated aggregates of this algorithm with varying fractal dimension D_f^m. A verification of the results can be concluded from this picture since for $D_f^m \rightarrow 1$ the aggregate resembles a chain while for $D_f^m \rightarrow 3$ a hexagonally close packed structure occurs.

The morphology of the generated aggregates generally depends on the choice of the lattice. However, Bedrich has shown that the computed hydrodynamic and structural properties are independent of the lattice (a lattice with 12 points and 120 points per primary particle was compared) so this poses no restraint on the algorithm [167]. For large N_{prim} the number of lattice points naturally rises and the algorithm becomes very slow. This disadvantage is outweighed by the fact that the fractal dimension is nearly independent of the number of primary particles with this algorithm. In Fig. 5.4 the evolution of the fractal dimension is compared to DLA aggregation (Witten and Sander [29]). DLA has been chosen as this algorithm also starts with a seed particle and the fractal growth can be followed with each added primary particle.

While DLA generally shows large variations at small N_{prim}, the fractal dimension of the model aggregate remains nearly constant even for only a few primary particles. This fast adjustment to the desired value is, however, not always obtained, especially in the extreme cases $D_f^m \rightarrow 1$

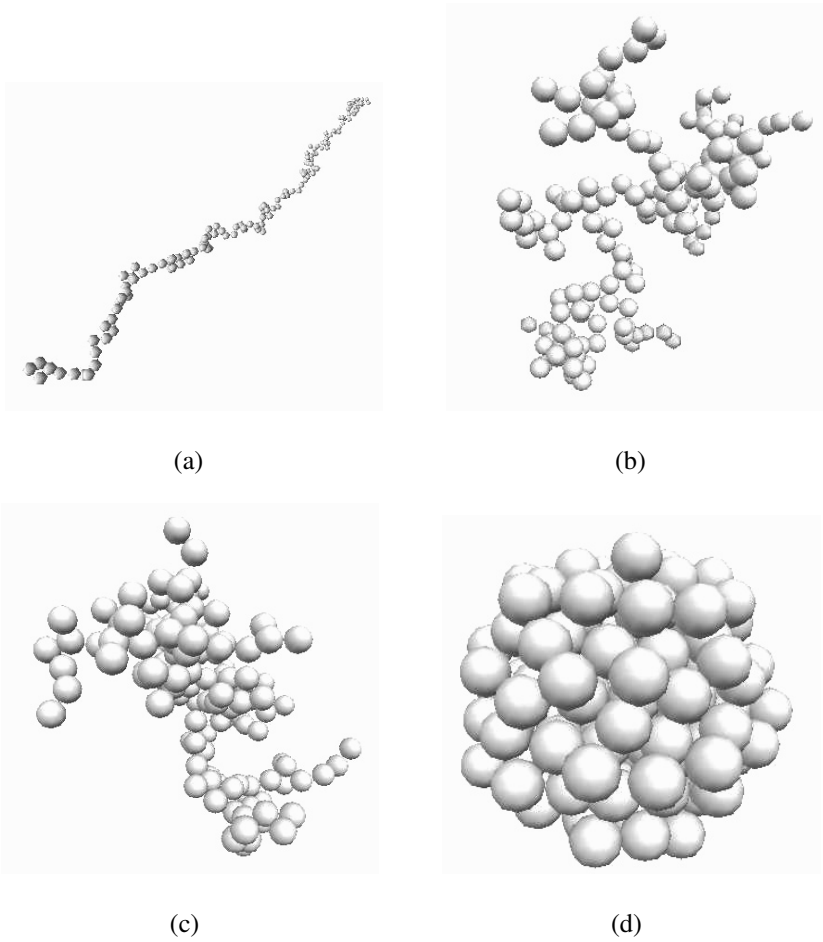

Figure 5.3: Generated aggregates ($N_{prim} = 150$) with predefined fractal dimension of a) 1.10, b) 1.70, c) 1.90 and d) 2.76 [167].

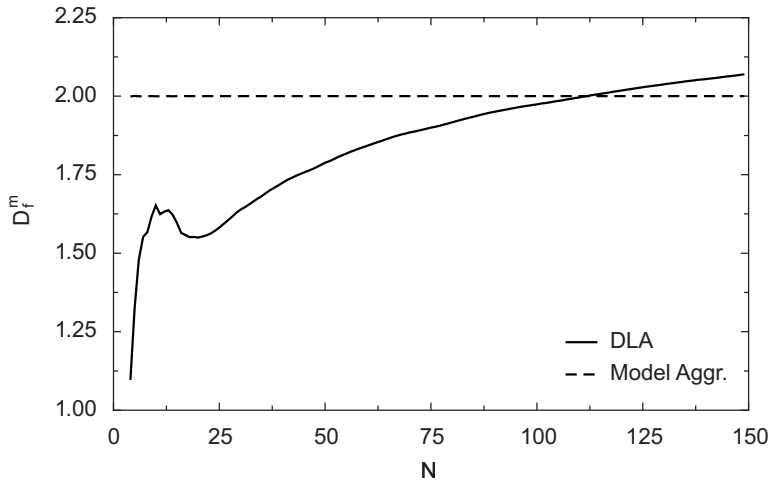

Figure 5.4: Evolution of the fractal dimension D_f^m with the number of primary particles in a DLA aggregate [29] and a model aggregate with predefined $D_f^m = 2$ [167].

and $D_f^m \to 3$. With this algorithm at hand, it should be possible to determine general relations between the structure of fractal aggregates and their hydrodynamics.

5.3 Determination of Diffusional Properties

5.3.1 The Simulation Algorithm

To determine the diffusion coefficients of fractal aggregates their Brownian motion has to be simulated. For this purpose generalized Langevin equations can be applied for the translation and rotation, respectively [168]:

$$m\,\frac{d^2\mathbf{r}}{dt^2} = -6\pi\eta R_{prim}\boldsymbol{\Psi}\,\frac{d\mathbf{r}}{dt} + \mathbf{F}_{stoch} \tag{5.7}$$

$$\boldsymbol{\Theta}\,\frac{d^2\boldsymbol{\phi}}{dt^2} = -8\pi\eta R_{prim}^3\boldsymbol{\Xi}\,\frac{d\boldsymbol{\phi}}{dt} + \mathbf{T}_{stoch} \tag{5.8}$$

where m is the mass of the fractal aggregate, $\boldsymbol{\Psi}$ is the dimensionless translation matrix which is obtained from the total drag force on the aggregate, $\boldsymbol{\Theta}$ is the inertia tensor, $\boldsymbol{\phi}$ is the three-dimensional rotation angle and $\boldsymbol{\Xi}$ is the rotation matrix, an analogue to $\boldsymbol{\Psi}$ obtained from the total torque on the aggregate. When looking at these two equations they resemble Newton's second law of motion. The Brownian behavior is introduced by the stochastic contributions of the force vector $\mathbf{F}_{stoch}$ and the torque vector $\mathbf{T}_{stoch}$.

The translation matrix in eq. 5.7 can be diagonalized by a principal axis transformation. Afterwards, the three-dimensional equation can be split into three one-dimensional equations and solved straightforwardly. This is not the case for eq. 5.8 since the principal axes of $\boldsymbol{\Theta}$ and $\boldsymbol{\Xi}$ are normally not equal and thus only one matrix can be diagonalized. However, Bedrich [167] gave an explanation to overcome this restriction. The inertia tensor is only relevant for very short time scales smaller than the typical observation time in a DLS experiment. Thus, it is possible to choose a matrix with the same principal axes as the rotation matrix and even the identity matrix for the inertia tensor. Then, the separation can also be conducted and the translational and rotational diffusion coefficient of the aggregate can be determined from the eigenvalues (which are just the diagonal elements if the matrix is diagonalized) of $\boldsymbol{\Psi}$ and $\boldsymbol{\Xi}$, respectively [167]:

$$D_t = \frac{\mathrm{k_B}T}{3\pi\eta R_{prim}}\frac{1}{3}\left(\frac{1}{\Psi_1}+\frac{1}{\Psi_2}+\frac{1}{\Psi_3}\right) \tag{5.9}$$

$$\Theta_{rot} = \frac{\mathrm{k_B}T}{8\pi\eta R_{prim}^3}\frac{1}{3}\left(\frac{1}{\Xi_1}+\frac{1}{\Xi_2}+\frac{1}{\Xi_3}\right) \tag{5.10}$$

These equations resemble the Stokes-Einstein formulation (eq. 2.30 and 2.72) so the hydrody-

namic radii can be defined accordingly:

$$R_{h,t} = 3R_{prim}\left(\frac{1}{\Psi_1}+\frac{1}{\Psi_2}+\frac{1}{\Psi_3}\right)^{-1} \tag{5.11}$$

$$R_{h,rot} = R_{prim}\sqrt[3]{3\left(\frac{1}{\Xi_1}+\frac{1}{\Xi_2}+\frac{1}{\Xi_3}\right)^{-1}} \tag{5.12}$$

As a consequence, to determine the hydrodynamic radii of a simulated aggregate, the translation and rotation matrix have to be computed. This can be done by calculating the total drag force and the total torque acting on an aggregate for three independent directions of flow, e.g. in cartesian coordinates the X-, Y- and Z-direction.

For this computation a solution of the governing equations of the flow field around an aggregate is required. For Newtonian media this can be described by the Navier-Stokes equation [169]. In the case of the diffusion of submicron particles in liquid media several simplifications can be made, e.g. creeping ($Re \ll 1$) and incompressible flow. The partial differential equation obtained is typically called the Stokes equation:

$$\eta_f \cdot \operatorname{div}\operatorname{grad}\mathbf{v} = \operatorname{grad} p \tag{5.13}$$

Additionally, the mass conservation law must be fulfilled:

$$\operatorname{div}\mathbf{v} = 0 \tag{5.14}$$

To solve this system of partial differential equations boundary conditions have to be established:

1. The fluid velocity in a large distance from the aggregate shall be the mean fluid velocity.

$$\mathbf{v}_\infty = \bar{\mathbf{v}} \tag{5.15}$$

   In the specific case of diffusion $\mathbf{v}_\infty = 0$.

2. Another boundary condition is the specification of the fluid velocity at the surface of a primary particle in the aggregate. Typically, sticky-boundaries are applied, i.e. $\mathbf{v}(R_{prim}) = 0$. However, the solution of the equations is easier if at first a fluid slip is allowed [167]. Then, the second boundary condition can be formulated as:

$$\mathbf{v}_{slip} = \frac{\delta}{\eta_f}\mathbf{\Pi}_{rt} \tag{5.16}$$

   where $\mathbf{\Pi}_{rt}$ is the tangential component of the pressure tensor in spherical coordinates (the tangential shear stress). The sliplength δ designates the penetration depth of the linear

velocity profile into the primary particle. After the solution of the velocity field, the limit of $\delta \rightarrow 0$ can be carried out.

It is obvious that the implementation of sintered primary particles circumvents the analytical solution of the problem since the second boundary condition ($\mathbf{v}(R_{prim}) = 0$) cannot be applied. Here, a discretization of the surface, e.g. via DEM or CFD would have to be used which is also a computationally expensive solution especially for 3D-aggregates. Another approach which might be implemented in the future is the use of rotating epicycloids to simulate sintered particles in an aggregate.

Having formulated the boundary conditions, the system of partial differential equations can be solved. The principle applied here is a multipole expansion of the flow field as implemented by Lamb [169]. As proposed by Filippov [158] this one-sphere solution can be expanded to aggregates of N spheres by the use of addition theorems to transfer the origin of the applied solid spherical harmonics from the i-th particle to the j-th particle. These addition theorems are also used to compute the scattering behavior of agglomerates [164]. The derivation of the solution is quite elaborate and has been conducted by Bedrich [167]. The solution without derivation is given in Annex B. The functionality of the developed algorithm was tested using aggregates resembling linear chains and hexagonally close-packed spheres. A good agreement with theoretically expected values has been found so the program may be applied for the fractal aggregates that are of interest here.

5.3.2 Results

The first objective of the simulations was to find a relation between the structural properties (D_f^m, R_g) and the hydrodynamic properties, namely the hydrodynamic radius R_h for DLCA and CCA aggregates since these generation procedures are typical for pyrogenic silica. However, not one simulated aggregate gives the same values as another even when the number of primary particles is kept constant. Thus, the results have to be averaged over many single aggregates to obtain reliable data for low numbers of primary particles. For DLCA 19×100 aggregates were generated with logarithmically spaced numbers of primary particles. For CCA the same was done for 100 aggregates, the numbers of primary particles have to be spaced here as powers of 2 due to the generation procedure. Tables 5.1 and 5.2 show the computed hydrodynamic radii of translation and rotation in comparison to the obtained radius of gyration.

Table 5.1: Relation between the hydrodynamic radii and the radius of gyration for DLCA aggregates. Values have been averaged over 100 aggregates per primary particle number. Standard deviation is given in the table [167].

N_{prim}	$R_{h,t}/R_{prim}$ [-]	$R_{h,rot}/R_{prim}$ [-]	R_g/R_{prim} [-]
2	1.39	1.40	1.0
3	1.70 ± 0.03	1.72 ± 0.02	1.43 ± 0.14
4	1.95 ± 0.04	2.00 ± 0.04	1.76 ± 0.17
5	2.18 ± 0.07	2.24 ± 0.06	2.04 ± 0.26
6	2.38 ± 0.08	2.45 ± 0.08	2.27 ± 0.29
8	2.76 ± 0.09	2.87 ± 0.11	2.73 ± 0.33
10	3.09 ± 0.12	3.22 ± 0.13	3.11 ± 0.39
12	3.37 ± 0.13	3.53 ± 0.17	3.41 ± 0.38
15	3.77 ± 0.17	3.94 ± 0.18	3.91 ± 0.56
19	4.30 ± 0.18	4.52 ± 0.22	4.59 ± 0.59
24	4.80 ± 0.22	5.05 ± 0.27	5.08 ± 0.64
31	5.52 ± 0.24	5.85 ± 0.31	5.92 ± 0.72
38	6.10 ± 0.28	6.45 ± 0.35	6.56 ± 0.86
48	6.87 ± 0.34	7.28 ± 0.41	7.42 ± 1.04
60	7.79 ± 0.38	8.28 ± 0.47	8.52 ± 1.15
76	8.79 ± 0.43	9.35 ± 0.54	9.71 ± 1.28
95	9.81 ± 0.44	10.5 ± 0.53	10.7 ± 1.35
120	11.2 ± 0.50	11.9 ± 0.60	12.4 ± 1.61
150	12.5 ± 0.57	13.3 ± 0.75	13.7 ± 1.60

Table 5.2: Relation between the hydrodynamic radii and the radius of gyration for CCA aggregates. Values have been averaged over 100 aggregates per primary particle number. Standard deviation is given in the table [167].

N_{prim}	$R_{h,t}/R_{prim}$ [-]	$R_{h,rot}/R_{prim}$ [-]	R_g/R_{prim} [-]
2	1.39	1.40	1.0
4	1.91 ± 0.10	1.96 ± 0.11	1.64 ± 0.25
8	2.66 ± 0.14	2.76 ± 0.16	2.52 ± 0.37
16	3.64 ± 0.21	3.80 ± 0.23	3.49 ± 0.52
32	5.07 ± 0.27	5.31 ± 0.30	5.04 ± 0.69
64	7.11 ± 0.35	7.49 ± 0.44	7.15 ± 0.84
128	9.90 ± 0.51	10.4 ± 0.61	10.0 ± 1.24

If now the radii are plotted against the number of primary particles (see Fig. 5.5) it can be concluded that similarly to the fractal dimension for the radius of gyration (c.f. eq. 2.2) there can as well power laws be defined for the hydrodynamic radius of translation and rotation, respectively:

$$N_{prim} = k_f^{h,t} \left(\frac{R_{h,t}}{R_{prim}} \right)^{D_f^{h,t}} = k_f^{h,rot} \left(\frac{R_{h,rot}}{R_{prim}} \right)^{D_f^{h,rot}} \tag{5.17}$$

The exponents $D_f^{h,t}$ and $D_f^{h,rot}$ will be called hydrodynamic dimensions. For the simulations con-

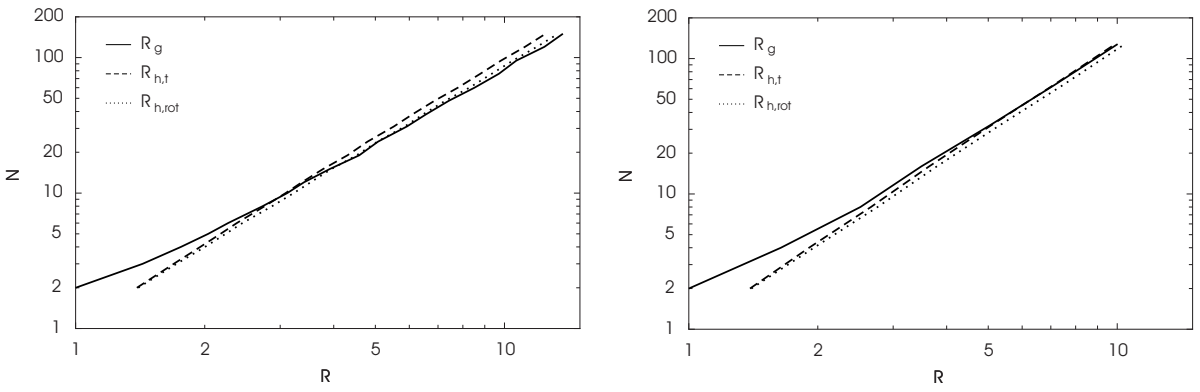

(a) DLCA aggregates (b) CCA aggregates

Figure 5.5: Power law behavior of the hydrodynamic radii for (a) DLCA and (b) CCA aggregates compared to the radius of gyration [167].

ducted here, the following numbers have been recieved for DLCA (from a linear fit in Fig. 5.5):

$$N_{prim} = 1.57 \left(\frac{R_g}{R_{prim}}\right)^{1.71} = 1.09 \left(\frac{R_{h,t}}{R_{prim}}\right)^{1.96} = 1.07 \left(\frac{R_{h,rot}}{R_{prim}}\right)^{1.91} \tag{5.18}$$

and for CCA:

$$N_{prim} = 1.73 \left(\frac{R_g}{R_{prim}}\right)^{1.83} = 1.01 \left(\frac{R_{h,t}}{R_{prim}}\right)^{2.12} = 0.99 \left(\frac{R_{h,rot}}{R_{prim}}\right)^{2.07} \tag{5.19}$$

From Fig. 5.5 and the equations above it can be concluded that the two hydrodynamic radii are nearly the same over the entire range considered here. The radius of gyration instead deviates for very small aggregates but is comparable to the hydrodynamic radius for $N \simeq [10, 100]$. For larger aggregates the deviation will again grow due to the difference in the exponents of the power law, the fractal and hydrodynamic dimension.

It is a very interesting fact that the hydrodynamic dimensions show a distinct off-set to the fractal dimension. If this is a generous finding it could explain the differences measured in the fractal exponents for pyrogenic silica with static scattering techniques (~ 1.8 [58, 59]) which measure the structural properties and rheometric experiments (~ 2.0 [54]) that measure hydrodynamic properties. To verify the generality of this relation, model aggregates (c.f. Chap. 5.2.3) with $D_f^m = [1, 3]$ and $\Delta D_f^m = 0.025$ were generated and their hydrodynamic properties computed. Fig. 5.6 shows the relation of the hydrodynamic dimensions and the fractal dimension.

Indeed, the hydrodynamic dimensions are always larger than the fractal dimension (in fact the curves touch each other at $D_f^m = 3$ which is the expected behavior for spheres) and except for low fractal dimensions (i.e. chain-like aggregates) the dimension of translation is very close to

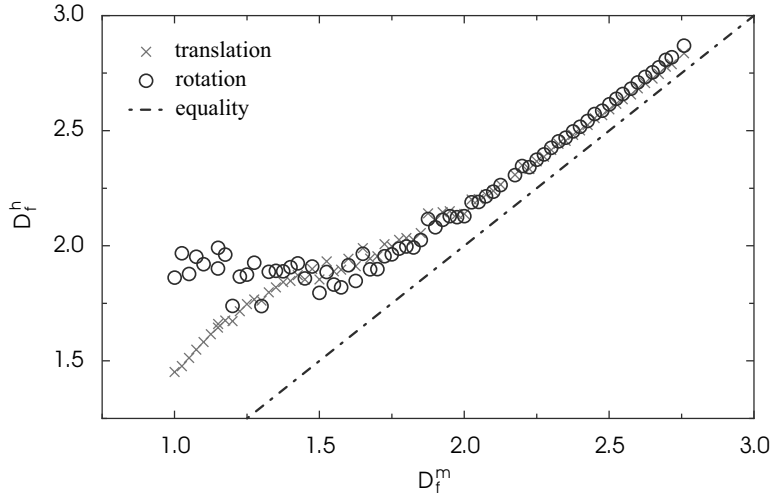

Figure 5.6: Hydrodynamic and fractal dimensions of model aggregates with $N_{prim} = 150$. The scatter in the region $D_f^m < 1.75$ results from slight deviations from the power law behavior for the rotational diffusion [167].

the dimension of rotation. Bedrich [167] additionally examined whether the obtained relation between the hydrodynamic and geometric properties of the aggregates can be considered a general rule for fractal aggregates by comparing Fig. 5.6 with DLA, DLCA, CCA and ballistic aggregates. A very close agreement was found. A similar behavior can also be found for the hydrodynamic prefactors.

Thus, it is possible to find a general function that relates the hydrodynamic properties D_f^h and k_f^h to the geometric property D_f^m. The fit function in general form is:

$$f(D_f^m) = C_0 + C_1 D_f^m + C_2 D_f^m \exp(-C_3 D_f^m) \tag{5.20}$$

and in the specific forms determined from nonlinear least squares:

$$D_f^{h,t} = -4.01 + 2.10 D_f^m + 11.51 D_f^m \exp(-1.22 D_f^m) \tag{5.21}$$

$$k_f^{h,t} = 5.60 - 1.41 D_f^m - 8.56 D_f^m \exp(-1.15 D_f^m) \tag{5.22}$$

$$D_f^{h,rot} = -0.37 + 1.16 D_f^m + 14.04 D_f^m \exp(-2.50 D_f^m) \tag{5.23}$$

$$k_f^{h,rot} = -0.56 - 0.14 D_f^m + 3.15 D_f^m \exp(-0.61 D_f^m) \tag{5.24}$$

The relative error of the above equations is smaller than 2 % for the model aggregates and always smaller than 10 % for DLCA and CCA aggregates. Thus, it is now possible to compute the hydrodynamic properties of a given aggregate, once the fractal dimension D_f^m, the size of the primary particles R_{prim} and the number of primary particles per aggregate N_{prim} is known.

Additionally, with these simulations an explanation of the difference in fractal dimensions measured with static scattering techniques and hydrodynamic (rheometric) techniques could be found and proven. This will open up more characterization possibilities for fractal aggregates and increase their intercomparability.

5.4 Relation to Dynamic Light Scattering

The main concern for the analysis of dynamic light scattering is the relation of the measured hydrodynamic radii to the structural radius of gyration and the influence of rotational diffusion on the obtained results. From the simulations in the previous chapter both relations can be deduced in dependence of the fractal dimension D_f^m (see Fig. 5.7 and Fig. 5.8).

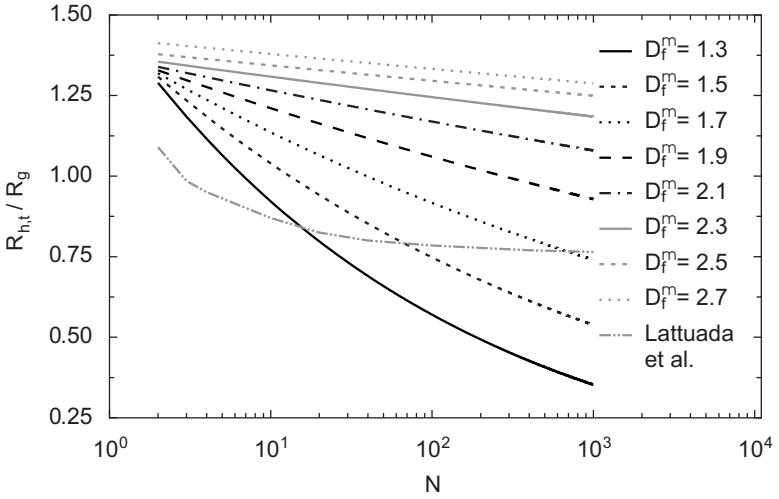

Figure 5.7: Relation between the hydrodynamic radius of translation and the radius of gyration in dependence of the number of primary particles and the fractal dimension [167]. The results of Lattuada et al. [153] have additionally been given for comparison.

As the most relevant generation process for pyrogenic silica is diffusion-limited cluster aggregation, the region of interest is $D_f^m = [1.5; 1.85]$. The number of primary particles per aggregate has been estimated from TEM images of pyrogenic silica. It is usually in a range of $[10; 1000]$. Therefore, simulations have not been conducted for larger aggregates.

Contrary to the results of Lattuada et al. [153] who used Kirkwood-Riseman theory for their calculations, no plateau value is obtained but a continuous decrease of the relation between

translational diffusion and the radius of gyration. This is due to the simulation result that the hydrodynamic dimension is always larger than the fractal dimension. This effect is largest for low fractal dimensions. In the region of interest it can be concluded that the hydrodynamic radius of translation is somewhat smaller than the radius of gyration with values between $(0.7\ldots1)\cdot R_g$. Thus, the radius of gyration can be determined from DLS measurements if the measurement result contains only translational contributions.

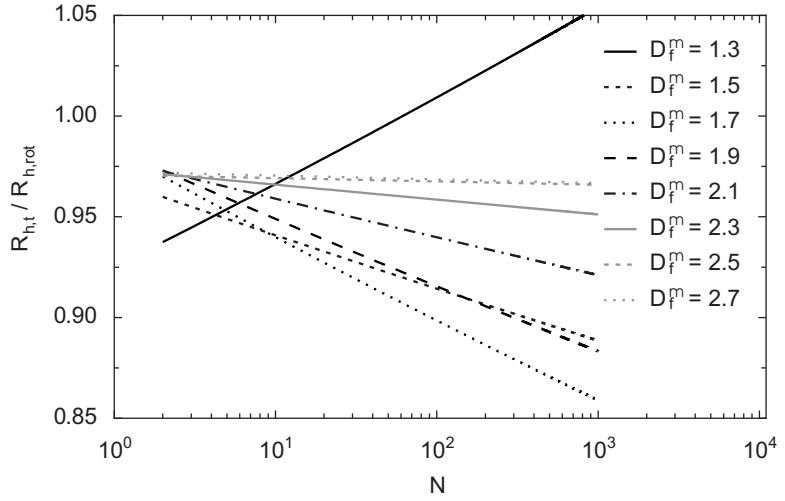

Figure 5.8: Relation between the hydrodynamic radius of translation and the hydrodynamic radius of rotation in dependence of the number of primary particles and the fractal dimension [167].

To evaluate the influence of rotational diffusion on DLS results it is necessary to resort to the simulations of Lindsay et al. [161] and Lattuada et al. [155]. Lindsay et al. obtained an overestimation of the measured mean diffusion coefficient up to 70 % if $sR_g > 1$ provided that $R_{h,t} = R_{h,rot}$. Based on their result that $R_{h,t} = 0.8\,R_{h,rot}$ for DLCA aggregates (again using Kirkwood-Riseman theory) Lattuada et al. concluded that this overestimate rises only up to 45 %. In view of Fig. 5.8 it can be seen that the hydrodynamic radius of translation is smaller than the radius of rotation but varies just between $(0.88\ldots0.95)\cdot R_{h,rot}$. Thus, without conducting the same simulations as Lindsay et al. and Lattuada et al. it can be deduced that the influence of rotational diffusion leads to an overestimation of the measured diffusion coefficients by $\sim 55-65\,\%$.

This still is a remarkable effect. For the determination of the *true* hydrodynamic diameter of translation s-dependent measurements have to be conducted and the results extrapolated to $s = 0$. Since the effect of polydispersity is superimposed, it is questionable whether these theoretically expected values can be found in static and dynamic scattering experiments.

6 Experimental Verification of Simulation Results

6.1 Preliminary Considerations

As derived in the last chapter there is one main objective to pay attention to in experiments with pyrogenic silica, the relation between the structural and the hydrodynamic properties. To account for the effect of different primary particle sizes and polydispersity different grades of pyrogenic silica with specific surface areas (BET) ranging from $S_m = 50$ - 400 m^2/g were used.

The characterization of the samples then involves two different experimental tasks. Firstly, the structure was characterized using static scattering techniques. The s-range of interest required that both SAXS and SLS measurements had to be conducted.

To accomplish a comparison of the obtained structural properties with hydrodynamic (i.e. DLS) measurements the influence of rotational diffusion has to be accounted for. Therefore, DLS measurements on the goniometer system were conducted (angular range 30°- 150°). The HPPS system was used additionally with a scattering angle of 173°. Finally, the results can be compared and related to the simulations of the previous chapter.

6.2 Structural Properties

6.2.1 SAXS

Measurements were conducted in 0.1 wt.-% suspensions stabilized at pH 9 with KOH and an ionic background of 0.001 M KNO_3. The SAXS experiments took place at the University of

Karlsruhe. However, the samples were prepared at the TU Dresden with their state of dispersion characterized via laser diffraction. All measurements were finished during one week after preparation. Reference analyses at the TU Dresden confirmed that the samples remained stable during this period. Fig. 6.1 shows the measured scattered intensity in dependence of the scattering vector s.

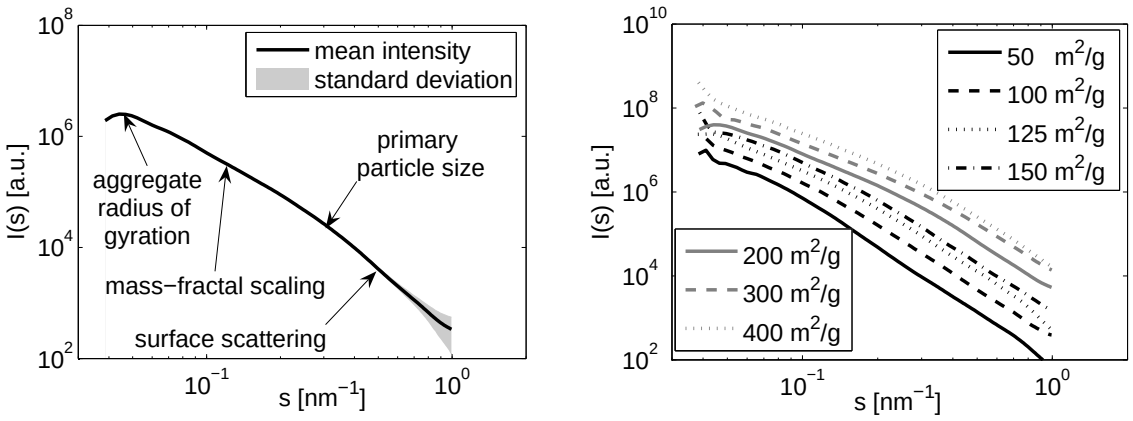

(a) HDK® N20, $S_m(\mathrm{BET}) = 200\,\mathrm{m}^2/\mathrm{g}$

(b) Different HDK® grades, curves have been shifted on the y-axis for a better visual discrimination

Figure 6.1: Measured X-ray scattering intensity profiles for 0.1 wt.-% samples of HDK® in 0.001 M KNO_3 solution at pH 9: (a) Mean intensity and data scatter for HDK® N20, (b) Comparison of different HDK® grades.

In Fig. 6.1(a) a single scattering profile has been given and the relevant regions designated. Obviously, the determination of the surface fractal dimension and the primary particle size is hampered by the larger uncertainty of the data in this region. Additionally, it is not easy to conclude a mass-fractal dimension D_f^m for low specific surface area grades since the polydispersity of the samples affects the linearity of the fractal scaling (see Fig. 6.1(b)). This difficulty also holds for the aggregate radius of gyration as the Guinier regime cannot be easily distinguished.

The unified equation of Beaucage [50, 51] (c.f. eq. 2.11) was used to fit the data and to obtain the fractal parameters. Additionally, the specific surface area has been computed (for details see e.g. [170]) to enable a comparison with the gas adsorption values (BET). The results are given in Tab. 6.1. These data do not correspond to the expectations at first sight. The most controversial feature is the large difference between the fractal dimension determined here and the fractal dimension which is expected from the generation mechanism and measurements of other authors for pyrogenic silica [58, 59]. This deviation is not only due to the deformation of

the profile caused by polydispersity. There must be other reasons for this behavior.

Table 6.1: Structural properties of pyrogenic silica samples determined from SAXS.

S_m (BET) $\left[\mathrm{m}^2/\mathrm{g}\right]$	S_m (SAXS) $\left[\mathrm{m}^2/\mathrm{g}\right]$	R_g [nm]	D_f^m [-]
50	95.1	37.25	-
100	145.4	>80	2.46
125	158.1	48.92	2.51
150	177.4	30.85	-
200	271.4	31.06	2.48
300	361.7	29.29	2.36
400	297.9	67.25	2.33

A second observation, which can be made, is that the radius of gyration measured with SAXS does not correspond to the aggregate size that can be estimated from TEM (c.f. Chap. 1.2). On the other hand, the data can be compared to the SANS results of Bugnicourt et al. [21] who used the same silica grades as in this work. They also obtained fractal dimensions in the range of $2.23 - 2.61$ and radii of gyration between $25 - 32$ nm. However, for one sample they also obtained another radius at low s ($\sim$ 210 nm for a HDK® N20) that was interpreted as an interparticle distance. This order of magnitude is, however, expected for the aggregate radius of gyration from TEM images. Regarding this expectation it has to be noticed that the available s-range in the SAXS experiments is not sufficient and even for SANS this is the edge of the measurable range. Thus, it can be assumed that the observable structure of the pyrogenic silica samples with SAXS is not representative for the whole aggregates since only an incomplete scattering profile is recorded in the experiments (c.f. Fig. 2.2).

This hypothesis is additionally supported by the comparison of the specific surface areas. If large primary particles and aggregates were excluded in the static scattering experiments, the value should actually be higher as with gas adsorption measurements. That this is truly the case can be easily concluded from Tab. 6.1. HDK® T40 has to be excluded here, since the primary particles are intrinsically porous for this grade, so the specific surface area value is underestimated.

To further substantiate the above hypothesis, a comparison with SLS and DLS has to be drawn, since smaller s values are probed with these techniques. Finally, the question which radius of gyration is determined from SAXS and SANS, respectively, may be answered.

6.2.2 Static Light Scattering

Static light scattering results are often hampered by multiple scattering contribution. Thus, only highly diluted samples may be examined. This increases the purity requirements for the sample since already some dust contributions may affect the measurement results.

On the other hand, a higher sample concentration is advantageous for the dispersion of the pyrogenic silica powder. Thus, 5 wt.-% suspensions have been prepared. Afterwards, a single droplet of these suspensions was added to 100 ml of deionized water. To further remove dust contributions the suspensions were filtered through a 20 µm paper filter under clean room conditions. Silica drying agglomerates were removed from the flask and the filter housing with 1 M NaOH in advance. Finally, the flask was sealed and the sample characterized.

The measurement signal again is the scattering intensity in dependence of the scattering vector s. Fig. 6.2 shows the results as a double-logarithmic plot to visualize the fractal features.

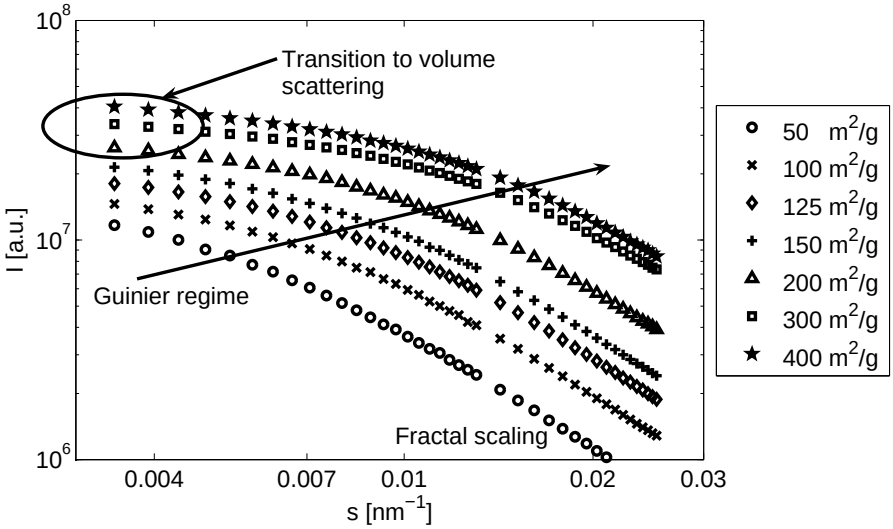

Figure 6.2: Measured scattered light intensity (SLS) over scattering vector s. Curves have been shifted on the y-axis for visual discrimination. Relevant regions are marked in the diagram.

There are three regimes that can be distinguished among the grades. For high surface area grades at low s a transition to volume scattering is observed, i.e. the intensity approaches a constant value. A Guinier regime related to a radius of gyration is visible for all pyrogenic silica grades. However, this exponential decrease is shifted to lower s-values with decreasing specific surface area of the grades, thus indicating a larger size. The radius of gyration has been computed from the profiles by fitting a Guinier plot (which is the standard procedure for SLS,

see Fig. 6.3) of the data with:

$$\ln\left(\frac{1}{I}\right) = (sR_g)^2 + C_1 s^4 + C_2 s^6 \tag{6.1}$$

The constants C_1 and C_2 do not have a physical meaning here, but are used to deal with the curvilinear shape of the intensity profiles.

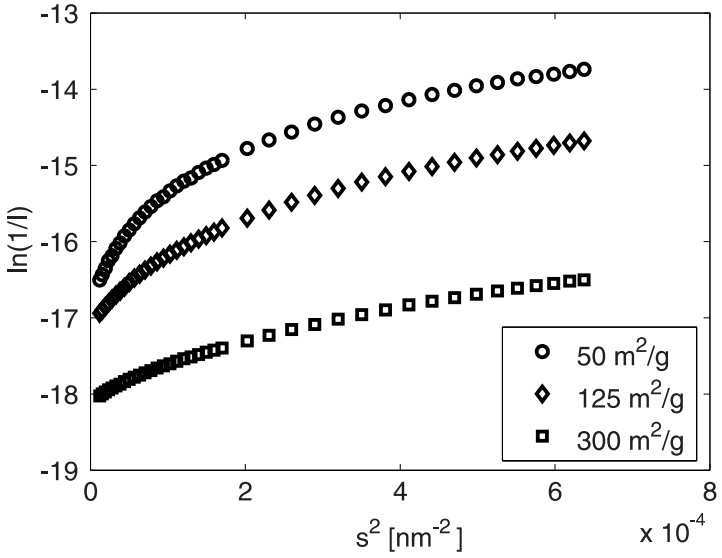

Figure 6.3: Guinier plot of the measured scattered light intensity with SLS for different grades of pyrogenic silica.

Furthermore, in Fig. 6.2 at large s a power-law behavior can be observed corresponding to a fractal scaling of the measured size. A fractal dimension has been determined from the slopes in the log-log plot. The radii of gyration and the fractal dimensions are given in Tab. 6.2.

Table 6.2: Structural properties of pyrogenic silica samples determined from SLS.

S_m (BET) $\left[\mathrm{m}^2/\mathrm{g}\right]$	R_g [nm]	D_f^m [-]
50	202	1.77
100	187	1.78
125	167	1.76
150	163	1.77
200	140	1.72
300	116	1.54
400	117	1.58

Though this procedure gives reliable results for low surface area grades (up to 150 m^2/g) since more than 15 data points can be fitted, uncertainties occur for the high surface area grades. Here, only 4 or 5 points can be incorporated in the analysis but as can be seen for HDK® T30 and T40 they are still affected by the Guinier regimes.

Interestingly, both values (R_g, D_f^m) differ remarkably from the SAXS and SANS results [21]. The radii of gyration are much larger which is obviously due to the accessible *s*-range of the methods. Contrary, the fractal dimensions are smaller than those obtained by X-ray or neutron scattering. Additionally, there is a clear decrease of the radius of gyration with increasing surface area of the grades which was not obtained for SAXS and SANS. As with SLS for some grades the volume scattering plateau is reached, it is likely that the radii of gyration determined here are the *true* aggregate radii. Also, the fractal dimension rather corresponds to the theoretically expected DLCA generation than D_f^m obtained from SAXS. However, the SAXS and SANS results cannot just be dismissed. Clarification can only be anticipated from the DLS results since the hydrodynamic diameter should scale with the radius of gyration of the aggregates.

6.3 Hydrodynamic Properties

The sample preparation for the DLS goniometer was the same as for the SLS measurements. For the HPPS a slightly larger solids concentration was used (~ 0.01 v.-%). Then, due to the larger contribution of scattering aggregates, no dust filtration was necessary. Fig. 6.4 shows the primary measurement result, the autocorrelation functions, for a HDK® V15. It is readily available from the figure that a reduction of the scattering angle leads to a shift of the measured ACF to larger lag times. Thus, the adjustment of the measurement duration (see Chap. 4.5) is verified.

For each scattering angle 9 single runs have been conducted. Afterwards, a unique ACF was obtained by a randomization procedure carried out with a MATLAB® script where for each lag time an autocorrelation value was chosen randomly from the single measurements. Therefore, all single runs had to be normalized by the maximum value of the according correlation function to neglect deviations in the coherence parameter *b*. This method stabilizes the subsequent data analysis since covariant measurement errors are minimized.

As a first analysis step a mean diffusion coefficient for each scattering angle has been determined by a cumulants analysis of the randomized ACF's. For this purpose a MATLAB® script was used. In the program the cumulants expansion is cut after the quadratic term as supposed in Chap. 2.3.2.1. Additional to the standard algorithm the baseline for the normalization of $G_2(\tau)$

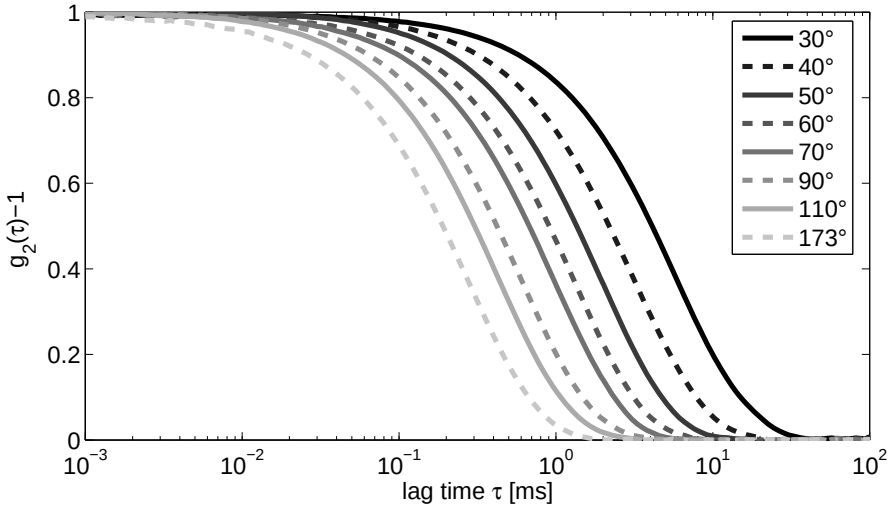

Figure 6.4: Autocorrelation functions for a diluted HDK® V15 suspension at different scattering angles. The scattering angles 35°, 45°, 55°, 65°, 75°, 80°, 85°, 95°, 100° and 105° have been omitted here but fit in the shown trend.

is corrected accounting for dust contributions in the samples that have a large decay time. Therefore, the gradient of the correlation function is computed and high frequency noise is removed using a low-pass filter in the power spectrum obtained from a Fast-Fourier transformation. Afterwards, the baseline may be found in the ACF when the smoothed gradient is firstly reduced to zero after its maximum value. The ACF is then again normalized to a maximum of 1 after the baseline is subtracted. Now, data truncation can be performed at a correlation value of 0.1 since all correlation functions have the same appearance and thus the comparability of the results is guaranteed. The further processing of the cumulants analysis resembles the description in Chap. 2.3.2.1.

The obtained mean diffusion coefficients are shown in Fig. 6.5(a) for the HDK® grades D05 up to V15 and in Fig. 6.5(b) for HDK® N20 – T40. The numerical values of the harmonic mean particle size and the polydispersity index are given in Annex C.

There is a strong variation of the mean diffusion coefficients when the scattering angle is changed. Thus, the influence of rotational diffusion has to be considered here. In view of the evolution of the scattering vector dependence two interesting features can be observed. First, at any scattering vector the different product grades can be distinguished by their diffusion coefficient. This is an important prerequisite for quality assurance purposes since there only one scattering angle is mostly used due to time requirements.

Secondly, for the high surface area grades HDK® T30 and T40 the mean diffusion coefficient

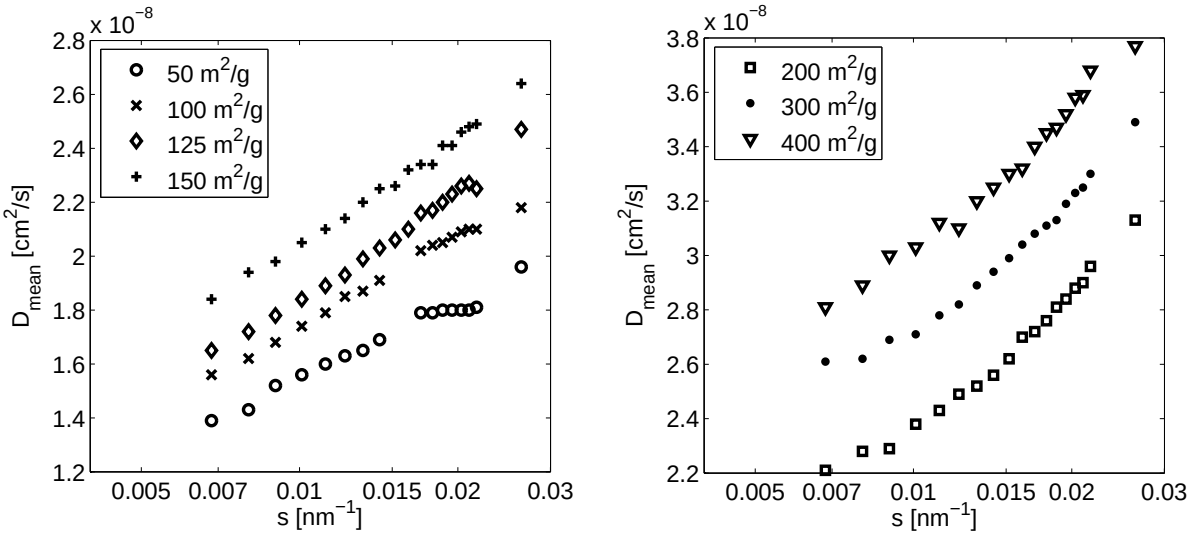

(a) Low specific surface area grades

(b) High specific surface area grades

Figure 6.5: Mean diffusion coefficients of the pyrogenic silica samples determined from a second cumulants analysis. The influence of rotational diffusion can be recognized from the scattering vector dependence. Note the different scales of the y-axes in the subfigures.

seems to approach a plateau at low scattering vector while for low surface area grades the plateau is not obtained. Additionally, the curves resemble the theoretically obtained trend of Lindsay et al. [161] (for DLCA aggregates, c.f. Fig. 2.13(b)). Therefore, the following empirical equation that approximates the step behavior with two plateaus in Fig. 2.13(b) was used to fit the measured data:

$$\frac{\bar{D}}{10^{-8}\,\frac{\mathrm{cm}^2}{\mathrm{s}}} = C_1 + \frac{C_2}{1+\left(\frac{\log_{10}(s\cdot\mu\mathrm{m})}{C_3}\right)^{C_4}} \tag{6.2}$$

An extrapolation to $s = 0$ gave the hydrodynamic diameter of translation. Fig. 6.6 shows the fits to three HDK® grades exemplarily. The y-axis has been changed to the harmonic mean size to enable the reader to obtain the hydrodynamic diameter visually.

The obtained hydrodynamic radii and diameter are finally summarized in Tab. 6.3. Additionally, the ratio between the upper and lower plateau is given. The hydrodynamic radii are always smaller but comparable to the radii of gyration determined from static light scattering. This result substantiates the above made hypothesis that the size measured with SLS corresponds to the *true* aggregate radius. A final conclusion will be drawn in the next chapter. It has to be noted that only for HDK® D05 and C10P the plateau can be extrapolated with small uncertainty. The upper plateau $D(s \to \infty)$ in Fig. 6.5 cannot be determined exactly for larger specific surface area

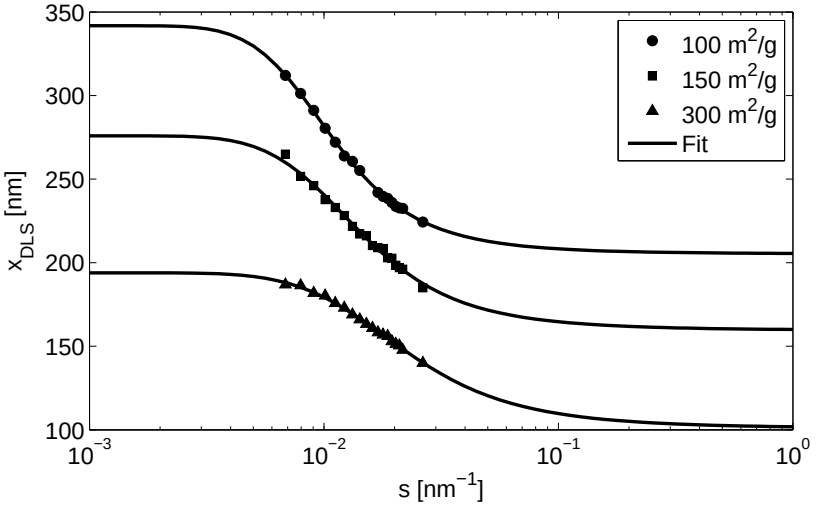

Figure 6.6: Fit of the effective hydrodynamic diameter of pyrogenic silica obtained from a second cumulants analysis of the DLS goniometer data with eq. 6.2 to obtain the hydrodynamic diameter of translation.

Table 6.3: Hydrodynamic radius and diameter of pyrogenic silica grades determined from multi-angle DLS. The ratio $D(s \to \infty)/D(s \to 0)$ determined from eq. 6.2 accounting for the influence of rotational diffusion is additionally given.

S_m (BET) $\left[\mathrm{m}^2/\mathrm{g}\right]$	$x_{h,t}$ [nm]	$R_{h,t}$ [nm]	D_∞/D_0 [-]
50	398.8	199.4	1.55
100	341.7	170.9	1.66
125	314.5	157.2	1.95
150	280.2	140.1	1.83
200	229.6	114.8	2.15
300	193.9	97.0	1.92
400	184.3	92.1	2.20

grades due to the limited range of scattering vectors.

In a second analysis the intensity-weighted size distributions were obtained via nonlinear regularization. Fig. 6.7 shows the results for a HDK® C10P. Again, the trend that the distributions are shifted to smaller sizes with increasing scattering angle can be observed.

Additionally, at small angles a bimodal distribution is obtained. The small peak is due to rotational diffusion and the second due to translational diffusion, i.e. a differentiation is possible. At larger angles, however, the contribution of rotation increases and the two peaks can no longer be distinguished by the inversion procedure. Thus, it seems that the whole distribution is shifted to smaller sizes. If on the other hand the distribution width is considered, it can be recognized

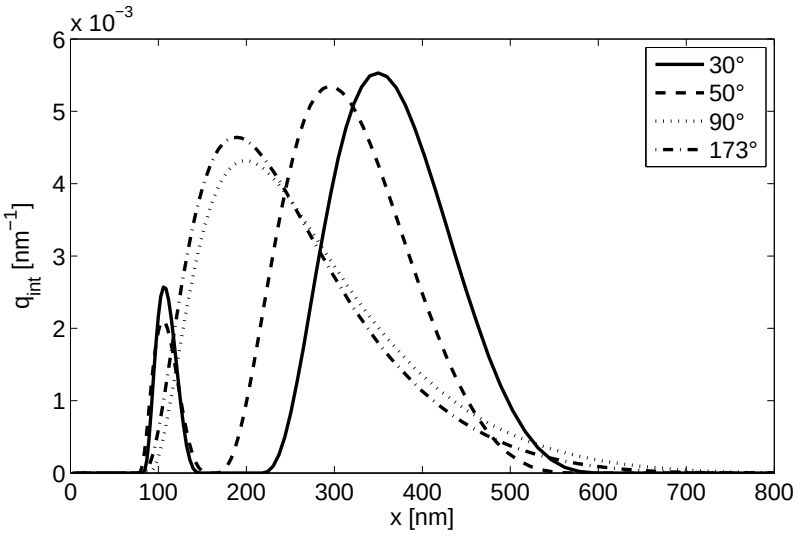

Figure 6.7: Intensity-weighted size distributions of a HDK® C10P at various scattering angles.

that the smallest and largest particle size is nearly constant for all angles. The deviations here are only due to the *smoothing* of the regularization.

Unfortunately, as rotational diffusion cannot be neglected even for the smallest angles measured it is not possible to obtain a distribution of hydrodynamic diameters of translation for pyrogenic silica with small specific surface areas. This is only accessible for a HDK® T30 or T40 at the smallest scattering angles (see Fig. 6.8).

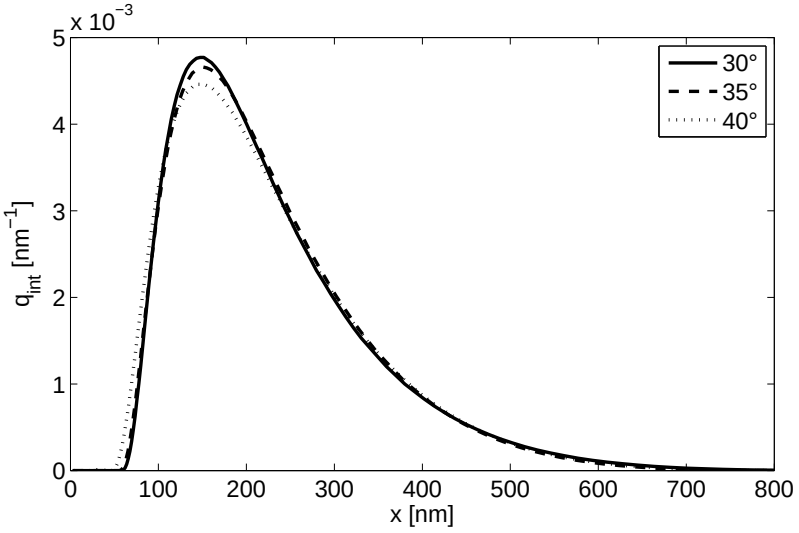

Figure 6.8: Intensity-weighted size distributions of a HDK® T30 at small scattering angles.

It is readily available from the figure that even though the primary particles have a narrow distribution of size for HDK® T30 the aggregate sizes show a broad distribution. Thus, the

question arises whether a comparison between structure and hydrodynamics can be drawn only in view of the mean diffusion coefficient and the harmonic mean diameter, respectively.

6.4 Comparison and Conclusion

The results of the structural analysis with SAXS and SLS show a distinct difference in the aggregate radius of gyration. Additionally, the values of the fractal dimension suggest different structures measured with the two methods.

The DLS data obtained at the same samples in the same medium gives hydrodynamic radii of translation (after extrapolation to $s = 0$) that are of the same order of magnitude as the SLS radii of gyration (see Tab. 6.4). The experimental ratios $R_{h,t}/R_g$ (values between 0.787 and 0.987) lie in the range of 0.7 to 1 which was predicted from simulation results in Chap. 5.4. This supports the assumption, that the best description of the generation of pyrogenic silica aggregates is a DLCA mechanism. Thus, the ratios may be employed to estimate the average number of primary particles per aggregate from Fig. 5.7. A mass-fractal dimension of 1.8 has been used as obtained from the SLS measurements. The results conform with the observations made in TEM images ($N_{prim} \approx [10; 1000]$).

Table 6.4: Ratio of the hydrodynamic radius of translation to the radius of gyration (SLS) of the pyrogenic silica samples and the estimated number of primary particles per aggregate from simulation results.

S_m (BET) $\left[\mathrm{m}^2/\mathrm{g}\right]$	$R_{h,t}/R_g$	$\bar{N}_{prim}$ estimated from Fig. 5.7 using $D_f^m = 1.8$
50	0.987	90
100	0.914	220
125	0.941	180
150	0.856	300
200	0.820	550
300	0.836	450
400	0.787	> 1000

If the ratio between the mean diffusion coefficient determined from cumulants analysis and the mean translational diffusion coefficient $D_0(s = 0)$ is plotted against the scaled structural axis

$s \cdot R_g$ (see Fig. 6.9), where R_g is the value obtained with static light scattering, an interesting observation can be made. The measured data points form a master curve for all silica grades except HDK® T40. Such a master curve has already been predicted in simulations of DLCA aggregates by Lindsay et al. [161].

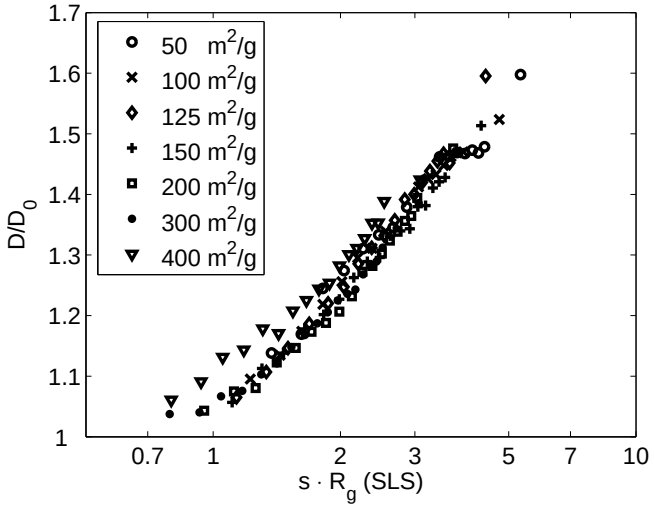

Figure 6.9: Master-curve of the influence of contributions of rotational diffusion on the mean diffusion coefficient D measured with DLS for pyrogenic silica. The values are scaled with the corresponding translational diffusion coefficient D_0 obtained at $s = 0$. The scattering vector s is scaled with the radius of gyration R_g from SLS. Plot as in the simulations of Lindsay et al. [161].

These measurement results can now be used to conclude the following:

1. Static light scattering measures the aggregate radius of gyration as well as the aggregate mass-fractal dimension D_f^m while the SAXS values remain ambiguous. A hypothesis for clarification will be given below.

2. The theoretically suggested generation procedure of diffusion-limited cluster aggregation has now been verified as a good description of pyrogenic silica powders (D_f^m determined with SLS ≈ 1.8, ratio $R_{h,t}/R_g$ between 0.7 – 1.0).

3. The fit equation (eq. 6.2) is a good approach to determine the hydrodynamic radius of translation from multi-angle DLS.

4. The intrinsic polydispersity of the pyrogenic silica grades does not hamper the comparison between static and dynamic scattering experiments. As shown in Fig. 6.9 the respective mean values give a good correlation.

5. The upper plateau of Lindsay et al. [161] in Fig. 2.13 cannot be determined exactly in the measurements here. The theoretical prediction of 1.55-1.65 (see Chap. 2.3.4) holds for HDK® D05 and C10P (see Tab. 6.3) and no data point is above the limit of 1.7. On the other hand, the limiting value of 1.45 of Lattuada et al. [155] is exceeded for nearly all grades. Thus, the simulation results are again verified.

The deviations of HDK® T40 can be explained in view of the porous structure of the primary particles which gives rise to doubts in the static as well as in the dynamic properties.

The interpretation of the SAXS and SANS results is still an open question. An explanation may be found in the generation process. Firstly, the primary particles are generated, so there is a large number concentration and, additionally, the particles are still solidifying. Thus, the aggregation is mostly driven by primary particle – primary particle collisions with a large sintering factor, small but strongly sintered aggregates are generated. Further down the flame, the temperature drops as well as the primary particle concentration. Now, cluster – cluster aggregation predominates. Besides, sintering is reduced but still existent. Now, the final aggregates evolve but only with a loose sintered contact. To conclude this hypothesis, the SAXS results represent another fractal scale in the aggregates with a specific radius of gyration and a fractal dimension that is larger than the aggregate fractal dimension, i.e. strongly sintered sub-aggregates.

This suggestion has to be substantiated so the following points are proposed for further investigations:

1. In static scattering the gap in the range of scattering vectors between SLS and SAXS has to be closed so that an unified analysis of the scattering intensity profile becomes possible. A feasible measurement technique for this purpose would be ultra-small angle X-ray scattering (USAXS). This is, however, a very laborious method that is only available at a few large laboratories with an own synchrotron source (e.g. the European Synchrotron Radiation Facility, Grenoble, France, or the German Electron Synchrotron DESY, Hamburg).

2. The DLCA generation mechanism has to be adapted to use varying sintering factors when the aggregates in the simulation box grow. Afterwards, the scattering behavior of these aggregates has to be computed using Rayleigh-Debye-Gans theory [171] where the aggregate scattering form factor can be derived from the computation of the radial density

distribution function. Then, the experimental values can be used to obtain a better theoretical understanding of the generation process of pyrogenic silica.

A broadening of the measurable range of scattering vectors would also be highly desirable for dynamic light scattering investigations. This would lead to an efficient determination of the upper ($s \rightarrow \infty$) and lower ($s \rightarrow 0$) plateau values to finally prove the simulation results and possibly improve the fit equation (eq. 6.2). However, at the moment dynamic X-ray scattering still gives a bad signal quality even with a synchrotron source. Dynamic light scattering with infrared and blue light from small angles up to the backscattering regime could possibly give the desired results.

That dynamic light scattering in the backscattering regime can be used unambiguously has been proven with the results of the HPPS system. The measured data points fit well within the trends obtained with the goniometer. Different HDK® grades can easily be distinguished. Additionally, a backscattering system has some advantages for the usage of DLS as a quality assurance tool:

1. As in this regime translational and rotational diffusion contributes to the measurement signal, changes in size of the aggregates as well as changes in the structure (e.g. resulting from different flame conditions) can be detected.
2. The measurement time needed to obtain the same photon count statistics is lowest in the backscattering regime.

In view of these features backscatter DLS is an ideal tool for quality assurance purposes.

7 DLS-Characterization of Interacting Suspensions

7.1 Introduction

The characterization of pyrogenic silica suspensions at moderate to high concentrations is highly desirable since these are industrially relevant. However, as outlined in Chap. 2.3.3 the measured distribution of diffusion coefficients is altered by hydrodynamic and interparticle interactions. Thus, it has to be examined which precautions in a measurement have to be thought of and what information can be deduced from such samples. As already the computation of the diffusion of a single aggregate as well as the calculation of the influence of interactions for hard-spheres are very elaborate, a theoretical approach is not considered here. Rather, a comprehensive experimental investigation will be conducted. Details of the experimental program will be depicted in the next section.

The following tasks will be adressed:

- How is the mean diffusion coefficient influenced by an increase in concentration for pyrogenic silica? Is it increased or decreased? What diffusion regime (self- or collective diffusion) is therefore observed?
- What is the largest tolerable concentration where interaction effects can be neglected? Can a simple method be found to recognize deviations already in the measurement data, i.e. the correlation functions?
- Is DLS in high concentrated pyrogenic silica suspensions applicable for quality assurance purposes or are there ambiguities in the data? Which parameters of the suspension should additionally be controlled?

- Can the concentration effects be approximated by the use of the models in Chap. 2.3.3.2? How should these be modified to attain validity for fractal aggregates?
- What conclusions can be drawn from the measurement results on the impact of interparticle interactions for pyrogenic silica suspensions?
- The present models only use the mean diffusion coefficient obtained from a cumulants analysis. Is additional information obtainable by an inversion of the measurement data?

7.2 Experimental Program

As a theoretical approach is not feasible, the experiments have to cope with all the above defined tasks. Therefore, a detailed description of the measurement program shall be given. First of all, it has to be ensured that the dispersed state of the examined suspensions is equal and independent of concentration. Therefore, suspensions of pyrogenic silica at two different solids concentrations (5 wt.-% and 15 wt.-%) were prepared and dispersed. The dispersed state was verified with DLS measurements at high dilution. For all HDK® grades a unique dispersion was obtained except for HDK® T40 which could not be completely dispersed at 15 wt.-% with the available dispersion techniques. Thus, care has to be taken in the interpretation of results for HDK® T40 at concentrations exceeding 5 wt.-%.

Concentration series were then conducted using a mother solution of 15 wt.-%. The required concentration was obtained by dilution. Thereby, pH 9 and the salinity of the dilution medium was kept constant to not alter the effect of interparticle interactions. As in these concentrated samples multiple scattering is present only the HPPS could be used as measurement instrument. Thus, the scattering angle was fixed at 173° and a scattering vector of 0.0264 nm^{-1}, i.e. the influence of rotational diffusion could not be considered separately. Again, for each concentration 9 single runs were measured from which a re-randomized ACF was achieved for data analysis.

In view of the impact of interparticle interactions pyrogenic silica suspensions with different ionic strengths were used in comparison to spherical colloidal sols. By varying the salinity the extension of the dielectric double layer (i.e. the range of the interparticle interactions) around the particles is varied as well as the maximum repulsion because the van-der-Waals attraction

remains essentially constant (c.f. Fig. 2.4). Here, ionic strengths of 10^{-3} M and 10^{-2} M corresponding to double layer thicknesses of 9.8 nm and 3.9 nm (eq. 2.24), respectively, were adjusted with KNO_3. This should lead to significant differences in the measurement results since the double layer thickness at low ionic strength is already of the order of the primary particle size. The higher ionic strength has been chosen so that the suspensions still remained stable even at high concentrations. It is assumed that a change in the measurement data upon dilution is mainly due to hydrodynamic interactions, i.e. these samples are taken as reference. Of course, a further reduction of the range of interparticle interactions would be desirable but this leads to a destabilization as will be shown in Chap. 8.1.

The use of colloidal silica sols enables the neglect of the influence of the fractal structure and the polydispersity of the primary particles and aggregates, respectively. Thus, interaction effects can be associated unambiguously.

7.3 Results and Discussion

7.3.1 The Principal Effect of Increasing Concentration

Fig. 7.1 shows the changes in the measured correlation functions when the concentration is increased. A HDK® V15 has been chosen exemplarily but the trend holds for all grades. The volume fractions in the figure have been computed from the mass concentrations using a solids density of 2200 m^2/g. The displayed ACF's are again composed of 9 single runs using the re-randomization procedure mentioned earlier.

It is readily available that with increasing concentration the autocorrelation functions are stretched and decay to zero only at lag times much larger than in diluted samples. Thus, the diffusion process is slowed down. If these ACF's would be used to compute a hydrodynamic diameter, a larger value would be obtained. However, this computation is not feasible since the requirements of the Stokes-Einstein relation (particles alone in a quiescent fluid) are violated. Therefore, results in this chapter will only be presented in terms of the diffusion coefficient which is the only available quantity in high-concentration DLS.

This decrease of the diffusion process in the suspension can be interpreted in two ways. First of all, self-diffusion can be considered as the relevant diffusion regime. As shown in Chap. 2.3.3.2

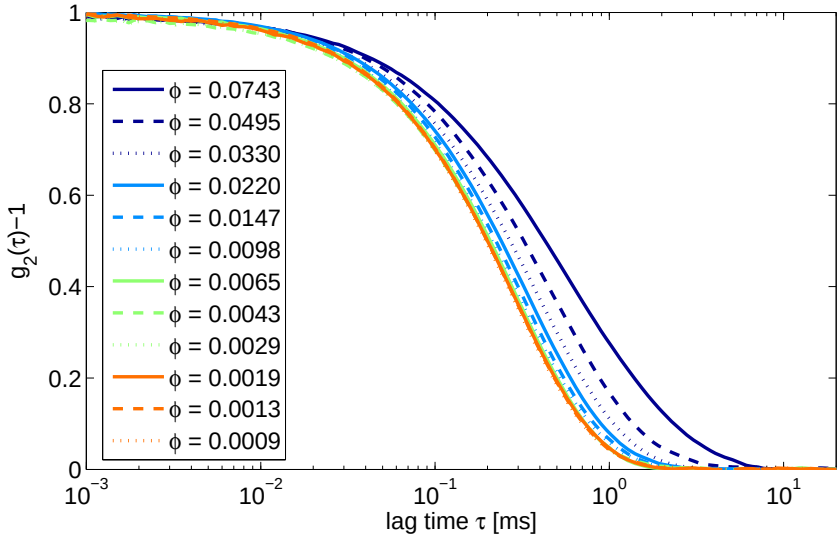

Figure 7.1: Autocorrelation functions of a concentration series for a HDK® V15 at pH 9 and 0.01 M KNO_3. The volume fraction ϕ is marked in the diagram.

this leads to a decrease. Additionally, interparticle interactions are superimposed. In a first consideration an attractive potential can be imagined as a source of the slow-down. This should be verified in further examinations.

In view of Fig. 7.1 up to a concentration of $\varphi = 0.0065$ (i.e. 1.42 wt.-%) no visible difference in the ACF is observed. If, however, the data are processed with a second cumulants analysis another result is obtained. In Fig. 7.2 the mean diffusion coefficient is plotted against the volume concentration.

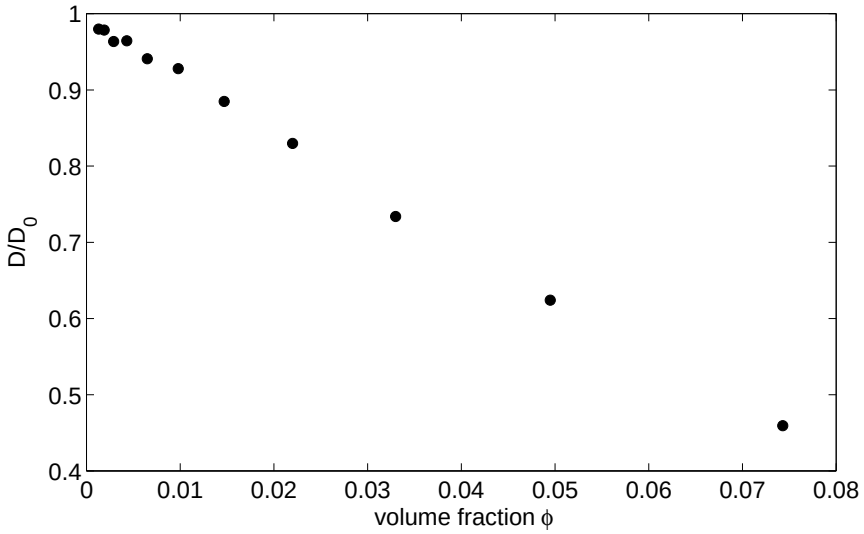

Figure 7.2: Concentration dependence of the mean diffusion coefficient of a HDK® V15 at pH 9 and 0.01 M KNO_3 determined by second cumulants analysis. Values relating to the effective particle diffusion coefficient at high dilution.

Here, a reduction of the mean diffusion coefficient by 7 % at $\varphi = 0.0065$ has to be recognized. This shows that a visual inspection of the ACF alone is not sufficient since a concentration influence cannot be easily recognized.

7.3.1.1 Principal Components Analysis

A visual inspection of the measured data is, however, desirable as it is the first detail of the data the user obtains. Any more elaborate data analysis incorporates knowledge of the system and of the algorithms behind. A cumulants analysis, for instance, can be fully distorted by choosing the wrong lag time for data cut-off (c.f. Chap. 2.3.2.1). The autocorrelation function in the present display is inappropriate since the region of interest (ROI), i.e. the decay, is only shown in a squeezed format.

Ideally, the coordinate system needs to be rotated so that the ROI can be optimally adjusted. For this purpose a principal components analysis (PCA) is used. This is a statistical method originally intended for finding patterns in multidimensional data where graphical representations are not available. It performs a linear transformation of the data in a way that the greatest variance in the data is assigned to the first factor, the first principal component. The second principal component then incorporates the second greatest variance and so forth. Basics of the method and applications may be found in the book of Jolliffe [172].

The PCA of the autocorrelation function is conducted in the following sequence:

1. The region of interest is defined. As this shall be the main decay of the ACF the correlation data bounded between $g_2(\tau) - 1 = [0.2;\ 0.8]$ is used to determine the transformation matrix.

2. In the measurement as well as in the present display the lag times are spaced logarithmically whilst the principal components are displayed linearly. Thus, the logarithm of the lag times $\log_{10}(\tau_i)$ is used.

3. Now the data are centralized according to:

$$(\mathbf{g_2} - 1)_i^c = \frac{(\mathbf{g_2} - 1)_i}{\overline{\mathbf{g_2} - 1}} \tag{7.1}$$

$$\mathbf{log\tau}_i^c = \frac{\log_{10}(\boldsymbol{\tau}_i)}{\overline{\log_{10}(\boldsymbol{\tau})}} \tag{7.2}$$

where the overline designates the mean value of the data vector. Now the boundaries determined in Step 1 are applied and the two centralized data vectors are assigned to the $(N_{data} \times 2)$-matrix $\mathbf{D}$.

4. The covariance matrix of the centralized and bounded data is computed:

$$\mathbf{M} = \frac{\mathbf{D}^T \cdot \mathbf{D}}{N_{data} - 1} \tag{7.3}$$

5. The eigenvalues of the covariance matrix give the variance of the data in the direction of the eigenvectors. If the eigenvalues are sorted in descending order ($\lambda_1 > \lambda_2$), the corresponding eigenvectors $\boldsymbol{\gamma}_1$ and $\boldsymbol{\gamma}_2$ give the basis of the rotated coordinate system so that the main variance is shown parallel to the x-axis and the second main variance is on the y-axis. Thus, the transformation matrix $\boldsymbol{\Gamma}$ contains the first two eigenvectors in the columns:

$$\boldsymbol{\Gamma} = [\,\boldsymbol{\gamma}_1 \quad \boldsymbol{\gamma}_2\,] = \begin{bmatrix} \gamma_{1,1} & \gamma_{2,1} \\ \gamma_{1,2} & \gamma_{2,2} \end{bmatrix} \tag{7.4}$$

6. Now, the original data can be transformed to give the principal components:

$$[\,\mathbf{PC}_1 \quad \mathbf{PC}_2\,] = [\,\mathbf{log\tau} \quad \mathbf{g_2} - 1\,] \cdot \boldsymbol{\Gamma} \tag{7.5}$$

Fig. 7.3 shows the resulting transformed correlation functions for 4 HDK® grades.

Of course, the above computation leads to varying transformation matrices for each correlation function and, especially, for each concentration. Thus, the comparison in a concentration series would be hampered. However, as the variations are generally small for each silica grade a single transformation matrix obtained at $\varphi = 0.0254$ was used for data analysis.

The diagrams in Fig. 7.3 have to be read in the following way. The initial plateau of the correlation function ($\tau \to 0$) is in the upper right corner. The main decay is nearly horizontal in the range $(2;4)$ since it designates the largest variance of the data and is therefore assigned to the first component. The long time tail can then be found in the lower left corner.

Now, the following conclusions can be drawn:

- Differing from the presentation in Fig. 7.1 a concentration dependence can be deduced from a visual inspection even for the lowest concentrations measured. However, the variations here are in the range of analysis uncertainty, e.g. of a cumulants analysis, so no further dilutions have been conducted.

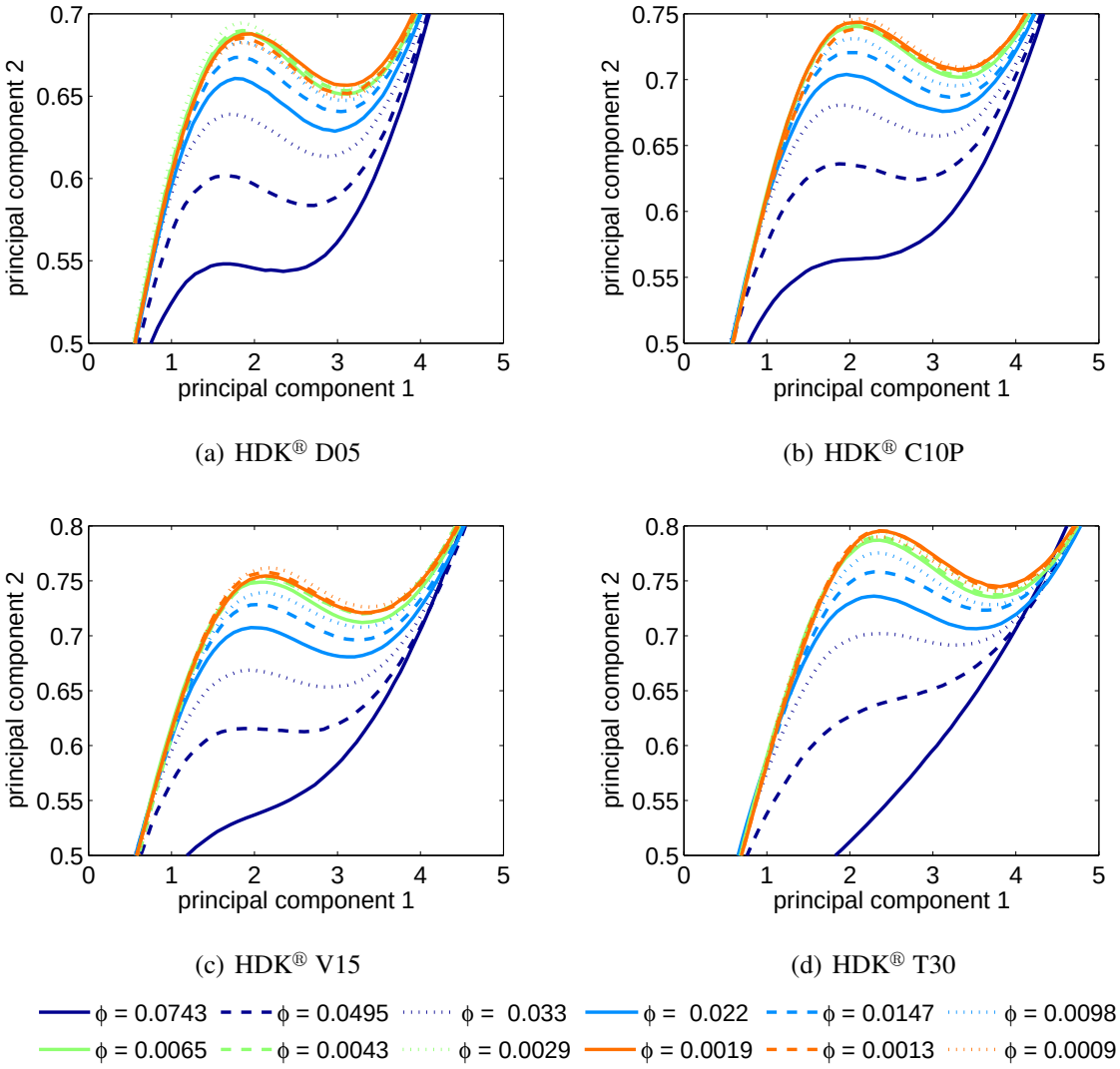

Figure 7.3: Correlation functions of a concentration series of different HDK® grades. The data have undergone a principal components analysis and, therefore, the functions are presented in terms of their principal components. The transformation matrix has been determined exclusively for each grade at a concentration of $\varphi = 0.0254$.

- While for the grades C10P, V15 and T30 a continuous trend can be deduced, there is a reversal for HDK® D05 at concentrations below $\varphi = 0.0029$. This might indicate a different interaction mechanism than can be suggested from the principal tendency. Clarifying experiments will be presented in the succeeding sections.

- The long-time stretching behavior is again observed for all grades. However, it is immediately accessible from Fig. 7.3 that this behavior grows with the specific surface area. A possible explanation is that since interparticle interactions act via the particles surfaces, a larger impact must be obtained when a larger total surface area is present in the suspension.

The above results prove the benefit of a principal components analysis of the measured autocorrelation functions. Differences between samples might be deduced without having to know how to handle data analysis algorithms. These advantages naturally arise only in the comparison of multiple data sets, single measurements are unaffected.

7.3.2 Are Models for Spheres Adequate?

After it has been shown that there are indeed strong concentration effects in the measurement data, it is necessary to quantify the strength of these impacts. Referring to Chap. 2.3.3.2 the state of the art is to perform a second cumulants analysis and observe the behavior of the mean diffusion coefficient when the concentration is increased.

The principal behavior has already been shown for a HDK® V15 in Fig. 7.2. Fig. 7.4 now shows the results of the second cumulants analysis for all grades at pH 9 and 0.01 M KNO_3.

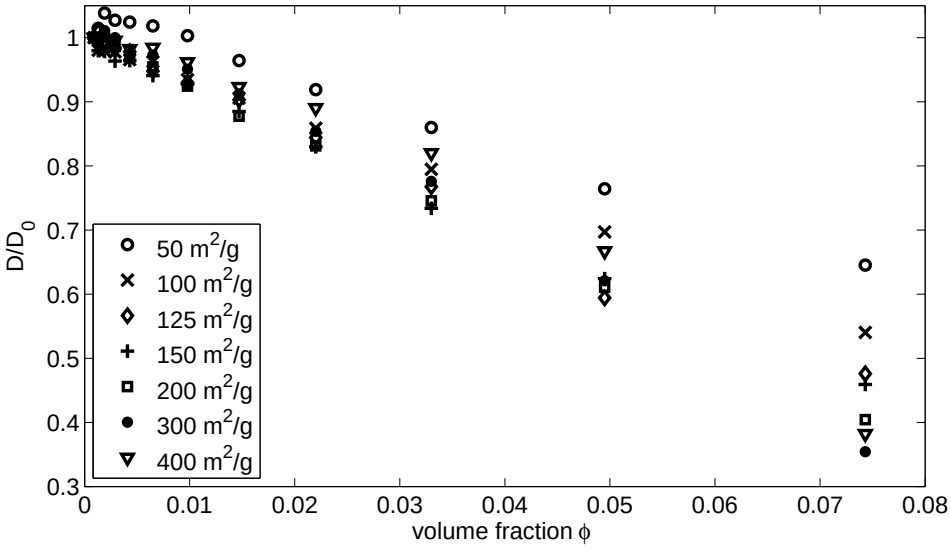

Figure 7.4: Concentration dependence of the mean diffusion coefficient determined by second cumulants analysis for all HDK® grades at pH 9 and 0.01 M KNO_3. Values relating to the effective diffusion coefficient at high dilution.

A nearly linear behavior is obtained for all samples except for HDK® T40. Again, these aggregates show differences that can be assigned to the porous structure of their primary particles. The linearity corresponds to the models in Chap. 2.3.3.2 for low concentrated systems. However, if pyrogenic silica could be compared to those HS models, all data should form a single line with slope $[-1.73 \rightarrow -2.5]$ depending on the chosen reference [74, 84–87, 141, 145]. This is not the case and, moreover, the obtained slopes in Fig. 7.4 exceed the HS values by far (see

Tab. 7.1). Additionally, as already recognized in Fig. 7.3 for HDK® D05 firstly an increase in the mean diffusion coefficient is measured which is also not explainable with a HS model. Therefore, there is a need for a model adaption. A possible approach will be depicted in the next section.

Table 7.1: Slopes of linear regression to the concentration dependence of the diffusion coefficient ratio D/D_0 for HDK® suspensions at pH 9 and 0.01 M KNO_3.

S_m (BET) $\left[\mathrm{m}^2/\mathrm{g}\right]$	Slope of D/D_0 vs. φ	Coefficient of Determination R^2
50	−5.135	0.9866
100	−6.130	0.9989
125	−7.418	0.9915
150	−7.375	0.9975
200	−8.023	0.9993
300	−8.374	0.9909
400	−7.719	0.9725

7.3.2.1 Effective Concentration Approach

The solids volume fraction in Figs. 7.1–7.4 has been computed using a density of 2200 m^2/g, i.e. assuming that pyrogenic silica aggregates are compact solid spheres. Obviously, the fractality of the aggregates requires that they occupy a larger volume in the suspension than is accounted for by the volume fraction. Thus, an effective volume fraction needs to be considered.

However, care has to be taken in the definition of the effective volume fraction. As the effect of interactions is measured as an increase or decrease of diffusivity it is a first approach to define the hydrodynamic diameter of an aggregate as an effective diameter. Then, the open fractal structure of an aggregate can firstly be expressed in terms of a porosity that gives the effective volume fraction for a HDK® grade:

$$\varphi_{\mathrm{eff}} = \frac{\varphi}{1-\varepsilon} \tag{7.6}$$

Still, the question remains, how such a porosity can be determined. Two different approaches have been pursued in this work. The first used centrifugation of the pyrogenic silica samples. The porosity was then determined from the porosity of the sediment. A second approach used the results of Chap. 5 and 6 to obtain the mass of a single aggregate and the hydrodynamic diameters of translation determined from multi-angle DLS. The details of the centrifugation

experiments would lead too far in this context and have, therefore, been shifted to Annex D. Tab. 7.2 lists the resulting porosities for the different silica grades obtained from the second approach. The first approach gives similar values but cannot be used for all silica grades.

Table 7.2: Hydrodynamically equivalent aggregate porosities of the pyrogenic silica grades.

HDK® grade	D05	C10P	S13	V15	N20	T30	T40
Porosity $\bar{\varepsilon}$	0.895	0.935	0.928	0.944	0.960	0.955	0.971

Fig. 7.5 shows the same data as in Fig. 7.4 but plotted over the respective effective volume fraction for each grade. Obviously, φ_{eff} does not bear a direct physical meaning since values up to 2.65 are obtained. However, it is possible to think of the meaning of this behavior in terms of interpenetration probability, i.e. at an effective volume fraction of 1 the aggregates are very likely to interpenetrate. Again the data of HDK® T40 show an unsual trend. This can be explained in view of the approach made in Annex D. The determined porosity additionally expresses the intrinsic porosity of the primary particles. The effect overscales the curve so the data will be neglected in the further progression.

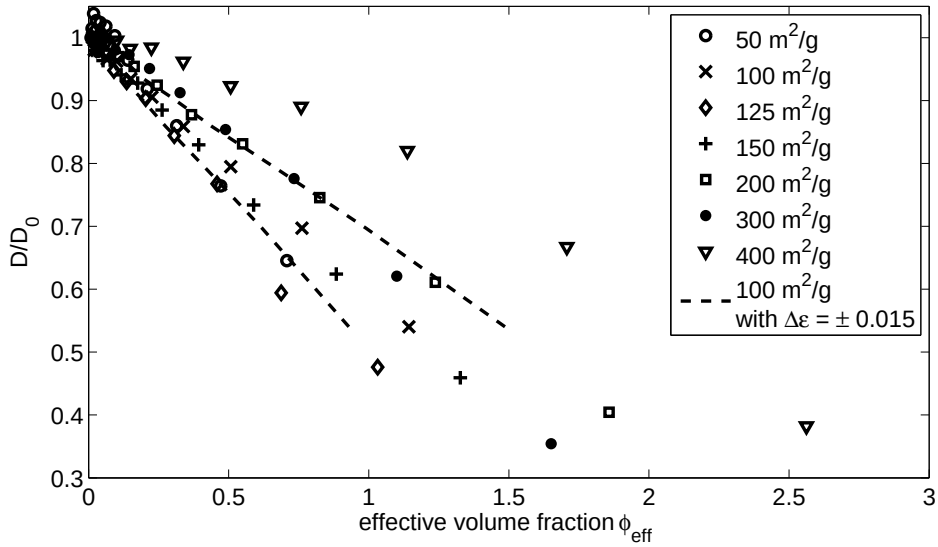

Figure 7.5: Concentration dependence of the mean diffusion coefficient determined by second cumulants analysis for all HDK® grades at pH 9 and 0.01 M KNO_3. An effective volume fraction determined from the aggregate porosities is used. Note, that now volume fractions larger than 1 are possible, this is only a scale effect but bears no direct physical meaning.

On the other hand, also the data of the other HDK® grades do not show a unique behavior which has been expected for the effective concentration approach. May this be explained with uncer-

tainties introduced in the determination of the volume fraction and the porosity, respectively? The values $1-\varepsilon$ in eq. 7.6 are quite small so that even a small uncertainty should have a significant impact. Therefore, an error propagation of eq. 7.6 has been computed to determine the relative error in φ_{eff}:

$$\Delta\varphi_{\text{eff}} = \sqrt{\left(\frac{1}{1-\bar{\varepsilon}}\right)^2 \cdot \Delta\varphi^2 + \frac{\bar{\varphi}^2}{(1-\bar{\varepsilon})^4} \cdot \Delta\varepsilon^2} \tag{7.7}$$

Indeed with a supposed error of $\Delta\varphi = 0.0002$ and $\Delta\varepsilon = 0.01$ relative deviations of φ_{eff} between 9 % and 25 % are obtained, $\Delta\varepsilon = 0.015$ already gives more than 40 % uncertainty. These errors in the determined porosity are still very small in view of the assumptions made in Annex D. The principal effect is shown in Fig. 7.5 where the two dashed lines show the data of HDK® C10P with $\bar{\varepsilon} - 0.015$ and $\bar{\varepsilon} + 0.015$, respectively. These two lines enclose nearly all measured data points except for HDK® T40.

Summarizing, it has to be said that a master-curve behavior using the effective concentration approach could not be completely approved. However, the data show that a scaling seems to be possible but the uncertainties introduced in the determination of the aggregate porosities are too large. Further progress may be achieved in future work when a more exact determination of the structural and hydrodynamic properties of pyrogenic silica enables a better estimate of the aggregate porosities.

The slopes determined in Fig. 7.5 are in a range of $[-0.3;\ -0.6]$. This is well below the known values for hard spheres which should be the lower boundary. For charged spheres a smaller slope is obtained [146] but the models only have a validity for low volume fractions so they cannot be applied in this case. Therefore, the meaning of the slope, i.e. the type of interactions that are dominant in pyrogenic silica suspensions, remains to be explained.

7.3.3 The Effect of Interparticle Interactions

7.3.3.1 A Comparison to Spherical Silica Sols

As a data treatment based on theoretically derived models in the previous section could not give exact information on the cause of the diffusivity change in concentrated pyrogenic silica suspensions explanations have to be sought by simplifying the material under consideration. Silica sols are ideal for this purpose since they show very similar interfacial properties as pyrogenic

silica but are mostly spherical. Additionally, the influence of polydispersity may be neglected for the two Levasil® samples. It can then be taken into account by using the Fuso and Köstrosol sample.

Firstly, the results of the cumulants analysis for the sample Levasil® 02T062 are given in Fig. 7.6.

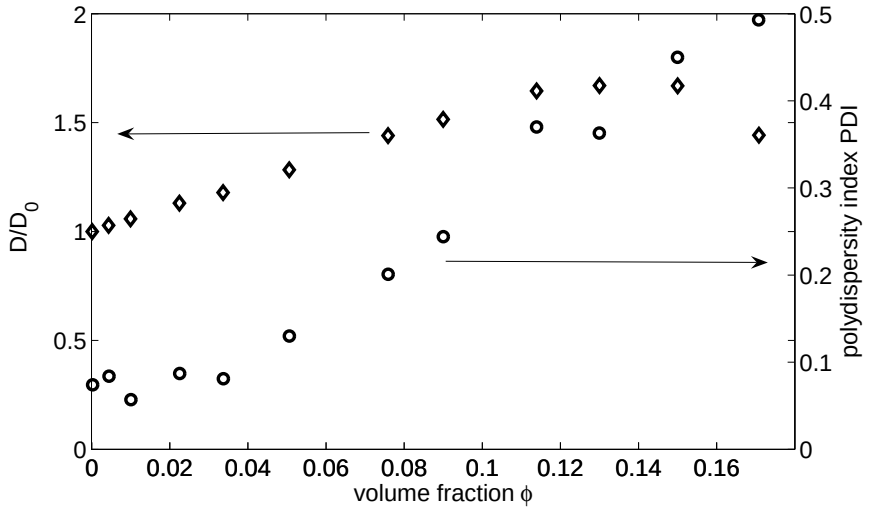

Figure 7.6: Concentration dependence of the mean diffusion coefficient and the polydispersity index determined by second cumulants analysis for Levasil® 02T062.

Contrary to the pyrogenic silica samples the diffusivity increases with concentration. Only at volume fractions above $\varphi = 0.12$ this trend is reversed. An explanation can be given simplistically by saying that below $\varphi = 0.1$ only pairwise interactions are present. The counterionic stabilization of the particles then results in an additional acceleration of the particles that causes the increase in diffusivity. Multi-body interactions at higher concentrations then lead to a structure formation in the suspension, a pseudo-lattice with lower individual particle mobility is formed. However, the situation is more complex, as can already be deduced from the behavior of the polydispersity index. As the particles are rather monodisperse, their change of diffusivity should not result in such a drastic increase of the *PDI*. Therefore, an inversion of the autocorrelation functions has been conducted to obtain the diffusion coefficient spectra (see Fig. 7.7).

The large alterations of the distribution functions with increasing concentration can easily be recognized. Firstly, a very narrow distribution is measured which shows the real distribution of Stokes-Einstein diffusion coefficients D_0. Only for this distribution eq. 2.30 can be used to compute a particle size distribution. When the concentration is increased to $\varphi = 0.0506$ faster diffusion components occur in the distribution. These can be at least partly attributed

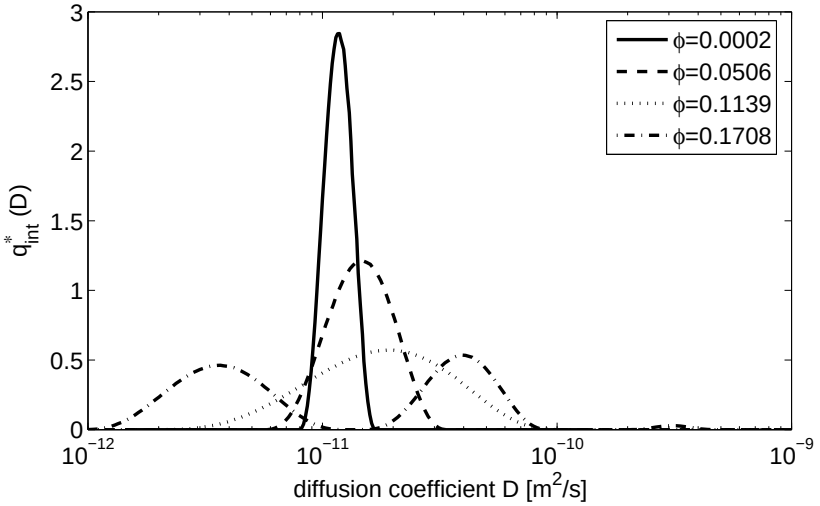

Figure 7.7: Intensity-weighted transformed density distributions of diffusion coefficients for Levasil® 02T062 at different concentrations. The Stokes-Einstein equation is valid only for the lowest concentration.

to the additional repulsion of the charged particles. Additionally, the observation range of the measurement instrument changes from self-diffusion to collective diffusion (c.f. Chap. 2.3.3.2). As collective diffusion coefficients are always smaller than self diffusion coefficients, the shift can also be attributed to this transition. This change of diffusion regime is even more visible at $\varphi = 0.1139$. Additionally, the distribution shows a stretch at lower diffusion coefficients. Here, the above mentioned structuring of the suspension occurs and a long-time diffusion coefficient[1] is measured that can be associated with structural relaxations. This structure is finally fully developed at $\varphi = 0.1708$, the original peak has disappeared, only collective diffusion and long-time diffusion remains.

If the primary particle size is increased (from 42.5 nm to 91.8 nm) by using the second Levasil sample 02T144 (see Tab. 4.2), the critical concentration φ_{krit} for the self-diffusion/collective diffusion transition is increased from 0.024 to 0.24 for the HPPS instrument. Therefore, collective diffusion is not measurable and only the structuring of the suspension should be visible in the diffusion coefficient spectra (see Fig. 7.8).

Indeed, the expectations are fulfilled. An increase in concentration does not lead to shifts of the distribution function to larger diffusion coefficients, the obtained portions larger than 10^{-11} m^2/s are only due to the smoothing of the inversion algorithm. The structuring at large

[1] The term long-time in this context means that the decay time of this process is large compared to the time necessary for a single particle to diffuse a distance comparable to the mean hydrodynamic particle size [141].

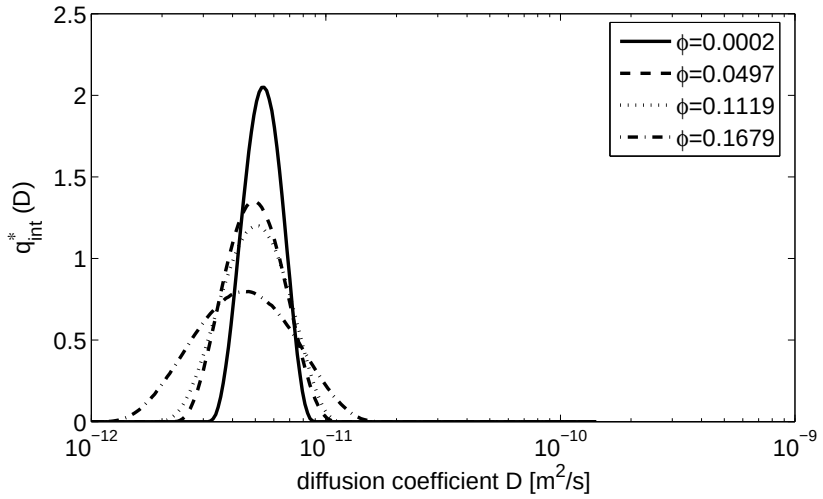

Figure 7.8: Intensity-weighted transformed density distributions of diffusion coefficients for Levasil® 02T144 at different concentrations.

concentrations, however, does not show a comparable impact to the smaller Levasil® sample. Two reasons can be given. Firstly, the interparticle distance is larger for the Levasil® 02T144 (42.5 nm compared to 19.7 nm at $\varphi = 0.17$) and additionally the larger particles have a lower mobility, i.e. the same degree of interaction is only obtained for a higher concentration. Secondly, the range of the counterionic repulsion is lower for the larger sample, since the suspension shows a higher conductivity (8.6 mS/cm compared to 1.9 mS/cm) that can be associated with a larger compression of the dielectric double layer. Thus, the structuring range is again increased.

Next, silica sols showing a considerable polydispersity in particle size were examined, again the systems differed in their mean particle size.. The behavior of distributed systems is difficult to predict since the transition range to collective diffusion is broader and the interparticle distance cannot be easily achieved. Fig. 7.9 shows the obtained distributions for comparable concentrations as for the Levasil® samples.

The relatively broad distributions at $\varphi = 0.0002$ can be readily identified from the diagrams. The effect of particle concentration is principally the same as for the Levasil® samples. Both mechanisms, collective diffusion and structuring, occur simultaneously when the concentration is increased. As already known from theoretical considerations (c.f. Chap. 2.3.3.2) the collective diffusion coefficients then increase with concentration while the structuring decreases the diffusion coefficients. Thereby, the whole measured distribution is broadened. This is the reason for the large increase of the polydispersity index when the cumulants method is used for

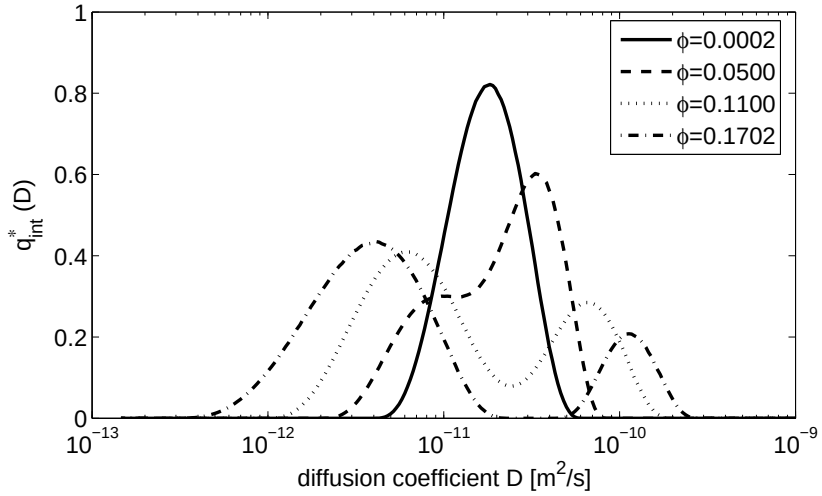

(a) Köstrosol AD

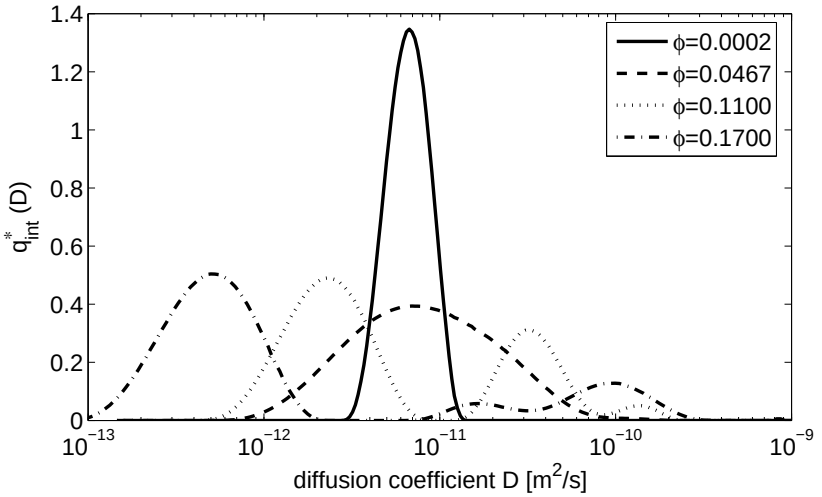

(b) Fuso PL-3

Figure 7.9: Intensity-weighted transformed density distributions of diffusion coefficients for a) Köstrosol AD and b) Fuso PL-3 at different concentrations.

data analysis. The same results can also be obtained for the Levasil® samples, however, the impact of the effects seems to be even more pronounced for the polydisperse samples.

Certainly, the question could be raised whether this larger effect could again be due to the counterionic repulsion of the particles. While this would be a good explanation for the Fuso sample (conductivity ≈ 0.2 mS/cm), the Köstrosol sample showed the same conductivity (1.9 mS/cm) as the small Levasil® sample.

Summarizing, there are a lot of impacts on the particles diffusivity that have to be considered when DLS measurements in concentrated suspensions are conducted. Examples are the dif-

fusion range, the structuring of the suspension and the effect of particle repulsion which acts as an additional structuring effect at high concentrations (an attraction is neglected for stable suspensions). Unfortunately, only for ideal particles the transition to collective diffusion and the structuring of the suspension can be predicted. The results show that the same effects also work for polydisperse sample, though, in a complicated mixed manner. It has to be noticed that the consideration of the mean diffusion coefficient alone does not give satisfying explanations of the underlying mechanisms. The width of the distribution of diffusion coefficients, either obtained from a second cumulants analysis or via an inversion of the data has been identified as an important carrier of information. Still, there are some open questions remaining. As the silica sols were already delivered as suspensions, unknown dispersing agents may have a significant impact on the stabilization mechanisms in the suspension. If there are adsorbed polymer chains or surfactants on the particles, even a centrifugation as carried out for the Fuso sample (c.f. Chap. 4.3) cannot remove all sterically acting substances. Therefore, the consideration of interparticle interactions could only be conducted with the pyrogenic silica suspensions as will be shown in the next section.

7.3.3.2 Pyrogenic Silica Revisited

If the questions from Chap. 7.1 are recalled, only two of them still need to be answered. What is the direct impact of interparticle interactions in pyrogenic silica suspensions and can high concentration DLS be applied for quality assurance purposes? As could be deduced from the last section the width of the distribution gives valuable information concerning these issues. So far, only the mean diffusion coefficient and its concentration dependence has been considered. Fig. 7.10 shows the corresponding values of the polydispersity index *PDI* for the suspensions at pH 9 and 0.01 M KNO_3. As the effective concentrations bear a too large uncertainty (c.f. Chap. 7.3.2.1) the results are again plotted versus the solid volume fractions. The data have been normalized to the *PDI* determined in high dilution to enable a comparison of the silica grades. As expected, the polydispersity index grows with increasing concentration, i.e. there are obviously again different interaction mechanisms present. Though, the trend is not that unambiguous as for the mean diffusion coefficient, it can be deduced that low surface area grades show a smaller increase than large surface area grades. However, it has to be noted that low surface area grades already show a larger *PDI* in high dilution.

Suppose that the same interaction mechanisms act in pyrogenic silica suspensions as in the

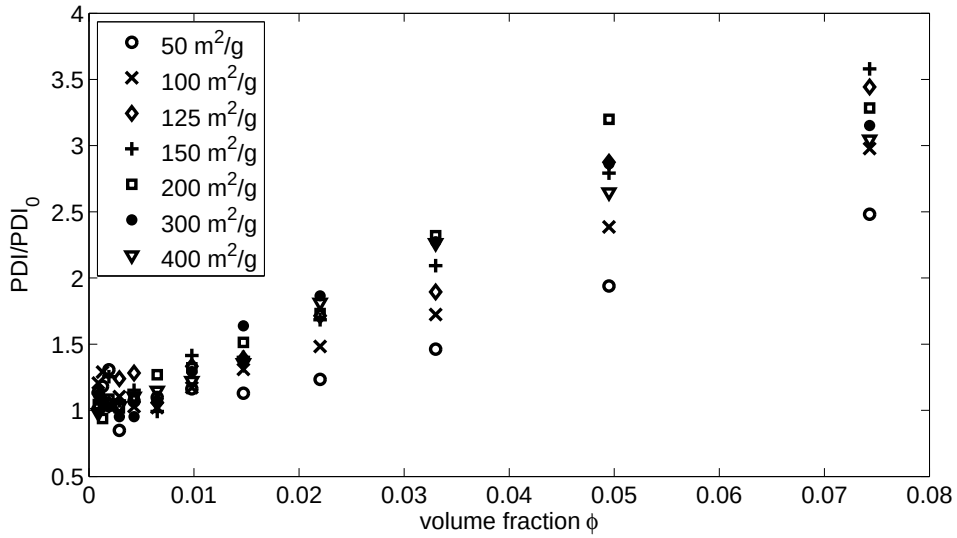

Figure 7.10: Concentration dependence of the normalized polydispersity index determined by second cumulants analysis for all HDK® grades at pH 9 and 0.01 M KNO_3.

colloidal silica sols. Then, taking the hydrodynamic diameter into account, no transition to collective diffusion should be visible since the critical volume fraction is larger than $\varphi = 1$. The only visible effect should be a structuring of the suspension associated with a distribution of long-time diffusion coefficients. An inversion of the data has, therefore, been conducted. The results of four exemplary HDK® grades are given in Fig. 7.11. HDK® T40 has been omitted in this discussion since the ambiguities already shown in Chap. 7.3.2 would complicate the interpretation of the results.

The results of the low surface area grade D05 are as expected. No collective diffusion is observed but the distribution is shifted to smaller diffusion coefficients that account for the structuring of the suspension. Contrarily, already in HDK® S13 at the highest measured concentration, a small peak is obtained accounting for a faster diffusion component. This shows that also for the consideration of collective diffusion an effective volume fraction needs to be used. As the aggregate sizes decrease with increasing specific surface area, collective diffusion components are more characteristically shown for the grades N20 and T30. Additionally, the increase of collective diffusion with concentration is visible. The structuring effect becomes more pronounced with increasing surface area. Two reasons may be given for this behavior. Firstly, as obtained in Annex D, the smaller aggregates show a more open structure than the larger aggregates of the low surface area grades. Thus, the hydrodynamic interactions are increased that lead to the observed effect. Secondly, the interparticle interactions act via the particles surfaces, i.e. that additionally the repulsive forces become larger with increasing specific surface area.

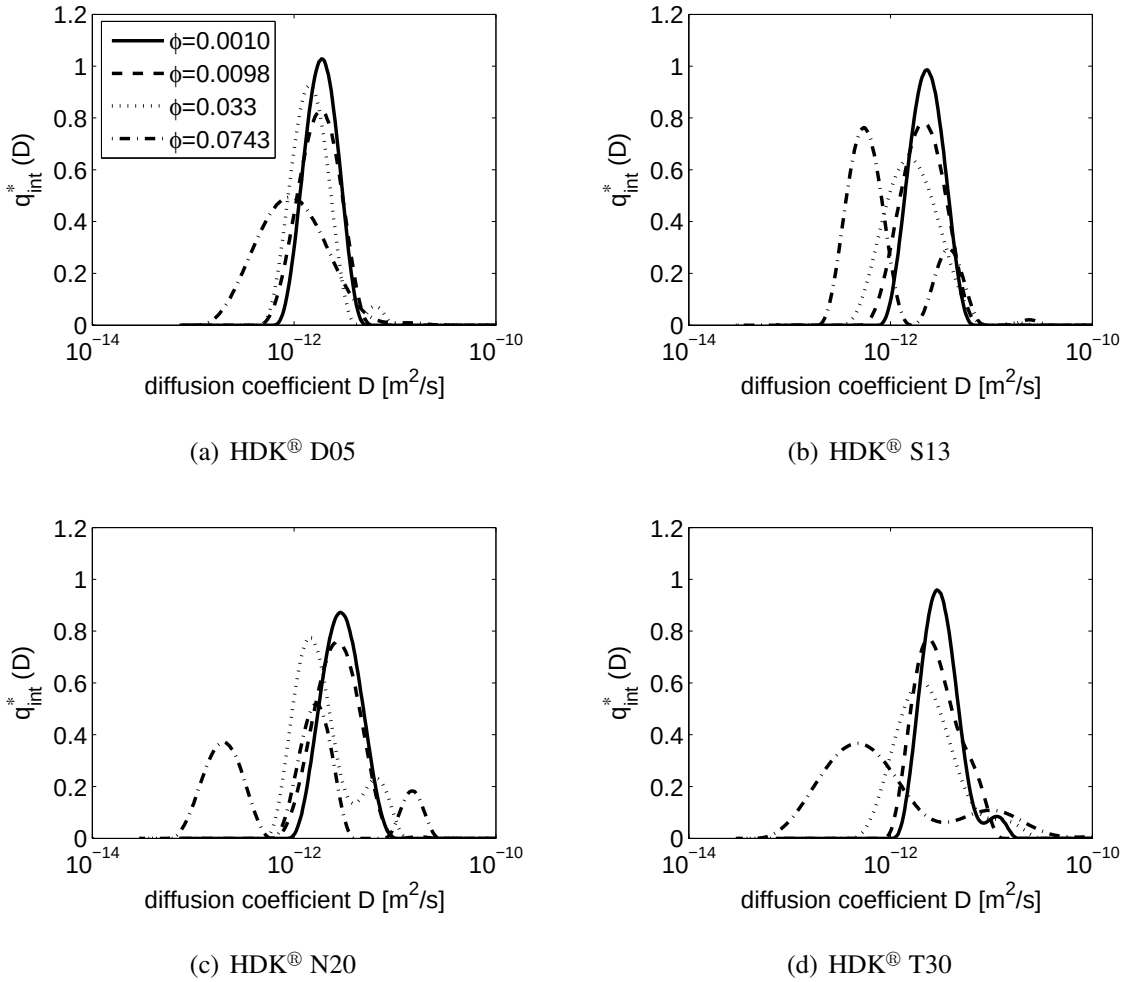

(a) HDK® D05

(b) HDK® S13

(c) HDK® N20

(d) HDK® T30

Figure 7.11: Intensity-weighted transformed density distributions of diffusion coefficients of different HDK® grades at pH 9 and 0.01 M KNO_3. Respective concentrations are denoted in (a).

To distinguish between the two structuring effects, the interparticle repulsion has been increased by using samples with reduced ionic strength (0.001 M instead of 0.01 M KNO_3). If hydrodynamic constriction outweighs the repulsive forces the measured structuring should not be changed while it should be more pronounced if the counterionic repulsion has a strong influence. Fig. 7.12 shows the results of the cumulants analysis of the concentration series with pH 9 and 0.001 M KNO_3. Tab. 7.3 again gives the values of the slopes of the linear fits.

At first sight a similar behavior is obtained as for the higher salinity samples. Only the linearity of the measured data points is somewhat reduced. In view of the slopes of the linear regression, however, an increase is obtained, i.e. the mean diffusivity is reduced more strongly when the dielectric double layer is extended. This shows that indeed the counterionic repulsion increases the structuring of the suspensions. The same results should be obtainable from an inversion

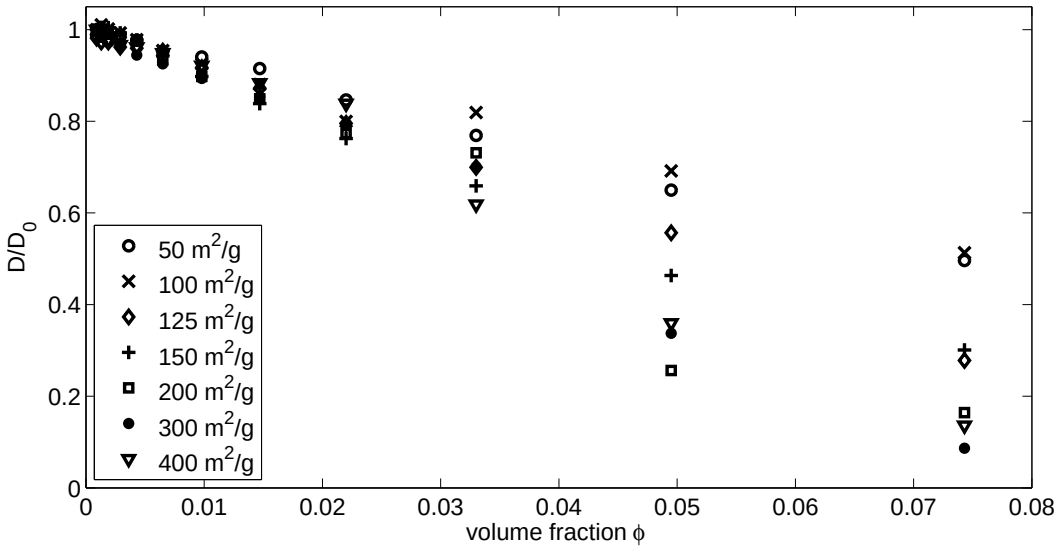

Figure 7.12: Concentration dependence of the mean diffusion coefficient determined by second cumulants analysis for all HDK® grades at pH 9 and 0.001 M KNO_3. Values relating to the effective diffusion coefficient at high dilution.

Table 7.3: Slopes of linear regression to the concentration dependence of the diffusion coefficient ratio D/D_0 for HDK® suspensions at pH 9 and 0.001 M KNO_3. The values from Tab. 7.1 determined at pH 9 and 0.01 M KNO_3 are additionally given for comparison.

S_m (BET) $\left[\mathrm{m}^2/\mathrm{g}\right]$	Slope of D/D_0 vs. φ	Coefficient of Determination R^2	Slopes at 0.01 M KNO_3
50	−6.860	0.9971	−5.135
100	−6.575	0.9816	−6.130
125	−9.403	0.9961	−7.418
150	−10.133	0.9914	−7.375
200	−12.244	0.9530	−8.023
300	−12.472	0.9804	−8.374
400	−12.171	0.9794	−7.719

of the measured autocorrelation functions. Fig. 7.13 gives a comparison of the distributions of diffusion coefficients. Each sub-figure draws the difference between the two ionic strengths while the effect of increasing concentration can be viewed in the rows of sub-figures and the effect of increasing specific surface area in the columns.

In the left column highly diluted samples are shown. The obtained distributions should, therefore, be independent of the increase in double layer thickness except when this thickness itself would be measurable with DLS as e.g. Xu proposed for small spherical particles [173]. In view of the obtained results this cannot be established for pyrogenic silica suspensions. The differ-

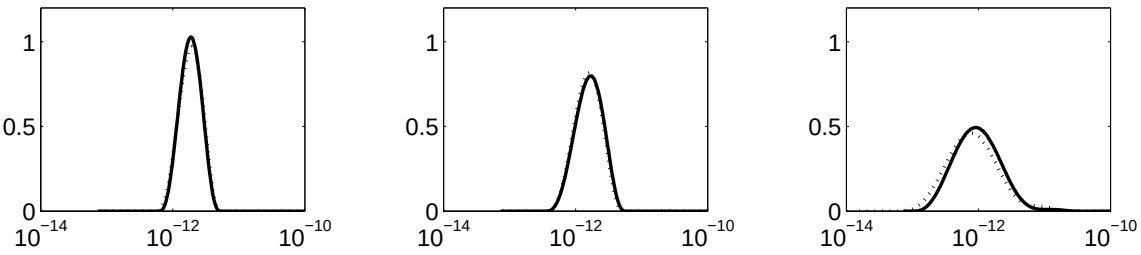

(a) HDK® D05 $\varphi = 0.0009$ (b) HDK® D05 $\varphi = 0.0220$ (c) HDK® D05 $\varphi = 0.0743$

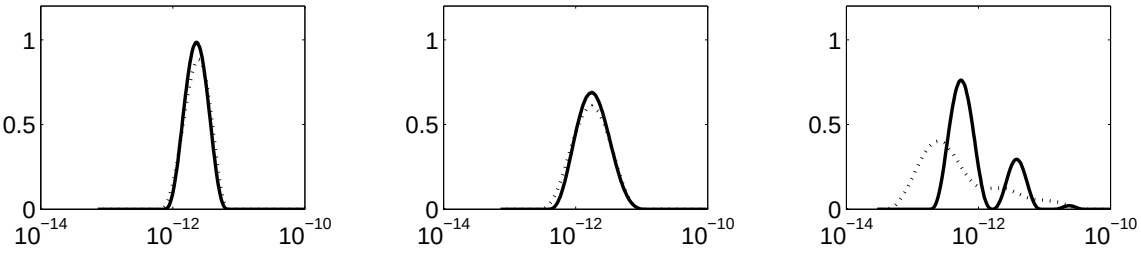

(d) HDK® S13 $\varphi = 0.0009$ (e) HDK® S13 $\varphi = 0.0220$ (f) HDK® S13 $\varphi = 0.0743$

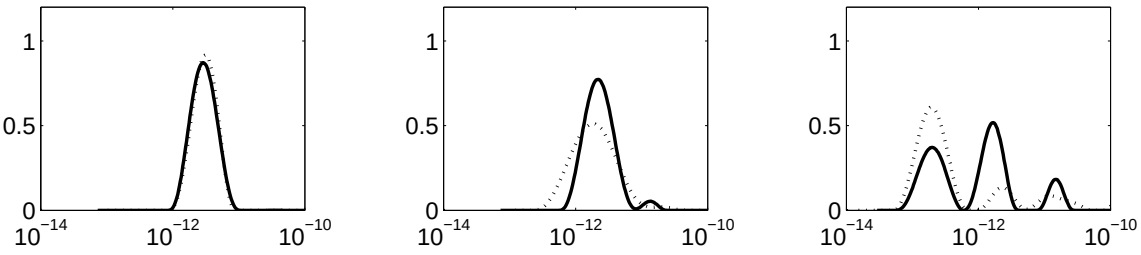

(g) HDK® N20 $\varphi = 0.0009$ (h) HDK® N20 $\varphi = 0.0220$ (i) HDK® N20 $\varphi = 0.0743$

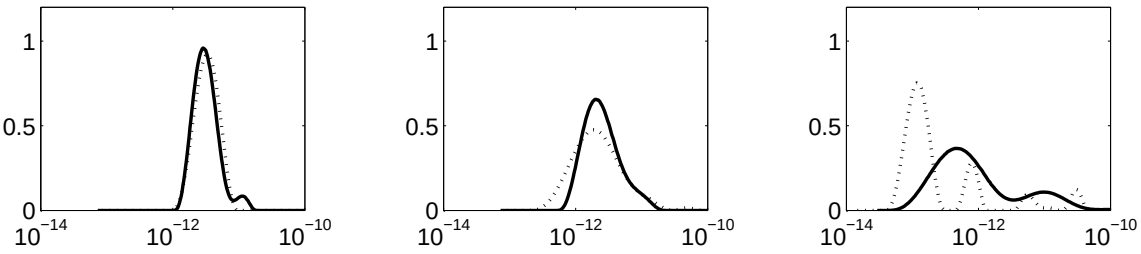

(j) HDK® T30 $\varphi = 0.0009$ (k) HDK® T30 $\varphi = 0.0220$ (l) HDK® T30 $\varphi = 0.0743$

Figure 7.13: Influence of the suspensions ionic strength on the concentration dependence of the distribution of diffusion coefficients for pyrogenic silica suspensions. The X-axes show the diffusion coefficient in m^2/s and the Y-axes show the intensity-weighted transformed density distribution $q^*_{int}(D)$. The solid line denotes suspensions at pH 9 and 0.01 M KNO_3, the dashed line corresponds to pH 9 and 0.001 M KNO_3.

ences in the distributions are very small what can be assigned to uncertainties introduced by the inversion algorithm. This again verifies the reproducibility of the sample preparation procedures so that the differences in higher concentration can clearly be ascribed to interparticle interactions.

The middle column shows samples at an intermediate concentration. For the low surface area grades only very small alterations occur at lower salinity. Again, the structuring is increased but no collective diffusion occurs. For HDK® N20 and T30 instead, collective diffusion is measured but these peaks show no dependence on the extension of the dielectric double layer. The structuring effect is, however, more pronounced. The same holds for the samples at $\varphi = 0.0743$ except for smoothing effects of the regularization procedure (samples HDK® S13 and T30).

These results depict the principal influence of interparticle interactions on the diffusivity in concentrated pyrogenic silica suspensions. For stable suspensions only a repulsive total interaction potential can be considered. At large concentrations the aggregates are hydrodynamically hindered in their mobility. The interaction is superimposed on that general effect and aggravates it. Additional to the diffusion coefficient spectrum that accounts for the different hydrodynamic size of the aggregates (though influenced by rotational contributions) a second distribution occurs. These so-called long-time diffusion coefficients describe the restricted movement of the aggregates past one another. Obviously, they are more pronounced when the concentration increases (i.e. the interparticle distance decreases) and the particles repel each other. It is, therefore, desirable to suppress the interparticle interactions to measure the *pure* hydrodynamic effect. Possibly, a steric stabilization combined with a high salinity of the suspension could produce stable suspensions with vanishing double layer interaction. Hitherto, a successful preparation of such suspensions of pyrogenic silica has not been reported and should thus be subject to further investigations.

7.4 Summary

The development of DLS instruments that can suppress multiple scattering contributions in the measurement signal has facilitated the measurement of colloidal suspensions at industrially relevant concentrations. For instance, suspensions of pyrogenic silica can be characterized at a solid content up to 15 wt.-% using the non-invasive backscattering technique of the HPPS.

It has been, however, shown that some precautions are necessary concerning data analysis and interpretation in terms of quality assurance purposes.

The results for a single grade are unambiguous so that the whole concentration range can be used. However, while for diluted measurements nearly no suspension data needs to be recorded in concentrated suspensions the solids concentration, the pH and amount and type of added electrolyte are important parameters that can alter the measurement result so they should additionally be controlled. The largest solids concentration where pyrogenic silica suspensions can be considered to show free diffusion is below $\varphi = 0.001$, i.e. the above mentioned parameters are important already at very low concentrations. A principal components analysis introduced in Chap. 7.3.1.1 may be used to compare measured autocorrelation functions for a concentration influence without any model describing the dependence of the ACF from the diffusional behavior of the particle system.

At high particle concentration the mean diffusion coefficient cannot be used as an unambiguous tool for the distinction of different silica grades. This is due to the stronger influence of hydrodynamic and interparticle interactions for high surface area grades. The mean diffusion coefficient might be equal or even larger than for a low surface area grade at a certain concentration. If further parameters, such as the polydispersity index or the distribution of diffusion coefficients, are additionally considered in such a comparison this problem can be solved so that DLS remains a valuable tool for quality assurance.

8 Application-Oriented Analysis of DLS Data

8.1 Gelling Suspensions

8.1.1 Introduction

Interparticle interactions influence the stability of suspensions. As shown in the previous chapter they additionally alter the diffusivity. If the counterionic repulsion between pyrogenic silica aggregates is screened by a high ionic strength and the concentration of the suspension is large enough a specific destabilization behavior occurs. The aggregates flocculate but due to their large occupied volume they do not settle. Instead, an interconnected network is formed that spans the whole suspension and entraps the liquid phase [174]. Thus, the suspension solidifies.

This phase transition process is called gelation. Research on phase transitions has gained much attention in the last years. Depending on the acting mechanisms, the solid phases are distinguished in gels, Wigner glasses and attractive glasses [175]. The best examined colloidal system undergoing phase transitions is a synthetic clay material named Laponite (Southern Clay Products Inc., Gonzales, USA) because it is able to form all three solid phases only by changing the salinity of the suspension [175–182].

The process of gelation as observed for pyrogenic silica suspensions is important for many industrial applications. While a fast transition is wanted, e.g., for cosmetic or medical applications, it has to be completely avoided when stable paints or abrasives are to be produced. The most important parameter describing the gelation process is the phase transition time. It should be controllable and short for wanted transitions and very long if a solidification needs

to be obviated. The solids concentration, the salinity and the pH of a suspension are important parameters that can influence the phase transition time.

Dynamic light scattering techniques are often used for the observation of phase transitions [176, 177]. However, it has to be noticed that the principles of DLS are hurt when such systems are measured. The ergodic hypothesis of Boltzmann [183] is an inherent assumption for the validity of the field correlation function as obtained in Annex A. It assumes that the system under study is ergodic, i.e. that every particle is free to diffuse in the whole suspension space. This is obviously not the case for solidifying samples. Therefore, special data treatment is necessary to quantify structural changes from the measured autocorrelation functions (see Chap. 8.1.2).

The examinations in this work aimed at a first understanding of phase transitions in pyrogenic silica suspensions. Therefore, a parameter study was conducted to elicit the most important influences on the phase transition time. As known from Iler [184] and Knoblich and Gerber [91] pyrogenic silica is most likely to form gels at a pH of 6. Thus, this parameter was kept constant in the examinations. Additionally, also the solids concentration remained almost unchanged since at too low concentrations the phase transition lasts very long and the resulting gel might not span the whole suspension space so that water is *squeezed out* after a certain waiting time. This process is called syneresis and is best known in the production of cheese where the whey is separated from the cheese curd. If on the other hand the concentration was chosen too high, multiple scattering occured that could not be completely suppressed with the NIBS technique of the HPPS.

8.1.2 Analysis of Time-Dependent Correlation Functions

As DLS needs a non-changing spectrum of diffusion coefficients to obtain a reliable autocorrelation function, measurements can only be conducted for rather slow phase transitions. Then, a single measurement monitors the quasi-stationary state of the dispersion. By viewing analysis results over a multitude of autocorrelation functions the phase transition can be followed with DLS. Fig. 8.1 shows the typical progression of the measured ACF's during solidification for a HDK® V15.

It can be readily recognized from the diagram that with proceeding solidification of the suspension the measured exponential decay of the ACF is stretched to longer decay times. Thus, the data acquisition time has to be increased to obtain a good statistics of the correlation data.

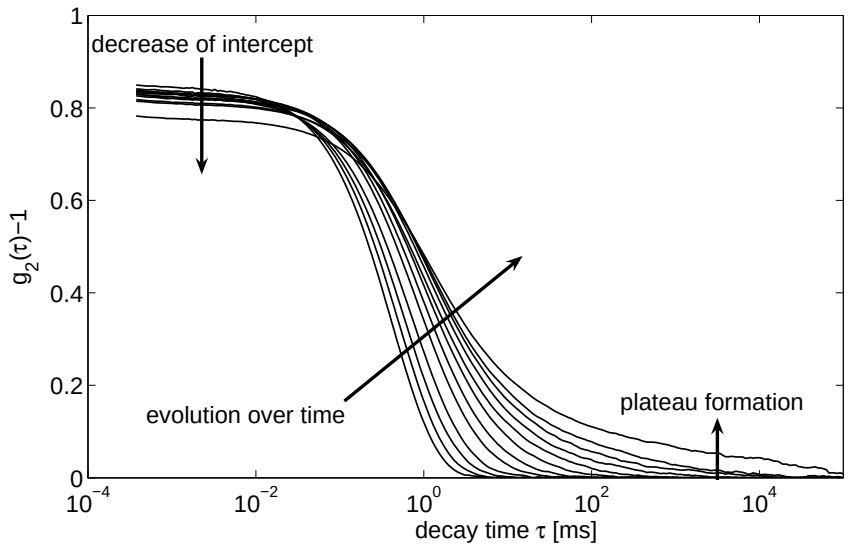

Figure 8.1: Characteristic progression of the autocorrelation functions measured at pyrogenic silica. HDK® V15, 9.9 wt.-%, pH 6, $I_s = 0.03$ M, total data acquisition time 42 h.

This has been done by using the script programming language of the ALV Correlator Software that enables a continuous change of the measurement parameters for each single run. Additionally, after long time spans the intercept of the ACF starts to decrease and the decay ends at a plateau value larger than 0. This behavior is associated with the increasing non-ergodicity of the sample [185, 186].

As stated in the last section non-ergodic systems disagree with the concept of DLS and, therefore, clearly non-ergodic ACF's must not be analyzed. Kroon et al. gave a possible circumvention of the problem [176]. The measured scattered intensity signal has to be decomposed into a fluctuating (and thus ergodic) part and in a static part:

$$\langle I(t)\rangle = \left\langle I_{fl}(t)\right\rangle + I_c \tag{8.1}$$

The condition for the definition of the fluctuating intensity $\left\langle I_{fl}(t)\right\rangle$ is that the mean of the complex fluctuating electric field is zero [186]. The static scattered intensity can then be defined as:

$$I_c = \sqrt{2\left\langle I(t)\right\rangle^2 - \left\langle I(t)^2\right\rangle} \tag{8.2}$$

A comparison to the definition of the autocorrelation function shows that if the static intensity is 0 a perfect correlation is obtained:

$$g_2(\tau) = \frac{\langle I(t)I(t+\tau)\rangle}{\langle I(t)\rangle^2} \Rightarrow \tau \to 0 \Rightarrow g_2(0) = 2 = \frac{\left\langle I(t)^2\right\rangle}{\langle I(t)\rangle^2} \Rightarrow I_c^2 = 0 \tag{8.3}$$

As the structuring of the phase transition is not unique in the suspension I_c is dependent on the position where the intensity is measured. Contrary, the fluctuating intensity is position

independent as it is an ergodic property. Fig. 8.2 shows the evolution of the two intensities during a phase transition of a HDK® C10P.

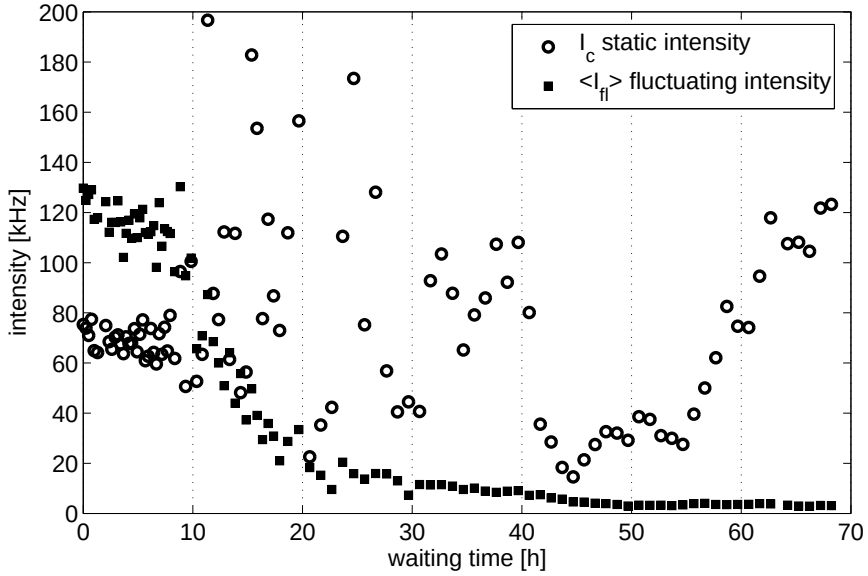

Figure 8.2: Evolution of the static scattered intensity I_c and the fluctuating scattered intensity $\langle I_{fl} \rangle$ during the gelation of a HDK® C10P at pH 6, 10.8 wt.-% and $I_s = 0.1$ M. As the total scattered intensity is measured as a photon count rate, the unit of the Y-axis is kHz.

As predicted, the fluctuating scattered intensity shows a continuous decrease during the solidification of the sample. This is due to the reduced free diffusion of the interconnecting pyrogenic silica aggregates. The static scattered intensity should ideally be zero at the beginning of the experiment, however, since the coherence factor is never 1 in the backscattering regime a plateau value is measured instead. After a certain period of time I_c starts to show strong variations between different measurement runs. This is a strong indication of non-ergodicity in the sample when I_c becomes position-dependent while the HPPS only measures at a fixed position. Kroon [186] considers this point to demark the phase transition time t_{pt}, i.e. the time when the system has completely come to arrest. However, the further decrease of $\langle I_{fl} \rangle$ shows that this is not the case and other analyses have to be conducted.

Thus, Kroon et al. [176] suppose to compute a correlation function solely for $\langle I_{fl} \rangle$ which is called CFF (Correlation Function of the Fluctuating field):

$$g_{fl}(\tau) = \frac{\langle I_{fl}(t) \cdot I_{fl}(t+\tau) \rangle}{\langle I_{fl}(t) \rangle^2} \tag{8.4}$$

The CFF can be directly computed from the measured autocorrelation function (see Annex E).

It can then be processed by data analysis algorithms. However, the question remains which analysis is best suited since in such dynamic processes it has to satisfy specific requirements:

- As for one phase transition up to 500 single measurement runs are recorded, data analysis must be fast and automated.
- The results of the analysis should scale with the progression of the solidification to elicit information e.g. on the phase transition time t_{pt}.

Thus, an inversion of the data is not helpful since the computational effort is too high and too much data are produced. Additionally, there are many parameters that can be altered so an automated comparison cannot be achieved. Cumulants analysis is fast and produces solely two parameters that describe the distribution of diffusion coefficients. Unfortunately, the expansion does not give good fits when the exponential decay is stretched. Therefore, other analysis schemes have been developed.

Often, the Kohlrausch-Williams-Watts approach introduced in 1863 to describe dielectric relaxations in polymers is used to fit the measured correlation functions [176, 179]:

$$g_1(\tau) = \exp\left[-(\tau/\tau_1)^{\beta}\right] \quad \text{or} \quad g_{fl}(\tau) = \exp\left[-(\tau/\tau_1)^{\beta}\right] \tag{8.5}$$

The difference to a linear cumulants analysis is the parameter β that accounts for the stretching of the ACF's at long lag times. However, Kroon et al. [176] could only fit their results at large lag times using this equation. The approach differed at short lag times.

In 2001 Abou et al. [187] modified the above approach with an additional exponential term:

$$g_1(\tau) = C_1 \exp\left[-(\tau/\tau_1)\right] + (1 - C_1) \exp\left[-(\tau/\tau_2)^{\beta}\right] \tag{8.6}$$

This gives a better fit to the measured data since the exponential accounts for remaining freely diffusing portions (rotational and translational). Thus, the decay time τ_2 and the stretching parameter β can be determined with more precision.

Ruzicka et al. [177] finally presented a mostly empiric approach to elicit the phase transition time and the transition kinetics from eq. 8.6. Therefore, the stretched exponential decay is supposed to be caused by a distribution of decay times. The mean decay time τ_m can then be obtained by:

$$\tau_m = \tau_2 \frac{1}{\beta} \Gamma\left(\frac{1}{\beta}\right) \tag{8.7}$$

where $\Gamma(1/\beta)$ is the Gamma function. The mean relaxation time increases during the solidification and diverges for long time periods. The phase transition time is, therefore, obtained from the fit equation:

$$\tau_m = \tau_0 \exp\left[C \frac{t}{t_{pt} - t}\right] \tag{8.8}$$

Certainly, other empirical equations might be found that fit the experimental values equally well but Ruzicka et al. [177] were able to correlate their obtained phase transition times for Laponite samples with the manually determined time when the suspension beaker was tilted without the suspension flowing.

For this reason, the above approach has been adopted here for the analysis of the phase transitions of pyrogenic silica. Differently to Ruzicka et al. and Abou et al. not the field-correlation function was fitted but the correlation function of the fluctuating field. This seems to be quite obvious since the ergodic hypothesis is never violated in data analysis which is a prerequisite for DLS. However, it has to this time not been carried out so a comparison of the fits to the FCF has additionally been conducted.

For this purpose a set of MATLAB® routines has been developed together with Richter [188] that offer the following analyses:

- Import of measured correlation functions and display. For large data sets, only every j-th set can be read.
- A second cumulants analysis with additional baseline correction as described in Chap. 6.3 using either the ACF or the CFF.
- A fit based on Ruzicka et al. [177] to determine τ_1, τ_2 and β as well as τ_m and t_{pt} either for the ACF or the CFF. Again, an additional baseline correction can be conducted.
- Decomposition of the measured count rates in static and fluctuating intensities and plot of the evolution of the mean count rate over the phase transition process. This option is not available if the sample was removed from the instrument during different runs as the laser attenuation may be changed by this procedure.

Richter [188] extended eq. 8.6 by an additional term that accounts for the plateau formation at long lag times:

$$g_{fl}(\tau) = (1 - C_2) \cdot \left\{ C_1 \exp\left[-(\tau/\tau_1)\right] + (1 - C_1) \exp\left[-(\tau/\tau_2)^{\beta}\right] \right\} + C_2 \tag{8.9}$$

However, it could be shown that the analysis of such clearly non-ergodic behavior leads to deviations of the expected evolution of τ_m as shown in Fig. 8.3. Thus, the use of eq. 8.9 does not reveal additional information on the phase transition behavior.

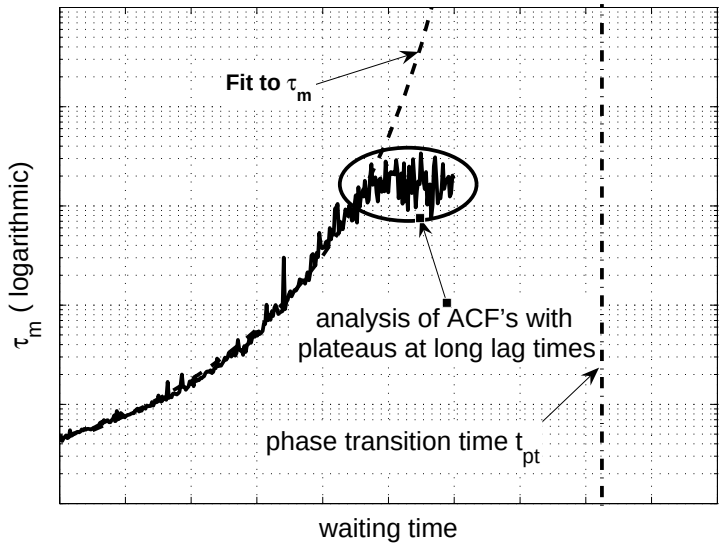

Figure 8.3: Determination of the phase transition time t_{pt} using eq. 8.8 from experimental data. The used τ_m-values deviate if autocorrelation functions with a plateau at long lag times are included in the analysis.

Finally, it should be noticed that all the above mentioned fits require nonlinear least squares algorithms. A reflective Newton method has been chosen due to the more robust results obtained compared to e.g. a Levenberg-Marquardt algorithm.

8.1.3 Measurement Results

In the conducted experiments pyrogenic silica grades HDK® D05, C10P, V15 and T30 were used to investigate the influence of the specific surface area and the respective primary particle and aggregate sizes. Each grade was suspended in water at pH 6 (KOH). The ionic strength was adjusted at 0.1 M and 0.03 M KNO_3 to disclose the effect of screening the counterionic repulsion. All samples revealed a phase transition in time periods ranging from 3 hours to 6 days. When weak ultrasound (50 W) was applied in a water bath only those with low ionic strength could be liquefied again. This already shows that the stability of the gels depends on the interparticle interactions. Tab. 8.1 shows the determined phase transition times for all examined samples except for HDK® T30 at $I_s = 0.1$ M because the phase transition was too fast to be

observed with DLS and for HDK® D05 at $I_s = 0.03$ M because the phase transition lasted too long (more than a week).

Table 8.1: Calculated phase transition times of pyrogenic silica samples. The approach of Ruzicka et al. [177] was applied to either the measured ACF's or the decomposed CFF's.

HDK® sample			phase transition time (t_{pt}) [h]	
S_m (BET) [m^2/g]	Concentration [wt.-%]	I_s [M]	ACF	CFF
50	11.0	0.10	22.4	23.6
100	10.8	0.10	22.7	24.7
100	10.0	0.03	116.5	136.8
150	13.4	0.10	2.8	3.0
150	10.7	0.10	3.3	3.3
150	9.9	0.03	49.0	50.4
300	10.1	0.03	5.3	5.6

The first obvious result that can be obtained from the table is that always the phase transition time computed using the ACF is smaller than t_{pt} from the CFF [189]. This can be attributed to the analysis of partly non-ergodic spectra when the ACF is used. The erroneously considered static intensity I_c results virtually in a faster solidification.

Generally, an increase of the specific surface area and the ionic strength, respectively, leads to a faster phase transition. The solids concentration was only varied for the HDK® V15 samples. The results show that an increase here also speeds up the solidification. An explanation for this behavior can be given in view of the gelation model proposed by Sandkühler et al. [174]. As gelation is a two-step scenario where firstly agglomerates are generated that finally interconnect, the velocity of the second process has to depend on the available interconnection points on the pyrogenic silica aggregates. These should clearly scale with the total particle surface area in the suspension. Thus, an increase in concentration as well as an increase in specific surface area leads to a faster phase transition. This model shows that the two parameters need not to be discussed separately so further investigations can make use of this finding to circumvent the solids concentration problems mentioned in Chap. 8.1.1.

The influence of the suspension's ionic strength is explicable by the screening of the counterionic repulsion forces. These affect the first gelation step, the agglomeration. At a higher ionic strength an aggregate needs less impacts with neighboring aggregates until it attaches. This

property may be the best process variable to influence phase transitions in technical applications.

To reveal the phase transition kinetics for all pyrogenic silica samples the evolution of the fit results τ_m, τ_2 and β are displayed versus the relative waiting time t/t_{pt} in Fig. 8.4.

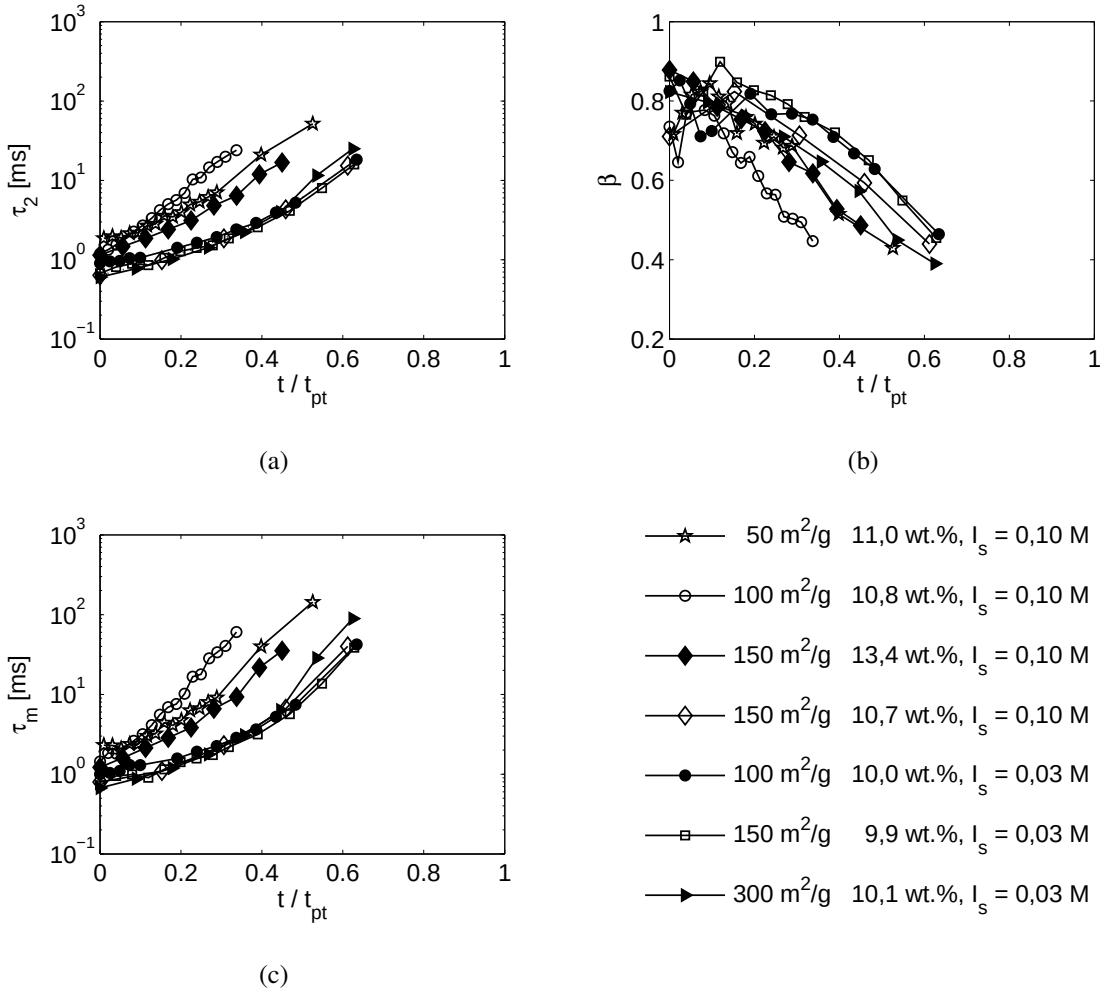

Figure 8.4: Evolution of the stretched exponential decay of the CFF characterized by (a) the decay time τ_2 and (b) the stretch parameter β. In (c) the mean decay time τ_m derived from eq. 8.7 is given. HDK® samples (at pH 6) with different specific surface area S_m, solids fraction and ionic strength I_s marked in the legend.

The plots of τ_2 and τ_m show a classification into two groups. The stretch parameter β decreases for $t/t_{pt} > 0.2$ but shows strong variations for a beginning phase transition. This is due to the applied fit equation (eq. 8.6). At the start of a gelation β takes values around 1, i.e. the CFF is not stretched yet. The two decays in the fit may then represent nearly the same section of the correlation function and, therefore, the algorithm has many variables (τ_1, C_1, τ_2 and β) to minimize the residual. Thereby, the influence of measurement errors is strongly enhanced which

leads to variations in the fit parameters. However, also at $t/t_{pt} > 0.2$ no clear classification for β is obtained. Only, the HDK® C10P sample differs slightly.

The two obtained phase transition kinetics have also been measured for clay samples [177]. This suggests an universal character of the phase transition. However, an explanation of this effect would lead too far here but should be part of further investigations. Ruzicka et al. [177] did only vary the solids concentration when the transition from one regime to the other occured. According to the above made assumption, the same effect should be visible when either the concentration or the specific surface area is changed in the experiments. However, the diagram shows a more complex correlation. Seemingly, the main influence has to be attributed to the ionic strength of the suspension. All samples with $I_s = 0.03$ M show a relatively slower kinetic. Due to the stronger repulsion of the aggregates at lower ionic strength, the agglomeration of pyrogenic silica aggregates is hindered. As reported by Sandkühler et al. [174] this step determines the speed of the total gelation process because the interconnection step is faster by far. The same assertion holds true for the two samples of HDK® V15 at $I_s = 0.1$ M. The higher solids content causes a smaller inter-aggregate distance, thus, agglomeration is enhanced simply by the shorter diffusion paths. However, the formation of two kinetic groups remains to be explained.

Summarizing, it can be concluded that the analysis of time-series of DLS measurements enables the observation of dynamic processes such as a solid-liquid phase transition. Using the approach of Ruzicka et al. [177] it is possible to determine the phase transition time and the kinetic of the solidification. In technical applications the method may be used to detect the onset of sample alterations so that a shelf-life control can be achieved. For this purpose it is not necessary to keep the samples in the DLS instrument. They may just be stored as usual and only measured in distinct periods. Of course, the influence of storage temperature should be accounted for in the measurement settings.

The experiments conducted here reveal the total available particle surface area and the ionic strength of the suspension to be significant factors that affect the phase transition time. To explicitly explain the underlying mechanisms of the gelation of pyrogenic silica further investigations are necessary. The model of Sandkühler et al. [174] offers a good starting point as the two step scenario is represented in the phase transition kinetics. Continuative experiments should include variations of the solids content[1] as the HDK® V15 results show that an alteration may

[1] This parameter is, however, limited as already pointed out in Chap. 8.1.1.

lead to different kinetics. Additionally, the two transition groups have to be verified by conducting measurements in samples with ionic strengths > 0.1 M so that finally the universal behavior of phase transitions can be validated or vitiated.

8.2 Determination of Contaminations by Coarse Particles

8.2.1 Purity Requirements in Colloidal Suspensions

Technical applications involving colloidal material systems often require a high purity of the product. The term *purity* in this context does not only apply to chemical substances such as e.g. precursors in sol-gel processes but particularly to unwanted coarse particles (normally particles > 1 µm are called coarse in these applications) since they affect the product properties in a negative manner. Examples are the disturbance of the generation of colloid crystals, the alteration of gloss and opacity of pigment dispersions or paper coatings and the perturbation of self-organizing colloidal layers.

Another important process that probably raises the highest purity requirements to this time is Chemical-Mechanical Planarization (CMP). It is chiefly used in the microelectronics and optics industry to achieve planar surfaces (e.g. on integrated circuits or mirrors) with tolerances in the range of a few nanometers. The occurrence of unwanted coarse particles in the suspensions used for the CMP process leads to defects on the surfaces such as micro-scratches and gouges. These in turn impair the functionality of the product. Kuntzsch [163] showed that the defects can be related to the content of coarse contaminants and hard agglomerates of the colloidal particles. With continuing reduction of the average feature size (currently (2006) 65 nm, the next steps are 45 nm (announced for mid 2007), 32 nm, ...) the purity requirements will even increase, the term *coarse* may then already apply to particles > 100 nm.

Current control of coarse particle fractions is carried out using single particle counters and eventually DLS techniques [163]. Particle counters have a high sensitivity to particles > 1 µm but bear some intrinsic disadvantages. As only one particle may be present in the measurement volume to be counted, the suspensions mostly need to be diluted which may lead to a destabilization of a CMP slurry. The measured number of coarse particles is, therefore, difficult to

interpret. The measurement principle can on the other hand not be extended down to sizes of 100 nm for unwanted particles. The scattering of light by particles being of the same size as the wavelength of light hampers the measurement.

DLS on the other hand measures diffusion coefficients of the whole particle ensemble in the measurement volume. The contributions of only a few coarse particles to the ensemble average diffusion coefficient or the polydispersity index in a second cumulants analysis is minimal. Thus, in the practical applications suspensions deviating just one or two nanometer in the harmonic mean particle size from the standard are considered to be suspicious in principle. However, to this time neither the sensitivity of the common data analysis techniques to coarse particles has been thoroughly investigated nor have other analyses been developed specifically for this purpose. Therefore, this task will be treated in the present chapter.

8.2.2 Current Possibilities of DLS Data Analysis

To quantify the measurable impact in a HDK® slurry using standard analysis algorithms (cumulants and inversion techniques), the amount of coarse particles needs to be known from preparation. Therefore, a suspension of HDK® S13 (which is the standard grade for preparing CMP slurries) was doped with different fractions (ranging from $\varphi = 10^{-5}, \ldots, 10^{-1}$) of a monodisperse spherical silica sol (Geltech 1500, LightPath Technologies Inc., Orlando, USA) with a size of 1.45 micron. Both powders were dispersed in advance and counterionic stabilized at pH 9 (KOH) and $I_s = 0.001$ M (KNO_3). The doping was then conducted using mother solutions of HDK® S13 ($\varphi = 2.40$ v.-%) and of GT1500 ($\varphi = 1.0$ v.-%) to finally obtain a suspension of $\varphi_{\text{total}} = 0.02$. These samples were then measured in the HPPS.

Fig. 8.5 shows the results of the cumulants analysis of the doped suspensions. A mean value and standard deviation has been computed from the results of the 12 single runs. It can be readily obtained from the diagrams that although x_{DLS} as well as *PDI* begin to increase at $\varphi_{\text{doped}} = 3 \cdot 10^{-3}$ an unambiguous proof of the existence of coarse particles can only be evidenced for $\varphi_{\text{doped}} > 1 \cdot 10^{-1}$ due to the variance of the data. This is, however, unsatisfactory. In the application of CMP typically a purity in the ppm-region is required. This can clearly not be measured using DLS with cumulants analysis. Additionally, the results show that a small variation in the mean particle size can simply be due to random errors in the correlation function and is not indicative to coarse fractions in the sample.

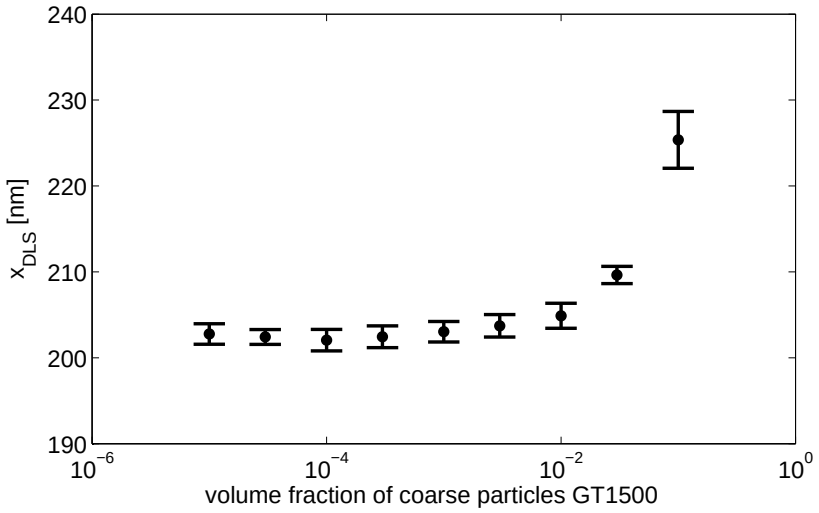

(a) Harmonic mean particle size x_{DLS}

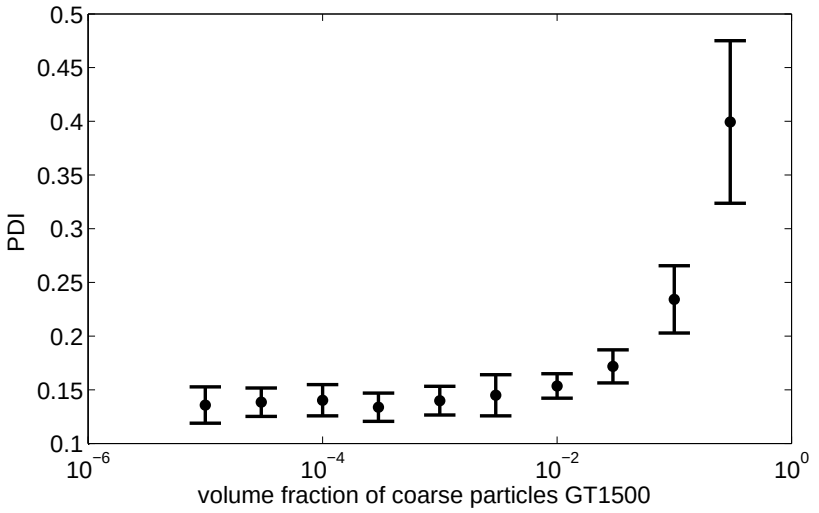

(b) Polydispersity index *PDI*

Figure 8.5: Sensitivity of second cumulants analysis (harmonic mean particle size (a) and polydispersity index (b)) to fractions of coarse particles of 1.45 micron in a suspension of HDK® S13.

An explanation of the obtained results can be given in view of the truncation of the autocorrelation function that is carried out before the fit of the second cumulants function (c.f. Chap. 2.3.2.1). In the present investigations, the standard 10 % cut-off was used (i.e. $g_2(\tau)/g_2(\tau = 0) = 0.1$). As coarse particles have a larger decay time than the main distribution they contribute to the ACF only at large lag times that are mostly neglected by the data cut-off. Thus, the measured insensitivity is inherent in this data analysis technique.

Inversion techniques do not use such an early cut-off of the correlation function. Thus, they

should be more sensitive to coarse particles in principle. Fig. 8.6 shows the obtained cumulative distributions of particle size for the differently doped suspensions.

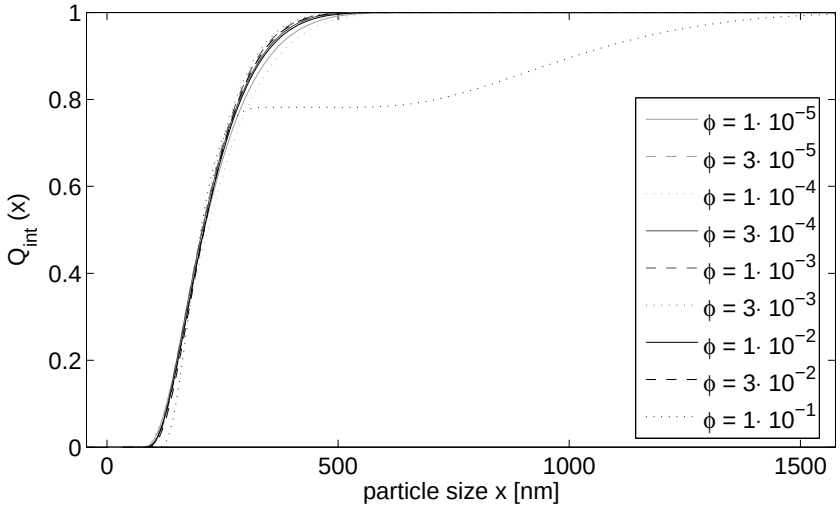

Figure 8.6: Sensitivity of an intensity-weighted cumulative size distribution obtained by non-linear regularization to fractions of coarse particles (GT1500) marked in the diagram in a suspension of HDK® S13.

However, the same result as for cumulants analysis is obtained. Even worse, for $\varphi_{\text{doped}} < 0.1$ no trend is obtained and all distributions look similar in the range of uncertainty introduced by the inversion. It has to be concluded that the principle of parsimony used to constrain the possible solutions in the inversion process rather neglects small fractions of coarse particles than to produce a multi-modal distribution. In the literature a typical statement is that regularization procedures are able to distinguish between two different modes when the size of the larger mode is at least twice the size of the smaller mode [1, 6]. However, these results have been obtained by mixing two monodisperse samples. In the measurements conducted here, the smaller peak shows a non-negligible distribution width. Therefore, a multimodal solution becomes even more unlikely. Additionally, in the investigations mentioned above the necessary portion of the larger peak to be distinguished has not been examined.

Summarizing, it has to be stated that the currently available data analysis algorithms in commercial DLS instruments do not provide a sensitive measure on unwanted fractions of coarse particles in a colloidal suspension. The situation changes when the main distribution is shifted to smaller sizes, since the difference in scattered intensity is increased. Thus, a colloidal sol of 20 nm in size might be controlled using the above mentioned analyses but they will never become available for suspensions of pyrogenic aggregates.

8.2.3 A New Approach - Principal Components

8.2.3.1 Principle

Up to this time, the whole correlation function has been analyzed to get information on unwanted coarse particles. As already stated in the last section, they mostly have an influence at large lag times, i.e. at the long time tail of the decaying ACF. Thus, the sensitivity can be increased for an analysis that treats specifically this region.

In a technical application slurries are produced each day from different charges of pyrogenic silica powders. In most cases, the product is good, i.e. it does not contain significant fractions of coarse particles and thus the CMP process works as usual. Only in some lots unwanted fractions occur. These have to be recognized and rejected. In the end this scenario means that it is possible to use *known-good* products and their measurement results as reference data. Then, every new product can be compared to the reference to check for significant alterations in the ROI, e.g., of the correlation function.

In Chap. 7.3.1.1 principal components analysis has been used to conduct a principal axes transformation in the correlation functions to highlight small differences between suspension data that are due to concentration effects. However, the same principle may be used to check for changes between different ACF's that are due to unwanted fractions in the product. Fig. 8.7 compares the resolution of the long-time tail of an ACF in the standard representation and after undergoing a principal axes transformation for a suspension of HDK® S13. The PCA enables a better representation of the ROI also in the case of the long-time tail. An additional existence of coarse fractions should result in a shift of the relative maximum marked in Fig. 8.7(a) to lower values. This can then be used for a comparison to reference data.

8.2.3.2 Simulations

Before an analysis method based on principal components can be implemented, it should be known which improvement in sensitivity can be achieved. Therefore, field correlation functions of a mixture of two particle fractions resembling HDK® S13 and a typical spectrum of unwanted coarse particles have been computed. Tab. 8.2 gives the simulation input data. The computation of the FCF is straightforward and follows an integration scheme described elsewhere [6].

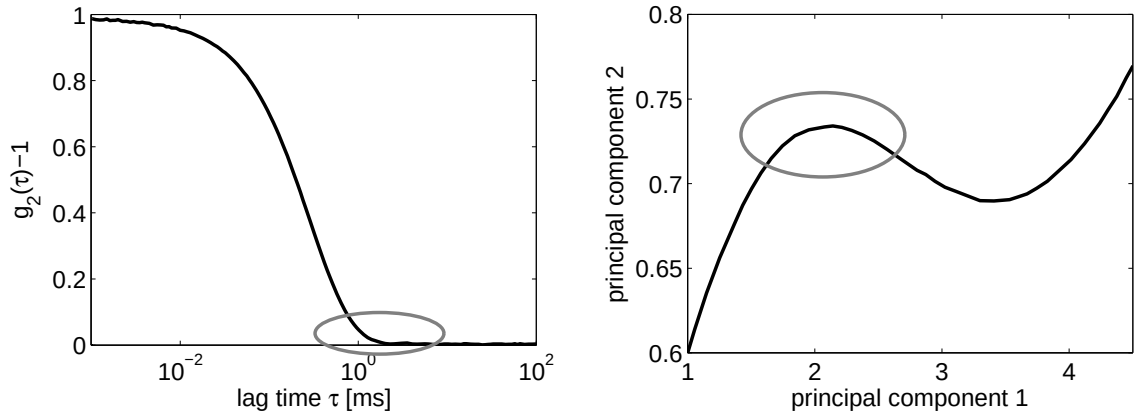

(a) (b)

Figure 8.7: Transformation of the long-time tail of the autocorrelation function (a) indicative for coarse particle fractions of a HDK® S13. In (b) the principal axes transformation is shown. ROI marked in the diagrams.

Table 8.2: Input data for the computation of field correlation functions simulating an increasing fraction of coarse particles.

Parameters	Main Distribution	Coarse Particles
Distribution type	log-normal	log-normal
x_{50}	165	1500
σ_{ln}	0.3	0.3
intensity fraction	$1; 0.99999 \ldots 0.999$	$0; 1 \cdot 10^{-5} \ldots 1 \cdot 10^{-3}$

The transformation matrix was then determined from the FCF with $\varphi_{\text{doped}} = 0$ using the correlation data between $g_1(\tau) = 0.2$ and $g_1(\tau) = 0.05$ via a PCA as described in Chap. 7.3.1.1. As the components of the matrix do not change much for the doped FCF's, the same matrix has been used for the transformation of all functions to obtain a maximum comparability. Fig. 8.8 shows the transformed long-time tail of the correlation functions for the different simulated correlation functions. It is conceivable from the diagram that already at $\varphi_{\text{doped}} = 1 \cdot 10^{-4}$ a significant difference in the spectra can be distinguished.

However, up to this time the simulations have been conducted using ideal field correlation functions that only incorporate rounding errors from the computation of the FCF. In contrast, a measurement always involves errors consisting of electronic noise, finite detector area, imperfect alignment of the set-up and so forth. These will have an impact on the distinguishable

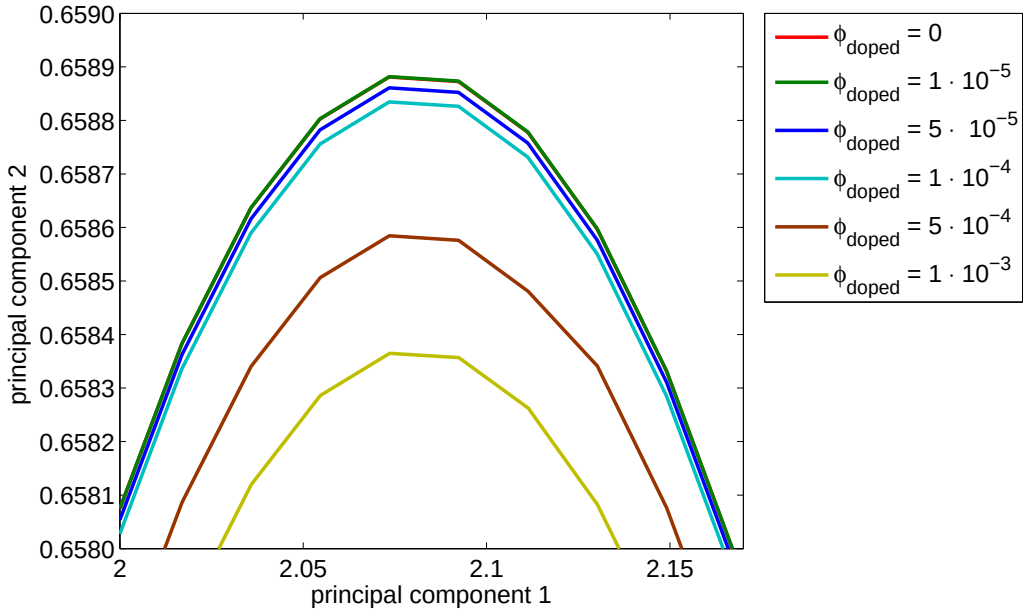

Figure 8.8: Transformed long-time tail of simulated field correlation functions with different amounts of coarse particle fractions.

portion of coarse particles. Fig. 8.9 shows the transformed long-time tail of simulated FCF's that have been superimposed with white noise (i.e. a random number with expectation value 0) with a standard deviation of 0.001.

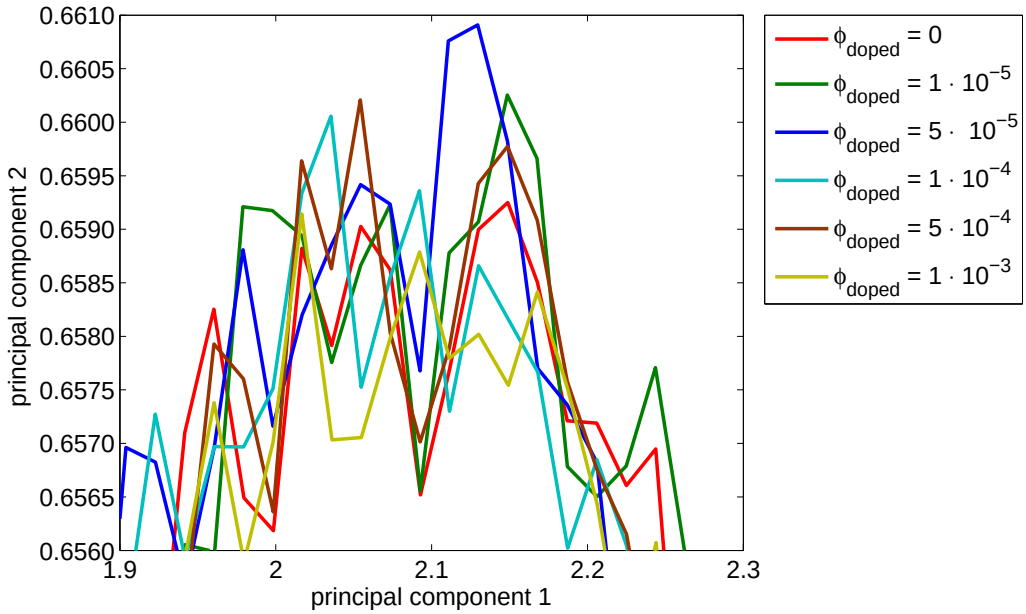

Figure 8.9: Transformed long-time tail of simulated field correlation functions superimposed with white noise (standard deviation 0.001) with different amounts of coarse particle fractions.

The clear correlation obtained above is lost when errors are introduced in the spectra. How-

ever, there still seems to be a shift of the maximum to smaller values of the second principal component with increasing coarse fractions. To reveal the possibilities of the principal axes transformation, now two further questions have to be answered:

- What is the noise level one is faced with in standard DLS experiments and how can it be influenced by the measurement parameters?

8.2.3.3 Determination of Random Error in Correlation Functions

The single data points in the autocorrelation function are obtained by simply multiplying intensity values that have a distinct lag time. The results are then averaged over the whole measurement run-time. Thus, in principle a data point at lag time τ is the average of t_{meas}/τ single values. From this point of view, the measurement error should rise with increasing lag time since there are less values measured in a single run. This thought additionally reveals two methods to minimize the measurement error. One is to prolong the run time of a single measurement, the other is to conduct multiple runs and average the correlation functions afterwards. If the errors in the correlation function would be statistically independent, then both methods should produce identical results.

To prove these theoretical considerations, measurements with diluted HDK® suspensions were conducted. As statistical confidence of the mean value and the standard deviation can only be obtained for a large number of measured correlation functions, overnight runs were established. The same sample was measured 200 times with the standard run-time of 90 s. Afterwards, the run-time was increased to 180 s and 360 s, respectively. To keep the total experiment duration comparable, only 100 and 50 runs, respectively, were conducted. This scheme was again set with the script programming language of the ALV correlator software.

From the data a mean correlation function as well as the standard deviation of each data point has been computed. Fig. 8.10 gives the results for different HDK® grades. This shows that the above made assumption of a noise standard deviation of 0.001 was a good estimate for the total ACF. Unfortunately, in the region of interest (i.e. for $g_2(\tau) - 1 < 0.1$) the standard deviation reaches a maximum value and keeps nearly constant afterwards. It is, however, interesting that although the total experiment time is the same for the three run times the random error is minimized when the duration of a single run is increased. This shows that the errors are not statistically independent which is an important feature in DLS measurements. A deeper

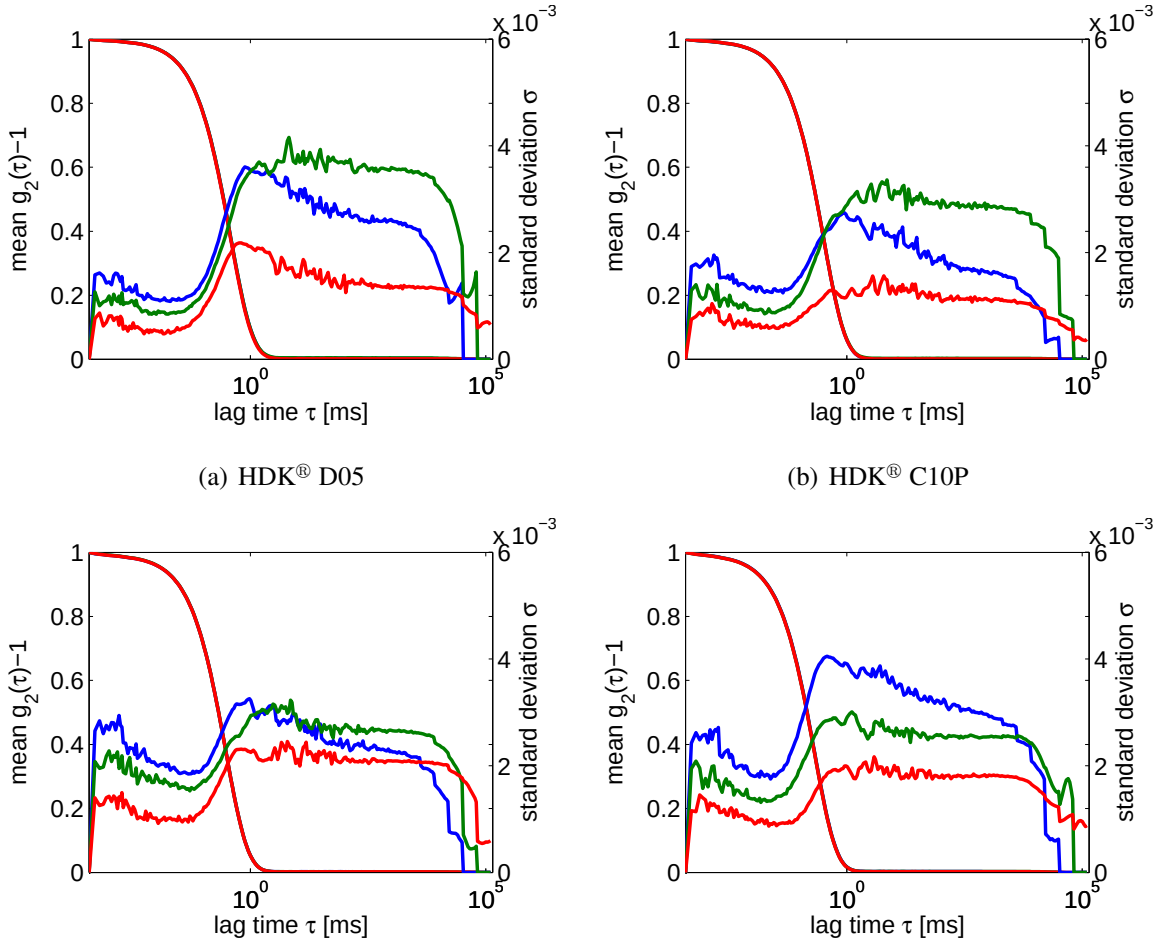

(a) HDK® D05

(b) HDK® C10P

(c) HDK® S13

(d) HDK® T30

Figure 8.10: Mean autocorrelation function (left y-axis) and standard deviation (right y-axis) computed from 200 single runs with 90 s duration (blue), 100 single runs with 180 s duration (green) and 50 runs with 360 s duration (red), respectively.

understanding of the error correlations is desirable in terms of the information content of the autocorrelation function but would lead too far in this context. It should therefore be subject to further investigations. For the purpose of quality control a simple but important conclusion can be drawn. If the sensitivity to coarse particle fractions in the spectrum shall be enhanced it is favorable to choose a long run time of the DLS measurement instead of averaging many short runs.

8.2.3.4 Doped Suspensions

Based on the simulations in Chap. 8.2.3.2 and on the error estimates made above a MATLAB® script named *Coarsealert* has been developed that incorporates the following:

1. Read the autocorrelation data (in ASCII files exported from the HPPS) of a reference suspension.

2. Read the autocorrelation data of the sample to be tested against the reference.

3. Perform a principal axes transformation as described in Chap. 7.3.1.1. The transformation matrix is kept constant in this procedure and has been chosen from the simulations.

4. In transformed coordinates the long-time tail occurs as a relative maximum. This is the ROI where coarse particles are most likely to contribute to the ACF's. Therefore, in the next step this relative maximum is sought.

5. In the vicinity of the maximum (currently -6 and $+8$ data points from the maximum optimized at the simulated data, i.e. $N_{\text{Data}} = 15$) the deviations of the measured ACF's have to be checked for statistically significant differences between reference and test data. For this purpose a Fisher F-test is used. For each single data point the variance of the second principal component of the reference values as well as the mean-square distance between the data points of the test ACF's and the mean of the reference is computed:

$$Var_1 = \sum_{i=1}^{N_{\text{Data, Ref}}} \left[\mathbf{PC}_{2,i} - \frac{1}{N_{\text{Data, Ref}}} \sum_{j=1}^{N_{\text{Data, Ref}}} \mathbf{PC}_{2,j} \right]^2 \tag{8.10}$$

$$Var_2 = \sum_{i=1}^{N_{\text{Data, Test}}} \left[\mathbf{PC}_{2,i} - \frac{1}{N_{\text{Data, Ref}}} \sum_{j=1}^{N_{\text{Data, Ref}}} \mathbf{PC}_{2,j} \right]^2 \tag{8.11}$$

$$F = \frac{Var_2}{Var_1} \tag{8.12}$$

The F value gives the relation between both terms and is compared to the F-distribution with a probability of rejection $p_r = 0.05$ and degrees of freedom $15 \cdot N_{\text{Test ACF's}}$ and $15 \cdot N_{\text{Ref ACF's}} - 15$.

6. If the F test variable is larger than the value obtained from the F-distribution the hypothesis that both data sets represent the same suspension must be rejected. If, additionally, the test ACF's show smaller second principal components than the reference a contribution of coarse particle fractions is likely. The script therefore generates an alert and plots the analyzed long-time tail for a visual inspection by the user. A probability of rejection of 5 % is the best alternative between the error of the first kind (i.e. accepting the hypothesis although coarse particle fractions are present) and second kind (i.e. rejecting the hypothesis although no significant coarse particle fractions are present) and is chiefly used in statistical data analysis.

Of course, a final decision on the rejection of the respective sample that produces an alert is still up to the user. This program at least enables another indicator that alleviates quality control together with the currently used methods such as particle counting.

The HDK® S13 suspensions doped with the monodisperse GT1500 particles as used in Chap. 8.2.2 have been applied to reveal the achievable differentiation of coarse particle amounts with the new approach. Fig. 8.11 shows the results of *Coarsealert*. The reference here was a HDK® S13 suspension without added GT1500.

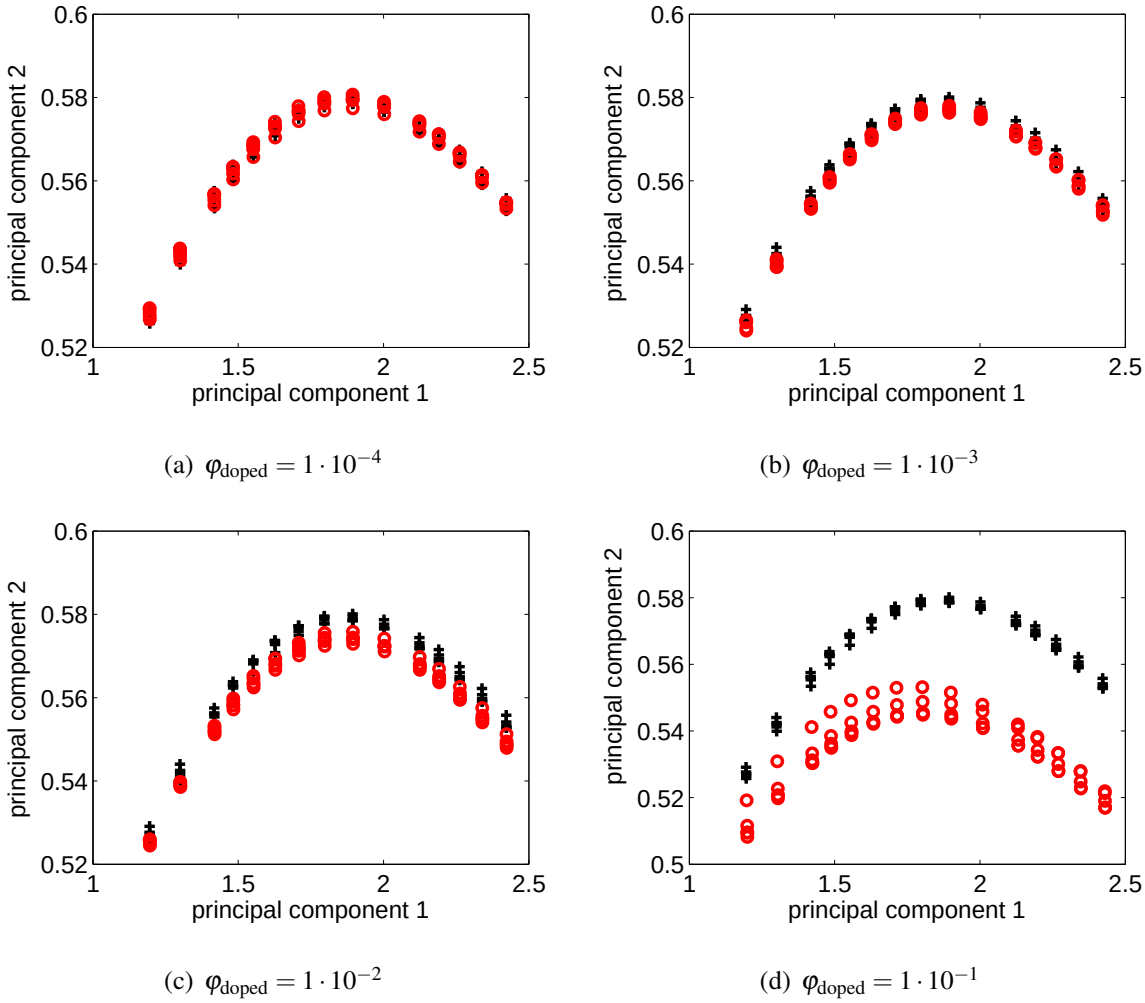

(a) $\varphi_{\text{doped}} = 1 \cdot 10^{-4}$

(b) $\varphi_{\text{doped}} = 1 \cdot 10^{-3}$

(c) $\varphi_{\text{doped}} = 1 \cdot 10^{-2}$

(d) $\varphi_{\text{doped}} = 1 \cdot 10^{-1}$

Figure 8.11: Transformed long-time tail of autocorrelation functions of a HDK® S13 doped with different fractions of coarse GT1500 particles (red circles) in comparison to a pure HDK® S13 suspension (black crosses). Fractions are marked in the subfigures.

Coarsealert produces an alert already at $\varphi_{\text{doped}} = 1 \cdot 10^{-3}$, the variance between test ACF's and the reference is significantly larger than the variance in the reference data. The same can be obtained by visual inspection, however, it is difficult to conclude a statistical significance

for the user. With this result, the method has been proven to successfully check colloidal suspensions for coarse particles. In comparison to the hitherto existing cumulants analysis and inversion techniques the sensitivity is enhanced by two orders of magnitude. This can also be obtained from Fig. 8.11 since at $\varphi_{\text{doped}} = 0.1$ (the recognizability limit of the standard analyses) already a visual inspection shows a very large difference between the reference and the test autocorrelation functions.

8.2.3.5 On-Road Test in Quality Assurance

The successful test at model doped suspensions shall now be transferred to an industrial application. Therefore, a test run was conducted together with Wacker-Chemie AG, Burghausen. Two commercially applied slurries of which the end-user had given a feedback that they are misbehaving in the CMP process (i.e. the wafers polished with these slurries showed an increased number of micro-scratches and gouges) underwent an overnight run where 240 ACF's were measured with a Zetasizer Nano (Malvern Instruments Ltd., Worcestershire, UK) which is the successor of the HPPS. Reference data were obtained from a retained sample that was *known-good* concerning the response of the end-user as well as all currently available characterization techniques. To include variances that may result from different measurement instruments the reference data were measured on two Zetasizer Nano. Fig. 8.12 shows the results of *Coarsealert*.

For the first sample a significant fraction of coarse particles is obtained while the second sample does not show any conspicuousness compared to the *known-good* slurry. Though the obtained result militates against the introduced method, it is qualitatively verified by the results of particle counting conducted at the slurry manufacturer. The first sample showed an increased large-particle-count while the second was within the required limits. This strengthens the significance of *Coarsealert*. However, the reason why slurry B was characterized as bad by the end-user remains an open question.

To further elucidate this question, overnight runs were as well conducted for the HDK® S13 suspensions that were the basis of the above mentioned slurries. Fig. 8.13 displays the results.

Again, the same principal effect is obtained. The deviation of sample A is even more pronounced for the HDK® suspensions. In view of these results it is quite assured that there are some unwanted fractions in sample A. On the other hand, for the second sample this conclusion

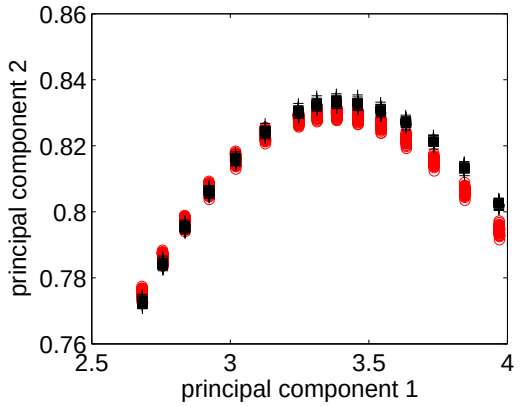

(a) CMP slurry A, *known-bad*, significance test positive

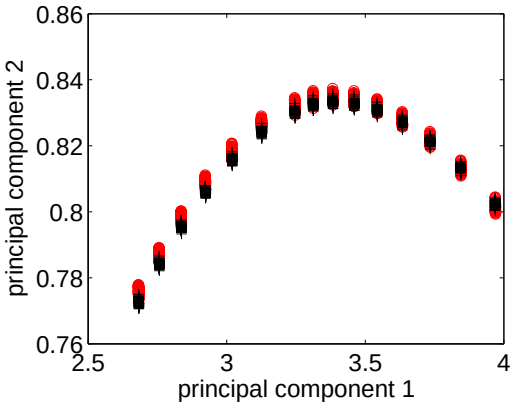

(b) CMP slurry B, *known-bad*, significance test negative

Figure 8.12: Transformed long-time tail of autocorrelation functions for two *known-bad* CMP slurries (end-user response) (red circles) in comparison to a *known-good* slurry (black crosses). In (a) *Coarsealert* produces an alert while in (b) the test ACF's fit nearly perfectly on the reference data.

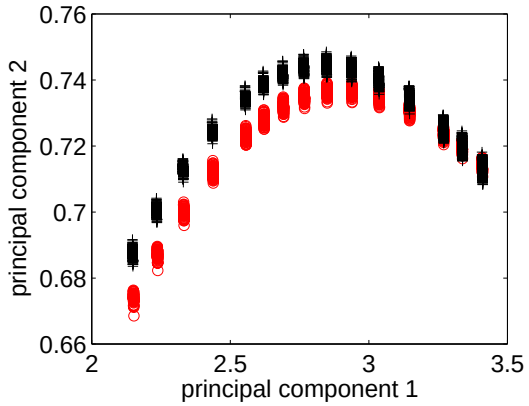

(a) HDK® suspension A, *known bad*, significance test positive

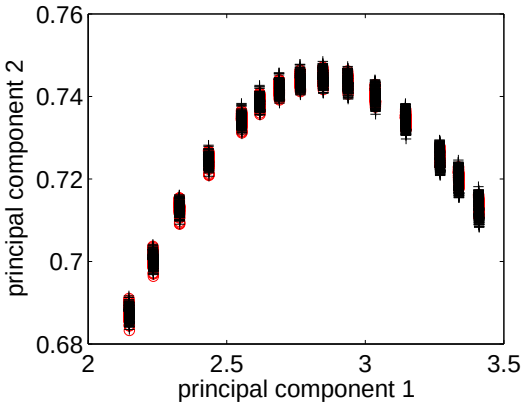

(b) HDK® suspension B, *known bad*, significance test negative

Figure 8.13: Transformed long-time tail of autocorrelation functions for two *known-bad* HDK® suspensions (end-user response of the manufactured CMP slurries) (red circles) in comparison to a *known-good* HDK® suspension (black crosses). In (a) an alert is produced while in (b) no significant contamination with unwanted coarse particles is obtained.

cannot be drawn. Possibly, coarse fractions were generated in the slurries after the manufacture. This is, however, speculative and cannot be proven from the current point of view.

Concluding, *Coarsealert* has proven its reliability in an industrial application. An increased

sensitivity to coarse particles can be certified as results of second cumulants analysis did not show significant increases, neither of x_{DLS} nor of the *PDI*. However, a warning needs to be given for the use of *Coarsealert*. When choosing a reference data set it is extremely important to check for a product that has undergone the same manufacturing steps as the test data. In Fig. 8.14 an example is shown where a HDK® suspension has been erroneously tested against a reference CMP slurry. Slurries are pretreated by depth filtration to remove coarse particles. The employed filter removal characteristics show that they also remove wanted particles from a HDK® suspension. Thus, both systems cannot be compared using *Coarsealert* since then the effect of filtration is measured instead of coarse particle fractions.

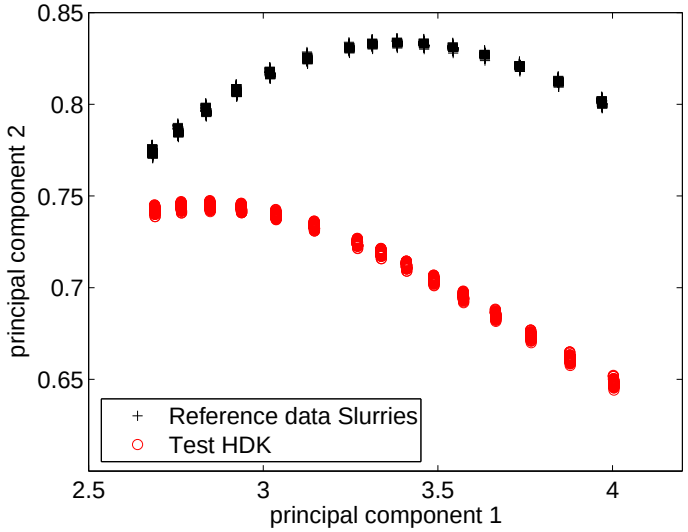

Figure 8.14: Effect of erroneously choosing a wrong reference data basis for *Coarsealert*. Here, a reference CMP slurry was used to be tested against a HDK® suspension.

8.3 Conclusions

The preceding sections show that DLS is not only a method to obtain distributions of diffusion coefficients or mean diffusion coefficients that may be used for particle sizing in dilute dispersions. If specific applications are to be considered customized data analysis techniques open up a variety of characterization tasks. The tracing of dynamic gelation processes and the detection of contaminations by coarse particles are only two examples that have been chosen due to their high relevance for industrial processes.

In gelling systems data pretreatment may be used to even neglect non-ergodic contributions in the scattering signal up to a certain level that hamper the principle of DLS. The constriction

of the analysis method to only a few parameters to be obtained from a single CFF enables the analysis of several thousands of single runs in an acceptable computation time. Using a model of Abou et al. [187] and Ruzicka et al. [177] the phase transition time and kinetics can be obtained that readily reveal the influence of suspension parameters such as solids concentration, ionic strength and specific surface area on the gelation process. However, the underlying mechanisms of the gelation process for pyrogenic silica still need to be explained in detail.

The control of suspension purity is an ever growing necessity in the application of colloidal suspensions. The applied principal axes transformation together with a Fisher F-test to reference measurements enables a product control that may be established alongside with the existing particle counting methods. The sensitivity in comparison to DLS standard analysis techniques is improved here by two orders of magnitude for suspensions of pyrogenic silica. Moreover, this sensitivity will even rise if the size of the main distribution is decreased as is the case for CMP slurries made from colloidal silica sols. Here, the increasing difference in scattered intensity between contaminants and product will possibly extend the recognizability to the ppm-region which should be verified in further investigations. Such advance finally implies that with ongoing decrease of feature size in the microelectronics industry, DLS may even replace particle counters as standard quality assurance measurement method.

9 Summary and Outlook

9.1 Results Recapitulation

The present thesis adresses the application of dynamic light scattering for the characterization of suspensions of polydisperse fractal materials. As an important and representative industrial example different grades of pyrogenic silica were used. This work pursued two main goals. The first was to give an understanding of the measured spectrum of diffusion coefficients in terms of the relation to the fractal structure of the aggregates and of the dependency on hydrodynamic and interparticle interactions in concentrated suspensions. The second goal was to develop application-based analysis schemes of the measured autocorrelation functions to extend the potential of DLS to industrially relevant applications. Concerning these issues five questions have been formulated at the beginning of this thesis. They will now be discussed consecutively.

The first question was, which geometrical property of a single pyrogenic silica aggregate determines the diffusional behavior. Computer simulations have been employed to generate virtual aggregates with defined structural properties and to study the hydrodynamic behavior of these aggregates. The choice of an adequate aggregate generation algorithm is crucial for the transferability of the simulation results to pyrogenic powders. In earlier investigations diffusion-limited cluster aggregation has been proposed as the best description of the production process of pyrogenic powders. As this Monte-Carlo simulation inherently involves a certain variability of the structural properties of the generated aggregates, a clear relation to hydrodynamics has not yet been achieved. In this work a new algorithm was developed that enables the generation of fractal aggregates with a predefined fractal dimension. This algorithm has been compared to a standard DLCA and another cluster generation algorithm for large clusters (CCA).

The total force and torque on an aggregate were determined by a multipole expansion of the Stokes equation around the generated aggregate with a no-slip boundary condition at the pri-

mary particles surfaces. From the eigenvalues of the translation and rotation matrix the respective diffusion coefficients and hydrodynamic radii could be calculated. It was a new result that the hydrodynamic radii of translation and rotation show a power law behavior similar to the structural radius of gyration but with a larger exponent (which represents the fractal dimension D_f^m for the radius of gyration). To account for this off-set the concept of a hydrodynamic dimension of rotation and translation, respectively, has been introduced. This simulation result is supported by experimental results in the literature for methods that determine such a power law behavior (rheometric and static scattering techniques). Finally, a general function relating the fractal dimension D_f^m to the hydrodynamic dimension D_f^h and the fractal prefactor k_f^h could be found. The Monte Carlo generation algorithms fit well within this relation so that it is now possible to determine the diffusional behavior from structural properties of a given aggregate.

Based on these simulation results it was examined to which degree the structural properties can be elicited in a conventional DLS experiment. This is the second question formulated in the introduction. Depending on the number of primary particles per aggregate and the fractal dimensions, the hydrodynamic radius determined with DLS should be of the order $(0.7\ldots1)\cdot R_g$. However, this relation only holds if contributions of rotational diffusion to the ACF can be neglected. Otherwise, due to the fast decay of rotational diffusion the mean decay rate is overestimated by $\sim 55-65\,\%$ as has been obtained by a consideration of the ratio $R_{h,t}/R_{h,rot} = (0.88\ldots0.95)$ in comparison to literature. The results obtained in the simulations therefore had to be verified by experiments revealing the structural and hydrodynamic properties of pyrogenic silica aggregates.

The radius of gyration and the fractal dimension were determined by SAXS and SLS, respectively. The hydrodynamic aggregate radii determined from multi-angle DLS (results extrapolated to $s = 0$) scale with the SLS radii of gyration (ratio $R_{h,t}/R_g$ between 0.787 and 0.987) which supports the simulation results (see above) for a DLCA-like generation mechanism. The fractal dimension ($D_f^m(\mathrm{SLS}) \approx 1.8$) gives an additional indication. However, the structural properties determined with SAXS differ remarkably from the SLS results. Since both methods measure at different ranges of the scattering vector this suggests that different details of the aggregate structure are observed. For SAXS, the strong sintering of primary particles at the beginning of the aggregation in the production process has been hypothesized to explain the large fractal dimensions measured at sub-structures of the aggregates.

The results of DLS show a strong angular dependence caused by influences of rotational diffu-

sion. If the ratio $D/D(s=0)$ is plotted versus the dimensionless structure size $s \cdot R_g$ pyrogenic silica grades form a master-curve if the primary particles in the aggregates are non-porous. Such a behavior had been predicted from the simulations, the maximum overestimate was roughly verified to be in the range of 60 %. This shows that the polydispersity of the primary particles and of the aggregate sizes does not influence the comparability of structural and diffusional analysis of pyrogenic silica. Thus, both simulations and experiments gave a valuable insight into the relation between structure and hydrodynamics and their impact on measurement results for polydisperse fractal systems.

The simulation and experimental study of the structure-diffusion-relationship were conducted for highly diluted suspensions of pyrogenic silica. A further question, which is of great relevance for industrial systems, is the influence of solids concentration on DLS results for fractal materials. Therefore, a comprehensive experimental investigation has been conducted. Firstly, a principal axes transformation of the autocorrelation function was used to enable a fast comparison of measured ACF's for occurring interaction effects. This is an important prerequisite for data analysis. The method does not require any a priori information, what makes it particularly suitable for routine analyses.

A detailed comparison of concentration series in mono- and polydisperse silica sols and pyrogenic silica suspensions then highlighted the origin of the interaction effects that have an impact on the measured autocorrelation functions. The mean diffusion coefficient obtained by a second cumulants analysis generally decreases with increasing concentration for pyrogenic silica. Another influencing factor is the specific surface area of the pyrogenic silica grade. A scaling of the decrease in diffusivity was tested, which accounts for the porous structure of the aggregates using an effective volume fraction. Due to the uncertainties introduced in the determination of the aggregate porosities the validity of this scaling law could not be proven.

Hence, it became necessary to consider the whole distribution of diffusion coefficients determined by an inversion of the measured ACF's. In monodisperse sols the effects of the measured diffusion regime (i.e. self- or collective diffusion), of hydrodynamic hindering and of the structuring of the suspension by counterionic repulsion could be clearly distinguished as different modes in the distribution function. For polydisperse sols these effects cannot be separated in the experimental data and occur over a larger concentration range but are the same in principal. Counterionic stabilized pyrogenic silica suspensions are expected to behave similarly to polydisperse sols. Indeed, at large concentrations pyrogenic silica aggregates are hindered in

their mobility by hydrodynamic constriction and multi–body repulsion. Thus, a second peak accounting for long-time diffusion coefficients is measured with DLS that gets more pronounced when the range of the counterionic repulsion is extended. For high surface area grades a third peak occurs that can be associated with collective diffusion of smaller aggregates. This finally concludes that the measured distribution of diffusion coefficients is no longer a single aggregate property but reflects the state of the whole suspension including aggregate sizes and their distribution, solids concentration, pH and salinity.

If the counterionic repulsion is screened pyrogenic silica suspensions form gels at a high enough solids concentration. Thus, another question was the observation of the gelation process with DLS. This facilitates the determination of the phase transition time which is the most important process variable. DLS is best suited for this purpose as it offers a non-intrusive measurement. Within this thesis DLS was used the first time to observe phase transitions for pyrogenic silica. Consecutively measured ACF's were converted to correlation functions of the fluctuation field to neglect non-ergodic contributions in the measurement signal. An automated fit procedure based on a literature approach then gave the phase transition time and the transition kinetic. Important parameters influencing the total phase transition time are the total available surface area of the particles in suspension (i.e. either varied by the solids content or the specific surface area) and the ionic strength of the suspension as it controls the screening of the stabilizing repulsive interparticle forces. The two obtained kinetic regimes that also occur for clay suspensions finally suggest a universal behavior of phase transitions, which, however, has to be further substantiated.

A further point to be discussed is the determination of coarse particle fractions in the measured spectrum since this control of suspension purity is of great relevance for many colloidal systems. By conducting experiments with a HDK® suspension doped with coarse silica spheres it was shown that the commonly applied data analysis techniques, second cumulants and inversion, are not sensitive to such contaminations (minimum detectable coarse fraction ≈ 10 %). The sensitivity can, however, be enhanced by two orders of magnitude (≈ 0.1 %) by applying a principal axes transformation of the long-time tail of the autocorrelation function together with a Fisher F-test of the deviations of a test sample to a reference sample. This enables a product quality control that gives precious additional information on contaminations in colloidal suspension besides the hitherto mostly used particle counting techniques. This has been verified in an on-road test of slurries for Chemical-Mechanical Planarization.

9.2 Implications for the Technical Application of DLS for Fractal Materials

The results summarized in the previous section will now be discussed with regard to their relevance for product development and quality assurance of polydisperse fractal aggregates such as pyrogenic silica. Typical objectives of suspension characterization are:

1. Control of hydrodynamic particle size and state of dispersion. Typically, measurements in diluted suspensions are carried out for this purpose.
2. Control of the suspension state in concentrated dispersions.
3. Shelf-life control of suspensions. Check for alterations that may lead to a solidification over time of storage. A contrary goal of product development might be a fast gelation of the final product.
4. Control of suspension purity in terms of coarse particle contaminations.

For all these goals, a high precision and repeatability of the DLS autocorrelation data is necessary. As obtained in this work it is therefore better to prolong the run time of a single run than to conduct multiple runs of short lengths. This minimizes random error contributions. Additionally, the statistics at the same run time are better for large scattering angles as this shifts the decay of the ACF to smaller lag times.

Concerning point 1 it has to be stated that a neglect of contributions of rotational diffusion is justified only by using very small scattering angles for pyrogenic aggregates with sizes of $100-500$ nm. The determined effective hydrodynamic radius in all other measurement set-ups reflects translational as well as rotational contributions and is, therefore, always smaller than the hydrodynamic radius of translation. However, this is not necessarily a drawback for quality assurance purposes as it enables the detection of deviations in size as well as in structure of the aggregates with a single measurement, though it should be kept in mind.

In concentrated suspensions the measurement results of DLS only remain unambiguous if additionally the solids concentration, pH and amount and type of added electrolyte are controlled. The principal axes transformation may be used in advance of any data analysis algorithm to check for concentration influences.

The developed strategy of analyzing time-series of DLS measurements can be readily applied to a shelf-life control when the measurement temperature is set to the storage temperature. It has to be noted, however, that an analysis of the ACF may include non-ergodic contributions so that the decomposition in the CFF is advised. The developed analysis scheme may then be used to detect the onset of an occurring phase transition. The property that may be best used to control the speed of solidification is the ionic strength of the suspension medium.

In view of the control of suspension purity the developed program *Coarsealert* may be used as an additional indicator. Though it does not reach the required ppm-sensitivity for pyrogenic silica, it gives another clue whether coarse particle fractions are present in a suspension.

9.3 Proposal for Future Investigations

Based on the results acquired in this thesis suggestions for further research may be deduced that can be divided into two general groups:

- Theory and simulations
- Continuative experiments

In the simulations conducted here, possibly the largest restraint was the limitation to non-sintered primary particles in the aggregates since the no-slip condition at the surface may not be described analytically for sintering. Thus, in the future either a discretization of the surface combined with a numerical solution of the Stokes equation (via DEM or CFD) has to be sought or sintered particles have to be represented by analytically describable bodies such as rotating epicycloids. Another simulation method to be used could be the Lattice Boltzmann simulation method developed by Binder et al. [160].

Further, as obtained from the static scattering experiments, the structure of pyrogenic aggregates may vary when they are viewed from different length scales (i.e. scattering vectors). A decreasing sintering factor of the aggregates has been hypothesized as they grow and move towards lower flame temperatures. Thus, the DLCA algorithm should be altered to use different sintering factors. The scattering behavior of the resulting aggregates should then be computed and compared to static scattering results.

This in turn requires that a scattering profile of pyrogenic silica should be measurable without a gap in the scattering vector range. Therefore, USAXS measurements are proposed. Though, these are quite laborious and expensive, it is the only available technique covering the whole necessary range for pyrogenic silica aggregates.

The primary goal of these investigations is to further elucidate the structure of pyrogenic aggregates and their origin from the production process. For an improvement in the relation to the DLS measurements, also an extension of the measurable angular range is suggested for a more precise determination of the hydrodynamic radii of translation and the influence of rotational diffusion. Amendatory computations of this impact compared to hitherto existing literature models with the use of the developed fixed-structure model aggregates are desirable to highlight the influence of structure on the contribution of rotational diffusion to DLS results.

In concentrated suspensions a theoretical treatment is not likely to become available in the near future. Therefore, the experimental framework should be further substantiated. The effective volume fraction approach shall not be dismissed but a more exact determination of the aggregate porosities should be sought. Also a differentiation between the impact of hydrodynamic and interparticle interactions would be beneficial. This will possibly provide further insight into the diffusional behavior of pyrogenic silica and their respective rheological behavior. However, mostly interparticle interactions may not be suppressed since this would destabilize the suspensions. Steric stabilization (e.g. with adsorbed short polymer chains) has only a limited range of a few nanometers, so this can possibly be used as a reference.

In gelling pyrogenic silica suspensions investigations are necessary to explain the underlying mechanisms. Based on literature models the phase transition kinetics should be further examined by varying the solids content and adding more data points for different ionic strengths of the suspensions. Finally, the universality of phase transitions can also be proven by using further material systems.

Concerning the sensitivity of DLS measurements for coarse particles, experiments should be conducted for differently doped CMP slurries consisting of colloidal silica sols. As the size of these sols is much smaller than for pyrogenic silica aggregates the difference in scattered intensity to coarse contaminants is drastically increased so that the sensitivity of the developed program *Coarsealert* should be enhanced.

9.4 Conclusion

The examination of the diffusional behavior of colloidal particles in suspension with dynamic light scattering techniques spans a multitude of characterization tasks. In this thesis the specific application to polydisperse fractal systems was treated by the example of pyrogenic silica suspensions.

In diluted samples it is possible to reveal information on the structure of the fractal aggregates in terms of their translational and rotational diffusion though it is at the moment not possible to distinguish between both effects at an arbitrary scattering angle.

The development of measurement instruments that may physically suppress the contributions of multiple scattering has enabled experiments in concentrated suspensions of up to 15 wt.-% for pyrogenic silica. Here, DLS does not only measure a single aggregate or particle property but the behavior of the whole suspension under consideration since the measured spectra of diffusion coefficients are influenced by hydrodynamic and interparticle interactions that are in turn dependent on suspension properties such as pH and ionic strength.

Thus, DLS techniques are best suited for measurement tasks that deal with the characterization of the size distribution and the suspension structure of colloidal suspensions. It was shown in this thesis that the specific structural properties of polydisperse fractal materials such as pyrogenic silica can be measured with good resolution for the requirements of industrial quality assurance or product development. Specific applications then necessitate the development of new data analysis algorithms for the interpretation of the correlation functions as was successfully realized in this thesis for the observation of gelation processes and for the detection of coarse contaminants.

References

[1] Finsy, R.: Particle sizing by quasi-elastic light scattering. *Adv. Colloid Interface Sci. 52* (**1994**), 79–143.

[2] Müller, R.H.; Schuhmann, R.; Thode, K.: *Teilchengrößenmessung in der Laborpraxis (Particle size analysis in laboratory practice)*. Wissenschaftliche Verlagsgesellschaft mbH, Stuttgart, **1996**.

[3] ISO 13321: *Particle Size Analysis: Photon Correlation Spectroscopy*. International Standard, Beuth-Verlag, Berlin, **1996**.

[4] Mazo, R.M.: *Brownian Motion: Fluctuations, Dynamics and Applications*. No. 122 in International Series of Monographs on Physics, Oxford University Press, Oxford, **2002**.

[5] Xu, R.: *Particle Characterization: Light Scattering Methods*. Particle Technology Series, Kluwer Academic Publishers, London, **2000**.

[6] Kätzel, U.: *Analyse von Partikelgrößenverteilungen mit Hilfe der Photonenkorrelationsspektroskopie (Analysis of particle size distributions by means of photon correlation spectroscopy)*. Student Project, TU Dresden, **2003**.

[7] Irwin, C.L.: Carbon products for industrial cross-cut technologies. *Presentation: U.S. DOE Office of Industrial Technologies 2nd Industrial Energy Efficiency Symposium and Expo*, Feb. 24-26, Arlington, Virginia, USA, **1997**.

[8] Kammler, H.K.; Mädler, L.; Pratsinis, S.E.: Flame synthesis of nanoparticles. *Chem. Eng. Technol. 24*, 6 (**2001**), 583–596.

[9] Flörke, O.W.; Graetsch, H.; Brunk, F.; Benda, L.; Paschen, S.; Bergna, H.E.; Roberts, W.O.; Welsh, W.A.; Chapman, D.M.; Ettlinger, M. et al.: Silica. In *Ullmann's Ency-*

clopedia of Industrial Chemistry, edited by Pelc, H.; Elvers, B.; Hawkins, S., 7th edn., Wiley-VCH, Weinheim, **2005**, pp. 57–64, doi:10.1002/14356007.a23583.

[10] DIN 53206-1: *Prüfung von Pigmenten; Teilchengrößenanalyse, Grundbegriffe (Testing of pigments; particle size analysis, fundamental terms)*. German Standard, Beuth-Verlag, Berlin, **1972**.

[11] Batz-Sohn, C.: Particle sizes of fumed oxides: A new approach using PCS signals. *Part. Part. Syst. Charact. 20* (**2003**), 370–378.

[12] Fabry, L.; Hoelzl, R.; Kotz, L.; Ehmann, T.; Barthel, H.; Goldstein, M.; Stintz, M.: Monocrystalline silicon under controlled CMP process conditions. *Lecture: NSF/SRC and JSPE Planarization & CMP Technical Committee (Part 1) Conference*, San Francisco, July 14, **2004**.

[13] Leschonski, K.: Particle size analysis and characterization of a classification process. In *Ullmann's Encyclopedia of Industrial Chemistry*, edited by Pelc, H.; Elvers, B.; Hawkins, S., 7th edn., Wiley-VCH, Weinheim, **2005**, doi:10.1002/14356007.b02_02.

[14] Pahl, M.; Schädel, G.; Rumpf, H.: Zusammenstellung von Teilchenformbeschreibungsmethoden (Compilation of particle shape description methods). *Aufbereit. Techn. 14*, 5 (**1973**), 257–264.

[15] Heywood, H.: Numerical definitions of particle size and shape. *Chem. Ind. 15* (**1937**), 149–154.

[16] Wadell, H.: Volume, shape and roundness of rock particles. *J. Geol. 40* (**1932**), 443–451.

[17] Mandelbrot, B.B.: *The Fractal Geometry of Nature*. W.H. Freeman, New York, **1982**.

[18] Richardson, L.F.: The problem of contiguity: an appendix of statistics of deadly quarrels. *Gen. Syst. 6* (**1961**), 139–187.

[19] Chan, L.C.Y.; Page, N.W.: Boundary fractal dimensions from sections of a particle profile. *Part. Part. Syst. Charact. 14* (**1997**), 67–72.

[20] Schaefer, D.W.; Hurd, A.J.: Growth and structure of combustion aerosols. *Aerosol Sci. Technol. 12* (**1990**), 876–890.

[21] Bugnicourt, E.; Galy, J.; Gérard, J.F.; Boué, F.; Barthel, H.: Structural investigations of pyrogenic silica - epoxy composites by small-angle neutron scattering and transmission electron microscopy, **2006**. Submitted for publication.

[22] Veerapaneni, S.; Wiesner, M.R.: Hydrodynamics of fractal aggregates with radially varying permeability. *J. Colloid Interface Sci. 177* (**1996**), 45–57.

[23] Robert, C.P.; Casella, G.: *Monte Carlo Statistical Methods*. Springer-Verlag, Berlin, **2004**.

[24] Lattuada, M.: *Aggregation Kinetics and Structure of Gels and Aggregates in Colloidal Systems*. Ph.D. thesis, ETH Zürich, **2003**.

[25] Sandkühler, P.; Lattuada, M.; Wu, H.; Sefcik, J.; Morbidelli, M.: Further insights into the universality of colloidal aggregation. *Adv. Colloid Interface Sci. 113*, 2-3 (**2005**), 65–83.

[26] Asnaghi, D.; Carpineti, M.; Giglio, M.; Sozzi, M.: Coagulation kinetics and aggregate morphology in the intermediate regimes between diffusion-limited and reaction-limited cluster aggregation. *Phys. Rev. A 45* (**1992**), 1018–1023.

[27] Schaefer, D.W.: Fractal models and the structure of materials. *Mat. Res. Soc. Bull. 13*, 2 (**1988**), 22–27.

[28] Meakin, P.: Computer simulation of growth and aggregation processes. In *On Growth and Form: Fractal and Non-Fractal Patterns in Physics*, edited by Stanley, H.E.; Ostrowsky, N., NATO Science Series E, Martinus-Nijhoff, Boston, **1986**, pp. 111–135.

[29] Witten, T.A.; Sander, L.M.: Diffusion-limited aggregation, a kinetic critical phenomenon. *Phys. Rev. Lett. 47* (**1981**), 1400–1403.

[30] Witten, T.A.; Sander, L.M.: Diffusion-limited aggregation in three dimensions. *Phys. Rev. B 27* (**1983**), 5686–5697.

[31] Sander, L.M.; Cheng, Z.M.; Richter, R.: Diffusion-limited aggregation in three dimensions. *Phys. Rev. B 28* (**1983**), 6394–6396.

[32] Meakin, P.: Formation of fractal clusters and networks by irreversible diffusion-limited aggregation. *Phys. Rev. Lett. 51*, 13 (**1983**), 1119–1122.

[33] Kolb, M.; Botet, L.; Jullien, R.: Scaling of kinetically growing clusters. *Phys. Rev. Lett. 51*, 13 (**1983**), 1123–1126.

[34] Meakin, P.; Wasserman, Z.R.: Some universality properties associated with the cluster cluster aggregation model. *Phys. Lett. A 103*, 6-7 (**1984**), 337–341.

[35] Jullien, R.; Kolb, M.: Hierarchical model for chemically limited cluster cluster aggregation. *J. Phys. A 17*, 12 (**1984**), L639–L643.

[36] Brown, W.D.; Ball, R.C.: Computer-simulation of chemically limited aggregation. *J. Phys. A 18*, 9 (**1985**), L517–L521.

[37] Weitz, D.A.; Lin, M.Y.: Dynamic scaling of cluster-mass distributions in kinetic colloid aggregation. *Phys. Rev. Lett. 57*, 16 (**1986**), 2037–2040.

[38] Ball, R.C.; Weitz, D.A.; Witten, T.A.; Leyvraz, F.: Universal kinetics in reaction-limited aggregation. *Phys. Rev. Lett. 58*, 3 (**1987**), 274–277.

[39] Lin, M.Y.; Lindsay, H.M.; Weitz, D.A.; Ball, R.C.; Klein, R.; Meakin, P.: Universality in colloid aggregation. *Nature 339* (**1989**), 360–362.

[40] Lin, M.Y.; Lindsay, H.M.; Weitz, D.A.; Klein, R.; Ball, R.C.; Meakin, P.: Universal diffusion-limited colloid aggregation. *J. Phys.: Condens. Matter 2*, 13 (**1990**), 3093–3113.

[41] Liu, J.; Shih, W.Y.; Sarikaya, M.; Aksay, I.A.: Fractal colloidal aggregates with finite interparticle interactions: Energy dependence of the fractal dimension. *Phys. Rev. A 41*, 6 (**1990**), 3206–3213.

[42] González, A.E.: Universality of colloid aggregation in the reaction limit: The computer simulations. *Phys. Rev. Lett. 71*, 14 (**1993**), 2248–2251.

[43] Gimel, J.C.; Durand, D.; Nicolai, T.: Transition between flocculation and percolation of a diffusion-limited cluster-cluster aggregation process using three-dimensional monte carlo simulation. *Phys. Rev. B 51*, 17 (**1995**), 11348–11357.

[44] Gimel, J.; Nicolai, T.; Durand, D.: 3d monte carlo simulations of diffusion limited cluster aggregation up to the sol-gel transition: Structure and kinetics. *J. Sol-Gel Sci. Techn. 15*, 2 (**1999**), 129–136.

[45] Iranipour, G.T.; Garcia-Rubio, L.H.; Harmon, J.P.: Modeling and simulation of aggregation processes in colloidal systems. *J. Disp. Sci. Technol. 25*, 4 (**2004**), 555–565.

[46] Sandkühler, P.: *Kinetics of Aggregation and Gel Formation in Colloidal Dispersions*. Ph.D. thesis, ETH Zürich, **2004**.

[47] Lindsay, H.M.; Klein, R.; Weitz, D.A.; Lin, M.Y.; Meakin, P.: Structure and anisotropy of colloid aggregates. *Phys. Rev. A 39*, 6 (**1989**), 3112–3119.

[48] Porod, G.: Die Röntgenkleinwinkelstreuung von dichtgepackten kolloiden Systemen. 1. Teil (X-ray low angle scattering of dense colloid systems. Part I.). *Kolloid-Z. 124* (**1951**), 83–114.

[49] Porod, G.: Die Röntgenkleinwinkelstreuung von dichtgepackten kolloiden Systemen. 2. Teil (X-ray low angle scattering of dense colloid systems. Part II.). *Kolloid-Z. 125* (**1952**), 51–57, 109–122.

[50] Beaucage, G.: Approximations leading to a unified exponential/power-law approach to small-angle scattering. *J. Appl. Cryst. 28* (**1995**), 717–728.

[51] Beaucage, G.: Small-angle scattering from polymeric mass fractals of arbitrary mass-fractal dimension. *J. Appl. Cryst. 29* (**1996**), 134–146.

[52] Guinier, A.; Fournet, J.: *Small-Angle Scattering of X-rays*. Structure of matter series, John Wiley & Sons, New York, **1955**.

[53] Barnes, H.A.; Hutton, J.F.; Walters, K.: *An Introduction to Rheology*. 1st edn., Elsevier Science Publishers, Amsterdam, **1989**.

[54] Gottschalk-Gaudig, T.: Viscoelastic properties of unsaturated polyester - styrene mixtures containing PDMS-treated pyrogenic silica, **2006**. Submitted for publication.

[55] Buscall, R.; Mills, P.D.A.; Goodwin, J.W.; Lawson, D.W.: Scaling behaviour of the rheology of aggregate networks formed from colloidal particles. *J. Chem. Soc. Faraday Trans. 1 84*, 12 (**1988**), 4249–4260.

[56] Wu, H.; Morbidelli, M.: A model relating structure of colloidal gels to their elastic properties. *Langmuir 17*, 4 (**2001**), 1030–1036.

[57] Shih, W.H.; Shih, W.Y.; Kim, S.I.; Liu, J.; Aksay, I.A.: Scaling behavior of the elastic properties of colloidal gels. *Phys. Rev. A 42*, 8 (**1990**), 4772–4779.

[58] Piau, J.M.; Dorget, M.; Palierne, J.F.; Pouchelon, A.: Shear elasticity and yield stress of silica–silicone physical gels: Fractal approach. *J. Rheol. 43*, 2 (**1999**), 305–314.

[59] Saint-Michel, F.; Pignon, F.; Magnin, A.: Fractal behavior and scaling law of hydrophobic silica in polyol. *J. Colloid Interface Sci. 267*, 2 (**2003**), 314–319.

[60] Khan, S.A.; Zoeller, N.J.: Dynamic rheological behavior of flocculated fumed silica suspensions. *J. Rheol. 37*, 6 (**1993**), 1225–1235.

[61] Yziquel, F.; Carreau, P.J.; Tanguy, P.A.: Non-linear viscoelastic behavior of fumed silica suspensions. *Rheol. Acta 38*, 1 (**1999**), 14–25.

[62] Kawaguchi, M.; Mizutani, A.; Matsushita, Y.; Kato, T.: Molecular weight dependence of structures and rheological properties for fumed silica suspensions in polystyrene solutions. *Langmuir 12*, 26 (**1996**), 6179–6183.

[63] van der Aerschot, E.; Mewis, J.: Equilibrium properties of reversibly flocculated dispersions. *Coll. Surf. 69*, 1 (**1992**), 15–22.

[64] Gmachowski, L.: Aggregate structure and hydrodynamics of aggregated systems. *Coll. Surf. A 255* (**2005**), 105–110.

[65] Gmachowski, L.: Estimation of the dynamic size of aggregates. *Coll. Surf. A 170* (**2000**), 209–216.

[66] Gmachowski, L.: Calculation of the fractal dimension of aggregates. *Coll. Surf. A 211* (**2002**), 197–203.

[67] Gmachowski, L.: Mass-radius relation for fractal aggregates of polydisperse particles. *Coll. Surf. A 224* (**2003**), 45–52.

[68] Gmachowski, L.: Hydrodynamics of dense arrangement of aggregates. *Coll. Surf. A 234* (**2004**), 103–107.

[69] Brinkman, H.C.: On the permeability of media consisting of closely packed porous particles. *Appl. Sci. Res. A1* (**1947**), 81–86.

[70] Hunter, R.J.: *Foundations of Colloid Science*, vol. 1. Oxford University Press, Oxford, **1993**.

[71] Elimelech, M.; Jia, X.; Gregory, M.; Williams, R.: *Particle Deposition and Aggregation: Measurement, Modelling and Simulation*. Colloid and Surface Engineering Series, Butterworth-Heinemann, Oxford, **1995**.

[72] Morrison, I.D.; Ross, S.: *Colloidal Dispersions: Suspensions, Emulsions and Foams*. John Wiley & Sons Inc., New York, **2002**.

[73] Dukhin, A.S.; Goetz, P.J.: *Ultrasound for Characterizing Colloids*, *Studies in Interface Science series*, vol. 15. Elsevier, Amsterdam, **2002**.

[74] Pusey, P.N.: Colloidal suspensions. In *Liquides, Cristallisation et Transition Vitreuse (Liquids, Freezing and the Glass Transition)*, edited by Hansen, J.P.; Levesque, D.; Zinn-Justin, J., North-Holland, Amsterdam, **1991**, pp. 763–942.

[75] Lewis, J.A.: Colloidal processing of ceramics. *J. Am. Ceram. Soc. 83*, 10 (**2000**), 2341–2359.

[76] Ackler, H.D.; French, R.H.; Chang, Y.M.: Comparisons of hamaker constants for ceramic systems with intervening vacuum or water: From force laws and physical properties. *J. Colloid Interface Sci. 179*, 2 (**1996**), 460–469.

[77] Derjaguin, B.V.; Landau, L.D.: Theory of stability of highly charged lyophobic sols and adhesion of highly charged particles in electrolytes. *Acta Physicochim. URSS 14* (**1941**), 633–652.

[78] Verwey, E.J.W.; Overbeek, J.T.G.: *Theory of Stability of Lyophobic Colloids*. Elsevier, Amsterdam, **1948**.

[79] Atkins, P.; de Paula, J.: *Physical Chemistry*. 8th edn., W.H. Freeman, New York, **2006**.

[80] Feke, D.L.; Prabhu, N.D.; Mann, J.A.: A formulation of the short-range repulsion between spherical colloidal particles. *J. Phys. Chem. 88*, 23 (**1984**), 5735–5739.

[81] Ong, Y.L.; Razatos, A.; Georgiou, G.; Sharma, M.M.: Adhesion forces between *E. coli* bacteria and biomaterial surfaces. *Langmuir 15*, 8 (**1999**), 2719–2725.

[82] Bergendahl, J.; Grasso, D.: Prediction of colloid detachment in a model porous media: Thermodynamics. *AIChE J. 45*, 3 (**1999**), 475–484.

[83] Batchelor, G.K.: Brownian diffusion of particles with hydrodynamic interaction. *J. Fluid Mech. 74* (**1976**), 1–29.

[84] Beenakker, C.W.J.; Mazur, P.: Diffusion of spheres in suspension: Three-body hydrodynamic interaction effects. *Phys. Lett. A 91*, 6 (**1982**), 290–291.

[85] Beenakker, C.W.J.; Mazur, P.: Self-diffusion of spheres in a concentrated suspension. *Physica A 120* (**1983**), 388–410.

[86] Beenakker, C.W.J.; Mazur, P.: Diffusion of spheres in a concentrated suspension: Resummation of many-body hydrodynamic interactions. *Phys. Lett. A 98*, 1 (**1983**), 22–24.

[87] Beenakker, C.W.J.; Mazur, P.: Diffusion of spheres in a concentrated suspension II. *Physica A 126* (**1984**), 349–370.

[88] Paciejewska, K.M.; Babick, F.: The influence of aluminium (III) and iron (III) ions on the electrokinetic potential of silica suspensions, **2006**. Submitted for publication.

[89] Binks, B.P.; Lumsdon, S.O.: Stability of oil-in-water emulsions stabilised by silica particles. *Phys. Chem. Chem. Phys. 1*, 12 (**1999**), 3007–3016.

[90] Grasso, D.; Subramaniam, K.; Butkus, M.; Strevett, K.; Bergendahl, J.: A review of non-dlvo interactions in environmental colloidal systems. *Rev. Env. Sci Bio/Technol. 1*, 1 (**2002**), 17–38.

[91] Knoblich, B.; Gerber, T.: Aggregation in SiO_2 sols from sodium silicate solutions. *J. Non-Cryst. Solids 283*, 1-3 (**2001**), 109–113.

[92] Einstein, A.: Über die von der molekularkinetischen Theorie der Wärme geforderte Bewegung von in ruhenden Flüssigkeiten suspendierten Teilchen (On the motion of suspended particles in quiescent fluids required by the molecular-kinetic theory of heat). *Ann. Phys. 17* (**1905**), 549–560.

[93] Einstein, A.: Zur Theorie der Brownschen Bewegung (On the theory of Brownian motion). *Ann. Phys. 19* (**1906**), 371–381.

[94] Willemse, A.: *Optical measuring techniques for particulate systems at the fringes of concentration*. Ph.D. thesis, TU Delft, **1998**.

[95] Richtering, W.; Müller, H.: Comparison between viscosity and diffusion in monodisperse and bimodal colloidal suspensions. *Langmuir 11*, 10 (**1995**), 3699–3704.

[96] Schätzel, K.: Single-photon correlation techniques. In *Dynamic Light Scattering: The method and some applications*, edited by Brown, W., no. 49 in Monographs on the physics and chemistry of materials, Clarendon Press, Oxford, **1993**, pp. 76–148.

[97] Berne, B.J.; Pecora, R.: *Dynamic Light Scattering - with Applications to Chemistry, Biology, and Physics*. Robert E. Krieger Publishing Company, Malabar, **1990**.

[98] Siegert, A.J.F.: On the fluctuations in signals returned by many independently moving scatterers. *MIT Rad. Lab. Rep. 465*, Massachusetts Institute of Technology, **1943**.

[99] Finsy, R.; de Jaeger, N.; Sneyers, R.; Gelade, E.: Particle sizing by photon correlation spectroscopy. part iii: Mono and bimodal distributions and data analysis. *Part. Part. Syst. Charact. 9* (**1992**), 125–137.

[100] Štěpánek, P.: Data analysis in dynamic light scattering. In *Dynamic Light Scattering: The method and some applications*, edited by Brown, W., no. 49 in Monographs on the physics and chemistry of materials, Clarendon Press, Oxford, **1993**, pp. 177–240.

[101] Ruf, H.: Data accuracy and resolution in particle sizing by dynamic light scattering. *Adv. Colloid Interface Sci. 46* (**1993**), 333–342.

[102] Koppel, D.E.: Analysis of macromolecular polydispersity in intensity correlation spectroscopy: The method of cumulants. *J. Chem. Phys. 57*, 11 (**1972**), 4814–4820.

[103] Finsy, R.; de Groen, P.; Deriemaeker, L.; van Laethem, M.: Singular value analysis and reconstruction of photon correlation data equidistant in time. *J. Chem. Phys. 91*, 12 (**1989**), 7374–7383.

[104] Finsy, R.; de Groen, P.; Deriemaeker, L.; Geladé, E.; Joosten, J.: Data analysis of multi-angle photon correlation measurements without and with prior knowledge. *Part. Part. Syst. Charact. 9* (**1992**), 237–251.

[105] Abramowitz, M.; Stegun, I.A. (eds.): *Handbook of Mathematical Functions With Formulas, Graphs and Mathematical Tables*. 10th edn., no. 55 in Applied Mathematics Series, US Department of Commerce, National Bureau of Standards, Washington D.C., **1973**.

[106] Hassan, P.A.; Kulshreshtha, S.K.: Modification to the cumulant analysis of polydispersity in quasielastic light scattering data. *J. Colloid Interface Sci. 300*, 2 (**2006**), 744–748.

[107] Ostrowsky, N.; Sornette, D.; Parker, P.; Pike, E.R.: Exponential sampling method for light-scattering polydispersity analysis. *Opt. Acta 28*, 8 (**1981**), 1059–1070.

[108] Grabowski, E.F.; Morrison, I.D.: Particle size distributions from analyses of quasi-elastic light-scattering data. In *Measurement of Suspended Particles by Quasi-Elastic Light Scattering,*, edited by Dahneke, B.E., John Wiley & Sons Inc., New York, **1983**, pp. 199–236.

[109] Morrison, I.D.; Grabowski, E.F.; Herb, C.A.: Improved techniques for particle size determination by quasi-elastic light scattering. *Langmuir 1*, 4 (**1985**), 496–501.

[110] Livesey, A.; Licinio, P.; Delaye, M.: Maximum entropy analysis of quasielastic light scattering from colloidal dispersions. *J. Chem. Phys. 84*, 9 (**1986**), 5102–5107.

[111] Nyeo, S.L.; Chu, B.: Maximum-entropy analysis of photon correlation spectroscopy data. *Macromolecules 22*, 10 (**1989**), 3998–4009.

[112] Provencher, S.W.: Inverse problems in polymer characterization: Direct analysis of polydispersity with photon correlation spectroscopy. *Makromol. Chem. 180*, 1 (**1979**), 201–209.

[113] Provencher, S.W.: A constrained regularization method for inverting data represented by linear algebraic or integral equations. *Comp. Phys. Comm. 27*, 3 (**1982**), 213–227.

[114] Provencher, S.W.: Contin: A general purpose constrainded regularization program for inverting noisy linear algebraic and integral equations. *Comp. Phys. Comm. 27*, 3 (**1982**), 229–242.

[115] Provencher, S.W.; Štěpánek, P.: Global analysis of dynamic light scattering autocorrelation functions. *Part. Part. Syst. Charact. 13*, 5 (**1996**), 291–294.

[116] Tikhonov, A.N.; Goncharsky, A.; Stepanov, V.; Yagola, A.: *Numerical Methods for the Solution of Ill-Posed Problems*. Kluwer Academic Publishers, Dordrecht, **1995**.

[117] Calvetti, D.; Reichel, L.; Shuibi, A.: L-curve and curvature bounds for Tikhonov regularization. *Numer. Algorithms 35*, 2-4 (**2004**), 301–314.

[118] Honerkamp, J.; Maier, D.; Weese, J.: A nonlinear regularization method for the analysis of photon correlation spectroscopy data. *J. Chem. Phys. 98*, 2 (**1993**), 865–872.

[119] Maier, D.; Marth, M.; Honerkamp, J.; Weese, J.: Influence of correlated errors on the estimation of the relaxation time spectrum in dynamic light scattering. *Appl. Opt. 38*, 21 (**1999**), 4671–4680.

[120] Buttgereit, R.; Marth, M.; Honerkamp, J.: Estimation of distribution functions in light scattering: The regularization method and bayes' ansatz. *Macromol. Symp. 162* (**2000**), 149–171.

[121] Roths, T.; Marth, M.; Weese, J.; Honerkamp, J.: A generalized regularization method for nonlinear ill-posed problems enhanced for nonlinear regularization terms. *Comp. Phys. Comm. 139*, 3 (**2001**), 279–296.

[122] Weese, J.: A regularization method for nonlinear ill-posed problem. *Comp. Phys. Comm. 77*, 3 (**1993**), 429–440.

[123] Schätzel, K.: Noise on photon correlation data: I. autocorrelation functions. *Quantum Opt. 2* (**1990**), 287–305.

[124] Schätzel, K.: Suppression of multiple scattering by photon cross-correlation techniques. *J. Modern Opt. 38*, 9 (**1991**), 1849–1865.

[125] Kätzel, U.: Application of photon correlation spectroscopy to concentrated dispersions. *in Proceedings PARTEC 2004, International Congress for Particle Technology,* , Nuremberg, March 16-18, **2004**.

[126] Maret, G.; Wolf, P.E.: Multiple light scattering from disordered media. The effect of brownian motion of scatterers. *Z. Phys. B - Condensed Matter 65*, 4 (**1987**), 409–413.

[127] Pine, D.J.; Weitz, D.A.; Chaikin, P.M.; Herbolzheimer, E.: Diffusing wave spectroscopy. *Phys. Rev. Lett. 60*, 12 (**1988**), 1134–1137.

[128] Riese, D.O.; Vos, W.L.; Wegdam, G.H.; Poelwijk, F.J.; Abernathy, D.L.; Grübel, G.: Photon correlation spectroscopy: X rays versus visible light. *Phys. Rev. E 61*, 2 (**2000**), 1676–1680.

[129] Riese, D.O.: *Fluid Dynamics in Charge Stabilized Colloidal Suspensions*. Ph.D. thesis, University of Amsterdam, **2000**.

[130] Phillies, G.D.J.: Suppression of multiple scattering effects in quasielastic light scattering by homodyne cross-correlation techniques. *J. Chem. Phys. 74*, 1 (**1981**), 260–262.

[131] Drewel, M.; Ahrens, J.; Podschus, U.: Decorrelation of multiple scattering for an arbitrary scattering angle. *J. Opt. Soc. Am. A 7*, 2 (**1990**), 206–210.

[132] Aberle, L.B.; Hulstede, P.; Wiegand, S.; Schroer, W.; Staude, W.: Effective suppression of multiply scattered light in static and dynamic light scattering. *Appl. Opt. 37*, 27 (**1998**), 6511–6524.

[133] Aberle, L.B.; Staude, W.; Hennemann, O.D.: Three-dimensional cross correlation technique: influence of multiply scattered light in the rayleigh-gans regime. *Phys. Chem. Chem. Phys. 1*, 17 (**1999**), 3917–3921.

[134] Peters, R.; Georgalis, Y.; Sänger, W.: Accessing lysozyme nucleation with a novel dynamic light scattering detector. *Acta Cryst. D54*, 5 (**1998**), 873–877.

[135] Wiese, H.; Horn, D.: Single-mode fibers in fiber-optic quasielastic light scattering: A study of the dynamics of concentrated latex dispersions. *J. Chem. Phys. 94*, 10 (**1991**), 6429–6443.

[136] Kätzel, U.; Stintz, M.; Ripperger, S.: Untersuchungen zur Photonenkorrelationsspektroskopie im Rückstreubereich (Research of applications for photon correlation spectroscopy in the backscatter area). *Chem. Ing. Tech. 76*, 1 (**2004**), 66–69.

[137] Auweter, H.; Horn, D.: Fiber-optical quasi-elastic light scattering of concentrated dispersions. *J. Colloid Interface Sci. 105*, 2 (**1985**), 399–409.

[138] Müller, H.: *Diffusion und Viskosität von monodispersen und bidispersen konzentrierten Dispersionen (Diffusion and viscosity in monodisperse and bisdisperse concentrated dispersions)*. Diploma thesis, University of Freiburg, **1995**.

[139] Felderhof, B.U.: Diffusion of interacting brownian particles. *J. Phys. A.: Math. Gen. 11*, 5 (**1978**), 929–937.

[140] Ohtsuki, T.; Okano, K.: Diffusion coefficients of interacting brownian particles. *J. Chem. Phys. 77*, 3 (**1982**), 1443–1449.

[141] Mazur, P.; Geigenmüller, U.: A simple formula for the short-time self-diffusion coefficient in concentrated suspensions. *Physica A 146*, 3 (**1987**), 657–661.

[142] Saitô, N.: Concentration dependence of the viscosity of high polymer solutions. I. *J. Phys. Soc. Japan 5*, 1 (**1950**), 4–8.

[143] Batchelor, G.K.: Diffusion in a dilute polydisperse system of interacting spheres. *J. Fluid Mech. 131* (**1983**), 155–175.

[144] Finsy, R.: Use of one-parameter models for the assessment of particle interactions by photon correlation spectroscopy. *Part. Part. Syst. Charact. 7*, 2 (**1990**), 74–79.

[145] Nägele, G.: On the dynamics and structure of charge-stabilized suspensions. *Phys. Rep. 272* (**1996**), 215–372.

[146] Overbeck, E.; Sinn, C.; Watzlawek, M.: Enhanced structural correlations accelerate diffusion in charge-stabilized colloidal suspensions. *Phys. Rev. E 60*, 2 (**1999**), 1936–1939.

[147] van Saarloos, W.: On the hydrodynamic radius of fractal aggregates. *Physica A 147*, 1-2 (**1987**), 280–296.

[148] Vanni, M.: Creeping flow over spherical permeable aggregates. *Chem. Eng. Sci. 55*, 3 (**2000**), 685–698.

[149] Chernyakov, A.L.: Hydrodynamic drag of a fractal cluster. *J. Exp. Theor. Phys. 93*, 4 (**2001**), 771–776.

[150] Riseman, J.; Kirkwood, J.G.: The intrinsic viscosity, translational and rotatory diffusion constants of rod-like macromolecules in solution. *J. Chem. Phys. 18*, 4 (**1950**), 512–516.

[151] Meakin, P.; Chen, Z.Y.; Deutch, J.M.: The translational friction coefficient and time dependent cluster size distribution of three dimensional cluster–cluster aggregation. *J. Chem. Phys. 82*, 8 (**1985**), 3786–3789.

[152] Wiltzius, P.: Hydrodynamic behavior of fractal aggregates. *Phys. Rev. Lett. 58*, 7 (**1987**), 710–713.

[153] Lattuada, M.; Wu, H.; Morbidelli, M.: Hydrodynamic radius of fractal clusters. *J. Colloid Interface Sci. 268* (**2003**), 96–105.

[154] Lattuada, M.; Sandkühler, P.; Wu, H.; Sefcik, J.; Morbidelli, M.: Aggregation kinetics of polymer colloids in reaction limited regime: experiments and simulation. *Adv. Colloid Interface Sci. 103* (**2003**), 33–56.

[155] Lattuada, M.; Wu, H.; Morbidelli, M.: Rotational diffusivity of fractal clusters. *Langmuir 20* (**2004**), 5630–5636.

[156] Griffin, W.G.; Griffin, M.C.A.: Time-dependent polydispersity of growing colloidal aggregates: Predictions from dynamic light scattering theory. *J. Chem. Soc. Faraday Trans. 89*, 15 (**1993**), 2879–2889.

[157] Ju, R.T.C.; Frank, C.W.; Gast, A.P.: CONTIN analysis of colloidal aggregates. *Langmuir 8* (**1992**), 2165–2171.

[158] Filippov, A.V.: Drag and torque on clusters of *N* arbitrary spheres at low reynolds number. *J. Colloid Interface Sci. 229*, 1 (**2000**), 184–195.

[159] Coelho, D.; Thovert, J.F.; Thouy, R.; Adler, P.M.: Hydrodynamic drag and electrophoresis of suspensions of fractal aggregates. *Fractals 5*, 3 (**1997**), 507–522.

[160] Binder, C.; Feichtinger, C.; Schmid, H.J.; Thürey, N.; Peukert, W.; Rüde, U.: Simulation of the hydrodynamic drag of aggregated particles. *J. Colloid Interface Sci. 301*, 1 (**2006**), 155–167.

[161] Lindsay, H.M.; Klein, R.; Weitz, D.A.; Lin, M.Y.; Meakin, P.: Effect of rotational diffusion on quasielastic light scattering from fractal colloidal aggregates. *Phys. Rev. A 38*, 5 (**1988**), 2614–2626.

[162] Garcia de la Torre, J.; Lopez Martinez, M.C.; Garcia Molina, J.J.: Approximate methods for calculating rotational diffusion constants of rigid macromolecules. *Macromolecules 20*, 3 (**1987**), 661–666.

[163] Kuntzsch, T.: *Erfassung und Beeinflussung des Zustandes von Poliersuspensionen für das chemisch-mechanische Polieren (CMP) in der Halbleiterbauelementfertigung - (Aquisition and manipulation of the disperse state of polishing suspensions for chemical-mechanical planarization (CMP) in the production of semiconductor components)*. Ph.D. thesis, TU Dresden, **2004**.

[164] Kätzel, U.: *Studying particle clusters with optical particle measurement techniques*. Diploma thesis, TU Dresden, **2003**.

[165] Vorbau, M.: *Ultraschalldämpfungsverhalten von pyrogenen Kieselsäuren - (Ultrasonic attenuation behavior of pyrogenic silica suspensions)*. Student project, TU Dresden, **2006**.

[166] Dingenouts, N.: *Röntgenkleinwinkelstreuung als Methodik der Strukturanalyse teilgeordneter kolloidaler Systeme (Small angle X-ray scattering as a methodology for the structural analysis of partly-ordered colloids*. Ph.D. thesis, University of Karlsruhe, **1999**.

[167] Bedrich, R.: *Geometrische und hydrodynamische Eigenschaften fraktaler Aggregate (Geometric and hydrodynamic properties of fractal aggregates)*. Diploma thesis, TU Dresden, **2006**.

[168] Langevin, P.: Sur la théorie du mouvement Brownien (On the theory of Brownian motion). *Compt. Rend. Acad. Sci. 146* (**1908**), 530–533.

[169] Lamb, H.; Caflisch, R.: *Hydrodynamics*. 6th edn., Cambridge University Press, Cambridge, UK, **1993**.

[170] Hyeon-Lee, J.; Beaucage, G.; Pratsinis, S.E.; Vemury, S.: Fractal analysis of flame-synthesized nanostructured silica and titania powders using small-angle X-ray scattering. *Langmuir 14*, 20 (**1998**), 5751–5756.

[171] Kerker, M.: *The Scattering of Light and Other Electromagnetic Radiation*. No. 16 in Physical Chemistry: A Series of Monographs, Academic Press, New York, **1969**.

[172] Jolliffe, I.T.: *Principal Components Analysis*. 2nd edn., Springer series in statistics, Springer-Verlag, Berlin, **2002**.

[173] Xu, R.: Shear plane and hydrodynamic diameter of microspheres in suspension. *Langmuir 14*, 10 (**1998**), 2593–2597.

[174] Sandkühler, P.; Sefcik, J.; Morbidelli, M.: Kinetics of gel formation in dilute dispersions with strong attractive particle interactions. *Adv. Colloid Interface Sci. 108-109* (**2004**), 133–143.

[175] Tanaka, H.; Jabbari-Farouji, S.; Meunier, J.; Bonn, D.: Nonergodic states of charged colloidal suspensions: Repulsive and attractive glasses and gels. *Phys. Rev. E 69*, 3 (**2004**), Art. No. 031404.

[176] Kroon, M.; Wegdam, G.H.; Sprik, R.: Dynamic light scattering studies on the sol-gel transition of a suspension of anisotropic colloidal particles. *Phys. Rev. E 54* (**1996**), 6541–6550.

[177] Ruzicka, B.; Zulian, L.; Ruocco, G.: Ergodic to non-ergodic transition in low concentration laponite. *J. Phys.: Condens. Matter 16* (**2004**), S4993–S5002.

[178] Mongondry, P.; Tassin, J.F.; Nicolai, T.: Revised state diagram of laponite dispersions. *J. Colloid Interface Sci. 283* (**2005**), 397–405.

[179] Bandyopadhyay, R.; Liang, D.; Yardimci, H.; Sessoms, D.A.; Borthwick, M.A.; Mochrie, S.G.J.; Harden, J.L.; Leheny, R.L.: Evolution of particle-scale dynamics in an aging clay suspension. *Phys. Rev. Lett. 93* (**2004**), Art. No. 228302.

[180] Tanaka, H.; Jabbari-Farouji, S.; Meunier, J.; Bonn, D.: Kinetics of ergodic-to-nonergodic transitions in charged colloidal suspensions: Aging and gelation. *Phys. Rev. E 71* (**2005**), Art. No. 021402.

[181] Li, L.; Harnau, L.; Rosenfeldt, S.; Ballauff, M.: Effective interaction of charged platelets in aqueous solution: Investigations of colloid laponite suspensions by static light scattering and small-angle X-ray scattering. *Phys. Rev. E 72* (**2005**), Art. No. 051504.

[182] Nicolai, T.; Cocard, S.: Structure of gels and aggregates of disk-like colloids. *Eur. Phys. J. E 5* (**2001**), 221–227.

[183] Szász, D.: Boltzmann's ergodic hypothesis, a conjecture for centuries? *Studia Sci. Math. Hung. 31* (**1996**), 299–322.

[184] Iler, R.K.: *The Chemistry of Silica*. Wiley Interscience, New York, **1979**.

[185] Bonn, D.; Tanaka, H.; Wegdam, G.; Kellay, H.; Meunier, J.: Aging of a colloidal wigner glass. *Europhys. Lett. 45*, 1 (**1998**), 52–57.

[186] Kroon, M.: *Structure and Formation of a Gel of Colloidal Discs*. Ph.D. thesis, University of Amsterdam, **1998**.

[187] Abou, B.; Bonn, D.; Meunier, J.: Aging dynamics in a colloidal glass. *Phys. Rev. E 64* (**2001**), Art. No. 021510.

[188] Richter, T.: *Beschreibung von Phasenübergängen in kolloidalen Systemen (Characterization of phase transitions in colloidal systems)*. Diploma thesis, TU Dresden, **2005**.

[189] Kätzel, U.; Richter, T.; Stintz, M.; Barthel, H.; Gottschalk-Gaudig, T.: Phase transitions of pyrogenic silica suspensions: A comparison to model Laponite. *Phys. Rev. E*, Accepted for publication.

List of Figures

List of Tables

A Relation between Diffusion Coefficients and the Field Correlation Function

The field correlation function is defined as the first-order correlation of the far field amplitudes of the scattered electric field:

$$G_1(\tau) = \langle u(\mathbf{s},t) \cdot u(\mathbf{s},t+\tau)^* \rangle \tag{A.1}$$

where the asterisk denotes the complex conjugate value. This equation can now be explicitly expressed as a sum over N particle contributions (see eq. 2.34):

$$\begin{aligned} G_1(\tau) = \Bigg\langle \sum_{i=1}^{N} E_{inc}(X_i,Y_i) a_i \exp\left[\mathrm{i}\mathbf{s}\mathbf{r}_i(t)\right] \cdot \ldots \\ \ldots \cdot \sum_{j=1}^{N} E_{inc}(X_j,Y_j) a_j^* \exp\left[-\mathrm{i}\mathbf{s}\mathbf{r}_j(t+\tau)\right] \Bigg\rangle \\ = \sum_{i=1}^{N}\sum_{j=1}^{N} E_{inc}^2 \left\langle a_i a_j^* \right\rangle \left\langle \exp\left[\mathrm{i}\mathbf{s}\Delta\mathbf{r}_i(\tau)\right] \right\rangle \end{aligned} \tag{A.2}$$

The first term in the double sum is just the average scattering amplitude squared times the average number of particles in the intersection of the incident beam and the aperture of the detection optics, the measurement volume. The second term is an ensemble average over all particles in the measurement volume. Thus, it gives identical values for each particle and can be factored out:

$$\begin{aligned} G_1(\tau) &= N E_{inc}^2 \left\langle |a_i|^2 \right\rangle \left\langle \exp\left[\mathrm{i}\mathbf{s}\Delta\mathbf{r}(t)\right] \right\rangle \\ &= N E_{inc}^2 \left\langle |a_i|^2 \right\rangle F_s(\mathbf{s},\tau) \end{aligned} \tag{A.3}$$

Note, that in going from eq. A.2 to A.3 it is implicitly assumed that the time average is equal to the spatial ensemble average. This assumption is known as the ergodic hypothesis of Boltzmann [183] and as such is only valid for ergodic systems, i.e. a system where each particle can capture every point in space. This is usually the case in suspensions except for high concentrations or systems undergoing a phase transition.

The self-intermediate scattering function $F_s(\mathbf{s},t)$ is the Fourier transform of the probability distribution $q(\mathbf{R},\tau)$ which describes the probability that a particle i will experience a displacement $\mathbf{R}$ in time τ:

$$q(\mathbf{R},\tau) = \langle \delta\left(\mathbf{R} - [\mathbf{r}_i(\tau) - \mathbf{r}_i(0)]\right)\rangle \tag{A.4}$$

$$F_s(\mathbf{s},\tau) = \int_0^\infty \exp\left(\mathrm{i}\mathbf{s}\mathbf{R}\right) q(\mathbf{R},\tau)\, d^3\mathbf{R} \tag{A.5}$$

where δ is the Delta function. Since $\Delta\mathbf{r}(0) = 0$:

$$q(\mathbf{R},0) = \langle \delta(\mathbf{R})\rangle = \delta(\mathbf{R}) \tag{A.6}$$

$$\Downarrow$$

$$F_s(\mathbf{s},\mathbf{0}) = 1 \tag{A.7}$$

If a particle with size x and translational diffusion coefficient D_t can move freely in space (dilute limit) then $q(\mathbf{R},\tau)$ can be considered to be a solution to Fick's second law of diffusion [97]:

$$\frac{\partial}{\partial\tau} q(\mathbf{R},\tau) = D_t\, \nabla^2 q(\mathbf{R},\tau) \tag{A.8}$$

Application of a Fourier transformation to eq. A.8 yields:

$$\frac{d}{d\tau} F_s(\mathbf{s},\tau) = D_t s^2 F_s(\mathbf{s},\tau) \tag{A.9}$$

This equation can be solved by a separation of variables and the use of the initial condition eq. A.7 to give:

$$F_s(\mathbf{s},\tau) = \exp\left(-D_t s^2 \tau\right) \tag{A.10}$$

By combination of eq. A.10 with eqns. A.3 and 2.37 the usual forms of the normalized electric field and intensity autocorrelation functions are obtained:

$$g_1(\tau) = \exp\left(-D_t s^2 \tau\right) \tag{A.11}$$

$$g_2(\tau) - 1 = b \exp\left(-2D_t s^2 \tau\right) \tag{A.12}$$

B Computation of the Translation and Rotation Matrix for a Given Aggregate

Here, the solution of the Stokes equation for a predefined aggregate is given. Derivation has been carried out by Bedrich [167] following Filippov [158]. Symbols used here do not necessarily correspond to the list of symbols in the front matter of this thesis, relevant connections will be explained.

The translation and rotation matrix are computed from the total drag force and the total torque on an aggregate considering flow in three independent directions, e.g. the X-, Y- and Z-direction in Cartesian coordinates.

$$\mathbf{F} = -6\pi\eta_f R_{prim} \boldsymbol{\Psi} \cdot \mathbf{v} \tag{B.1}$$

$$\mathbf{T} = -8\pi\eta_f R_{prim}^3 \boldsymbol{\Xi} \cdot \boldsymbol{\omega} \tag{B.2}$$

In the program, the algorithm is run six times with different initial velocities $\mathbf{v}$ and rotations $\boldsymbol{\omega}$, respectively (e.g. $\mathbf{v}_1 = [1, 0, 0]$ then $\mathbf{v}_2 = [0, 1, 0], \ldots$).

The total force on an aggregate is calculated as a superposition of the forces on the single primary particles:

$$\mathbf{F} = \sum_{i=1}^{N_{prim}} \mathbf{F}_i \tag{B.3}$$

Similarly, the total torque can be computed from the single torques and the drag forces together with the distance of the primary particle to the center of gravity of the aggregate:

$$\mathbf{T} = \sum_{i=1}^{N_{prim}} \mathbf{T}_i + \mathbf{r}_i \times \mathbf{F}_i \tag{B.4}$$

As the center of gravity is assigned the null vector after the generation of the aggregate, only

the position vector $\mathbf{r}_i$ is needed. The multipole expansion solution for $\mathbf{F}_i$ and $\mathbf{T}_i$ is given by:

$$\mathbf{F}_i = -4\pi\eta_f \left[-\left(b^i_{11} - \frac{1}{2} b^i_{-11} \right) \mathbf{e}_x - i \left(b^i_{11} + \frac{1}{2} b^i_{-11} \right) \mathbf{e}_y + b^i_{01} \mathbf{e}_z \right] \tag{B.5}$$

$$\mathbf{T}_i = -8\pi\eta_f \left[-\left(c^i_{11} - \frac{1}{2} c^i_{-11} \right) \mathbf{e}_x - i \left(c^i_{11} + \frac{1}{2} c^i_{-11} \right) \mathbf{e}_y + c^i_{01} \mathbf{e}_z \right] \tag{B.6}$$

where $\mathbf{e}$ is the unit vector. The expansion coefficients can be determined from the solution of a system of linear equations as given by the matrix equation:

$$\begin{bmatrix} D^{ij}_{klmn} & E^{ij}_{klmn} & F^{ij}_{klmn} \\ G^{ij}_{klmn} & H^{ij}_{klmn} & L^{ij}_{klmn} \\ 0 & M^{ij}_{klmn} & N^{ij}_{klmn} \end{bmatrix} \cdot \begin{bmatrix} a^i_{mn} \\ b^i_{mn} \\ c^i_{mn} \end{bmatrix} = \frac{1}{R^n_i} \begin{bmatrix} X^i_{mn} \\ 0 \\ Z^i_{mn} \end{bmatrix} \tag{B.7}$$

The size of the equation system is determined by the indices k, l, m, n and i, j. While i and j run over the number of primary particles in the aggregate and are, therefore, restricted, n and l are typically infinite, i.e. $l, n = [1, \infty)$ and $k = [-l, l]$ as well as $m = [-n, n]$. Thus, a cut parameter L has to be defined to make the summation finite:

$$\sum_{l=1}^{\infty} \Rightarrow \sum_{l=1}^{L} \tag{B.8}$$

The cut parameter influences the accuracy of the solution on the one hand and the computational effort on the other hand. The number of coefficients that have to be determined for the solution of the equation are [167]:

$$N_{Coef} = 3 N_{prim} L (L+2) \tag{B.9}$$

i.e. the accuracy shows a square dependence while the number of primary particles is linearly correlated. Bedrich [167] has conducted examinations on the convergence of the algorithm in dependence of L and found that already for $L = 2$ the relative error compared to high L-values is smaller than 1 %. All results presented in this work have been carried out using a cut parameter of $L = 2$.

If now the number of unknown coefficients is determined, it is possible to compute the matrix elements of eq. B.7. If $j = i$ then:

$$F^{ii}_{klmn} = L^{ii}_{klmn} = M^{ii}_{klmn} = 0 \tag{B.10}$$

If additionally $k \neq m$ or $l \neq n$:

$$D^{ii}_{klmn} = E^{ii}_{klmn} = G^{ii}_{klmn} = H^{ii}_{klmn} = N^{ii}_{klmn} = 0 \tag{B.11}$$

else:

$$D^{ii}_{mnmn} = -(n+1)R_i^{-2(n+1)} \tag{B.12}$$

$$E^{ii}_{mnmn} = \frac{n+1}{2(2n-1)}R_i^{-2n} \tag{B.13}$$

$$G^{ii}_{mnmn} = (n+1)(n+2)\left(1+2n\frac{\delta}{R_i}\right)R_i^{-(2n+3)} \tag{B.14}$$

$$H^{ii}_{mnmn} = -\frac{n+1}{2(2n-1)}\left(n+2(n^2-1)\frac{\delta}{R_i}\right)R_i^{-(2n+1)} \tag{B.15}$$

$$N^{ii}_{mnmn} = n(n+1)\left(1+(n+2)\frac{\delta}{R_i}\right)R_i^{-(2n+1)} \tag{B.16}$$

Here, R_i is the radius of the i-th primary particle and δ is the sliplength as defined in Chap. 5.3 which may now be set to zero to obtain a sticky boundary.

If now interactions between particles $i \neq j$ are to be considered, the expansion coefficients are defined based on the addition theorems for solid spherical harmonics that lead to [167]:

$$C^{ij}_{mnkl} = (-1)^{l+k}\frac{(n+l-m+k)!}{(l+k)!(n-m)!}u_{(m-k)(n+l)}(\mathbf{r}_{ij}) \tag{B.17}$$

where $u_{mn}(\mathbf{r}_{ij})$ is the irregular solid spherical harmonic defined as:

$$u_{mn}(\mathbf{r}_{ij}) = \frac{1}{r^{n+1}}P_n^m(\cos\theta)\exp(\mathrm{i}m\varphi) \tag{B.18}$$

Here, the distance vector $\mathbf{r}_{ij}$ between particle i and particle j has to be given in spherical coordinates $\mathbf{r}_{ij}(r,\theta,\varphi)$. $P_n^m(x)$ is the associated Legendre polynomial in the following notation:

$$P_n^m(x) = (-1)^m\frac{1}{2^n n!}(1-x^2)^{\frac{m}{2}}\frac{d^{n+m}}{dx^{n+m}}(x^2-1)^n \tag{B.19}$$

Based on this definition there are some special cases in which:

$$C^{ij}_{klmn} = 0 \quad \Longleftrightarrow \quad \begin{cases} |k| > l \\ |m| > n \end{cases} \tag{B.20}$$

Once the C^{ij}_{klmn} are computed all the other coefficients D, E, F, G, H, L, M and N can be obtained:

$$D^{ij}_{klmn} = \frac{n}{R_i}C^{ij}_{klmn} \tag{B.21}$$

$$
\begin{aligned}
E_{klmn}^{ij} = & \frac{(2(l+1)-n(l-2))R_i^2 - n(l-2)r_{ij}^2}{2l(2l-1)R_i} C_{klmn}^{ij} \\
& -(n-m)\,\zeta_{ij}\frac{1}{R_i}\Lambda_{ln}^{-} C_{klm(n-1)}^{ij} - (n+m+1)\,\zeta_{ij} R_i \Lambda_{ln}^{+} C_{klm(n+1)}^{ij} \\
& +\eta_{ij}\frac{1}{R_i}\Lambda_{ln}^{-} C_{kl(m-1)(n-1)}^{ij} - \eta_{ij} R_i \Lambda_{ln}^{+} C_{kl(m-1)(n+1)}^{ij} \\
& -(n-m)(n-m-1)\,\xi_{ij}\frac{1}{R_i}\Lambda_{ln}^{-} C_{kl(m+1)(n-1)}^{ij} \\
& +(n+m+2)(n+m+1)\,\xi_{ij} R_i \Lambda_{ln}^{+} C_{kl(m+1)(n+1)}^{ij}
\end{aligned}
\tag{B.22}
$$

$$
F_{klmn}^{ij} = \frac{i}{R_i}\left[(n+m+1)(n-m)\,\xi_{ij} C_{kl(m+1)n}^{ij} + m\,\zeta_{ij} C_{klmn}^{ij} + \eta_{ij} C_{kl(m-1)n}^{ij}\right] \tag{B.23}
$$

$$
G_{klmn}^{ij} = \frac{n}{R_i^2}\left[n-1-2\frac{\delta}{R_i}\left(n^2-1\right)\right] C_{klmn}^{ij} \tag{B.24}
$$

$$
\begin{aligned}
H_{klmn}^{ij} = & \left(n+1-2\frac{\delta}{R_i}n(n+2)\right)\left[\frac{2(l+1)-n(l-2)}{2l(2l-1)} C_{klmn}^{ij}\right. \\
& -(n+m+1)\,\Lambda_{ln}^{+}\zeta_{ij} C_{klm(n+1)}^{ij} - \Lambda_{ln}^{+}\eta_{ij} C_{kl(m-1)(n+1)}^{ij} \\
& \left.+(n+m+2)(n+m+1)\,\Lambda_{ln}^{+}\xi_{ij} C_{kl(m+1)(n+1)}^{ij}\right] \\
& -\frac{1}{R_i^2}\left(n-1-2\frac{\delta}{R_i}\left(n^2-1\right)\right)\left[\frac{n(l-2)r_{ij}^2}{2l(2l-1)} C_{klmn}^{ij}\right. \\
& +(n-m)\,\Lambda_{ln}^{-}\zeta_{ij} C_{klm(n-1)}^{ij} - \Lambda_{ln}^{-}\eta_{ij} C_{kl(m-1)(n-1)}^{ij} \\
& \left.+(n-m-1)(n-m)\,\Lambda_{ln}^{-}\xi_{ij} C_{kl(m+1)(n-1)}^{ij}\right]
\end{aligned}
\tag{B.25}
$$

$$
L_{klmn}^{ij} = \frac{1}{R_i}\left(n-1-2\frac{\delta}{R_i}\left(n^2-1\right)\right) F_{klmn}^{ij} \tag{B.26}
$$

$$
M_{klmn}^{ij} = \frac{R_i}{l}\left(1+\frac{\delta}{R_i}(n-1)\right) F_{klmn}^{ij} \tag{B.27}
$$

$$
\begin{aligned}
N_{klmn}^{ij} = & \left(1+\frac{\delta}{R_i}(n-1)\right)\left[n(n+1)\,C_{klmn}^{ij} + n(n+m+1)\,\zeta_{ij} C_{klm(n+1)}^{ij}\right. \\
& \left.-n(n+m+1)(n+m+2)\,\xi_{ij} C_{kl(m+1)(n+1)}^{ij} + n\,\eta_{ij} C_{kl(m-1)(n+1)}^{ij}\right]
\end{aligned}
\tag{B.28}
$$

In the eqns. B.21-B.28 R_i means the radius if the i-th sphere, δ is the sliplength and r_{ij} the shortest center-to-center distance between particle i and j.

The terms Λ_{ln}^{+}, Λ_{ln}^{-}, ξ_{ij}, η_{ij} and ζ_{ij} are auxiliary variables defined as:

$$\Lambda_{ln}^{+} = \frac{(n+1)(l-2)-(l+1)}{(2n+3)\,l\,(2l-1)} \tag{B.29}$$

$$\Lambda_{ln}^{-} = \frac{(n-1)(l-2)-(l+1)}{(2n-1)\,l\,(2l-1)} \tag{B.30}$$

$$\xi_{ij} = \frac{1}{2}\left(r_{ij}^{x} + \mathrm{i}\, r_{ij}^{y}\right) \tag{B.31}$$

$$\eta_{ij} = \frac{1}{2}\left(r_{ij}^{x} - \mathrm{i}\, r_{ij}^{y}\right) \tag{B.32}$$

$$\zeta_{ij} = r_{ij}^{z} \tag{B.33}$$

Here, r_{ij}^{x}, r_{ij}^{y} and r_{ij}^{z} are the x-, y- and z-component of the distance vector $\mathbf{r}_{ij}$ in Cartesian coordinates.

Now, the matrix on the left-hand side of eq. B.7 is defined. The vector on the right-hand side incorporates the initial velocities and rotations in the following form:

$$X_{01}^{i} = v_{0z}^{i} \tag{B.34}$$

$$X_{11}^{i} = -\frac{1}{2}\left(v_{0x}^{i} - \mathrm{i}\, v_{0y}^{i}\right) \tag{B.35}$$

$$X_{-11}^{i} = v_{0x}^{i} + \mathrm{i}\, v_{0y}^{i} \tag{B.36}$$

$$Z_{01}^{i} = 2R_i\,\omega_{oz}^{i} \tag{B.37}$$

$$Z_{11}^{i} = -R_i\left(\omega_{ox}^{i} - \mathrm{i}\,\omega_{0y}^{i}\right) \tag{B.38}$$

$$Z_{-11}^{i} = 2R_i\left(\omega_{0x}^{i} + \mathrm{i}\,\omega_{0y}^{i}\right) \tag{B.39}$$

All other coefficients X_{mn}^{i} and Z_{mn}^{i} are equal to zero.

This is the principal solution of the Stokes equation. Special attention has to be paid to the cut parameter L. As it was sufficient in these examinations to use $L = 2$ it might be necessary to increase the value in other computations, e.g. when the primary particles are not equal in size.

C Scattering Angle Dependent Results of Cumulants Analysis

Table C.1: Harmonic mean diameter and polydispersity index of HDK® D05, C10P, S13 and V15 for scattering vectors from 0.0068 nm^{-1} – 0.0264 nm^{-1}.

Angle \ HDK®		D05		C10P		S13		V15	
θ [°]	s [nm^{-1}]	x_{DLS} [nm]	PDI	x_{DLS} [nm]	PDI	x_{DLS} [nm]	PDI	x_{DLS} [nm]	PDI
30	0.0068	350.4	0.142	312.0	0.154	295.7	0.137	265.0	0.174
35	0.0080	341.0	0.157	301.2	0.127	284.6	0.140	251.7	0.179
40	0.0090	320.3	0.137	291.1	0.123	274.8	0.143	246.1	0.166
45	0.0101	312.9	0.150	280.5	0.143	265.5	0.122	237.7	0.179
50	0.0112	304.3	0.146	272.1	0.142	258.2	0.138	233.0	0.122
55	0.0122	299.1	0.162	263.9	0.147	252.5	0.125	228.2	0.146
60	0.0132	296.4	0.148	260.7	0.136	245.1	0.132	221.7	0.085
65	0.0142	289.2	0.137	255.2	0.128	240.1	0.137	217.2	0.116
70	0.0152	—	—	—	—	236.5	0.133	216.1	0.114
75	0.0161	—	—	—	—	232.1	0.114	210.3	0.125
80	0.0170	272.8	0.154	242.0	0.137	226.4	0.119	209.0	0.104
85	0.0179	272.5	0.148	239.7	0.133	225.0	0.112	208.5	0.108
90	0.0187	271.5	0.141	238.5	0.139	221.9	0.093	202.9	0.120
95	0.0195	271.8	0.132	236.1	0.134	219.0	0.137	202.7	0.154
100	0.0203	270.7	0.150	233.7	0.136	216.5	0.119	198.5	0.095
105	0.0210	271.6	0.141	232.7	0.143	214.7	0.128	197.1	0.130
110	0.0217	269.7	0.139	232.5	0.143	217.0	0.113	196.1	0.128
173	0.0264	249.6	0.219	224.3	0.158	197.4	0.142	185.0	0.119

Table C.2: Harmonic mean diameter and polydispersity index of HDK® N20, T30 and T40 for scattering vectors from 0.0068 nm^{-1} – 0.0264 nm^{-1}.

HDK® / Angle		N20		T30		T40	
θ [°]	s [nm^{-1}]	x_{DLS} [nm]	PDI	x_{DLS} [nm]	PDI	x_{DLS} [nm]	PDI
30	0.0068	220.5	0.199	186.9	0.190	173.7	0.181
35	0.0080	214.0	0.157	186.4	0.169	168.9	0.182
40	0.0090	212.9	0.120	181.8	0.185	162.9	0.154
45	0.0101	204.9	0.159	180.3	0.205	161.2	0.155
50	0.0112	200.6	0.124	175.8	0.141	156.4	0.180
55	0.0122	196.0	0.152	173.0	0.156	157.4	0.147
60	0.0132	193.6	0.120	168.9	0.131	152.6	0.114
65	0.0142	190.6	0.107	166.0	0.158	150.4	0.159
70	0.0152	186.7	0.146	163.3	0.165	148.1	0.111
75	0.0161	180.7	0.146	160.9	0.120	147.0	0.138
80	0.0170	179.4	0.115	158.3	0.140	143.7	0.152
85	0.0179	176.6	0.131	156.9	0.126	141.7	0.148
90	0.0187	173.7	0.117	156.0	0.114	140.6	0.127
95	0.0195	171.9	0.114	152.9	0.131	138.8	0.142
100	0.0203	169.6	0.132	151.4	0.139	136.2	0.154
105	0.0210	168.6	0.127	150.4	0.136	136.2	0.124
110	0.0217	165.0	0.132	147.8	0.138	132.7	0.113
173	0.0264	155.8	0.187	140.0	0.162	129.4	0.174

D Computation of the Mean Aggregate Porosity

D.1 Sediment Porosity after Centrifugation

For this purpose a photocentrifuge (LUMiFuge 116, L.U.M. GmbH, Berlin, Germany) was used that allows for an online tracking of the sedimentation process by measuring space-resolved transmission profiles at fixed time intervals along the sedimentation cuvette. Two examples of the measured transmission profiles are given in Fig. D.1.

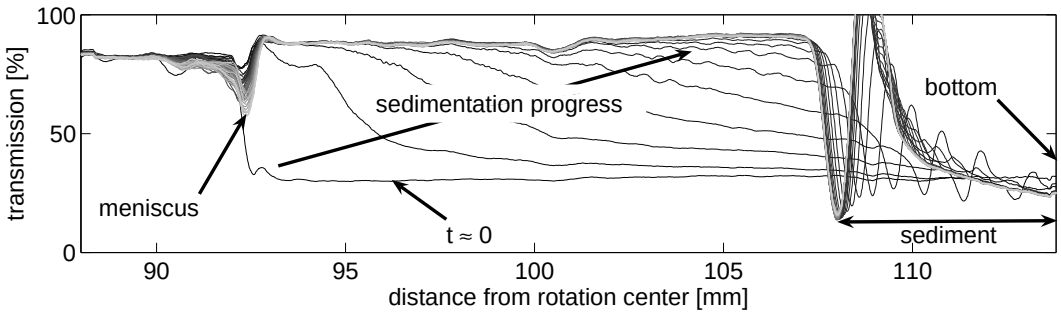

(a) $\varphi = 0.0743$, 3000 rpm, 10:44 h total centrifugation time

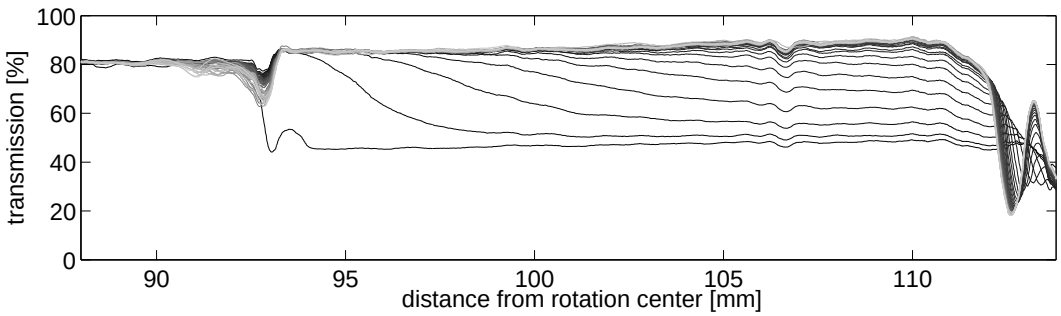

(b) $\varphi = 0.0200$, 3000 rpm, 3:30 h total centrifugation time

Figure D.1: Transmission profiles of the sedimentation of a HDK® D05 at pH 9, 0.01 M KNO_3 and (a) $\varphi = 0.0743$ and (b) $\varphi = 0.02$.

These profiles have to be read in the following way. The center of rotation (i.e. the axis of the rotor) is located on the left-hand side of the diagram. The meniscus designates the air/water interface in the cuvette. At the beginning of the centrifugation, the transmission drops immediately after the meniscus and attains a constant value down to the bottom of the cuvette, i.e. a constant particle concentration is measured. When centrifugation continues the suspension clarifies, a supernatant with a constant transmission is measured. The particles move to the bottom of the cuvette, where a sediment is built up (see Fig. D.1(a)). Since the position of the bottom of the cuvette is known on the x-axis, the height of the sediment h_{Sed} can be easily measured. From the volume fraction φ and the position of the meniscus (i.e. the height of the suspension in the cuvette h_{Susp}) the porosity of the sediment is computed by :

$$\varepsilon = 1 - \varphi \frac{h_{Susp}}{h_{Sed}} \tag{D.1}$$

Obviously, the determination of the sediment height is most accurate for high concentrated samples. This is counteracted by the long necessary centrifugation time. Therefore, a concentration of $\varphi = 0.02$ was used that gives a good compromise. To determine the compressibility of the sediment, suspensions of HDK® D05, S13 and V15 were used. Centrifugation was carried out at 1000 rpm until the suspension had completely settled. Then the number of revolutions was increased stepwise up to 3000 rpm and decreased again. Fig. D.2 shows the result exemplarily for a HDK® S13, the trend is the same for the other grades.

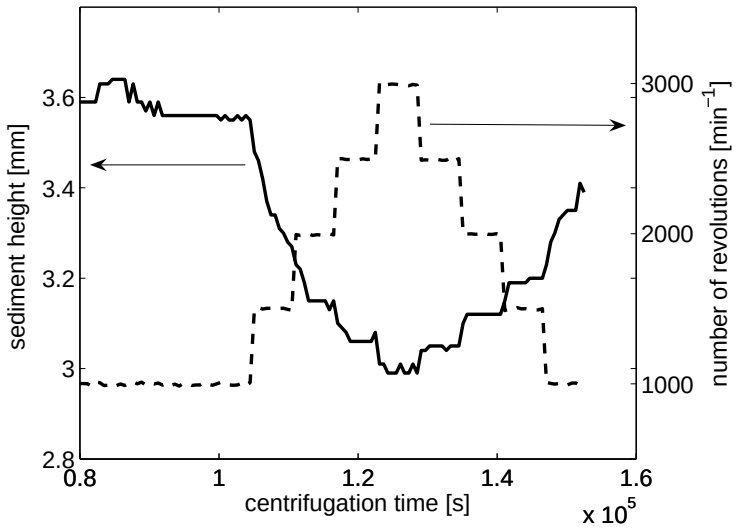

Figure D.2: Compressibility of the sediment determined at a HDK® S13 with $\varphi = 0.02$.

There is indeed a large dependence of the sediment volume on the force acting on the aggregates. The question arises, which sediment porosity can be chosen to describe pyrogenic silica

in suspension. The answer has to consider the fractal structure of the aggregates. Since the particles are rather open than compact they can interpenetrate if they come close enough. This will obviously decrease the determined porosity. This interpenetration increases when the force is increased. Therefore, a comparison has to be made concerning the force acting on the aggregates in suspension which is exactly $m_{agg} \cdot \mathrm{g}$. In Fig. D.3 the determined sediment porosities are plotted against the number of revolutions of the centrifuge. The number of revolutions resembling 1 g has been determined from the definition of the centrifugal number:

$$z = \frac{r\,\omega^2}{g} \quad \Rightarrow \quad n(z=1) = \sqrt{\frac{g}{4\pi^2 r_{Sed}}} \tag{D.2}$$

Then, a simple fit equation that approximates all three data sets equally well was used to determine the sediment porosity at 1 g:

$$\varepsilon = C_1 + C_2 \ln\left(\frac{N_{rev}}{s^{-1}}\right) \tag{D.3}$$

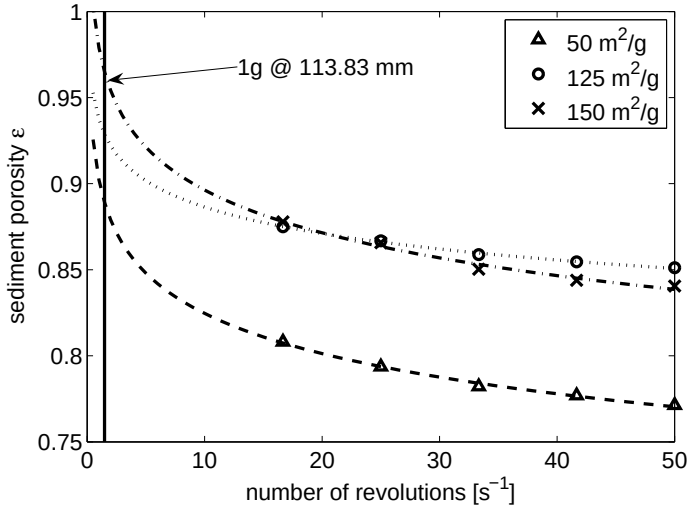

Figure D.3: Determination of the porosity of pyrogenic silica aggregates via extrapolation of sediment porosities.

The obtained porosities for pyrogenic silica aggregates are:

- $\varepsilon = 0.8891$ for HDK® D05
- $\varepsilon = 0.9288$ for HDK® S13 and
- $\varepsilon = 0.9650$ for HDK® V15.

These values show that pyrogenic silica indeed has a very open structure. With increasing size of the primary particles, the structure becomes denser. This is additionally verified by Tab. 6.4

since the grades with a small number of primary particles per aggregate should show a smaller porosity.

However, there are two constraints with the determination of the aggregate porosity using the centrifugation approach. Firstly, the results are obviously dependent on the chosen fit equation, an uncertainty of at least ± 0.02 is introduced. Additionally, it is not possible to conduct the same experiment for grades with a specific surface area larger than 150 m^2/g. Here, the sedimentation velocity at $\varphi = 0.02$ is so low that the maximum centrifugation time of ≈ 42.5 h for the LUMiFuge 116 is exceeded by far.

D.2 Porosity Estimate from Hydrodynamic and Structural Properties

This second approach uses the results of Chap. 5 and 6. Considering that an aggregate in suspension is equivalently described by a sphere having the same hydrodynamic radius of translation (see Tab. 6.3 and that it consists of a number of primary particles determined in Tab. 6.4, the mean radius of a primary particle can be determined from eq. 5.18 assuming DLCA generation mechanism for the aggregates:

$$R_{prim} = R_{h,t} \left(\frac{N_{prim}}{1.09} \right)^{-\frac{1}{1.96}} \tag{D.4}$$

Then, the radius of the volume-equivalent sphere R_V of an aggregate can be determined with:

$$R_V = R_{prim} \sqrt[3]{N_{prim}} \tag{D.5}$$

and finally the porosity ε is defined as:

$$\varepsilon = 1 - \frac{R_V^3}{R_{h,t}^3} \tag{D.6}$$

Tab. D.1 lists the results of the above equations. For comparison the primary particle size determined from gas adsorption (eq. 1.1) is given. Interestingly, the two radii are in good accordance, i.e. the porosity is not strongly dependent on the respective choice.

Again, the determined porosities show a very open structure of pyrogenic silica aggregates. Compared to the centrifugation results the porosities of HDK® D05 and S13 are very close but deviate slightly for HDK® V15. This, however, proves that both approaches give reliable values that can be used to determine effective concentrations of pyrogenic silica.

Table D.1: Computation of the mean hydrodynamic aggregate porosities for pyrogenic silica.

S_m (BET) $\left[\mathrm{m}^2/\mathrm{g}\right]$	$R_{h,t}$ [nm]	$R_{h,t}/R_g$	$\bar{N}_{prim}$ from Fig. 5.7 with $D_f^m = 1.8$	$\bar{R}_{prim}$ (eq. 5.18) with $R_{h,t}$ and $\bar{N}_{prim}$ [nm]	$\bar{R}_{prim}$ (BET) [nm]	R_V from R_{prim} [nm]	$\bar{\varepsilon}$
50	199.4	0.987	90	21.0	39.0−21.0	94.1	0.895
100	170.9	0.914	220	11.4	16.1−11.9	68.8	0.935
125	157.2	0.941	180	11.6	12.4−9.8	65.5	0.928
150	140.1	0.856	300	8.0	10.5−8.0	53.6	0.944
200	114.8	0.820	550	4.8	8.0−6.0	39.3	0.960
300	97.0	0.836	450	4.5	5.1−4.2	34.5	0.955
400	92.1	0.787	> 1000	2.8	3.8−3.1	28.4	0.971

E Relation between the Autocorrelation Function and the Correlation Function of the Fluctuating Field

The HPPS produces two results, the normalized autocorrelation function and a mean photon count rate that can be considered as mean scattered intensity $\bar{I} = \langle I(t) \rangle$. Then, the formulation of the static scattered intensity I_c can be reformulated using eq. 8.2 and eq. 8.3:

$$I_c = \sqrt{2 \langle I(t) \rangle^2 - g_2(0) \cdot \langle I(t) \rangle^2} = \bar{I} \sqrt{2 - g_2(0)} \tag{E.1}$$

The fluctuating intensity may now be substituted in eq. 8.1:

$$\frac{\langle I_{fl}(t) \rangle}{\langle I(t) \rangle} = \frac{\langle I(t) \rangle - I_c}{\langle I(t) \rangle} = 1 - \sqrt{2 - g_2(0)} \tag{E.2}$$

Kroon et al. [176] give the following equation for the computation of the CFF:

$$h(\tau) = 1 + \frac{\langle I(t) \rangle}{\langle I_{fl}(t) \rangle} \cdot \left\{ \sqrt{g_2(\tau) - g_2(0) + 1} - 1 \right\} \tag{E.3}$$

If eq. E.2 is now inserted the following relation is finally obtained:

$$h(\tau) = 1 + \frac{\sqrt{g_2(\tau) - g_2(0) + 1} - 1}{1 - \sqrt{2 - g_2(0)}} \tag{E.4}$$

Note that in going from the ACF to the CFF already a transformation of the second-order correlation to first-order has been conducted. Therefore, the CFF can be directly processed with algorithms requiring the field correlation function as input.